Bangor University

DOCTOR OF PHILOSOPHY

The Role of Clay Minerals in the Dynamics and Deposits of Sediment Gravity Flows

Baker, Meg

Award date:
2020

Awarding institution:
Bangor University

Bangor University

DOCTOR OF PHILOSOPHY

The Role of Clay Minerals in the Dynamics and Deposits of Sediment Gravity Flows

Baker, Meg

Award date:
2020

The Role of Clay Minerals in the Dynamics and Deposits of Sediment Gravity Flows

Megan Lorna Baker

Submitted in accordance with the requirements for the degree of Doctor of Philosophy

SCHOOL OF OCEAN SCIENCES
Bangor University
Menai Bridge
Isle of Anglesey
LL59 5AB
Wales

5TH FEBRUARY 2020

Declaration and Consent

Details of the Work

I hereby agree to deposit the following item in the digital repository maintained by Bangor University and/or in any other repository authorized for use by Bangor University.

Author Name: Megan Baker

Title: The role of clay minerals in the dynamics and deposits of sediment gravity flows

Supervisor/Department: Dr Jaco Baas, School of Ocean Sciences

Funding body (if any): Equinor

Qualification/Degree obtained: PhD

This item is a product of my own research endeavours and is covered by the agreement below in which the item is referred to as "the Work". It is identical in content to that deposited in the Library, subject to point 4 below.

Non-exclusive Rights

Rights granted to the digital repository through this agreement are entirely non-exclusive. I am free to publish the Work in its present version or future versions elsewhere.

I agree that Bangor University may electronically store, copy or translate the Work to any approved medium or format for the purpose of future preservation and accessibility. Bangor University is not under any obligation to reproduce or display the Work in the same formats or resolutions in which it was originally deposited.

Bangor University Digital Repository

I understand that work deposited in the digital repository will be accessible to a wide variety of people and institutions, including automated agents and search engines via the World Wide Web.

I understand that once the Work is deposited, the item and its metadata may be incorporated into public access catalogues or services, national databases of electronic theses and dissertations such as the British Library's EThOS or any service provided by the National Library of Wales.

I understand that the Work may be made available via the National Library of Wales Online Electronic Theses Service under the declared terms and conditions of use (http://www.llgc.org.uk/index.php?id=4676). I agree that as part of this service the National Library of Wales may electronically store, copy or convert the Work to any approved medium or format for the purpose of future preservation and accessibility. The National Library of Wales is not under any obligation to reproduce or display the Work in the same formats or resolutions in which it was originally deposited.

Statement 1:

This work has not previously been accepted in substance for any degree and is not being concurrently submitted in candidature for any degree unless as agreed by the University for approved dual awards.

Signed ………………………………………….. (candidate)

Date ……………………………………………..

<u>Statement 2</u>:

This thesis is the result of my own investigations, except where otherwise stated. Where correction services have been used, the extent and nature of the correction is clearly marked in a footnote(s).

All other sources are acknowledged by footnotes and/or a bibliography.

Signed …………………………………………. (candidate)

Date …………………………………………….

<u>Statement 3</u>:

I hereby give consent for my thesis, if accepted, to be available for photocopying, for inter-library loan and for electronic storage (subject to any constraints as defined in statement 4), and for the title and summary to be made available to outside organisations.

Signed …………………………………………. (candidate)

Date …………………………………………….

NB: Candidates on whose behalf a bar on access has been approved by the Academic Registry should use the following version of **Statement 3:**

<u>Statement 3 (bar)</u>:

I hereby give consent for my thesis, if accepted, to be available for photocopying, for inter-library loans and for electronic storage (subject to any constraints as defined in statement 4), after expiry of a bar on access.

Signed …………………………………………… (candidate)

Date ………………………………………………

<u>Statement 4</u>:

Choose **<u>one</u>** of the following options

a) I agree to deposit an electronic copy of my thesis (the Work) in the Bangor University (BU) Institutional Digital Repository, the British Library ETHOS system, and/or in any other repository authorized for use by Bangor University and where necessary have gained the required permissions for the use of third party material.	
b) I agree to deposit an electronic copy of my thesis (the Work) in the Bangor University (BU) Institutional Digital Repository, the British Library ETHOS system, and/or in any other	

repository authorized for use by Bangor University when the approved **bar on access** has been lifted.	
c) I agree to submit my thesis (the Work) electronically via Bangor University's e-submission system, however I **opt-out** of the electronic deposit to the Bangor University (BU) Institutional Digital Repository, the British Library ETHOS system, and/or in any other repository authorized for use by Bangor University, due to lack of permissions for use of third party material.	

Options B should only be used if a bar on access has been approved by the University.

In addition to the above I also agree to the following:

1. That I am the author or have the authority of the author(s) to make this agreement and do hereby give Bangor University the right to make available the Work in the way described above.
2. That the electronic copy of the Work deposited in the digital repository and covered by this agreement, is identical in content to the paper copy of the Work deposited in the Bangor University Library, subject to point 4 below.
3. That I have exercised reasonable care to ensure that the Work is original and, to the best of my knowledge, does not breach any laws – including those relating to defamation, libel and copyright.
4. That I have, in instances where the intellectual property of other authors or copyright holders is included in the Work, and where appropriate, gained explicit permission for the inclusion of that material in the Work, and in the electronic form of the Work as accessed through the open access digital repository, *or* that I have identified and removed that material for which adequate and appropriate permission has not been obtained and which will be inaccessible via the digital repository.
5. That Bangor University does not hold any obligation to take legal action on behalf of the Depositor, or other rights holders, in the event of a breach of intellectual property rights, or any other right, in the material deposited.
6. That I will indemnify and keep indemnified Bangor University and the National Library of Wales from and against any loss, liability, claim or damage, including without limitation any related legal fees and court costs (on a full indemnity bases), related to any breach by myself of any term of this agreement.

Signature: ……………………………………………………… Date : …………………………………………….

Abstract

Understanding cohesive, clay-laden subaqueous sediment gravity flows is vital, because clay is one of the most abundant sediment types on Earth and sediment gravity flows transport large volumes of this sediment into the ocean. Previous cohesive sediment gravity flow studies have overlooked the distinct cohesive strengths of different types of clay mineral. To isolate the effect of clay mineral type, lock-exchange experiments contrasted sediment gravity flows composed of weakly cohesive kaolinite clay, strongly cohesive bentonite clay, and non-cohesive silica flour at a wide range of volume concentrations. For high-density sediment gravity flows of the same concentration, kaolinite flows had a higher maximum head velocity and a longer runout distance than bentonite flows, because the bentonite flows were able to form a stronger network of particle bonds of greater rheological strength. Frictional forces reduced the mobility of the silica-flour flows at high concentrations. Dimensional analysis shows that the yield stress of the suspension can be used to predict the runout distance and the dimensionless head velocity of the sediment gravity flows, independent of the clay type. Clay mineral type within natural, cohesive, high-density sediment gravity flows is expected to control their runout distance and the geometry of their deposits. A metadata analysis was conducted to determine if the cohesive strength of different clay minerals left a signature in the geometry of modern, mud-rich submarine fans. For the fans studied, the normalised vertical-fan-growth-rate increased for fans dominated by kaolinite via illite to smectite, suggesting fans containing strongly cohesive clays may cover a smaller area and be thicker. The dominant clay mineral in the fans also appeared to have a latitudinal control, because the weathering intensity on adjacent continents controls clay mineral formation. These results suggest the relationships between latitude, clay mineral assemblage and the geometry of modern, mud-rich submarine fans should be further explored.

In the natural environment, cohesive sediment gravity flows are commonly composed of mixtures of clay minerals. Lock-exchange experiments produced sediment gravity flows carrying mixtures of bentonite and kaolinite at a fixed 20% volumetric concentration. Above bentonite proportions of 20%, further increasing the bentonite proportion increases the yield stress of the starting suspension and reduces the head velocity and runout distance of the flows. However, the mixture containing 10% bentonite had a lower yield stress and was more mobile than the pure kaolinite flow, suggesting that the small amount of bentonite reduced the cohesive strength of the suspension. In contrast, for pure-bentonite, high-density sediment gravity flows, increasing the volume concentration by adding 25% sand increases the yield stress of the suspension and reduces the runout distance and the velocity of the flows. This demonstrates that non-cohesive particles can contribute to the cohesive properties of a sediment gravity flow.

Geological fieldwork in the distal, mud-rich part of the submarine fan that makes up the Aberystwyth Grits Group and the Borth Mudstone Formation (Wales, U.K.) identified two novel mixed mud–sand bedforms: large current ripples and low-amplitude bed-waves (bedforms a few millimetres high and up to several meters long). The large ripples and low-amplitude bed-waves are interpreted to have formed under clay rich, transient-turbulent flows with enhanced and attenuated near-bed turbulence, respectively. These mixed sand-mud bedform types may be an important tool in interpreting fan fringe environments.

Acknowledgements

Many people have supported me during my PhD and helped make my time in North Wales really fun.

First of all I would like to thank my supervisors Jaco Baas and Simon Barker. Jaco, I want to thank you for your support, encouragement and endless enthusiasm. Thanks for designing such a brilliant PhD project and then allowing me to shape it into my own. Your excellent teaching and mentoring has enabled me to produce something I am very proud of. In particular I would like to thank you for introducing me to the Aberystwyth Grits Group and the wonder that is geological fieldwork, I have fond memories of us with our noses to the outcrop trying to understand these enigmatic rocks. Simon, the remote supervisor, thank you for your help in placing my research into a wider context. I really appreciated the time you dedicated to me during my placement at Equinor. Thanks to the whole of the Equinor team for being so welcoming.

I would like to thank Jonathan Malarkey for your help setting up the lock exchange experiments and the time you have dedicated my research. Obrigada to Ricardo Silva Jacinto for inviting me to conduct rheology experiments at IFREMER and for introducing me to the field of rheology. Merci to Stephanie Howlett and Gracias to Marta Payo Payo who helped make my time in Brest fun.

Thanks to all the other people in the School of Ocean Sciences. Firstly, thanks to Rob Evans for building the flume, David Roberts for your technical video advice, and Wendy Roberts and Stef Kraft for lending me numerous things from the teaching lab. Thank you to Ian Prichard for general technical support and guidance. Connor McCarron, thank you for lending me Katrien's SeaTek ranging system and your help in the lab. You are all busy people and I appreciate how you always found time to help me. Katrien and Dei, thank you for our interesting discussions and your guidance during my PhD progress meetings. I am grateful to Gareth Williams for helping me to include some cool statistics in my Metadata Analysis Chapter.

I have been lucky to make many friends during my PhD. A big thanks to all my fellow-PhD's for chats and tea breaks. Thanks to Melissa Craig for sharing the journey with me as a fellow "lock-exchange PhD student". Particular thanks go to Sophie Hage and Maria Azpiroz-Zabala who quickly befriended me and introduced me to the "Southampton gang" when I arrived at EGU on my own. Diolch yn fawr to the lovely members of Beaumaris Town Road Runners and Arfon Swimming Club for taking my mind off my PhD and making sure that Mondays and Fridays were always productive.

Thank you to my parents for all that you have done for me and for teaching me to be amazed at the world around us. To Tom, my partner in life, thank you for making me laugh and encouraging a good work-life balance. To my grandfathers, Dr Edward Baker and Alan Baldwin, whose love of science inspired their careers, and my grandmothers, Sheila Baker and June Baldwin, who did not have the opportunities I have now, this thesis is for you.

"Possibly many may think that the deposition and consolidation of fine-grained mud must be a very simple matter, and the results of little interest. However, when carefully studied experimentally it is soon found to be so complex a question, and the results dependent on so many variable conditions, that one might feel inclined to abandon the inquiry, were it not that so much of the history of our rocks appears to be written in this language."

Henry Clifton Sorby, 1908

Table of contents

List of Figures

List of Tables

List of Abbreviations

AGG	Aberystwyth Grits Group
BMF	Borth Mudstone Formation
C	Initial suspended-sediment concentration (%)
C_0	Concentration above which the flow cannot leave the reservoir (%)
C_b	Proportion of bentonite in the flow (%)
C_k	Proportion of kaolinite in the flow (%)
C_m	Suspended-sediment concentration at $U_{h,m}$ (%)
C_{m1}	Concentration of the maximum runout distance (%)
CMF	Cohesive mud flow
G	Complex shear modulus (Pa)
H	Average-vertical-fan-growth-rate
HDTC	High-density turbidity current
LABW	Low-amplitude bed-wave
LDTC	Low-density turbidity current
M	Mudstone
Msi	Silty-mudstone
NCMF	Noncohesive mud flow
p	Probability value
Re	Reynolds number
r_s	Spearman's rank-order correlation coefficient
Sc	Clast-rich sandstone
SGF	Sediment gravity flow
Si	Siltstone
Sma	Massive sandstone
SMh	Heterolithic sandstone-mudstone
Smu	Structured muddy sandstone
Ss	Structured sandstone
U_h	Maximum head velocity of the flows (m s^{-1})
$U_{h,m}$	Highest value of U_h for each sediment type (m s^{-1})
$U_{h,m,w}$	Highest maximum head velocity for the mixed-clay flows (m s^{-1})
V	Volumetric fan growth rate
wt %	Weight percentage (%)
x	Distance from the lock gate (m)
x_0	Runout distance of flows (m)
$x_{0,m}$	Maximum runout distance of flows composed of each sediment type (m)
τ_y	Yield stress (Pa)
$\tau_{y,0}$	Yield stress above which the flow cannot leave the reservoir (Pa)
$\tau_{y,m}$	Yield stress at $U_h = U_{h,m}$ and $C = C_m$ (Pa)

Author Contributions

In Chapter 3 I planned and conducted the laboratory experiments to produce the data and completed the data analysis. I wrote the manuscript which benefitted from contributions from all co-authors along with comments from the editor and two reviewers. This work is published in *Journal of Sedimentary Research.*

Baker, M.L., **Baas, J.H.**, **Malarkey, J.**, **Jacinto, R. S.**, **Craig, M.J.**, **Kane, I.A.** and **Barker, S.** (2017) The effect of clay type on the properties of cohesive sediment gravity flows and their deposits. *Journal of Sedimentary Research*, **87(11)**, 1176-1195.

In Chapter 6 I conducted the fieldwork with Jaco Baas. I then completed the data analysis and writing of the manuscript. Jaco Baas provided general comments, suggestions and editing of the manuscript. This chapter has benefited from comments from three reviewers and has been accepted pending moderate revisions for *Sedimentology*.

I undertook all the research and writing in Chapters 1, 2, 4, 5, 7 and 8 under the supervision of Jaco Baas.

1. Introduction

1.1 Motivation

Subaqueous sediment gravity flows (SGFs) are volumetrically one of the most important sediment transport processes on our planet, providing large quantities of sediment to lakes, seas and oceans (*e.g.*, Kneller & Buckee, 2000; Talling *et al.*, 2015). As a result of their unpredictability and often large magnitude, SGFs can pose a significant threat to engineering works in deep water, such as drilling rigs and communication cables (Piper *et al.*, 1999; Anthony *et al.*, 2008; Hsu *et al.*, 2008; Zakeri, 2008). The deposits of these flows produce submarine fans, which are amongst the largest sedimentary bodies on Earth, and store the world's greatest reserves of oil and gas (Middleton, 1993; Kneller & Buckee, 2000; Keevil *et al.*, 2006).

The majority of SGFs should contain mud, composed of clay- and silt- sized particles, since mud is one of the most common sediment types in the modern ocean and in oceans in the geological past (Flemming, 2002; Schindler *et al.*, 2015). The role of mud has been shown to be significant in a variety of flows, including SGFs, since clay particles have the unique ability to modulate turbulence in a predictable manner (Wang & Plate, 1996; Baas & Best, 2002; Baas *et al.*, 2009; Sumner *et al.*, 2009; Baas *et al.*, 2011). The cohesive forces within a clay flow, *i.e.,* its rheology, have been shown to change with clay concentration (Hampton, 1975; Baas *et al.*, 2009; Sumner *et al.*, 2009), but the type of clay mineral can also change the cohesive properties of the flow (Marr *et al.*, 2001; Baas *et al.*, 2016). This thesis aims to fill the knowledge gap on the effect of clay mineral type and mixtures of clay minerals on cohesive SGF behaviour and their corresponding deposits, and how the rheological properties of the starting suspension can predict the flow behaviour and deposit properties.

In the natural environment SGFs commonly consist of a mixture of sand, silt and clay (Reading & Richards, 1994; Marr *et al.*, 2001; Talling *et al.*, 2004; Amy *et al.*, 2006). Limited work has considered how adding minor amounts of sand may influence the flow behaviour and deposit properties of cohesive SGFs. Part of this thesis presents laboratory experiments considering how increasing the volume concentration of a pure-clay, high-density cohesive SGF by adding small amounts of fine sand changes the flow rheology, flow behaviour and deposits.

There are many examples of mud-rich and mixed sand-mud submarine fan systems in the natural environment, such as the Cretaceous Britannia Sandstone Member, North Sea (Barker *et al*., 2008), and the Silurian Aberystwyth Grits of Cardigan Bay, Wales (Wilson *et al.*, 1992; Talling *et al*., 2004). The properties of fine-grained deep-marine systems are gaining increasing attention as hydrocarbon exploration looks to target reservoirs of these systems, such as offshore West Africa (Sprague *et al.*, 2005) and in the Gulf of Mexico (Kane & Pontén, 2012). The facies in the fringe environments of these fine-grained systems have been shown to be complex, as the presence of clay promotes the development of transient turbulent flows with complex depositional properties (Kane *et al.*, 2017). Relatively little is known about the variation of current-induced sedimentary structures found within these facies. This thesis presents descriptions and interpretations of mixed sandstone-mudstone bedforms in the fringe region of the submarine fan that makes up the Silurian Aberystwyth Grits Group and the Borth Mudstone Formation in Wales (U.K.).

The distribution of different clay minerals in recent deep-sea sediments appears to be related to latitude (Biscaye, 1965; Griffin *et al.*, 1968; Rateev *et al.*, 1969; Chamley, 1989; Fagel, 2007). This latitudinal zonation of clay minerals is thought to be controlled by the climate on the adjacent continents, which controls the type and intensity of weathering (Biscaye, 1965; Griffin *et al.*, 1968; Chamley, 1981; Evans, 1992; Thiry, 2000; Fagel, 2007). This thesis presents a metadata analysis to determine if there is a relationship between the clay mineral assemblage in modern submarine fans and their latitude. The metadata also considers if the geometry of modern submarine fans can be related to the cohesive properties of their clay mineral assemblages.

This chapter will now provide a literature review of SGF dynamics and deposits, clay mineral structures and properties, and the link between clay minerals and climate. The final section presents the overall aims of the thesis and the thesis structure.

1.2 Sediment gravity flows

SGFs are produced when gravity acts on the density difference between two fluids, and the excess density is provided by suspended sediment (Middleton & Hampton, 1973; Kneller & Buckee, 2000). SGFs vary greatly in their sediment concentration, particle support mechanism, extent of particle cohesion, duration and rheology. There is thus a continuous spectrum of SGF types, extending from turbidity currents to debris flows, slumps, and slides. This chapter will now describe the different SGF types and the flow classification schemes that are used in this thesis.

1.2.1 Low-density and high-density turbidity currents

Low-density turbidity currents are characteristically defined as relatively dilute flows, in which the particles are supported by the upward component of fluid turbulence generated at the boundaries of the flow (Middleton & Hampton, 1973). The turbulent flow conditions are present throughout the flow, including near the bed, producing well-mixed flows without a density interface (Talling *et al.,* 2012). The point of transition from low-density turbidity current to high-density turbidity current is a controversial issue (Kuenen, 1950, 1951; Kuenen & Migliorini, 1950; Lowe, 1982; Talling *et al.,* 2012). It is also complex to apply this term, originally developed for non-cohesive SGFs, to the clay-rich cohesive SGFs discussed in this thesis. Therefore, a broad definition of the term high-density turbidity current is used herein to denote flows in which processes other than fluid turbulence play a role in supporting the sediment particles, particularly near the bed (Kuenen, 1950, 1951; Lowe, 1982; Talling *et al.*, 2012). For the cohesive high-density turbidity currents in this thesis, the sediment is interpreted to be supported primarily by increased fluid viscosity from higher clay concentrations promoting flocculation and gelling, although other grain-supporting processes (grain-to-grain interactions, hindered settling, development of excess pore pressure) may also play a role (Talling *et al.*, 2012; Sumner *et al.*, 2012). This definition means that high-density turbidity currents can be considered to have transitional, turbulence-modulated flow behaviour. In practice, high-density turbidity currents can be distinguished from low-density turbidity currents as they contain a density interface with a dense lower layer separated by a dilute upper layer.

1.2.2 Transitional flows

Transitional flows bridge the gap between debris flows and low-density turbidity currents and can be defined as flows with transient turbulent behaviour (Wang & Plate, 1996; Marr *et al.*, 2001; Mohrig & Marr, 2003; Baas *et al.*, 2009, 2011; Sumner *et al.*, 2009; Kane & Pontén, 2012; Kane *et al.*, 2017). This transient turbulent flow behaviour can be attributed to the presence of fine-grained sediment, in particular clay, within the flows. Clay minerals can bind together to form flocs and gels when the attractive Van der Waals forces outcompete the repulsive forces between the negatively charged surfaces of clay particles (Winterwerp & van Kesteren, 2004; see Chapter 1.5.1 for details). The presence of flocs within the flow increases the viscosity and yield stress and may thus affect the turbulence driving the flow (Fig. 1.1; Baas and Best 2002). The amount of flocculation and the size of the flocs generally increase as the bulk suspended clay concentration increases (Dyer & Manning 1999). Eventually, a “gelling” point may be reached at high clay concentration, which is characterized by the formation of a volume-filling network of particle bonds in the liquid (Fig. 1.1; Blackbourn & Thomson, 2000; Lowe & Guy, 2000; Baas *et al.*, 2009). A stable gel of linked clay minerals may be viscous enough to cause the total suppression of turbulence within the flow. Conversely, the attractive electrostatic bonds between the clay particles can be broken in regions of high shear. Thus, an increase in turbulence generation within the flows by, for example, an increasing slope gradient has the potential to break up bonds between the clay particles, and reduce the flow viscosity (Fig. 1.1). The dynamic structure of transitional flows is thus controlled by the interplay between turbulent and cohesive forces (Baas *et al.*, 2009).

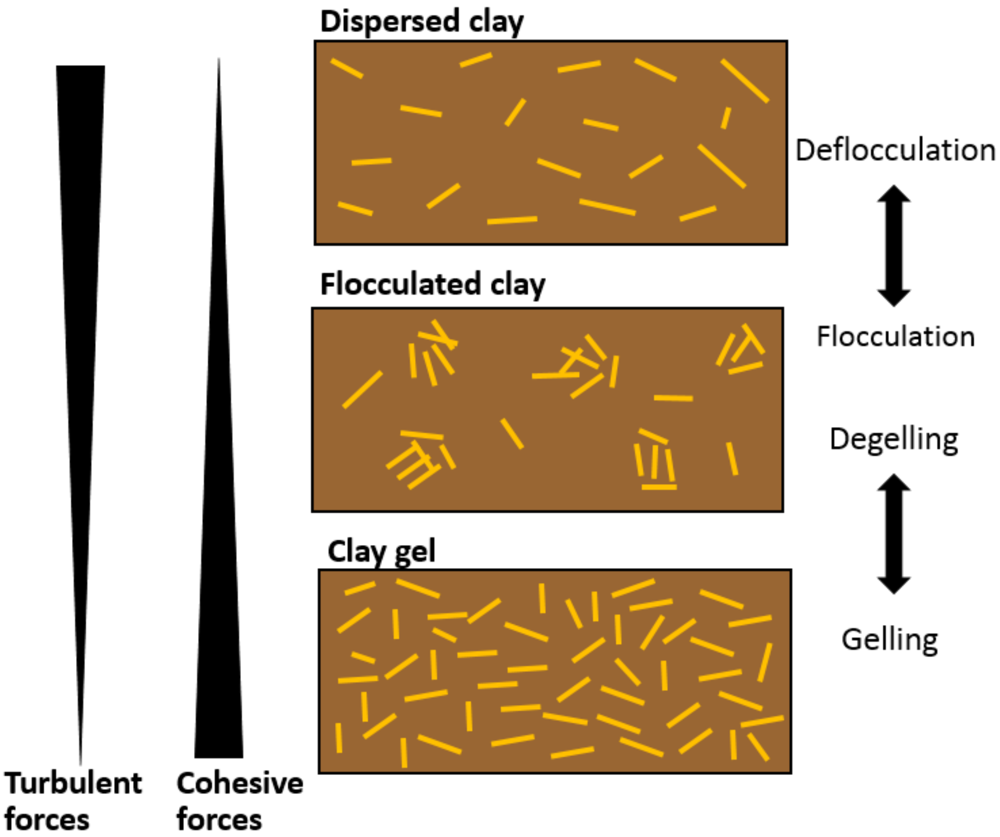

Figure 1.1: Schematic drawing of the balance between turbulent and cohesive forces that determines the flow behaviour of transitional flows.

Experiments have demonstrated that increasing the clay concentration in kaolinite-laden unidirectional flows changes the balance between the cohesive and turbulent forces (Baas & Best 2002; Baas *et al.*, 2009). Increasing the kaolinite clay concentration changed the flow from Newtonian to non-Newtonian, modifying the velocity and turbulence structure of the flows. The flow classification scheme of Baas *et al.*, (2009) defines five different flow phases in order of increasing clay concentration: a) turbulent flow; b) turbulence-enhanced transitional flow; c) lower transitional plug flow; d) upper transitional plug flow; and e) quasi-laminar plug flow (Baas *et al.*, 2009). These phases differed in their velocity and turbulence intensity profiles (Fig. 1.2):

a) Turbulent flows have a logarithmic profile of downstream velocity that obeys the 'law of the wall' for clay-free flows. Turbulence decreases with height above the bed.
b) Turbulent-enhanced transitional flows show a velocity decrease and turbulence intensity increase across the entire flow depth, whilst the logarithmic velocity profile is maintained.

The higher turbulence intensity compared to turbulent flows results from the development of a highly turbulent internal shear layer at approximately ~0.01 m above the bed.

c) Lower transitional plug flows contain a decreased near-bed velocity and increased near-bed turbulence. Turbulence decrease in the upper part of the flow results in the development of a plug flow.

d) Upper transitional plug flows comprise decreased near bed velocities and reduced turbulence intensity. The thickness of the plug flow increases with increasing clay content.

e) Quasi-laminar plug flows show a complete suppression of turbulence, producing a fully developed laminar plug flow. Some minor residual turbulence may occur at the base of the flow within a thin shear layer.

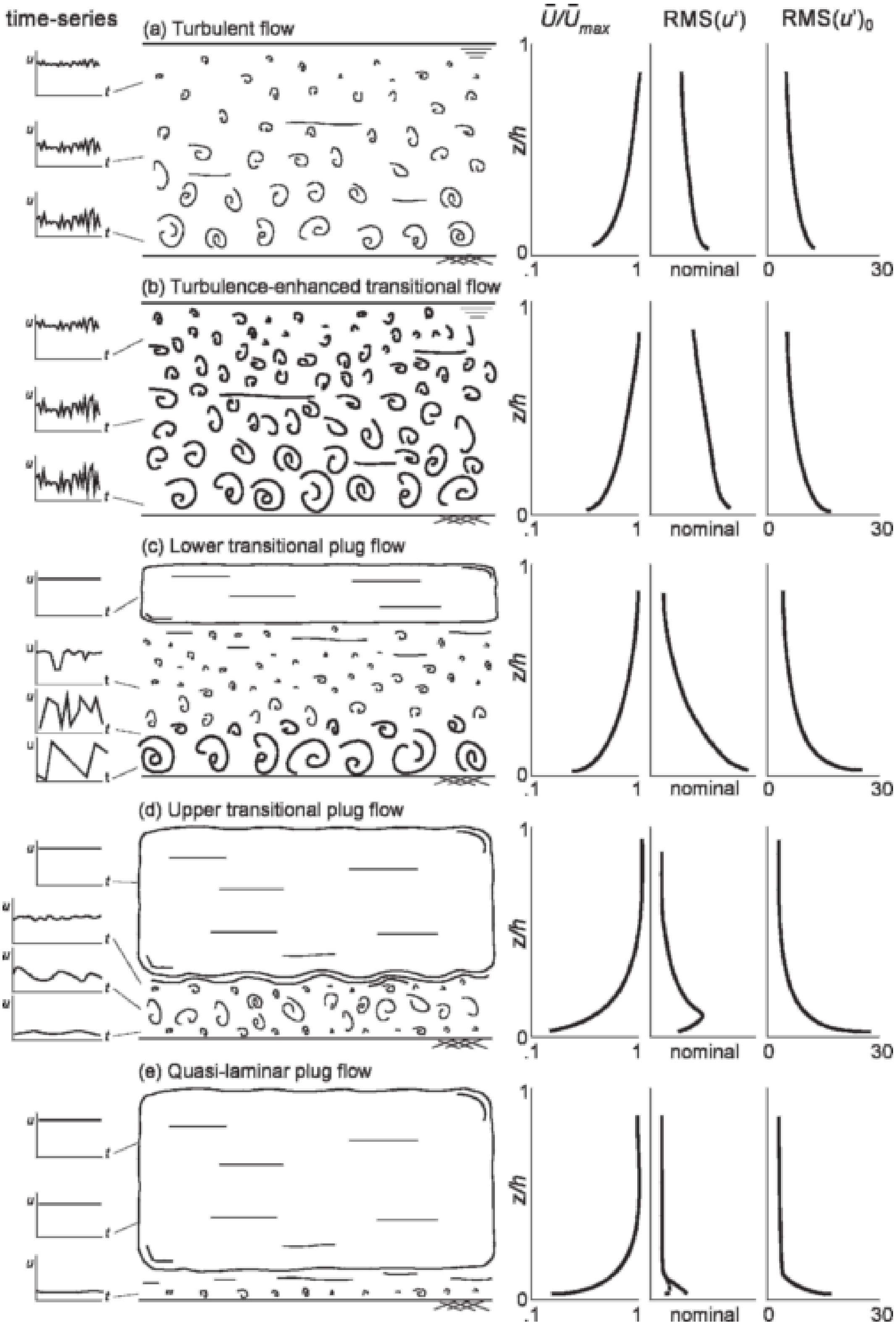

Figure 1.2: Schematic drawings of five different clay flow types. Graphs to the left of the drawings show the typical velocity time series at various heights within the flow. Plots to the right denote vertical profiles of (from left to right) dimensionless downstream velocity, root-mean-square of downstream velocity, and dimensionless turbulence intensity. From Baas et al. (2009).

The experiments of Baas and Best (2002) and Baas *et al.* (2009) produced open-channel flows which were not subjected to an upper boundary shear layer as subaqueous SGFs would be. Recent experiments by Hermidas *et al.* (2018) on the vertical flow structure in clay-laden SGFS aimed to address this problem. The flows were considered in terms of a free shear layer at the top of the flow, a laminar plug layer and a basal boundary layer. From the experimental observations, Hermidas *et al.* (2018) categorised flow types based on the existence of turbulence in the free shear and in the boundary layer, and the presence of a plug layer. The classification scheme by Hermidas *et al.* (2018) suggests four flow types in order of reducing clay concentration: a) plug flow; b) top transitional plug flow; c) transitional turbidity current; and d) turbidity current (Fig. 1.3). These flow types were defined as follows:

a) Plug flows contained a laminar free shear layer, a plug layer, and a laminar boundary layer.
b) Top transitional flows comprised a turbulent free shear layer, a plug layer, and a laminar boundary layer.
c) Transitional turbidity currents contained a turbulent free shear layer, no plug layer, and a laminar boundary layer
d) Turbidity currents were defined as fully turbulent flows.

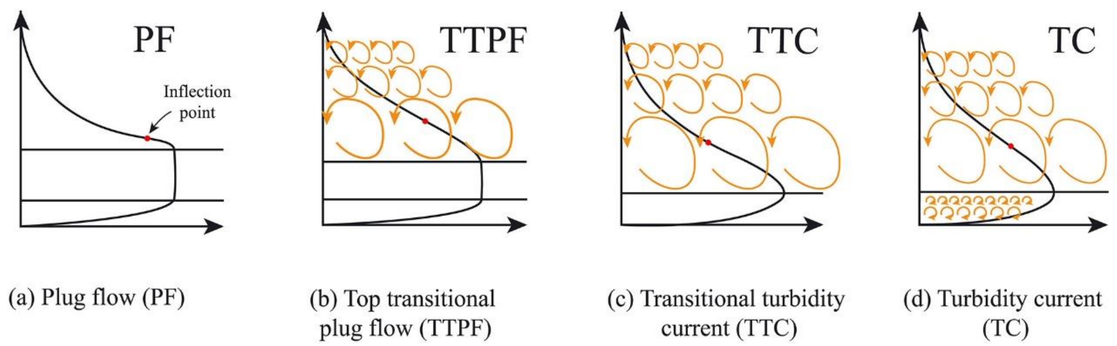

Figure 1.3: Schematic drawings of the velocity profile of clay-laden SGFs defined by Hermidas et al. (2018); from (A) to (D) the clay concentration in the flows decreases. The horizontal black lines on the profiles denote the transition between basal boundary layer, plug layer and free shear layer. Orange arrows indicate turbulent regions. Modified from Hermidas et al. (2018).

1.2.3 Debris flows, mud flows and slides

Debris flows and mud flows are defined as high-concentration SGFs with weak to no internal turbulence where cohesive sediment can provide grain support by yield strength (Middleton & Hampton, 1973; Marr *et al.*, 2001; Mulder & Alexander, 2001). The high density of debris flows means their particle support mechanisms can extend to grain-grain interaction and hindered settling (Manica, 2000; Sumner *et al.*, 2009). For the experimental flows in this thesis, debris flows and mud flows are differentiated by mud flows containing little or no coarse sediment, whereas debris flows contain poorly sorted sediment including clay and sand. Slides are also defined as flows where yield strength is the primary support mechanism and internal turbulence is negligible. Slides are distinguished from debris flows and mud flows based on the degree of internal deformation during transport (Mohrig & Marr, 2003). Slides a defined as flows that move as a coherent mass without significant internal deformation (Martinsen, 1994; Mohrig & Marr, 2003).

1.2.4 Sediment gravity flow classification schemes used in this thesis

The wide variety of natural flow types has resulted in various classification schemes of SGF behaviour (*e.g.*, Bouma, 1962; Lowe, 1982; Mutti, 1992; Haughton *et al.*, 2009; Talling *et al.*, 2012). This thesis uses two classification schemes. The first scheme is used to classify the flows produced by the laboratory experiments in Chapters 3 to 5. As there are no internal velocity measurements of these flows, a simple classification scheme is used based on visual observations of flow behaviour. The flows are classified as either low-density turbidity currents, high-density turbidity currents, mud flows or debris flows, or slides.

The second flow classification scheme used in this thesis is the transitional flow model of Baas *et al.* (2009) that describes flows based on internal velocity measurements (Fig. 1.2). This classification scheme is used in Chapter 6 to interpret the flows that deposited the mixed sandstone-mudstone bedforms in the field. The classification scheme of Baas *et al.* (2009) is utilised because the bedforms in the field are compared to bedforms produced in the laboratory by flows that were classified using this flow model. The two classification schemes can be integrated with each other, as shown in Figure 1.4. The main difference between the two flow classification schemes is that high-density turbidity currents can be subdivided into turbulence-enhanced transitional flow, lower transitional plug flow and upper transitional plug flow using the classification scheme of Baas *et al.* (2009; Fig. 1.4).

Laboratory flows	Low-density turbidity current	High-density turbidity current			Mudflow/ debris flow	Slide
Baas et al. (2009)	Turbulent flow	Turbulence-enhanced transitional flow	Lower transitional plug flow	Upper transitional plug flow	Quasi-laminar plug flow	
Velocity profile & turbulence schematic						
Deposit	Bouma sequence	Hybrid event beds/transitional flow deposits			Debrites	Slide deposits

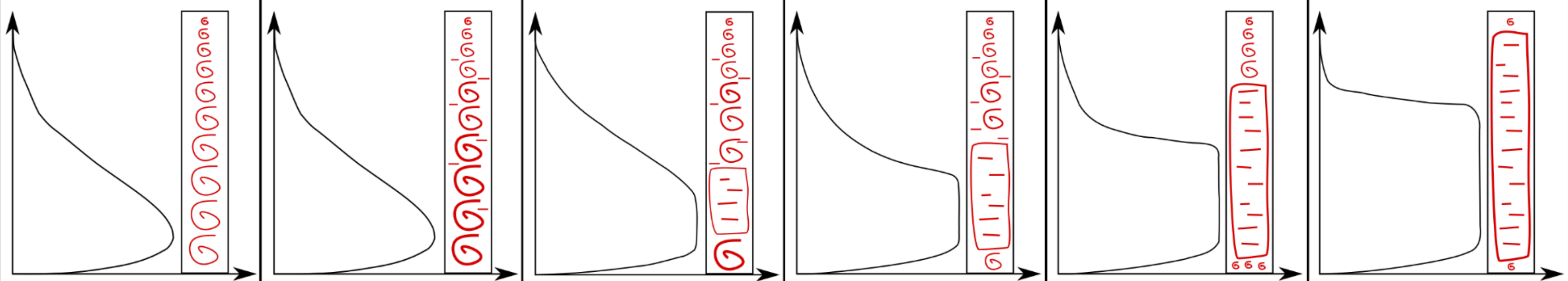

Figure 1.4: Summary of the two flow classification schemes used in this thesis and how they can be integrated with each other. The 'laboratory flows' classification is used in Chapters 3 to 5. The Baas et al. (2009) flow classification scheme is used in Chapter 6. The turbulence schematic shows the intensity of turbulent mixing by size and thickness of eddies and presence of a laminar plug layer.

1.3 Sediment gravity flow deposits

SGFs produce a range of deposit types. The deposits of turbidity currents are called turbidites. Bouma (1962) proposed an idealised turbidite bed sequence characterised by normal grading and a vertical sequence containing the following five divisions from base to top: massive sandstone; plane-parallel laminated sandstone; cross-laminated sandstone; laminated siltstone; and structureless mudstone. However, complete Bouma sequences are rarely encountered in nature, with partial sequences being much more common (Lowe, 1979). Lowe (1982) suggested that additional divisions could be added to the base of the Bouma sequence. These additional divisions were interpreted to record weakly turbulent, high-density turbidity currents with higher near-bed sediment concentrations and higher rates of suspension settling than low-density turbidity currents. The deposits of debris flows, called debrites, form by mass settling, which means that the majority of the larger and smaller grains do not segregate during deposition (Talling *et al.*, 2012). This leads to a massive deposit containing poorly sorted, horizontally orientated clasts within a fine matrix.

The deposits of transitional flows represent the complex transient turbulent-laminar behaviour of the flows (Haughton *et al.*, 2009; Baas *et al.*, 2011; Kane & Pontén, 2012). Haughton *et al.* (2009) called these deposits hybrid event beds and Kane and Pontén (2012) used the term transitional flow deposits. Haughton *et al.* (2009) proposed a hybrid event bed model, interpreted to be produced by a single flow event. The sequence is made up of the following five divisions, from base to top: H1) a clean sandstone layer that may contain mud clasts, deposited from a turbidity current; H2) a banded mud-poor sandstone and mud-rich sandstone, formed from a transitional flow; H3) an argillaceous sandstone that may contain mud clasts, sand patches, injections, outsized granules and shear fabrics, produced by a debris flow; H4) a thin, clean sandstone containing parallel and ripple cross-laminae, formed by a low-density turbidity current; and H5) a pseudonodular or massive mudstone, deposited by suspension fallout (Fig. 1.5).

Haughton *et al.* (2009) interpreted the hybrid event bed sequence to represent longitudinal flow transformation of flow behaviour from turbulent to increasingly more turbulence-suppressed. However, hybrid event beds may also be formed by the development of vertical rheological stratification within the flow (Talling *et al.*, 2007; Baas *et al*., 2011). Baas *et al.* (2011) proposed that vertical segregation of cohesive and non-cohesive particles may take place in combination with longitudinal transformation into different turbulent, transitional and laminar flow components. For example, the structureless sandstone in H1 (Fig. 1.5) was interpreted by Haughton *et al.* (2009) as a forerunning turbidity current. Yet, Baas *et al.* (2011) stated that a decelerating lower transitional plug flow, a upper transitional plug flow or a low concentration quasi-laminar plug flow, all of which contain a plug region, may produce a basal sandstone with internal properties comparable to the H1 deposit.

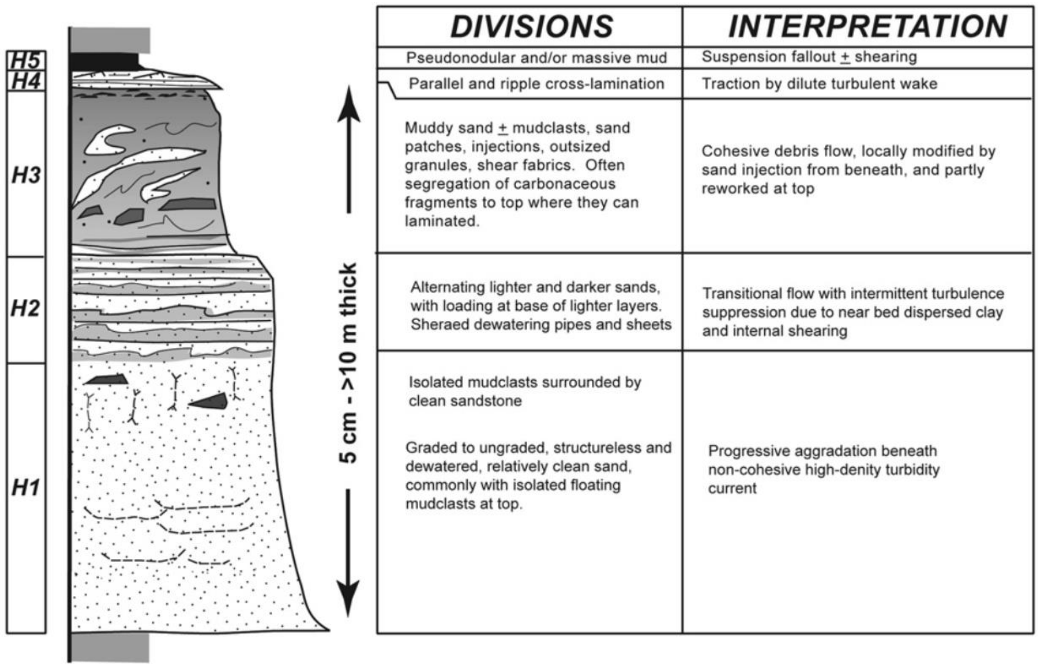

Figure 1.5: Schematic log of an idealised hybrid event bed sequence. From Haughton et al. (2009).

Hybrid event beds were first noted in the literature by Wood and Smith (1958). They have received increased attention, since it was identified that these deposits are common in many locations worldwide, often at the fringe of submarine fans (Haughton *et al.*, 2003; Talling *et al.*, 2004; Barker *et al.*, 2008; Haughton *et al.*, 2009; Hodgson, 2009; Kane & Pontén, 2012; Talling *et al.*, 2012; Fonnesu *et al.*, 2015; Kane *et al.*, 2017; Spychala *et al.*, 2017).

1.4 Sedimentary structures under high-density cohesive sediment gravity flows

The balance between the turbulent and cohesive forces in a high-density SGF determines the interaction of the flow with the sediment bed and its depositional properties. High-density SGFs that decelerate over a loose sediment bed may deposit sediment that is shaped into sedimentary structures (*e.g.*, Baas *et al.*, 2016). Analysis of these sedimentary structures in core and outcrop enables the reconstruction of depositional processes in ancient sedimentary environments. Many studies have investigated the development and stability of bedforms produced in cohesionless sediment under a variety of flow conditions (*e.g.,* Allen, 1968; see Baas *et al.* (2016) for a comprehensive list). This has resulted in bedform phase diagrams that define the boundaries between bedform types, based on variables that represent the strength and depth of the flow and the grain size of the sediment (*e.g.,* van Rijn, 1990, 1993; van den Berg & van Gelder, 1993). However, recent studies have demonstrated that adding even small volumes of clay to a sand bed or to a flow produces bedform types with different shapes and sizes compared to those in pure sand (Lowe, 1988; Baas *et al.*, 2011, 2013; Schindler *et al.*, 2015). Thus, applying the knowledge contained in bedform phase diagrams for pure sand in ubiquitous cohesive, mixed sand-mud environments should be done with care.

Laboratory experiments by Baas *et al.* (2011, 2013) investigated the sedimentary structures produced by a decelerated flow composed of sand, silt, and clay particles. A number of new, cohesive, mixed sand-silt-clay bedforms were identified and a new bedform phase diagram was proposed (Baas *et al.*, 2016). These novel bedforms include large current ripples, low-amplitude bed-waves, and scour and intrascour composite bedforms. The new bedform phase diagram of Baas *et al.* (2016) provides a potential resource to understand ancient sedimentary sequences that formed from rapidly decelerated flows composed of sand, silt, and clay. This requires the identification and process interpretation of these novel bedforms in their natural environment. The muddy fringes of fine-grained submarine fans are locations where these cohesive bedforms may be expected to be particularly common.

1.5 Clay minerals

When suspended in water, clay minerals have the unique ability to collide and flocculate, because of their specific mineral structure. This chapter first describes the structure of the four most common clay minerals (Chapter 1.5.1) and how this structure enables clay mineral flocculation (Chapter 1.5.2). The different structure of clay minerals helps control their cohesive strength, as explained in Chapter 1.5.3. The chapter concludes by presenting the work so far on how clay mineral type influences the properties of cohesive SGFs (Chapter 1.5.4).

1.5.1 Structure of clay minerals

When the structure of clay minerals is broken down, they are fundamentally layer silicates or phyllosilicates, composed of two units: octahedral and tetrahedral sheets. The tetrahedral sheets are composed of linked SiO_4^{4-} or AlO_4^{5-} tetrahedra. The octahedral sheets comprise connected octahedra, which contain a central Al^{3+}, Fe^{3+}, Fe^{2+}, or Mg^{2+} cation bonded to six O^{2-} or OH^- anions (Fig. 1.6; Velde & Meunier, 2008). Tetrahedral and octahedral sheets associate in two different combinations to create two kinds of layer structures. The 1:1 layer structure comprises one tetrahedral sheet covalently bonded to one octahedral sheet (Fig. 1.7; Brigatti *et al.*, 2006). The 2:1 layer structure comprises an octahedral sheet covalently bonded between two tetrahedral sheets (Fig.

1.7; Velde & Meunier, 2008). Lastly, these layers stack together in different combinations with different types of bonds to produce different clay minerals (Brigatti *et al.*, 2006; Velde & Meunier, 2008).

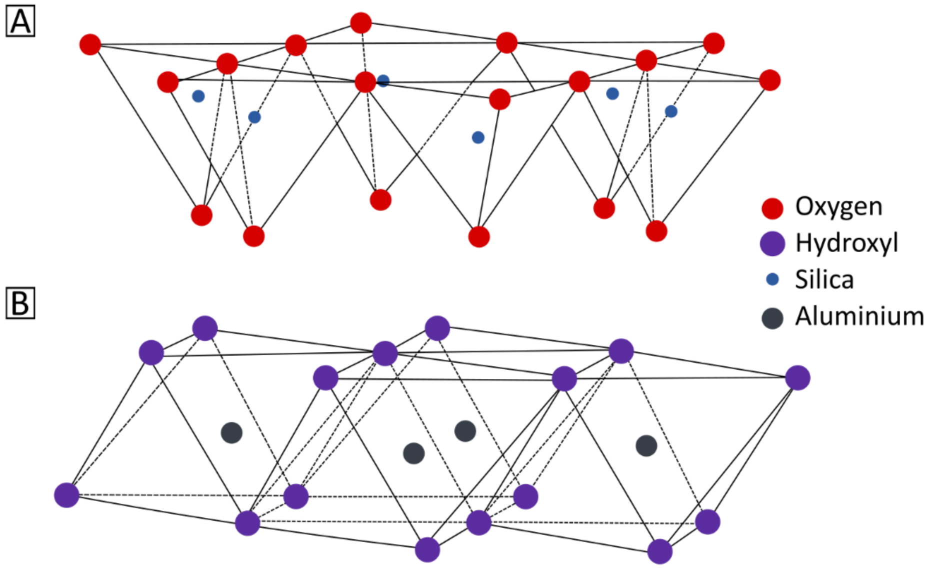

Figure 1.6: Examples of (A) a tetrahedral sheet composed of linked tetrahedra, and (B) an octahedral sheet containing connected octahedra. Redrawn from Murray (2006).

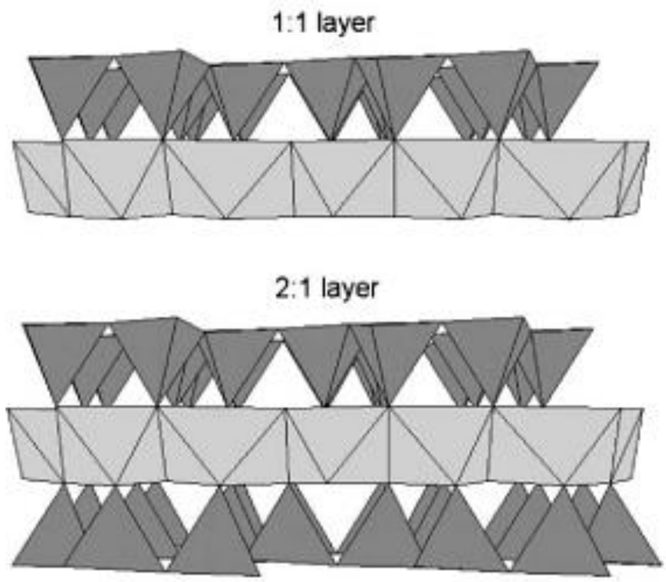

Figure 1.7: Models of the 1:1 and 2:1 layer structure of phyllosilicates. The dark grey represents tetrahedral sheets, whilst the light grey represents octahedral sheets. From Brigatti et al. (2006).

1.5.1.1 1:1 layer clay minerals

The clay mineral kaolinite is composed of 1:1 layer structures. The separate 1:1 layers are held together by hydrogen bonds between the oxygen atoms of the tetrahedral sheets and the hydrogen atoms of the hydroxyl groups in the octahedral sheets (Fig. 1.8; Brigatti *et al.*, 2006). For kaolinite, the multiple basal 1:1 layers stack up to form flake-like, hexagonal, phyllosilicate crystals with a thickness of ~100 nm and a plate diameter of 2 µm (Fig. 1.9D; Winterwerp & van Kesteren, 2004). The faces of kaolinite particles are permanently negative due to substitutions of Si^{4+} for Al^{3+} in the outer tetrahedral sheet (Winterwerp & van Kesteren, 2004; Cruz *et al.*, 2013). However, the charge on the edges of kaolinite particles are positive under acidic conditions and negative under neutral to alkaline conditions, because of the adsorption of hydrogen ions and hydroxyl groups, respectively (Tombácz & Szekeres, 2006; Au & Leong, 2013). The strong hydrogen bonds between the layers stops water penetrating this gap, making kaolinite a non-swelling clay mineral (Luckham & Rossi, 1999).

1.5.1.2 2:1 layer clay minerals

2:1 layer clay minerals, such as smectite, illite and chlorite (Fig. 1.9A, B, C), are the most common clay minerals in the natural environment (Velde & Meunier, 2008). In these clays, each layer is usually negatively charged because of cation substitutions. The magnitude of the negative layer charge varies for different cation substitutions. The negative charge of the basal layers causes repulsion, thus increasing the interlayer space and encouraging the occupancy of this space by exchangeable cations (Brigatti *et al.*, 2006; Velde & Meunier, 2008). The different negative charges of the layers encourages the occupancy of different cations, which produces different clay minerals (Brigatti *et al.*, 2006).

Smectite is a group of clay minerals which includes montmorillonite, which in industrial applications is also called bentonite. In smectites, both the octahedral and tetrahedral sheets undergo cation substitutions and create a high repulsive negative potential on the surface of the layers (Murray, 2000). This makes smectite a highly swelling clay mineral as water is adsorbed into the interlayer space between the 2:1 layers (Fig. 1.8). Smectites are able to expand and swell up to 10 times their dry volume (Murray, 1991; Au & Leong, 2013). If the interlayer spacing expands greatly, the smectite layers are able to delaminate into individual or thin packets of silicate layers (Lagaly & Ziesmer, 2003). Smectite clay minerals are thin flakes with a small particle size, large surface area and high layer charge (Fig. 1.9A). Illite clays also have a high negative layer charge. This encourages the interlayer space in illite to be occupied by anhydrous alkaline and alkaline earth cations, such as K^+ (Luckham & Rossi, 1999; Brigatti *et al.*, 2006). These cations form strong interlayer bonds, making illite a non-expanding clay mineral (Fig. 1.8). In chlorite, the negative layer charge from cation substitutions is cancelled out by an additional positively charged, continuous, octahedral sheet in the interlayer space, with hydrogen bonding between the adjacent layers (Fig. 1.8; Brigatti *et al.*, 2006; Velde & Meunier, 2008). Chlorite is therefore a non-expanding clay mineral.

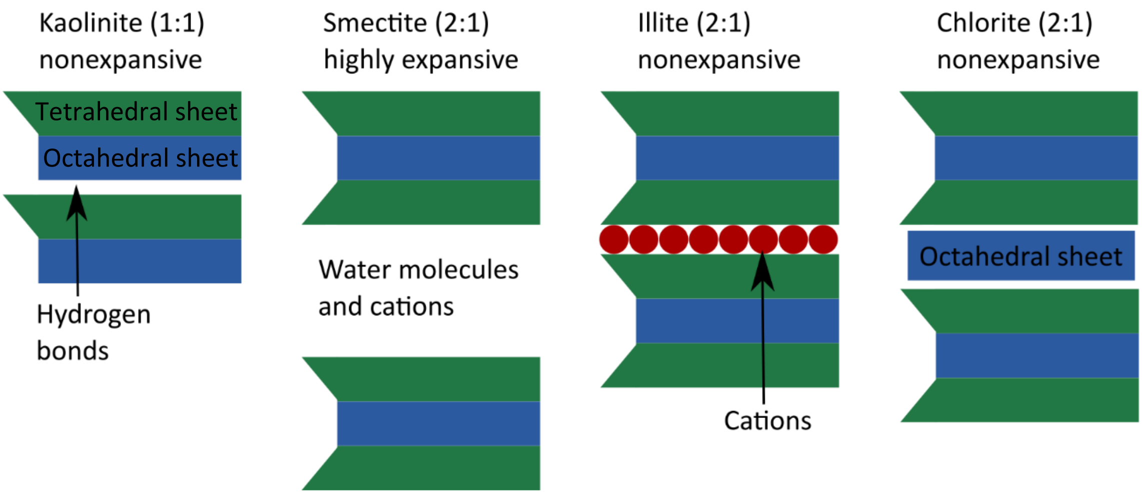

Figure 1.8: Models of the different methods of bonding between the phyllosilicate layers, which determines the clay mineralogy. Modified from Brigatti et al. (2006).

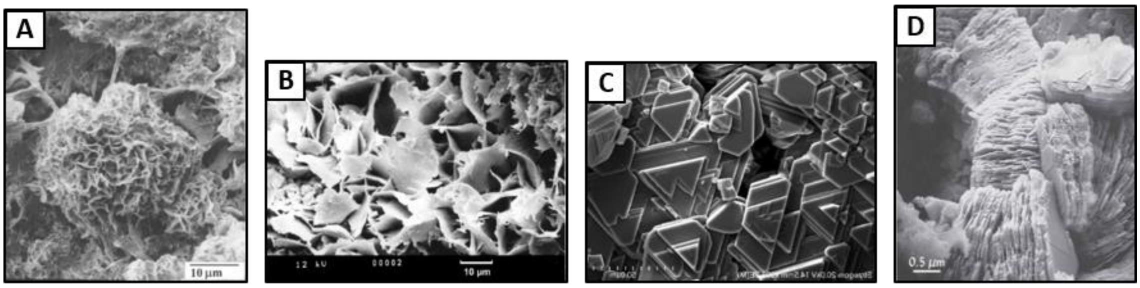

Figure 1.9: Scanning electron micrographs of (A) montmorillonite (a member of the smectite group), (B) illite, (C) chlorite, and (D) kaolinite. These images highlight differences in the structure of the different clay minerals. From the Mineralogical Society (n.d.).

1.5.2 Clay mineral suspensions

Cohesive SGFs are more complex than non-cohesive SGFs, because of the unique ability of suspended clay minerals to form flocs and gels (Winterwerp & van Kesteren 2004). Flocs are aggregates composed of clay particles that bind together when the attractive Van der Waals forces outcompete repulsive forces between the negatively charged surface of clay particles (Winterwerp & van Kesteren, 2004). Although the negative and positive charges are balanced within the clay mineral structure, clay minerals are left with an overall negative charge on the surface once the phyllosilicate lattice stops growing (Meunier, 2005). If these minerals are suspended within a fluid that contains cations, such as sea water, the positively-charged ions are attracted to the negatively-charged surface of the clays (Winterwerp & van Kesteren, 2004). The concentration of cations is highest close to the surface of the clay minerals, and the concentration of anions is lowest near the surface of the clay minerals, as the anions are electrostatically repelled (Luckham & Rossi, 1999). This interaction produces an exponential increase in the concentration of anions and an exponential decrease in concentration of cations away from the charged clay surface. This layer of anions and cations is called a diffuse electrical double layer (Oldham, 2008).

The presence of a cloud of anions and cations in the diffuse electrical double layer causes the clay particle to become neutrally charged at a certain distance from the surface of the clay particle. At this distance, the attractive Van der Waals forces are greater than the interparticle double layer repulsive forces, thus the net force becomes attractive, causing the particles to flocculate (Winterwerp & van Kesteren, 2004). The theory used to describe particle interaction by considering the opposing forces of double layer repulsion and Van der Waals attraction is called the Derjaguin Landau Verwey Overbeek model (Meunier, 2005).

The aggregation of clay minerals produces flocculated particles. Clay minerals can flocculate by three different methods: face-to-face, edge-to-face and edge-to-edge (Fig. 1.10; Meunier, 2005). At high clay concentrations a “gelling” point may be reached, where the clay minerals form a prevalent, volume-filling network of particle bonds in the liquid (Baas *et al.*, 2009). Within a gel, a “card-house” structure is build up by edge-to-face contacts, whereas face-to-face contacts produce a “card-pack” structure (Lagaly, 1989). The microstructure arrangement of clay gels is expected to control the overall strength of the gel (Lagaly, 1989; Nasser & James, 2009; Ndlovu *et al.*, 2011).

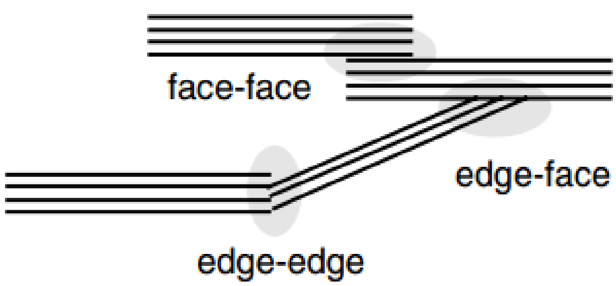

Figure 1.10: The three types of bonding between clay particles in a suspension. From Meunier (2005).

1.5.3 Cohesive strength of different clay minerals

Different clay minerals have different shapes, sizes, layer charges, cation exchange capacities, edge charge densities, and structures of the particle edges, as introduced to in Chapter 1.5.1. These different chemical and physical properties control the cohesive strength of the attractive forces between individual clay particles in a suspension (Lagaly, 1989). There is a general trend in the cohesive strengths of the common clay minerals: kaolinite and chlorite are generally considered to be weakly cohesive clay minerals, illite is considered to be moderately cohesive, and smectite is considered to be a strongly cohesive clay (Holtz & Kovacs, 1981; Hillel, 2003; Yu *et al.*, 2014).

The differences in the cohesive properties of different clay minerals can be explained by differences in their specific surface area, size, and cation exchange capacity (Holtz & Kovacs 1981; Yong *et al.*, 2012). The specific surface area of a particle is the ratio of the surface area of a material to either its volume or mass. The specific surface area of the particle controls the magnitude of the interparticle forces, with a larger specific surface area allowing greater interparticle forces (Atkinson, 2007). Table 1.1 demonstrates that kaolinite particles are relatively large and have a low specific surface area, and the size of the clay mineral decreases, and thus specific surface area increases from chlorite, via illite, to smectite. The large specific surface area of smectite is further increased by the ability of this clay mineral to swell. The cation exchange capacity is a measure of the potential chemical activity of a clay mineral, which in turn is directly related to cohesive forces (Kooistra *et al.*, 1998; Khabbazi Basmenj *et al.*, 2016). The cation exchange capacity of the clay minerals decreases from smectite, via illite and chlorite, to kaolinite, thus matching the trend of the cohesive properties of the clay minerals.

Table 1.1: Typical values of thickness, planar diameter, specific surface area, and cation exchange capacity of common clay minerals. Montmorillonite (also called bentonite) is part of the smectite group of clay minerals. The clay minerals are sorted from small to large. Modified after Hillel (2004) and Yong et al. (2012).

Edge view	**Typical thickness (nm)**	**Planar diameter (nm)**	**Specific surface area (m^2/kg)**	**Cation exchange capacity (mEq/100g)**
Smectite (inc. Montmorillonite)	2	10-1000	700-800	80-100
Illite	20	100-2000	80-120	10-40
Chlorite	30	100-2000	70-90	10-40
Kaolinite	100	10-1000	10-15	3-15

Yu *et al.* (2013) conducted laboratory experiments on the effect of montmorillonite (part of the smectite group), illite, chlorite, and kaolinite on the yield stress of subaerial debris flows. The yield stress is a convenient parameter to define the character of debris flows, as it defines the point of failure and the point of termination of the flow. The higher the yield stress value, the greater the strength of the attractive interparticle forces, *i.e.,* cohesive bonds, between the clay particles (Au & Leong, 2013; Lin *et al.*, 2016). The experiments took place at a fixed volume concentration and the ratio of cohesive to non-cohesive particles varied. As the percentage of clay in the suspensions was increased at the expense of sand and gravel, the rate of increase in the yield stress was greatest for montmorillonite, followed by illite and with a similar rate for kaolinite and chlorite (Fig. 1.11; Yu *et al.*, 2014). The concentration of clay needed to reach the same yield stress increased from montmorillonite, to illite, to kaolinite, to chlorite.

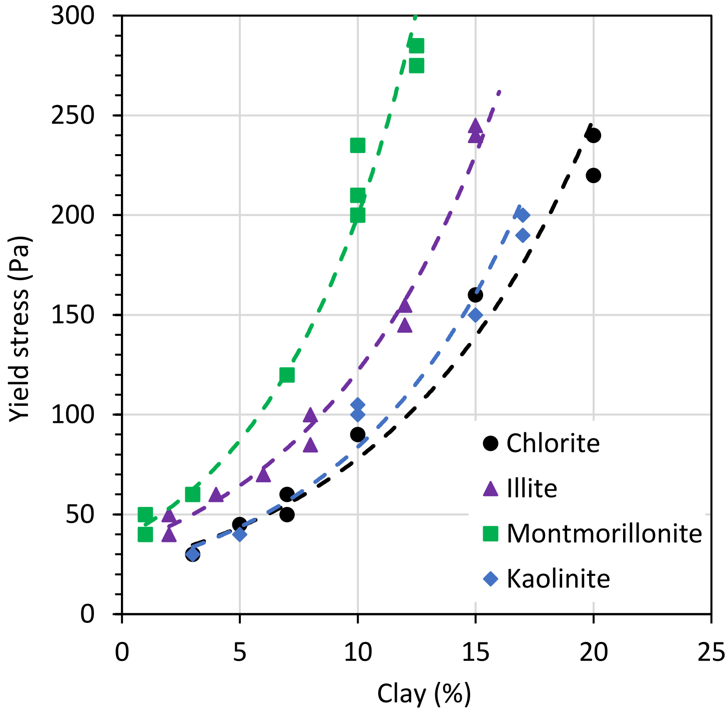

Figure 1.11: Yield stress of subaerial debris flow suspensions composed of gravel, sand and clay at a fixed volume concentration of solids of 58%. As the proportion of clay in the suspensions increases, the yield stress increases. The rate of increase reduces from montmorillonite, via illite, to kaolinite and chlorite mixtures. Redrawn from Yu et al. (2014).

1.5.4 Effect of clay type on sediment gravity flows

Investigations of the effect of clay type on the dynamics of SGFs began recently. Marr *et al.* (2001) conducted an experimental study of sand-rich subaqueous gravity flows, which also carried bentonite (montmorillonite) or kaolinite clay and found that 0.7% by weight of bentonite was sufficient to produce coherent flows, compared with 7% for kaolinite. Marr *et al.* (2001) defined coherent flows as flows that resist breaking apart and becoming completely turbulent under the dynamic stress associated with the head of a propagating debris flow. The lower threshold concentration of bentonite required to produce coherent gravity flows was attributed to the higher yield stress of bentonite mixtures compared to kaolinite mixtures of the same composition. Baas *et al.* (2016) found experimentally that the suspended sediment concentration needed to produce transitional flow behaviour (*sensu* Baas & Best 2002) is much lower in bentonite flows than in kaolinite flows. This was attributed to the greater cohesive strength of bentonite, producing flows with a significantly higher molecular viscosity and yield stress than kaolinite flows at concentrations above the gelling threshold.

1.6 Link between clay minerals and climate

In addition to their varying cohesive strength, clay minerals in the recent deep-sea sediments of the World Ocean have been observed to have a latitudinal distribution (Fig. 1.12; Biscaye, 1965; Griffin *et al.*, 1968; Rateev *et al.*, 1969; Chamley, 1989; Fagel, 2007). Chapter 7 presents a metadata analysis to asses if there is a relationship between the clay mineral assemblage in modern submarine fans and their latitude. Of the common clay minerals, kaolinite is abundant in equatorial sediment, whereas chlorite is typically found in the polar regions of the world (Griffin *et al.*, 1968). Illite and smectite have less distinct distribution patterns. However, illite can generally be found in moderate to high latitudes, whereas smectite is commonly located in tropical to moderate latitudes (Griffin *et al.*, 1968; Chamley, 1989; Thiry, 2000; Fagel, 2007).

These distinct patterns in the dominant clay mineral type in recent deep-sea sediments are thought to be related to the contemporary climates on the continents. Climate controls the intensity of physical and chemical weathering, and these weathering processes to a large extent dictate the type of clay minerals formed (Biscaye, 1965; Griffin *et al.*, 1968; Chamley, 1981; Evans, 1992; Thiry, 2000; Fagel, 2007). Physical weathering is the physical breakdown of the bedrock to produce primary minerals (Fagel, 2007). Chemical weathering refers to the chemical reactions which lead to the breakdown of pre-existing minerals and the formation of new, secondary minerals (Fig. 1.13; Allen, 2009). In areas where water is abundant and the temperature is high, such as in the tropics, chemical weathering and leaching are dominant (Chamley, 1989). This leaching can strip clay minerals of their cations, such as silica and iron, leading to stable clay mineral types, such as kaolinite and gibbsite (Allen, 2009). In contrast, in cold and arid climates, illite and chlorite, which are too unstable to be preserved in regions of intense chemical weathering, are inherited from the parent rock and remain the dominant clay minerals (Evans, 1992). Finally, under temperate climatic conditions, the chemical weathering is moderate and cations released from the bedrock encourage the formation of cation-bearing minerals, such as the clay minerals of the illite and smectite groups (Fagel, 2007; Allen, 2009). Possible changes in clay mineral type through chemical weathering are shown in selected reaction pathways in Figure 1.13 (Evans, 1992).

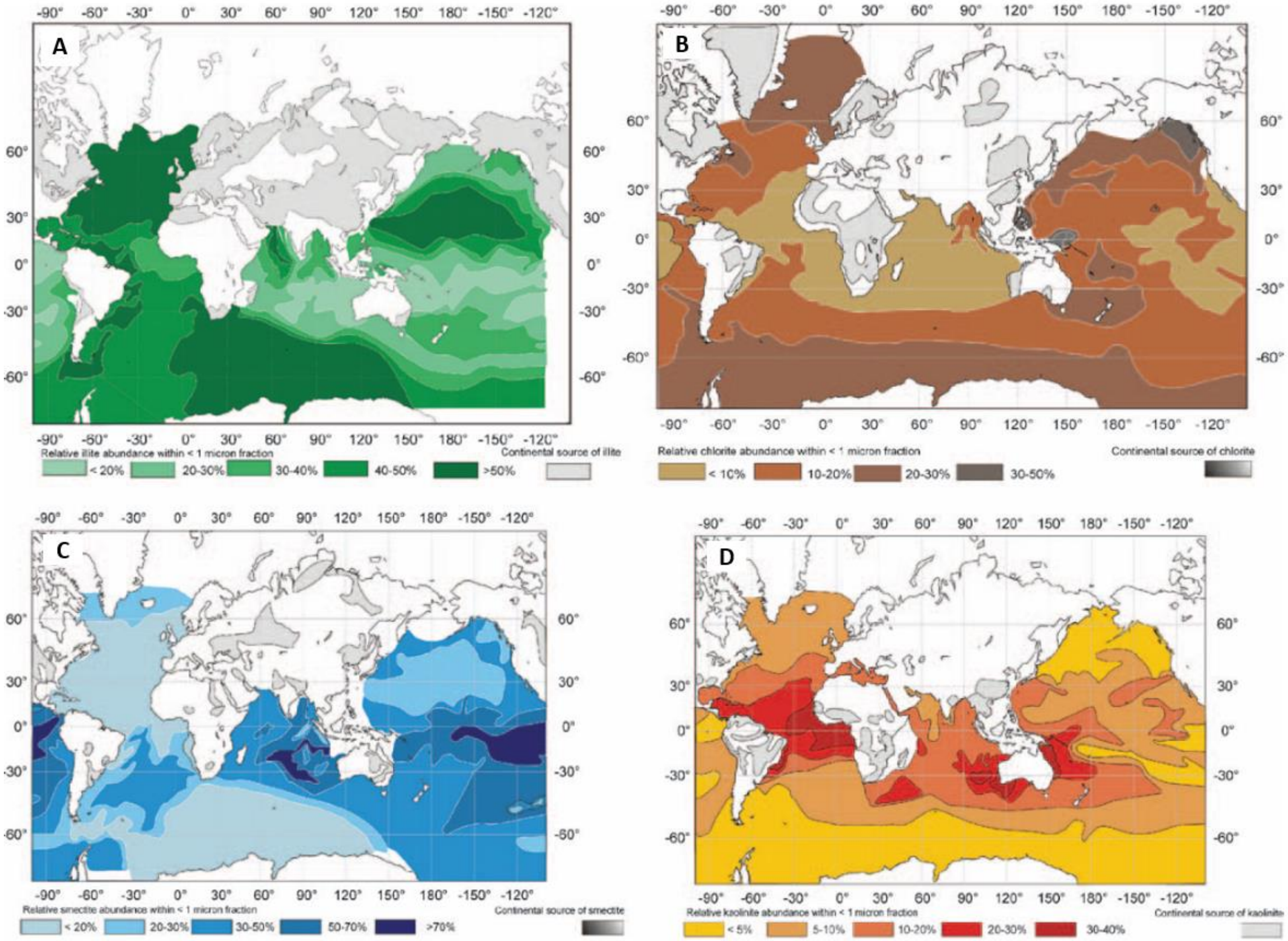

Figure 1.12: Distribution of (A) illite, (B) chlorite, (C) smectite, and (D) kaolinite in the <1μm fraction of surficial deep marine sediment. From Fagel (2007).

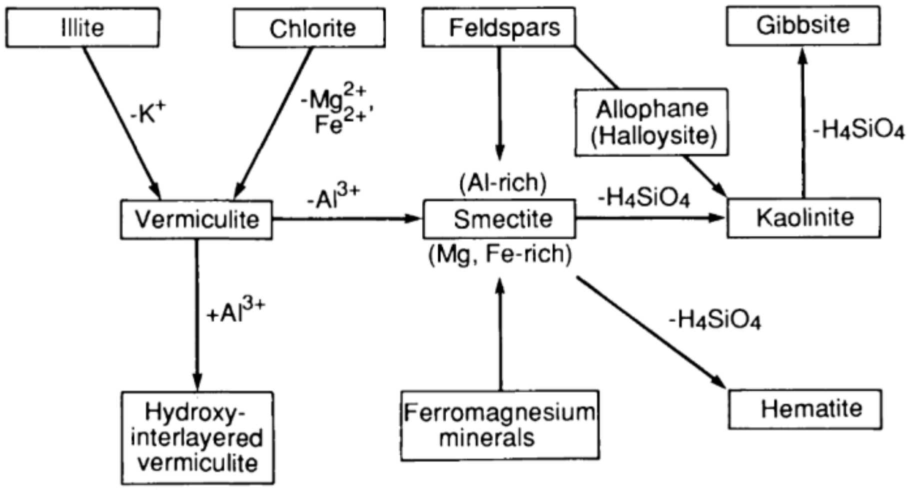

Figure 1.13: Possible reaction pathways of clay minerals formed during chemical weathering. Illite and chlorite are at the start of the reaction pathway (top left) and kaolinite and gibbsite are formed at the end (top right). The amount of chemical weathering is partly controlled by the climatic conditions. From Evans (1992).

It should be noted that a number of exceptions to the latitudinal zonation of clay minerals in the modern ocean have been identified, illustrating that there are other factors responsible for the global and regional distribution of clay minerals (Thiry, 2000). These controls include:

1) The acidic or basic composition of the source rock can determine the composition of the minerals formed by weathering.

2) The relief of the land can control the strength of the weathering, with greater physical weathering occurring in areas of high relief, potentially producing clay mineral types independent of climate and hence latitude (Singer; 1984; Thiry, 2000).

3) Size of the sedimentary basins can control the clay mineral assemblages reaching the ocean. Large sedimentary basins may stretch across climate zones and muddle the climate signal within clay mineral assemblages (Thiry, 2000; Dera *et al.*, 2009). However, the sedimentary basins need to be large enough to ensure that any local, non-climatic controls on clay mineral type are overridden by the climate control (Singer, 1984).

4) Selective sorting of clay minerals as they are transported to the deep-sea may distort the climate signal preserved in deep marine sediment (Singer, 1984; Thiry, 2000; Fagel, 2007; Berrocoso *et al.*, 2008).

5) Different clay minerals have different stabilities and some may transform into other clay minerals whilst in the sedimentary basin; this is particularly valid for smectite (Thiry, 2000).

6) Diagenetic reactions alter detrital clay assemblages and have the potential to completely remove the climate signal of clay mineral assemblages (Curtis, 1990; Fagel, 2007).

7) Clay minerals within marine sediment can also form via authigenesis, *i.e.,* in situ precipitation from a concentrated solution (Fagel, 2007). The smectite group of clay minerals is often of authigenic origin and can form locally from alteration of volcanic material, hydrothermal activity or diagenetic processes (Singer, 1984; Thiry, 2000; Berrocoso *et al.*, 2008).

1.7 Thesis structure

This thesis aims to combine laboratory experiments, geological fieldwork and a metadata analysis to further our understanding of the transport and deposition of clay minerals into deep-marine environments via cohesive SGFs. The thesis specifically investigates the role of clay mineral type in the behaviour and deposits of cohesive SGFs, the novel mixed sandstone-mudstone bedform types that may be deposited by clay-rich SGFs, and the question if the clay mineral assemblage in modern submarine fans can be linked to the latitude of the fans and their geometry. The thesis structure is as follows:

Chapter 2 provides the details of the experimental methods and materials used in the laboratory experiments presented in Chapters 3, 4, and 5.

Chapter 3 presents a series of experiments to investigate the effect of clay mineral type on the properties of cohesive SGFs and their deposits. The chapter tests if the rheological properties of the pre-failure suspension can be used to predict the flow velocity and runout distance of the laboratory SGFs.

Chapter 4 expands on the pure clay flow experiments presented in Chapter 3 by investigating SGFs composed of mixtures of clay minerals. The rheological properties of the starting suspension are used to understand the behaviour of the mixed-clay SGFS and the predictive equations presented in Chapter 3 are tested for use in the mixed-clay flows.

Chapter 5 adds another layer of complexity to Chapters 3 and 4 and considers the effect of small amounts of sand on the mobility of high-density cohesive SGFs. The effect of adding sand on the yield stress of the suspensions is tested and the physical explanations for the observed changes considered. Finally, the effect of adding a small amount of sand to cohesive SGFs across the full range of flow concentrations is discussed.

Chapter 6 provides the first comprehensive description and interpretation of mixed sandstone-mudstone bedforms observed in the fringe of the mud-rich submarine fan that makes up the Aberystwyth Grits Group and Borth Mudstone Formation (Wales, U.K.). The mixed sandstone-mudstone bedforms are interpreted to form beneath transient-turbulent clay-rich SGFs. Changes in the flow Reynolds number are used to interpret the downdip changes in the deposit properties and mixed sandstone-mudstone bedform type from the fringe to the distal fringe of the fan.

Chapter 7 presents a metadata analysis conducted to determine if there are relationships between the latitude, the clay mineral assemblages, and the geometry of modern submarine fans.

Chapter 8 integrates the findings from the results Chapters 3 to 7 and discusses their broader implications.

2. Experimental methods

Lock-exchange tank experiments were conducted in the Hydrodynamics Laboratory of Bangor University (Wales, U.K.). Chapter 2.1 describes the experimental set-up and data analysis of the lock-exchange tank experiments. The lock-exchange experiments produced sediment gravity flows composed of pure kaolinite, bentonite or silica flour (Chapter 3); mixtures of bentonite and kaolinite (Chapter 4), and mixtures of bentonite and ballotini (Chapter 5). Chapter 2.2 describes the grain-size analysis of the materials and Chapter 2.3 provides the physical and chemical properties of the sediments used. The rheological measurements of the starting suspensions using a rheometer or dam break experiments are explained in Chapter 2.4.

2.1 Lock-exchange tank

2.1.1 Experimental set-up

Experiments were conducted in a smooth-bottomed lock-exchange flume, 5 m long, 0.2 m wide, and 0.5 m deep, with a reservoir 0.31 m long at one end (Fig. 2.1). The flume walls are made of transparent plastic enabling the flows to be observed as they travel along the tank. In each experiment, the slope of the flume was set to 0^{o}, and the reservoir was filled with a suspension of sediment and seawater, separated by a lock gate from the main compartment of the flume filled with seawater. Filtered seawater from the Menai Strait (NW Wales, U.K.) with a density of 1027 kg m^{-3} was used to better mimic flows in the deep ocean. Seawater contains a higher concentration of cations compared to freshwater, which helps reduce the repulsive forces between the negatively charged clay particles and enhance flocculation and gelling (Tan *et al.*, 2014).

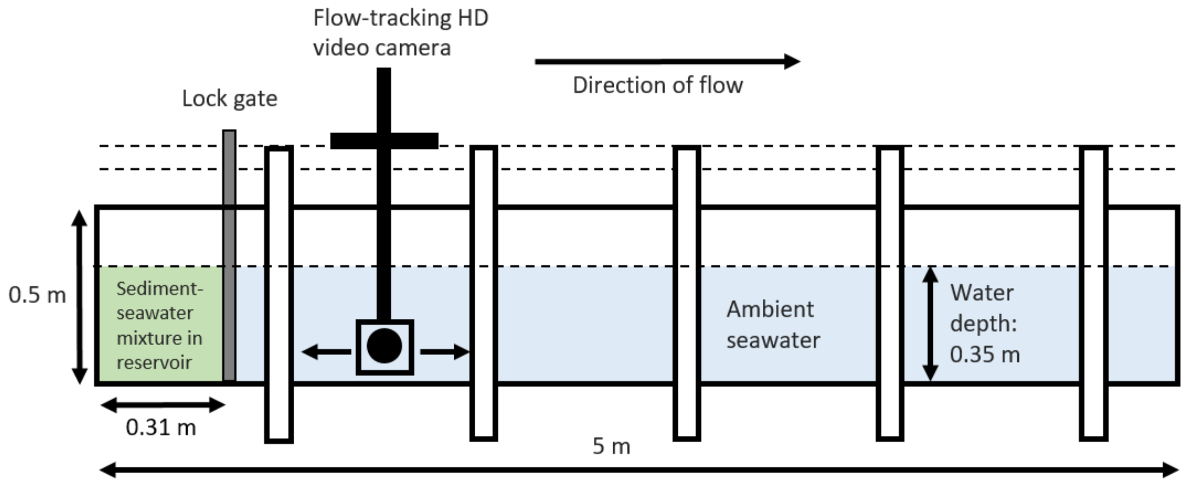

Figure 2.1: Experimental set-up for lock-exchange tank. HD = high-definition.

Each experiment required 24.5 L of suspension, and the suspensions were considered in terms of volume concentration. In order to anticipate possible time-dependent behaviour related to the material properties of the clay minerals, a consistent method was used to prepare each suspension. First, half of the seawater and the sediment were mixed in a Belle Group® Minimix 150 Electric Cement Mixer, with the mouth of the mixer covered to prevent spilling, for 15 minutes. After 15 minutes, the cement mixer was stopped and the sides of the cement mixer scraped using a rubber scraper to release unmixed clay caught in the fins of the mixer. The remaining seawater and sediment were then added and the suspension was mixed for a further 15 minutes. Subsequently, the sides of the cement mixer were scraped again and the mixture decanted into an 80 L bucket. The suspension was further mixed by a handheld mixer (Evolution® Twister 1110E Professional Variable Speed Mixer) for three minutes for kaolinite and silica flour suspensions and for 10 minutes for bentonite suspensions, to obtain lump-free mixtures.

The fully-mixed suspension was then progressively added to the reservoir with the lock gate in place while the flume filled with seawater, in order to keep similar fluid levels on each side of the lock gate to limit pressure differences across the lock gate. The sides and base of the lock gate were covered in a layer of grease to stop any of the suspension leaking into the rest of the tank. Each flow was generated from the same volume and depth of mixture into a body of seawater of the same depth (h = 0.35 m). Filling the lock gate and tank took approximately 25 minutes. The suspension in the reservoir was mixed using the handheld mixer for 60 s and then given *c.* 10 s to come to rest before lifting the gate and generating the SGF. A Sony® HDR-CX105E Digital Video Camera mounted on a frame attached to runners on the top of the tank tracked the front of the flow along the length of the tank. From this a time series of the head velocity of each SGF was obtained. The flows were also recorded using a background Canon® IXUS 160 Camera, set 4 m back from the tank to record a wide viewpoint, which captured changes in the evolution of the body and tail of the flow.

The morphology of the SGF deposits was measured along the center line of the flume using a SeaTek 5 MHz Ultrasonic Ranging System, comprising 16 transducers spaced 16.2 mm apart. The Ultrasonic Ranging System calculates the vertical distance to the deposit by means of the two-way travel time of an ultrasound pulse. SeaTek state that the vertical accuracy of the measurements is 1.0 mm. The housing array of the transducers was arranged parallel to the direction of flow and was moved 0.122 m downstream between individual readings, thus producing a profile with a data point every 8.1 mm along the centre line of the deposit. The runout distance of each deposit, defined as the distance the flows travelled from the lock gate before coming to a halt, was recorded for all flows that stopped before reaching the end of the flume. Several experiments were repeated (22%, 25%, 27% and 29% kaolinite and 17%, 18% and 20% bentonite) and showed good reproducibility. The difference in runout distance between repeat experiments was a maximum of 0.3 m and an average of 0.2 m. Indirectly, good reproducibility is also shown by the consistent trends in maximum head velocity and runout distance as a function of flow concentration and sediment type.

2.1.2 Data analysis

2.1.2.1 Head velocity

The HD video recordings tracking the head of the flows were analysed in MATLAB to produce velocity-distance series. First, the videos had to be converted from AVCHD video file format (.MTS) to Audio Video Interleaved file format (.AVI) using an online file converter (available at: https://video.online-convert.com/convert-to-avi) so that Matlab could read the video files. A Matlab script was developed using the Matlab function *mmread* which can transform video files into a format readable by Matlab and provides each video frame as an image with a time stamp *(*available at: https://uk.mathworks.com/matlabcentral/fileexchange/8028-mmread). The change in head position between the video frames was measured from the distance moved in pixels relative to a scale at the bottom of the flume, and velocity was then calculated using the time between each frame (0.08 s) to produce a velocity-distance plot. A 5-point moving average was applied to the velocity data and anomalous data points removed manually.

2.1.2.2 Deposit properties

The Ultrasonic Ranging System data were also analysed using Matlab. The deposit thickness was determined by subtracting values from a blank scan of the bottom of the flume from the values of the bed profile. Smoothing was applied to the data by way of a 5-point moving average.

2.1.2.3 Video analysis

The video footage was analysed to gain qualitative information on the shape and kinematic behaviour of the head and body of the flows. The focus was on the heads of the SGFs using the HD video camera recordings, but the background-video data suggest that the head behaviour is representative of the body behaviour of the flows.

2.2 Grain-size analysis

2.2.1 Sampling methods

Chapter 5 presents grain-size analysis results of sediment cores taken from the SGF deposits. Before taking the sediment cores, the deposit was first left to settle for 24 hours. The water above the deposit was then slowly drained and the final layer of water directly over the deposit carefully siphoned off using a thin tube to minimise disruption of the deposit, over another period of 24 hours. The deposit was then left to partially dry at room temperature for seven days. Thereafter, the deposits were dry enough to sample. Samples were taken every 0.2 m from the lock gate along the centre line of the deposit, using 30 mm diameter 60 ml syringe cores. The cores were then wrapped in Clingfilm and duct tape and frozen upright. The frozen cores were subsampled by cutting the core into horizontal slices using a hot scalpel. The subsampling aimed to cut the sample into 2.5 mm thick slices. However, sometimes this was not possible as the slices collapsed, so 5 mm thick slices were taken.

2.2.2 Malvern Mastersizer

Grain-size analysis was conducted on the sediment types used in the lock-gate experiments to compare their grain-size distributions. In addition, the sediment cores collected from the mixed bentonite-sand deposits in Chapter 5 were also tested for grain-size. Grain-size analysis was conducted on the samples using a Malvern 2000 laser particle sizer (Malvern Panalytical Limited, Malvern, U.K.), with the settings given in Table 2.1. Before the samples were processed by the

Mastersizer, a calibration sample of known grain-size distribution was measured to check the machine was working correctly. The Malvern provides the grain-size data as a volume fraction of 100 grain-size classes from 12.2 ϕ (0.2 µm) to -1 ϕ (2.0 mm).

Table 2.1: Malvern 2000 laser particle sizer settings

Machine settings	
Pump speed	2000 rpm
Ultrasound treatment time	60 s
Sonification	20.00
Obscuration	10-20%
Optical settings	
Refractive index	1.52
Absorption	0

In Chapter 5, the grain-size data of the mixed bentonite-sand deposits is given as percentage bentonite and sand. The frequency distribution of the bentonite and ballotini is shown in Figure 2.2. The two distributions are distinct with only a small amount of overlap. The grain-size data is presented as percentage bentonite and percentage ballotini in each sample. This was calculated as the percentage volume fraction below 57 µm for bentonite (shown by the black line in Figure 2.2). The slight overlap between the bentonite and ballotini above 57 µm may have introduced a small error in the percentage values of bentonite and ballotini. This error is considered to be negligible, and of no influence on the main conclusions of Chapter 5. The errors in the grain-size data were analysed by completing repeatability experiments on core slice samples taken from a control core. Three independent experiments were conducted on each core-slice sample. The standard deviation of the means of the percentage bentonite from the independent tests was between 0.3% and 1.6% for seven core slices.

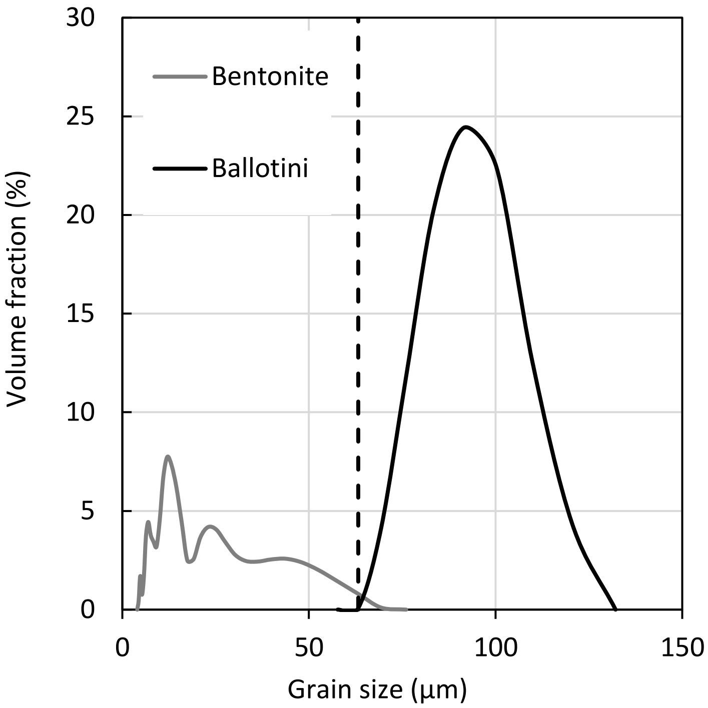

Figure 2.2: Grain-size distributions of bentonite and ballotini obtained from the Malvern 2000 laser particle sizer. Black line denotes 57 µm used to distinguish between the bentonite and ballotini in the deposit samples.

2.3 Sediment

2.3.1 Kaolinite clay

The kaolinite used in this study was Polwhite E, a medium particle size kaolinite produced by Imerys Ltd. from deposits in the South West of England. The grain-size distribution of the kaolinite clay was measured using the Malvern Mastersizer 2000 (Chapter 2.2.2) and has a D_{50} of 9.1 µm (Fig. 2.3A). The density of the kaolinite is 2600 kg m^{-3}. Kaolinites are naturally occurring minerals where impurities are bound to be present. The results of XRD analysis provided by the supplier are presented in Table 2.2. In addition, the detailed elemental composition of the kaolinite from X-ray fluorescence spectrometry is given in Table 2.3.

Table 2.2: Mineralogy of kaolinite used in experiments. QT = query trace. From Imerys Ltd.

Minerals	Kaolinite
Kaolinite	77%
Micas	13%
Feldspars	5%
Quartz	3%
Albite	QT

Table 2.3: Elemental composition of bentonite, kaolinite and silica flour by X-ray fluorescence spectrometry analysis. Data provided by suppliers.

Elements	Bentonite	Kaolinite	Silica Flour
SiO_2	57.1%	49.2%	99.1%
Al_2O_3	17.79%	35.4%	0.41%
Fe_2O_3	4.64%	1.0%	0.06%
CaO	3.98%	0.03%	0.03%
MgO	3.68%		0.02%
Na_2O	3.27%	0.2%	0.03%
K_2O	0.9%	2.9%	0.10%
TiO_2	0.77%	0.07%	0.015%
Mn_2O_3	0.06%		
LoI	7.85%	10.9%	

2.3.2 Bentonite clay

The bentonite clay used in the experiments was Bentontex SB produced by RS Minerals Ltd., which is a sodium bentonite mined from multiple deposits worldwide. The bentonite had a D_{50} of 5.6 µm (Fig. 2.3C) and a density of 2300 kg m^{-3}. The chemical composition and mineralogy of the bentonite are given in Tables 2.3 and 2.4.

Table 2.4: Mineralogy of bentonite used in experiments. Data provided by RS Minerals Ltd.

Minerals	Bentonite
Na-Montmorrilonite	92%
Calcite	4%
Feldspars	2%
Quartz	1%
Dolomite	1%

2.3.3 Silica flour

Silica flour is produced from milled silica sand and composed of quartz. The silica flour used in these experiments was SL 1/300 obtained from Richard Baker Harrison Ltd. The elemental composition of the silica flour is given in Table 2.3 and Figure 2.3B shows the grain-size distribution. The silica flour had a D_{50} of 18.2 µm and a density of 2650 kg m^{-3}.

2.3.4 Ballotini

Spherical glass ballotini provided by Potters Industry Inc. was used to simulate sand grains. The ballotini had a D_{50} of 98 µm and a narrow grain-size range of 63-132 µm (Fig. 2.3D). The glass beads are inert and composed of silica with some impurities. The ballotini was assumed to have a density of 2650 kg/m^3.

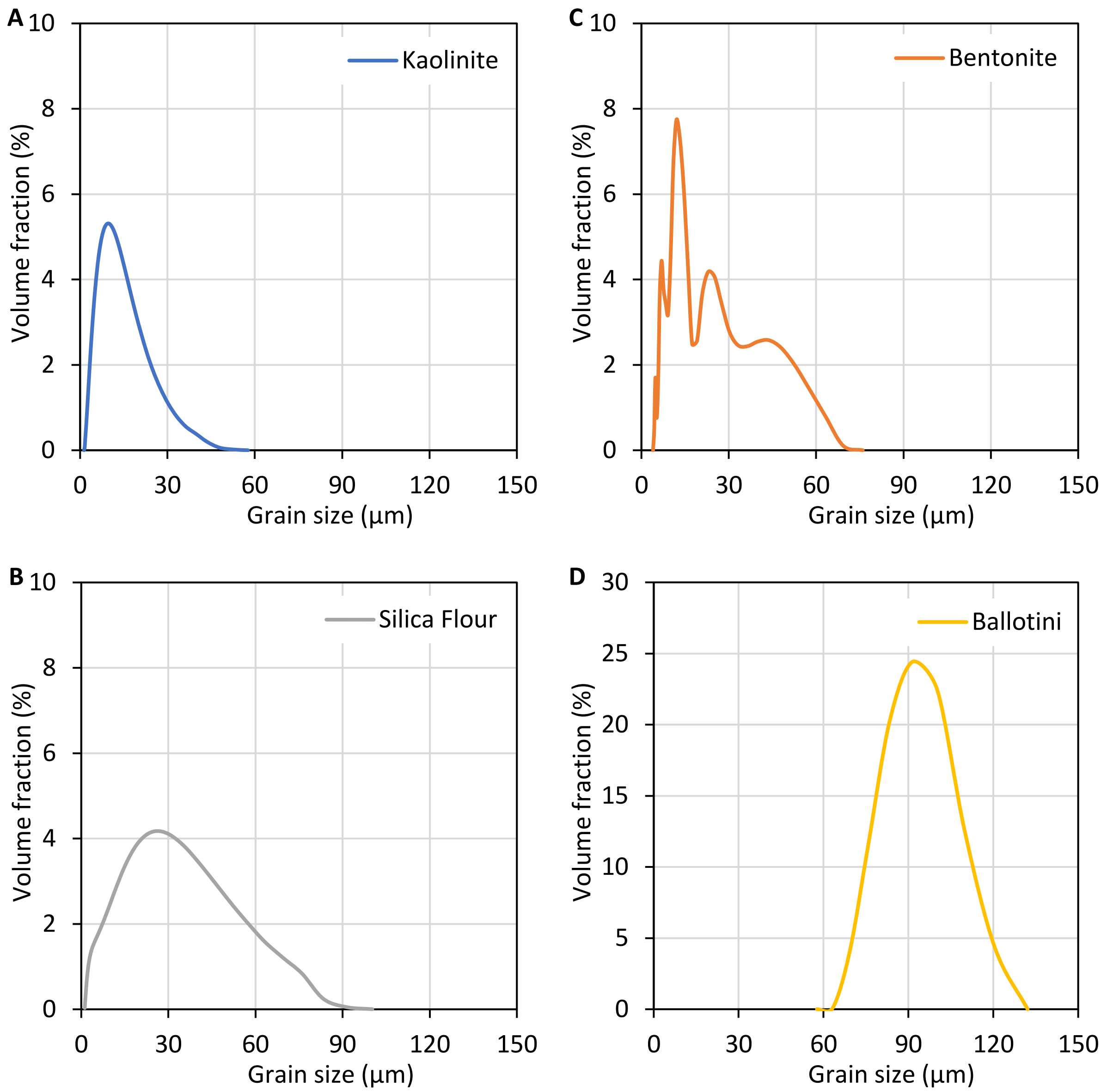

Figure 2.3: Grain-size distribution of (A) kaolinite clay, (B) silica flour, (C) bentonite and (D) ballotini. Note the different vertical scale for the ballotini.

2.4 Rheological measurements

This chapter describes the two methods used to measure the rheological parameters of the suspensions in the lock-exchange experiments. The first method used a rheometer to obtain the suspension yield stress, initial complex shear modulus and apparent viscosity (Chapter 2.4.1). The second method used dam break experiments, from which the yield stress of the suspension can be derived (Chapter 2.4.2). The three rheological parameters determined from the rheological measurements are first briefly defined. The yield stress of a suspension is a measure of the strength of the attractive interparticle forces, *i.e.,* cohesive bonds, between the clay particles (Au & Leong, 2013; Lin *et al.*, 2016). The initial complex shear modulus also gives information about strength of the interparticle forces, as it described the rigidity of the material and is defined as the shear stress over the strain (Mezger, 2006). Finally, the apparent viscosity of a suspension represents the resistance of the fluid to flow and is calculated from the ratio of shear stress to strain rate (Mezger, 2006). It should be noted that the rheological values derived from the rheometer and dam break experiments are not absolute, and can only be compared with values obtained using identical methods, equipment and sample history because of the complex structure and behaviour of clay suspensions (Laxton & Berg, 2006).

2.4.1 Rheometer

The rheological characteristics of sediment mixtures with the same composition as the suspensions used in the lock-exchange experiments presented in Chapters 3 and 4 were measured using the Anton Paar Physica MCR 301 rheometer at IFREMER (Brest, France). These experiments measured pure kaolinite and bentonite suspensions at concentrations between 5% to 29% and 5% to 20%, respectively (Chapter 3). As well as ten suspensions comprising different proportions of mixed bentonite-kaolinite at a fixed volume concentration of 20% (Chapter 4). The rheological data for the silica-flour suspensions and the 1% clay suspensions were discounted because particle settling changed the properties of the suspensions over the course of the rheometric tests.

2.4.1.1 Sample preparation

Each experiment used 200 cm^3 samples, prepared by weighing Menai Strait seawater and clay in a plastic bottle at the desired concentration. The bottle was then manually shaken for 10 minutes to produce a homogeneous suspension. A subsample of the suspension was measured for pH using a Metrohm 691 pH Meter which was calibrated before each series of measurements using two buffers with known pH. The calibration was tested with a third buffer and if within 0.05 of the expected value the calibration was correct. The pH of the suspensions were tested 4 times over a period of 24 hours.

Before adding the suspension to the rheometer cup, the sample was shaken for an additional 30 seconds immediately before the test to account for any settling that may take place at low clay concentrations. The experiments were carried out at 20°C with a concentric-cylinder geometry with a cone bottom (Fig. 2.4). This geometry was selected as it reduces side wall effects and prolongs the settling duration of the suspension; the sandblasted bob also reduces slip (Fig. 2.4). Time dependencies of the rheological parameters were tested and found to be insignificant over a period of up to 12 hours and thus negligible within the typical experimental time frame of 75 minutes. Three rheological tests were conducted using fresh subsamples for each suspension: oscillatory test, strain-controlled test and shear-controlled test. The agreement in trends of the rheological parameters with changing clay concentrations derived from the different tests was used to check the reliability of the results. Below, the basic principles of the three tests and the graphical methods to determine the yield stress and initial complex shear modulus are presented.

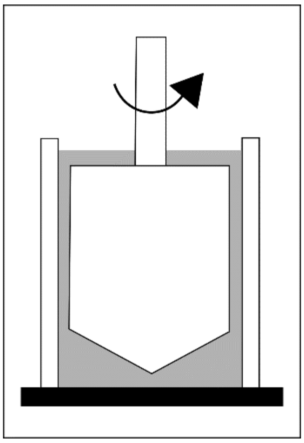

Figure 2.4: The cone bottom concentric-cylinder geometry of the bob used for the rheometer experiments.

2.4.1.2 Oscillatory test

In the oscillatory test, the inner cone rotates at a progressively increasing oscillating strain with a logarithmic ramp from 0.0001 to 100 and the resultant stress, loss modulus and storage modulus are measured (Fig. 2.5; van Vliet, 2013). The storage modulus and loss modulus represent the elastic component and viscous component of the complex shear modulus, respectively (Mezger, 2006). The yield stress was defined at the stress value where the storage modulus crosses the loss modulus, as this marks liquefaction (Fig. 2.5). The initial complex shear modulus was calculated from the shear stress to strain ratio at a low strain of 0.028.

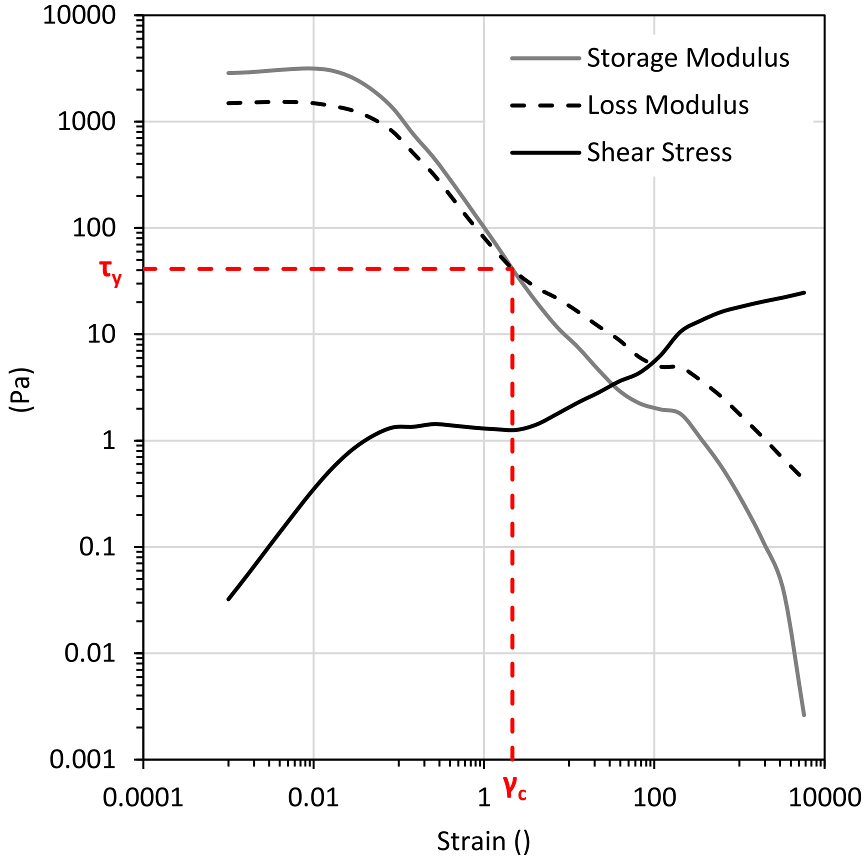

Figure 2.5: Oscillatory test results of the 22% kaolinite suspension. The yield stress (τ_y) is defined as the point where the storage modulus crosses the loss modulus and γ_c denotes the associated critical strain.

2.4.1.3 Strain-controlled test

In the strain-controlled test, the strain rate is ramped up linearly from 0.0001 to 0.01 s^{-1} and the resulting stress measured at each time step with a measurement point duration of 2 s. The yield stress is derived graphically from the strain-controlled curve as the maximum shear stress experienced before the sediment collapses (Fig. 2.6). The initial complex shear modulus is derived from the gradient of the slope of the curve at very low deformations (Fig. 2.6).

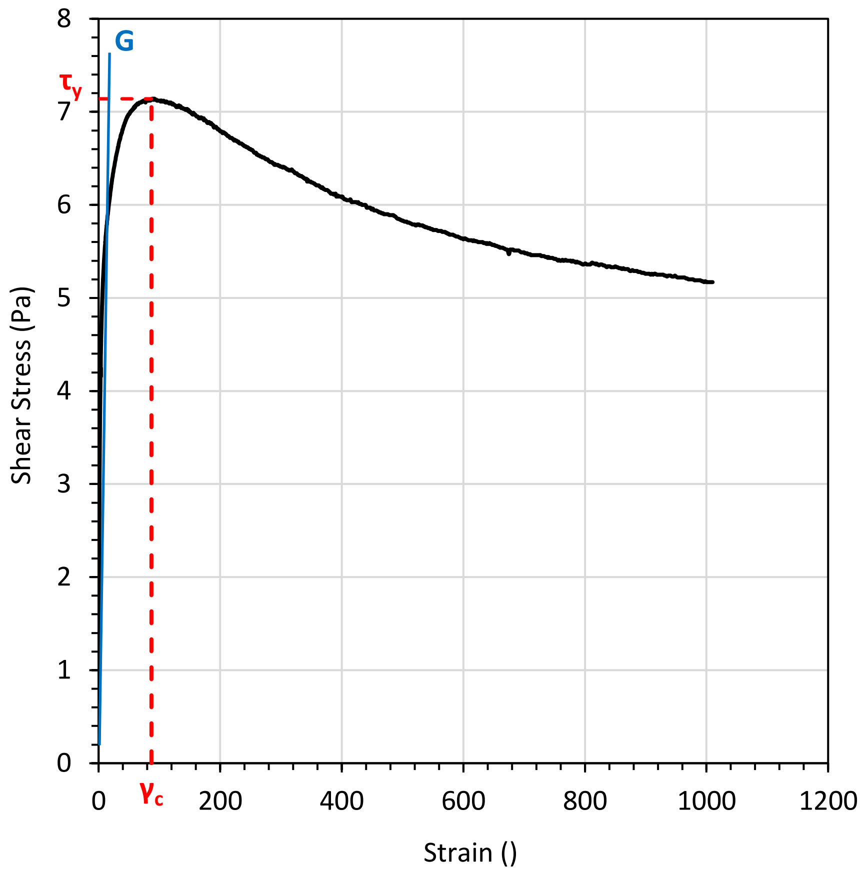

Figure 2.6: Strain-controlled test results for the 22% kaolinite suspension. The yield stress (τ_y) is defined as the maximum shear stress experienced by the sediment before it collapses and has an associated critical strain (γ_c). The gradient of the slope of the curve at low strain gives the initial complex shear modulus (G).

2.4.1.4 Stress-controlled test

In the stress-controlled test, the stress is increased logarithmically from 0.0001 Pa to 3 times the yield stress recorded from the strain-controlled test, and the resulting strain rate of the suspension is measured. The duration for obtaining each data point was 1 s. Figure 2.7 shows an example of the result from the stress-controlled test for the 22% kaolinite suspension. The yield stress was obtained from the stress versus strain curve as the point at which there is a jump in measured strain for constant stress value, denoting sediment collapse (Fig. 2.7). As for the strain-controlled tests, the initial complex shear modulus is determined from the gradient of the slope of the curve at very low deformations (Fig. 2.7). The apparent viscosity of the suspensions is recorded directly by the rheometer.

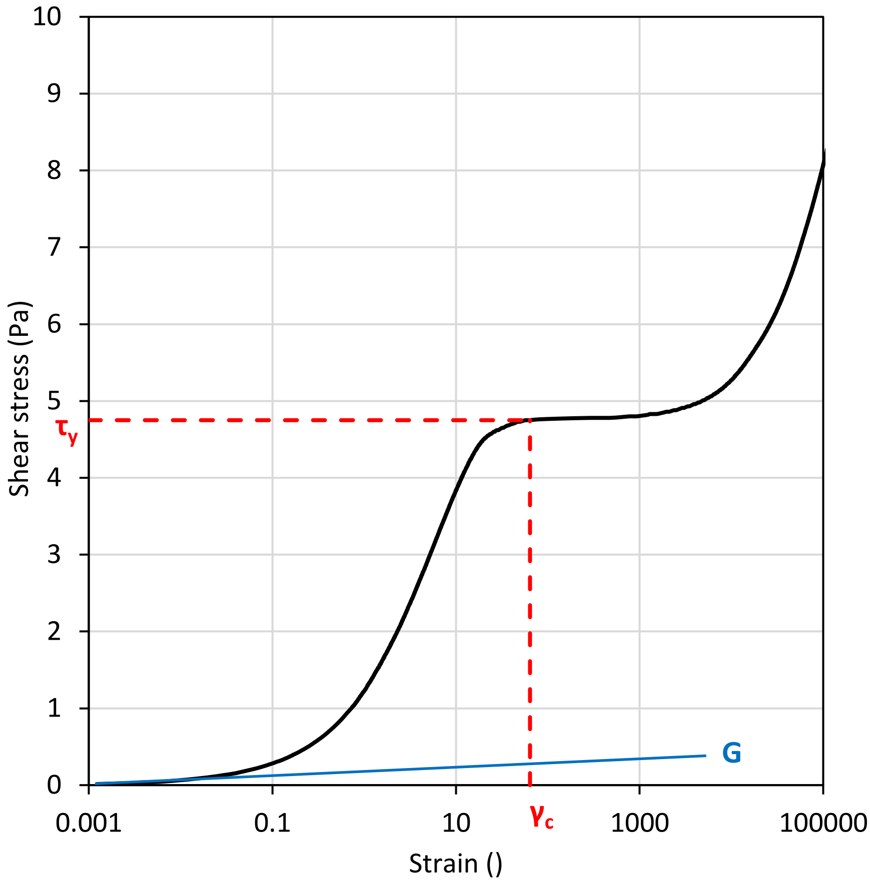

Figure 2.7: Rheological parameters of the 22% kaolinite suspension obtained from the stress-controlled test. τ_y and γ_c denote the yield stress and critical strain, respectively, and G represents the initial complex shear modulus.

2.4.2 Dam break method

For the mixed bentonite-sand suspensions, dam break experiments were conducted to determine the yield stress of the suspension (Balmforth *et al.*, 2007; Matson & Hogg, 2007). This method calculates the yield stress from the runout distance of the suspensions based on the idea that non-Newtonian fluids will become stationary when the gravitational forces are in equilibrium with the yield stress (Matson & Hogg, 2007). The experimental set up used a small lock-exchange tank, 0.105 m wide, 0.59 m long, 0.12 m deep, with a reservoir 0.95 m long. A 0.7 L suspension of bentonite-sand of the same composition as the suspensions used in the large lock-exchange experiments was prepared in a 1.5 L screw cap bottle and manually shaken for 10 minutes. The suspension was then put into the reservoir to a height of 0.05 m, the gate lifted and the distance the suspension travelled for was measured (Fig. 2.8). For each suspension concentration, three measurements of the suspension runout distance were made.

The yield stress, τ_y, was then determined based on a mathematical model of the slump of a viscoplastic fluid described using the Herschel-Bulkley constitutive law, where the equations were solved numerically using a finite difference scheme (Balmforth *et al.*, 2007; Matson & Hogg, 2007). The yield stress is calculated using:

$$\tau_y = \frac{B\rho g H^2}{L} \tag{2.1}$$

where ρ is the density of the suspension, g the acceleration due to gravity and H the height of the suspension. B is the Bingham number, defined as the ratio of yield stress relative to the stresses generated by the weight of the flowing layer (Matson & Hogg, 2007). If the Bingham number is < 1/3 all the fluid has flowed upon the gate being lifted, however a Bingham number of ≥ 1/3 means that part of the fluid has remained stationary in the reservoir after the gate was lifted. In these experiments the Bingham number was always less than 1/3 and can be calculated by:

$$B = \frac{9}{8X^3} \tag{2.2}$$

Where X is the runout distance of the suspension, dimensionalised by the length of the reservoir. To compare the bentonite-sand suspensions with the pure bentonite suspensions, the yield stress of the pure bentonite suspensions was also determined using this method.

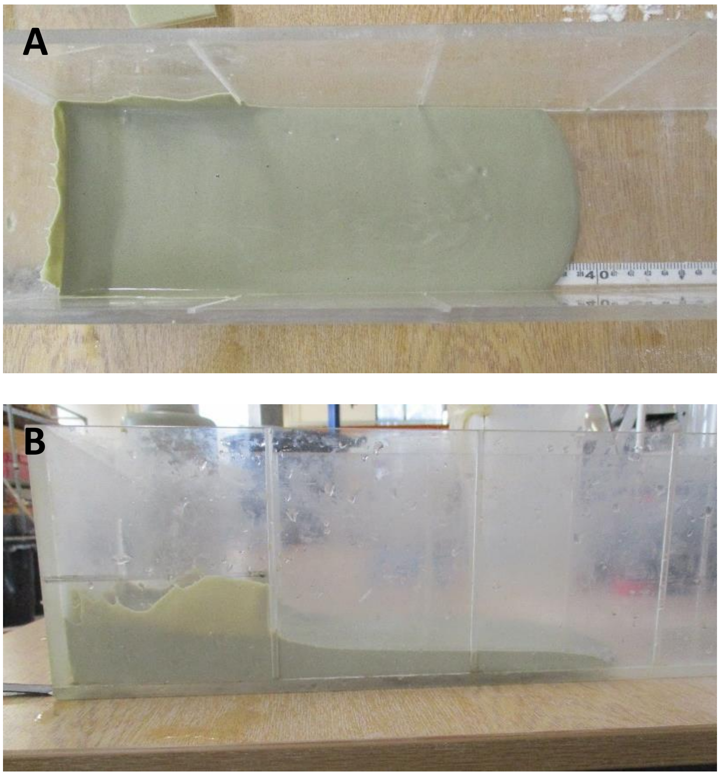

Figure 2.8: (A) View from above and (B) side view of the flume tank containing a 20% bentonite-sand suspension dam break experiment which travelled 0.29 m from the back of the reservoir.

2.5 How to apply the experimental results to natural, full-scale flows and their deposits

The laboratory experiments presented in Chapters 3 to 5 are a powerful method to visualise and understand cohesive SGFs. This chapter describes how the laboratory results can be applied to full-scale flows and deposits. Quantitative scaling of the experimental results to natural flows and their deposits is not possible at present, because full-scale sediment gravity flows are often faster and more turbulent (Talling *et al.*, 2013), and therefore more likely to break the bonds between clay particles. Thus, the concentration thresholds for the experimental flows where the balance between cohesive and turbulent forces change may occur at different concentrations for natural flows. However, the trends observed in these experiments are expected to hold true for flows in the natural environment and the following qualitative comparisons between the laboratory flows and full-scale, natural SGFs can be made.

- The progressive trends in flow behaviour and flow type observed with increasing sediment concentration and increasing rheological strength are expected to be mimicked by natural flows. However, the concentration or rheological boundaries for each flow type are expected to be higher for natural flows that have greater flow velocities and turbulent energy than those produced in the laboratory.

- The trends in maximum head velocity of the experimental flows should also occur in natural flows. However, the concentration values and flow rheological properties over which changes in head velocity are observed will be different.
- The rheological strength of natural SGFs should control their deposit geometry and runout distance in the same manner as observed in the laboratory flows. Flows with high rheological strength are expected to have a lower flow mobility, shorter runout distance and thicker deposits than flows of a lower rheological strength.
- The effect of clay mineral type, clay mineral mixtures and mixtures of sand and clay on the rheological strength of the flow suspensions will also be felt in natural flows.
- Certain small-scale flow features observed in the experimental flows could be due to the laboratory set up and may not occur in natural flows. These include the coherent fluid entrainment structures described in Chapters 3 to 5.

3. The effect of clay mineral type on the properties of cohesive sediment gravity flows and their deposits

3.1 Introduction

Understanding cohesive, clay-laden subaqueous sediment gravity flows (SGFs) is vital, because clay is the most abundant sediment type on the Earth surface and SGFs transport large volumes of this sediment into the ocean (Hillier, 1995; Healy *et al.*, 2002; Talling *et al.*, 2015). Owing to the dynamic interplay between turbulent and cohesive forces**,** the flow dynamics of cohesive SGFs and their corresponding deposits are more complex than non-cohesive SGFs, but less well studied (Baas *et al.*, 2009). The cohesive forces in cohesive SGFs have been shown to increase with increasing clay concentration (Hampton, 1975; Baas & Best, 2002; Felix & Peakall, 2006; Baas *et al.*, 2009; Sumner *et al.*, 2009). However, work by Maar *et al.* (2001) and Baas *et al.* (2016) has shown that the clay mineral type in a cohesive SGF can also influence the cohesive forces in the flow. Different clay minerals have different chemical and physical properties, which controls the strength of inter-particle forces (Lagaly, 1989). This chapter presents experiments conducted to further our understanding of the effect of clay type on cohesive SGFs and their deposits.

To isolate the effect of clay mineral type and concentration, lock-exchange experiments contrasted SGFs composed of weakly cohesive kaolinite clay, strongly cohesive bentonite clay, and non-cohesive silica flour at a wide range of volume concentrations in natural seawater. The experiments measured the head velocity of the flows, and their runout distance and deposit geometry, along with the rheological characteristics of the starting suspension. The principal aims of this research were:

1. To determine how clay concentration and clay type qualitatively affect the flow properties and quantitatively affect the flow velocity, runout distance, and deposit geometry of fine-grained SGFs.
2. To investigate if the rheological properties of the pre-failure suspensions can be used to predict the flow velocity and runout distance of the laboratory SGFs, independent of clay type and concentration.
3. To discuss the possible implications of the experimental data for natural SGFs and their deposits.

3.2 Methods

3.2.1 Lock-exchange experiments

Thirty-two SGF experiments were conducted in the lock-exchange tank, using the experimental methods described in Chapter 2. The experiments contrasted three different sediment types of contrasting rheological properties: (1) non-cohesive silica flour at initial volumetric sediment concentrations in seawater, C, of 1% to 52%; (2) weakly cohesive kaolinite ranging from C = 1% to C = 29%, and; (3) strongly cohesive bentonite with C values between 1% and 20%. For each experimental flow a velocity-distance series and deposit height-distance series were produced, using a high-definition video camera and a SeaTek 5 MHz Ultrasonic Ranging System, respectively. In addition, the visual behaviour of the flows was recorded using the video recordings. The rheological characteristics of sediment mixtures with the same composition as the suspensions used in the lock-exchange experiments were measured using the Anton Paar Physica MCR 301 rheometer, as outlined in Chapter 2. The details of all experiments discussed in this chapter are provided in Table 3.1.

Table 3.1: Experimental data. TC = turbidity current.

Run number	Sediment type	Initial sediment concentration, *C* (vol %)	Runout distance (m)	Maximum head velocity (m s^{-1})	Yield stress (Pa)	Flow type
1	Silica flour	1	-	0.11	-	Low-density TC
2	Silica flour	5	-	0.24	-	Low-density TC
3	Silica flour	10	-	0.34	-	Low-density TC
4	Silica flour	15	-	0.45	-	Low-density TC
5	Silica flour	25	-	0.58	-	Low-density TC
6	Silica flour	40	-	0.69	-	Low-density TC
7	Silica flour	44	-	0.71	-	Low-density TC
8	Silica flour	46	-	0.75	-	High-density TC
9	Silica flour	47	4.66	0.75	-	High-density TC
10	Silica flour	48	3.68	0.71	-	High-density TC
11	Silica flour	49	2.82	0.71	-	High-density TC
12	Silica flour	50	1.53	0.64	-	High-density TC
13	Silica flour	51	0.96	0.61	-	Mud flow
14	Silica flour	52	0.49	0.29	-	Slide
15	Kaolinite	1	-	0.11	-	Low-density TC
16	Kaolinite	5	-	0.28	0.34	Low-density TC
17	Kaolinite	10	-	0.33	8.77	Low-density TC
18	Kaolinite	15	-	0.41	15.5	Low-density TC
19	Kaolinite	22	4.35	0.50	41.2	High-density TC
20	Kaolinite	23	3.66	0.48	-	High-density TC
21	Kaolinite	25	2.09	0.48	67.2	High-density TC
22	Kaolinite	27	1.01	0.40	93.8	Mud flow
23	Kaolinite	29	0.45	0.29	141.2	Slide
24	Bentonite	1	-	0.10	-	Low-density TC
25	Bentonite	5	-	0.23	0.77	Low-density TC
26	Bentonite	10	-	0.31	7.35	Low-density TC
27	Bentonite	15	4.66	0.35	21.7	High-density TC
28	Bentonite	16	3.77	0.37	28.9	High-density TC
29	Bentonite	17	3.12	0.34	34.7	High-density TC
30	Bentonite	18	1.42	0.27	37.0	Mud flow
31	Bentonite	19	1.22	0.22	119.0	Mud flow
32	Bentonite	20	0.22	0.07	217.3	Slide

3.3 Experimental results

The behaviour of the experimental SGFs varied notably with the initial suspended-sediment concentration and the type of sediment. Below, observed differences in the shape and kinematic behaviour of the head of the flows, and spatial trends in their head velocity and deposit thickness, are described for the non-cohesive silica flour (Figs 3.1 to 3.3), the weakly cohesive kaolinite (Figs 3.4, 3.5, 3.7), and the strongly cohesive bentonite (Figs 3.4, 3.6, 3.8).The focus is on the heads of the SGFs, but the background-video data suggest that the head behaviour is representative of the body behaviour of the flows.

3.3.1 The effect of on increasing silica-flour concentration on the flows

3.3.1.1 Visual observations

Video recordings of the silica-flour-laden flows show marked changes in the behaviour of the heads of these flows, as the initial suspended-sediment concentration, C, was increased from 1% to 52%. Along the entire length of the flume, the flows that carried up to 44% silica flour were visually dominated by turbulent mixing, both within the head and body and at their boundaries (Fig. 3.1A, B). Upon leaving the reservoir, these flows developed a pointed semi-elliptically-shaped head with a prominent nose in flow-parallel vertical section. This shape, as well as the thickness of the head of these flows, remained constant along the flume. The height of the body fluctuated owing to the development of Kelvin-Helmholtz instabilities at the upper surface of the flows.

The flows that carried between 46% and 50% silica flour comprised two zones: a lower zone 1 without visible internal mixing and an upper zone 2 where ambient water was mixed into the flow (Fig. 3.1C). The boundary between these zones was well defined by a vertical change in colour (Fig. 3.1C). This colour contrast increased from C = 46% to C = 50%. The heads of the 46% to 48% silica-flour flows showed a semi-elliptical shape similar to the C < 46% flows. However, the nose gradually became more rounded, as the concentration increased. At $C \geq 49\%$, the shape of the head of the flows was rounded with a blunter nose than at lower C values. At $C \geq 47\%$, the flows stopped before reaching the end of the tank, but sediment from the dilute upper zone of the flow continued to travel along the length of the flume.

The C = 51% and C = 52% flows were poorly mixed internally and exhibited only minor mixing with ambient water (Fig. 3.1D). Instead, the ambient water was swept over the front and the top of the flows. The 52% flow was wedge-shaped, rendering it difficult to distinguish the head from the body of this flow. A dilute cloud of silica flour developed above the flows with C = 51% and C = 52% (Fig. 3.1D). This cloud travelled slowly down the length of the flume after the main flow had stopped.

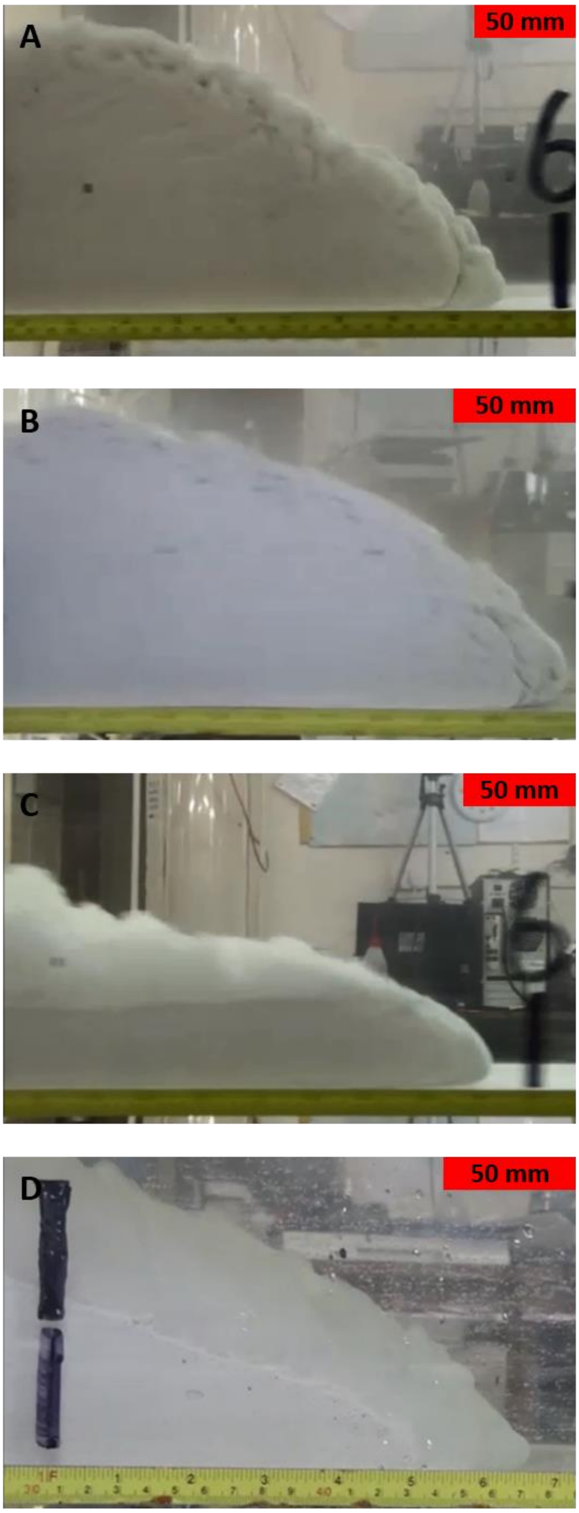

Figure 3.1: Video snapshots of the heads of the silica-flour flows at (A) C = 5%, where the flow was fully turbulent, at time, t = 8.00 s and at distance from the lock gate, x = 1.80 m along the tank; (B) C = 25%, which was also turbulence-dominated, at t = 1.70 s and x = 0.90 m; (C) C = 48%, showing a two-layer high-density turbidity current structure, at t = 3.40 s and x = 1.80 m; (D) C = 52%, a slide in its final stages, at t = 5.87 s and x = 0.43 m.

3.3.1.2 Flow velocities

Figure 3.2A and Figure 3.2B show that each SGF increased in velocity rapidly once the gate was lifted, reaching a maximum head velocity, U_h, that increased from 0.11 m s^{-1} to 0.75 m s^{-1}, as the suspended-sediment concentration of the flows was increased from 1% to 47%. At $C \geq 48\%$, U_h decreased progressively from 0.71 m s^{-1} to 0.29 m s^{-1} (Table 3.1). After the initial increase, the head velocity of all flows decreased along the remainder of the flow path. However, higher-frequency fluctuations were superimposed on this trend of reducing head velocity, especially in the denser flows. The maximum recorded fluctuation in head velocity was *c.* 0.2 m s^{-1} in the 46% flow (Fig. 3.2B), which is 27% of the maximum head velocity. Within the limits of the flume, the flows with $C \leq 25\%$ showed a gradual spatial decrease in head velocity, while the $C = 40\%$ to $C = 46\%$ flows exhibited a greater rate of decrease in the final flow stages, in addition to this gradual decrease. The flows with $C \geq 47\%$ also displayed a rapid decrease in velocity in the final stages, but the velocity decreased to zero before these flows reached the end of the flume. As the initial silica-flour concentration was increased from 47% to 52%, the maximum distance of travel of these flows progressively shortened (Fig. 3.2B, Table 3.1).

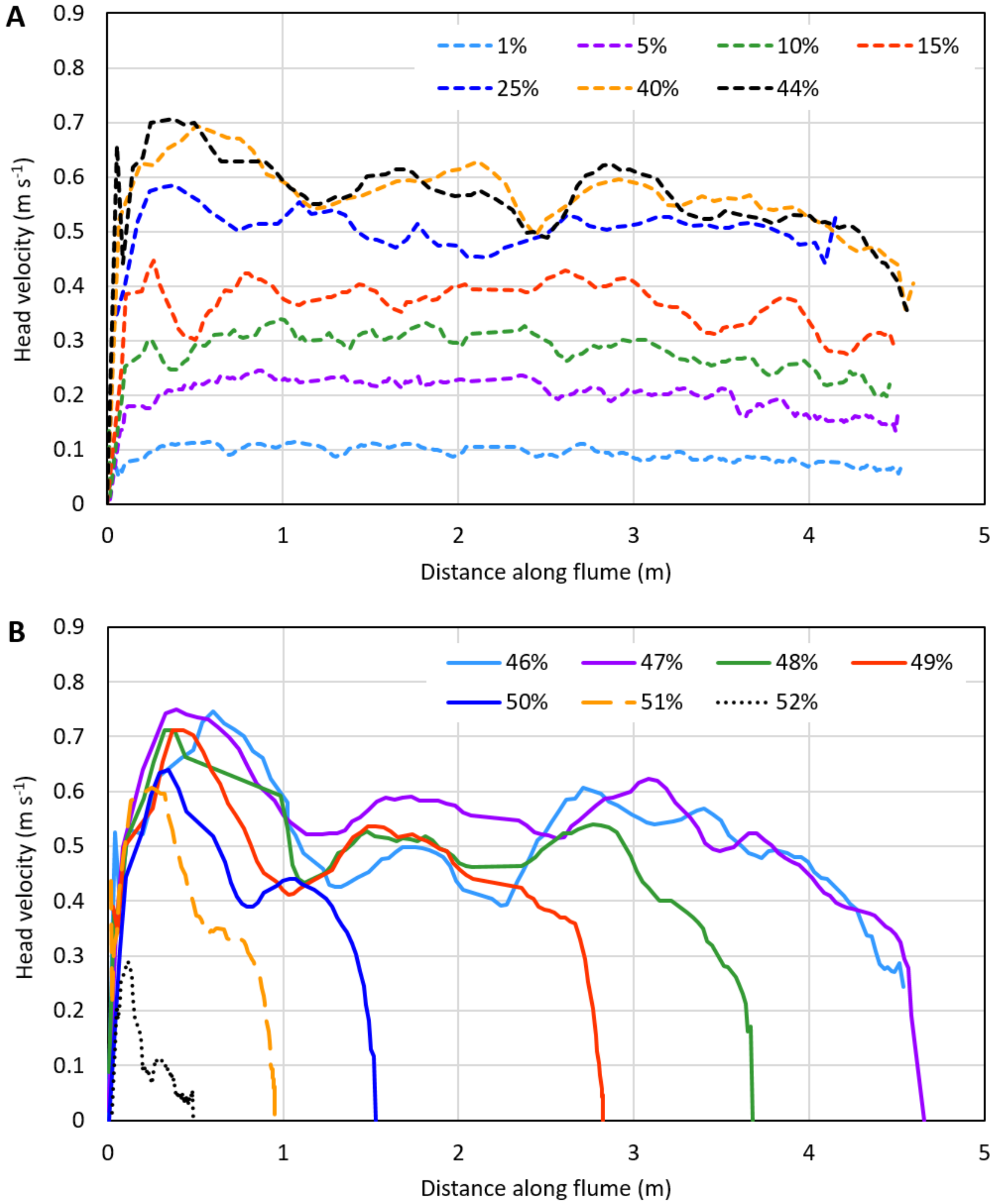

Figure 3.2: Changes in the head velocity of the silica-flour flows with suspended-sediment concentration, C, of: (A) 1% ≤ C ≤ 44%, and (B) 46% ≤ C ≤ 52%, along the length of the lock-exchange tank. The short-dashed, continuous, long-dashed, and dotted lines indicate low-density turbidity currents, high-density turbidity currents, non-cohesive mud flow, and slide, respectively.

3.3.1.2 Deposits

All the flows with $C \geq 47\%$ produced a measurable runout distance (Fig. 3.3), translating into deposit lengths that decreased from 4.66 m to 0.49 m as C was increased from 47% to 52% (Table 3.1). These deposits were thickest at the back of the reservoir, where also the maximum thickness increased with increasing flow density (Fig. 3.3). The deposits of the 47% to 49% flows decreased steadily in thickness from the back of the reservoir to horizontal distance from the lock gate, x, of 1.1 m, attaining a constant thickness thereafter. The termination of the deposit of the 47% flow was wedge-shaped, whereas the deposits of the 48% and 49% flows had abrupt terminations (Fig. 3.3). The 50% and 51% flows produced deposits that thinned from the back of the reservoir to x = 0.83 m and x = 0.65 m, respectively, before increasing in thickness again, thus exhibiting a distinct depression in the deposits. As with the 48% and 49% flows, the deposits of the 50% and 51% flows ended abruptly. The flow that carried 52% silica flour did not produce a depression in its deposit. Instead, this deposit dipped steeply and almost uniformly from the back of the reservoir to x = 0.49 m (Fig. 3.3).

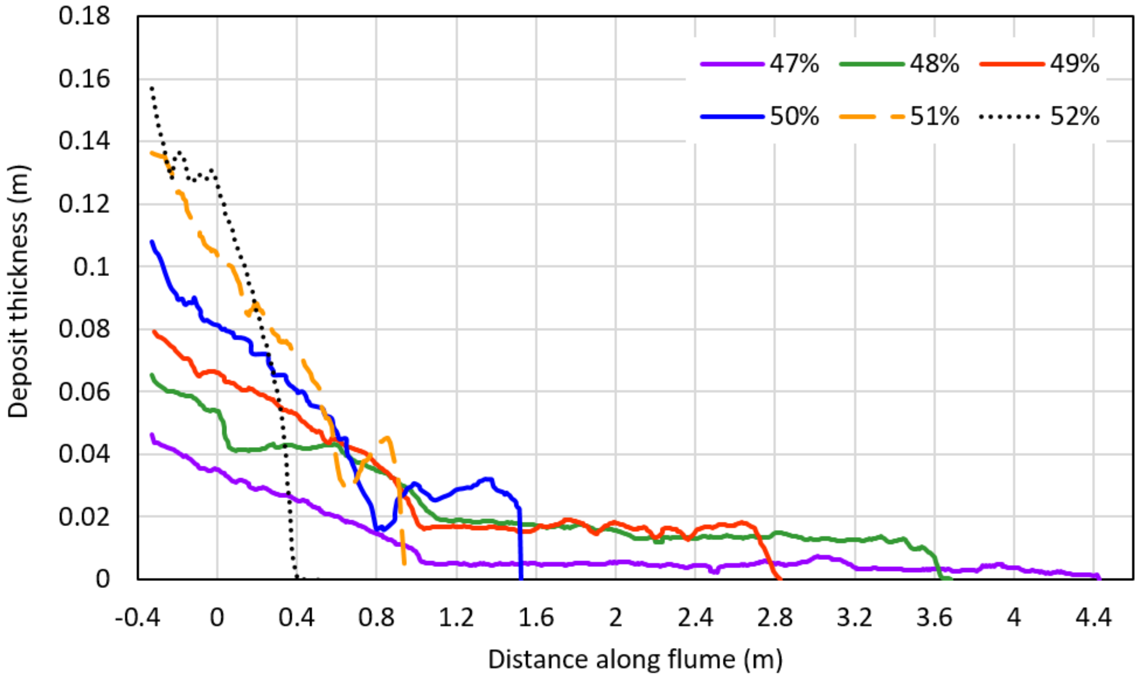

Figure 3.3: Deposit thickness against distance along the tank for all silica-flour flows with measurable runout distance. The continuous, long-dashed, and dotted lines indicate low-density turbidity currents, high-density turbidity currents, non-cohesive mud flow, and slide, respectively.

3.3.2 The effect of increasing kaolinite and bentonite concentration on the flows

3.3.2.1 Visual observations

The bentonite flows of $C \leq 10\%$ and the kaolinite flows of $C \leq 15\%$ behaved in a manner similar to that of to the low-concentration silica-flour flows (Fig. 3.4A), thus exhibiting strong turbulent mixing, both internally and at flow boundaries, pointed semi-elliptically shaped heads with a pronounced nose, and Kelvin-Helmholtz instabilities at the upper boundary.

The 22%, 23%, and 25% kaolinite flows and the 15% and 16% bentonite flows consisted of a dark lower zone 1, overlain by an upper zone 2 with a lighter shade, where ambient water mixed into the flow (Fig. 3.4B, E). These zones were separated by interfacial waves in the 15% and 16% bentonite flows. These waves were particularly prominent in the final flow stages of the 15% bentonite flow. Coherent fluid-entrainment structures, expressed as linear features of clear ambient water along the side wall of the flume, were present in zone 1 of the head of the 22% and 23% kaolinite flows until the final flow stages. coherent fluid entrainment structures also developed in zone 1 of the 15% and 16% bentonite flows, but these features were visible only in the midsection of the 15% bentonite flow. In the 16% bentonite flow, a long quasi-horizontal coherent fluid entrainment structure developed at $x \approx 0.60$ m, above which multiple angled coherent fluid entrainment structures were present (Fig. 3.4E). This layer of coherent fluid entrainment structures moved on top of a dense, featureless layer to $x \approx 3$ m, after which the entire dense zone 1 became featureless. The videos revealed packets of cohesive sediment in the head of the 15% bentonite flow and more frequently in the 16% flow (Fig. 3.4E). Occasionally, these packets were pushed over the top of the head before disintegrating or carried along at the floor of the flume before being incorporated into the head of the flow (Fig. 3.4E).

The head of the 17% bentonite flow had a three-part signature: (i) a dense lower zone 1a, which contained horizontal sheets of water; (ii) a middle zone 1b with active mixing and coherent fluid entrainment structures; and (iii) a dilute upper zone 2, dominated by mixing with the ambient water (Fig. 3.4F). This three-part structure was visible from $x = 1.05$ m to $x = 2.43$ m, after which the coherent fluid entrainment structures reached the base of the flow, producing a two-part structure. From 1.32 m, the head of the $C = 22\%$ kaolinite flow could be divided into the same three-part structure as the $C = 17\%$ bentonite flow, although zone 1a was featureless. This three-part structure was visible until $x = 3.30$ m, after which zone 1b and the coherent fluid entrainment structures ceased to exist.

The 22% ≤ C ≤ 25% kaolinite flows and the 15% and 16% bentonite flows had a pointed semi-elliptical head with a prominent nose, and all experienced hydroplaning (Fig. 3.4B, D). However, from x = 0.41 m to x = 1.35 m the head of the 25% kaolinite flow attained a rounded semi-ellipse shape, as sediment was thrown over the top of the head (Fig. 3.4B). The head of the hydroplaning 17% bentonite flow was semi-circular (Fig. 3.4F).

The head of the 18% and 19% bentonite flows and the 27% kaolinite flow lacked any noticeable internal turbulence and mixing with the ambient water, but a dilute suspension cloud developed at the front of the bentonite flows (Fig. 3.4C, G). The 27% kaolinite flow had a pointed, wedged-shaped hydroplaning head which produced an extremely weak suspension cloud as it travelled along the tank (Fig. 3.4C). The shape of the heads of the flows that carried 18% and 19% bentonite were unique compared with all other flows. Upon leaving the reservoir, the heads of these flows lifted off the base of the flume and folded back on themselves, thus attaining a distinct and persistent roller-wave-like shape (Fig. 3.4G). During the final flow stages, the fold at the top of the head dropped back towards the floor of the flume, resulting in a blunt semi-circular frontal shape. Both the 27% kaolinite and 19% bentonite flows developed vertical tension cracks (< 10 mm deep) oriented perpendicular to the side wall of the flume (Fig. 3.4C).

The highest-concentration kaolinite and bentonite flows, at C = 29% and C = 20% respectively, travelled out of the reservoir as coherent masses that neither mixed with the ambient water nor hydroplaned. The 29% kaolinite suspension produced a flow with a blunt, rounded head and a steeply inclined body (Fig. 3.4D). The 20% bentonite flow lacked a clearly defined head (Fig. 3.4H). However, minor folds developed in the front of the flow and tension cracks were present length-parallel to the flow direction in the two lowest folds.

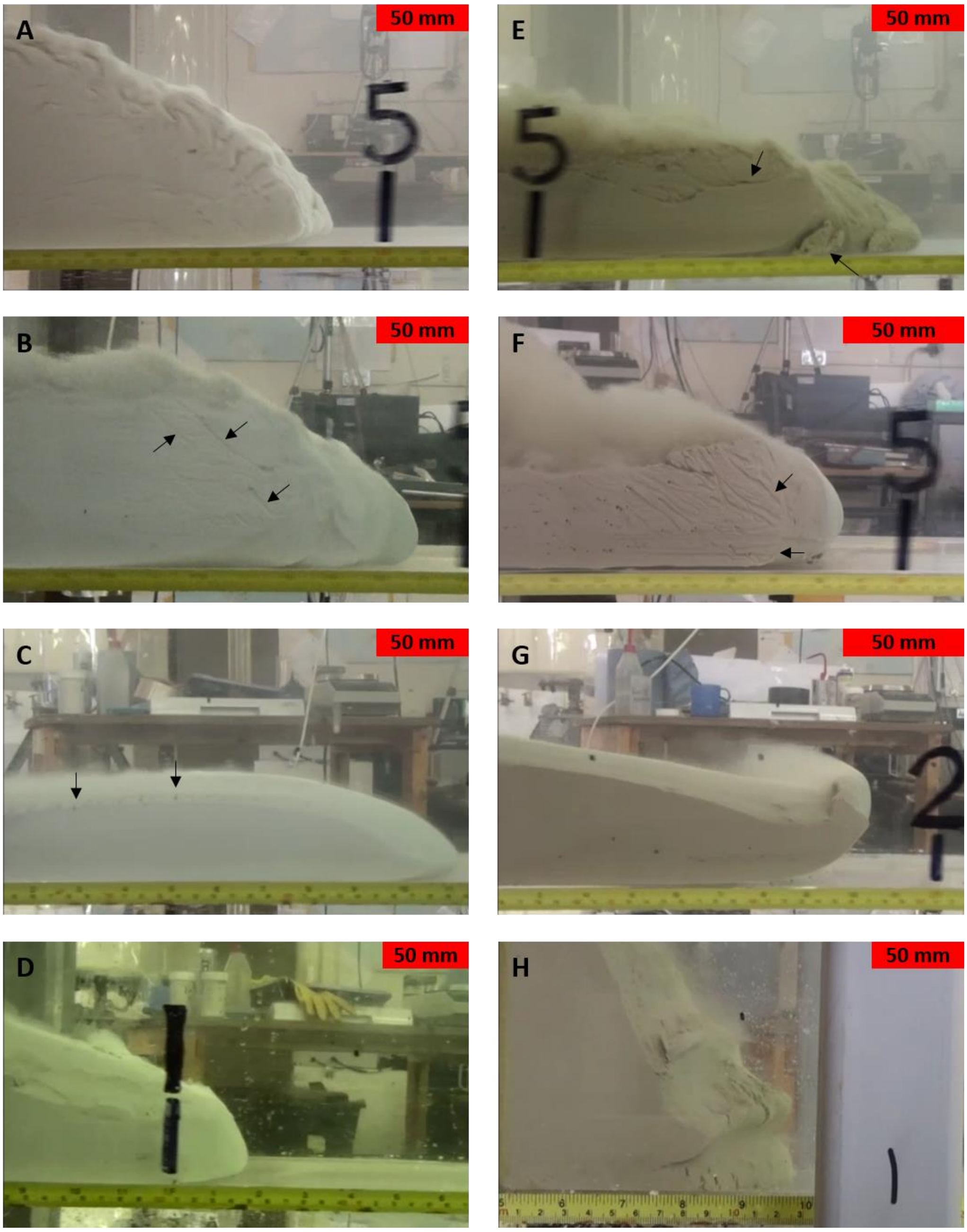

Figure 3.4: (A) Head of the turbulent 5% kaolinite LDTC at t = 6.60 s and x = 1.49 m. (B) Head of the 22% kaolinite flow at t = 3.50 s and x = 1.50 m; this HDTC hydroplaned and was divided into three parts; the arrows highlight the coherent fluid entrainment structures. (C) Pointed head of the kaolinite mud flow with C = 27% at t = 3.50 s and x = 0.89 m; small tension cracks, shown by the arrows, are visible on the top of the head of the flow. (D) Rounded head of the kaolinite slide with C = 29% at t = 2.50 s and x = 0.35 m. (E) Tripartite head of the 16% bentonite flow at t = 6.07 s and x = 1.77 m; a cohesive packet of clay is visible at the base of the head of this HDTC, shown by lower arrow; the upper arrow highlights a coherent fluid entrainment structure. (F) Head of the 17% bentonite flow at t = 5.40 s and x = 1.49 m; the horizontal sheets and angled coherent fluid entrainment structures are shown by the dashed and solid arrows, respectively. (G) Mud flow laden with 19% bentonite, showing a folded head, at t = 2.73 s and x = 0.56 m. (H) Front of the C = 20% bentonite slide at t = 5.43 s and x = 0.13 m.

3.3.2.2 Flow velocities

The head velocity of all the kaolinite and bentonite flows increased rapidly as the flows left the reservoir, after which the head velocity decreased as the flows travelled farther down the flume (Figs 3.5 and 3.6). The U_h of the bentonite flows increased from 0.10 m s^{-1} for C = 1% to 0.37 m s^{-1} for C = 16%, and then decreased to 0.07 m s^{-1} for C = 20%. In comparison, the U_h of the kaolinite flows increased from 0.11 m s^{-1} for C = 1% to 0.50 m s^{-1} for C = 22%, and then decreased to 0.29 m s^{-1} for C = 29% (Table 3.1). The flows with $C \geq 22\%$ kaolinite and $C \geq 15\%$ bentonite stopped before reaching the end of the flume, owing to a rapid decrease in velocity in the final flow phase (Figs 3.5 and 3.6). This phase of rapidly decreasing velocity occurred progressively closer to the lock gate, as the C values were increased above 15% bentonite and 22% kaolinite (Figs 3.5B and 3.6B). As in the silica-flour flows, all the clay flows exhibited velocity fluctuations superimposed on a longer trend of slowing flow. These fluctuations reached a maximum of *c.* 0.1 m s^{-1} in the 15% bentonite and kaolinite flows, which corresponds to 29% and 24% of U_h, respectively. The 29% kaolinite flow behaved somewhat differently, in that, after an initial decrease in velocity from 0.3 m s^{-1} to 0.01 m s^{-1}, the flow continued to move forward at 0.01 m s^{-1} for 0.33 m before stopping (Fig. 3.5B).

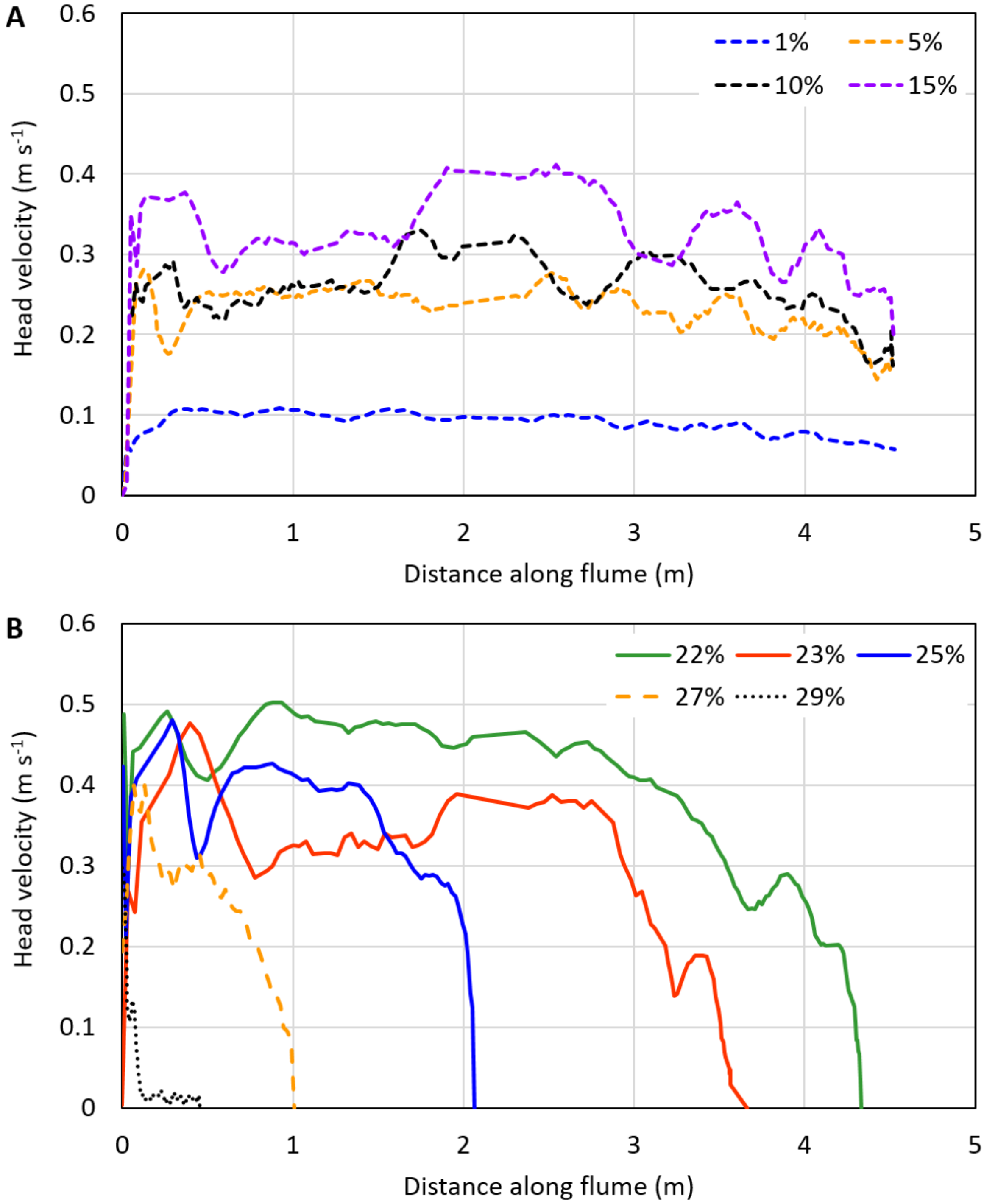

Figure 3.5: Changes in the head velocity of the kaolinite flows with (A) 1% ≤ C ≤ 15%, and (B) 22% ≤ C ≤ 29%, along the length of the lock-exchange tank. The short-dashed, continuous, long-dashed, and dotted lines indicate low-density turbidity currents, high-density turbidity currents, non-cohesive mud flow, and slide, respectively.

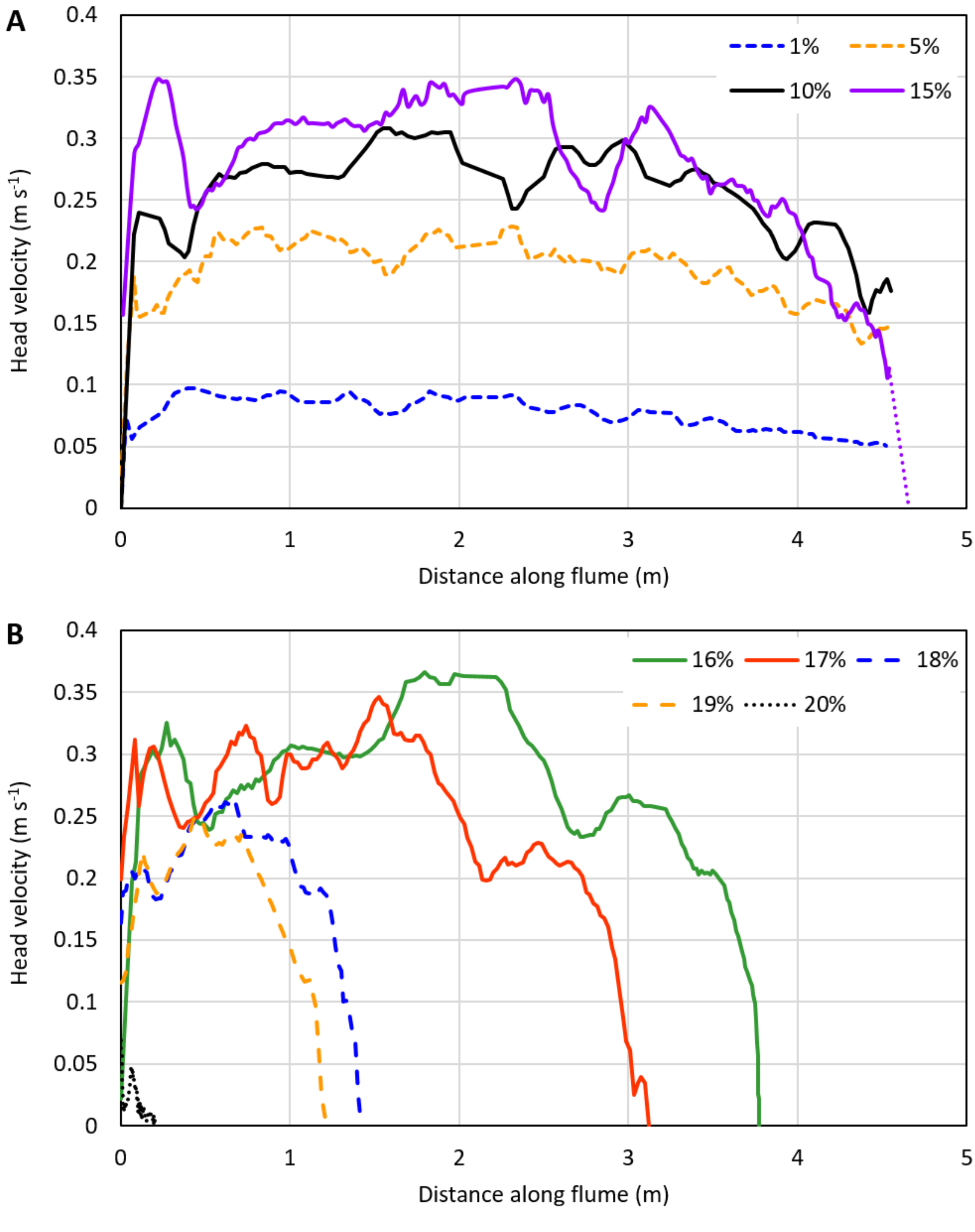

Figure 3.6: Changes in the head velocity of the bentonite flows with (A) 1% ≤ C ≤ 15%, and (B) 16% ≤ C ≤ 20%, along the length of the lock-exchange tank. The short-dashed, continuous, long-dashed, and dotted lines indicate low-density turbidity currents, high-density turbidity currents, non-cohesive mud flow, and slide, respectively. Purple dotted line in Part A denotes extrapolated velocity to the recorded runout distance.

3.3.2.3 Deposits

The flows with $C \geq 22\%$ kaolinite and $C \geq 15\%$ bentonite produced measurable runout distances in the 4.69-m-long tank (Figs 3.7 and 3.8). The deposits decreased in length from 4.66 m for 15% bentonite to 0.22 m for 20% bentonite, and from 4.35 m for 22% kaolinite to 0.46 m for 29% kaolinite. All the clay flow deposits were thickest near the back of the reservoir. The $15\% \leq C \leq 17\%$ bentonite flows and the 22% and 23% kaolinite flows thinned steadily from the back of the reservoir to $x \approx 1$ m; thereafter, the bed thickness remained constant until the deposits ended with a pronounced leading edge (Figs 3.7 and 3.8). The deposits of the 18% and 19% bentonite flows and the 25% and 27% kaolinite flows consisted of distinct depressions, which were 0.03-0.04 m deep at $x \approx 0.60$ m for the bentonite flows (Fig. 3.8). The depression in the deposit of the 25% kaolinite flow reached the floor of the flume at $x = 0.71$ m, whereas 0.016 m of sediment was deposited in the depression of the deposit of the 27% kaolinite flow at $x = 0.50$ m (Fig. 3.7). The flows laden with 29% kaolinite and 20% bentonite produced deposits which decreased rapidly from their maximum thickness to zero over a distance of 0.1 m for the bentonite flow and 0.5 m for the kaolinite flow to produce block-shaped and wedge-shaped deposits, respectively (Figs 3.7 and 3.8).

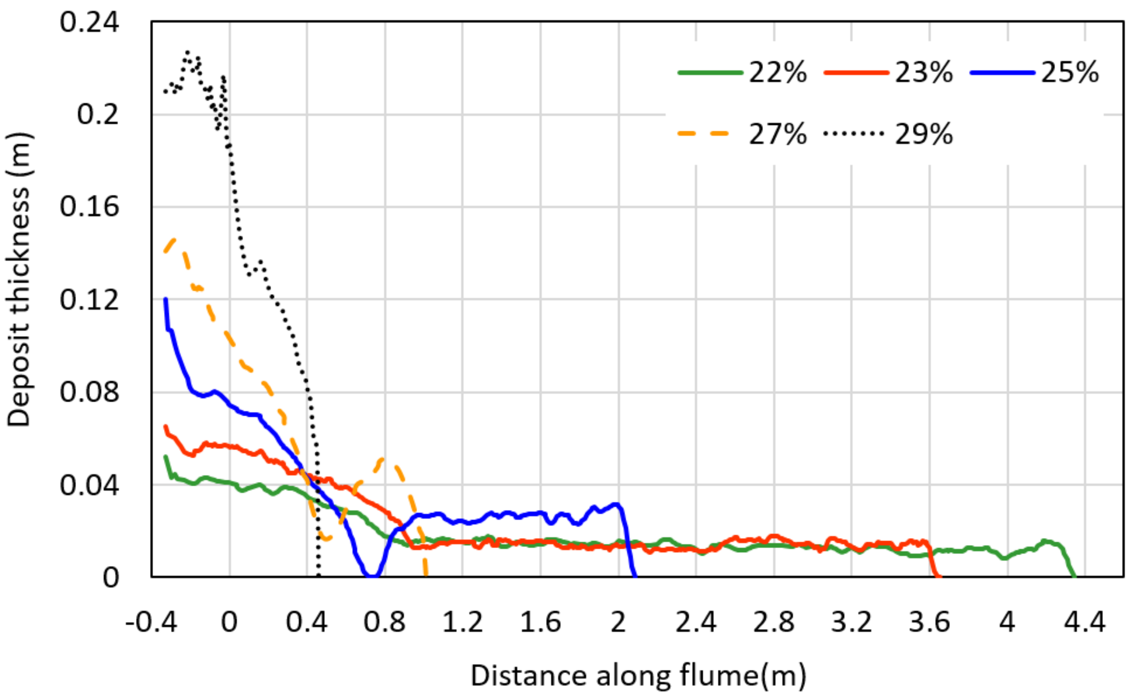

Figure 3.7: Deposit thickness against distance along the tank for all kaolinite flows with measurable runout distance. The continuous, long-dashed, and dotted lines indicate low-density turbidity currents, high-density turbidity currents, non-cohesive mud flow, and slide, respectively.

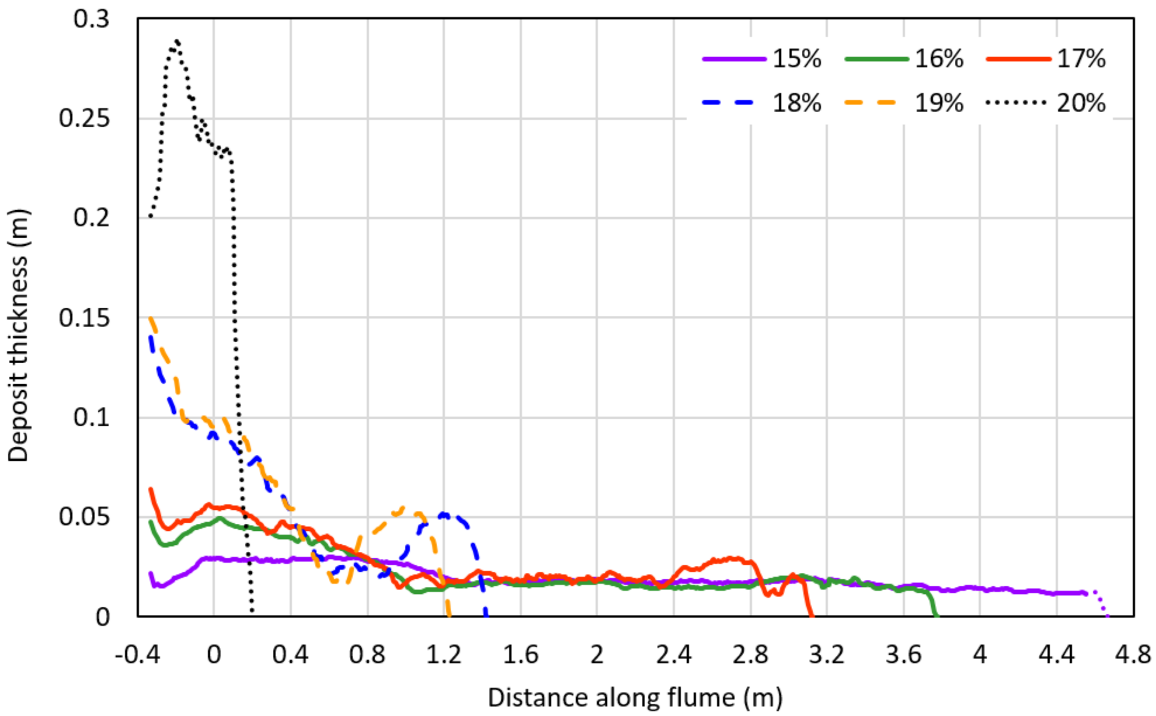

Figure 3.8: Deposit thickness against distance along the tank for all bentonite flows with measurable runout distance. The continuous, long-dashed, and dotted lines indicate low-density turbidity currents, high-density turbidity currents, non-cohesive mud flow, and slide, respectively. Dotted end of the deposit for the 15% flow was beyond the reach of the Ultrasonic Ranging System, and was measured by hand instead.

3.3.3 Comparison of maximum head velocities and runout distances for the three sediment types

Figure 3.9 compares the maximum head velocities and runout distances for the three sediment types as a function of initial suspended-sediment concentration. Up to C = 10%, U_h increased at a similar rate for these sediment types (Fig. 3.9A). As suspended-sediment concentration was increased further, U_h started to diverge, *e.g.,* attaining 0.35 m s^{-1} for bentonite, 0.41 m s^{-1} for kaolinite, and 0.45 m s^{-1} for silica flour at C = 15%. The bentonite flows achieved the highest U_h at C = 16%. With a further increase in bentonite concentration, U_h decreased rapidly until the bentonite was no longer able to flow out of the reservoir at an estimated $C \approx$ 20.5% (Fig. 3.9A). The C-U_h curves for the bentonite, kaolinite, and silica-flour flows have a similar shape, but the maximum U_h, and the suspended concentrations at which this maximum velocity was reached, were significantly higher for kaolinite and silica flour. The kaolinite flows reached U_h = 0.50 m s^{-1} at C = 22%, and the silica-flour flows attained U_h = 0.75 m s^{-1} at C = 47% (Fig. 3.9A). The kaolinite and silica-flour suspensions failed to leave the reservoir at estimated C values of 30.5% and 53%, respectively.

Within the confinement of the flume, the runout distance of the SGFs strongly depended on concentration and clay type (Fig. 3.9B). Progressively less suspended sediment was required to produce a deposit of comparable length for silica flour, kaolinite, and bentonite. For example, the 19%-bentonite flow had a runout distance of 1.22 m, whereas 27% of kaolinite and 51% of silica flour were needed to achieve a similar runout distance. 15% bentonite was required to produce deposits that were limited in length to the confinement of the flume (*i.e.*, $x \leq 4.69$ m). This threshold concentration was much higher for kaolinite, at C = 22%, and for silica flour, at C = 47% (Fig. 3.9B).

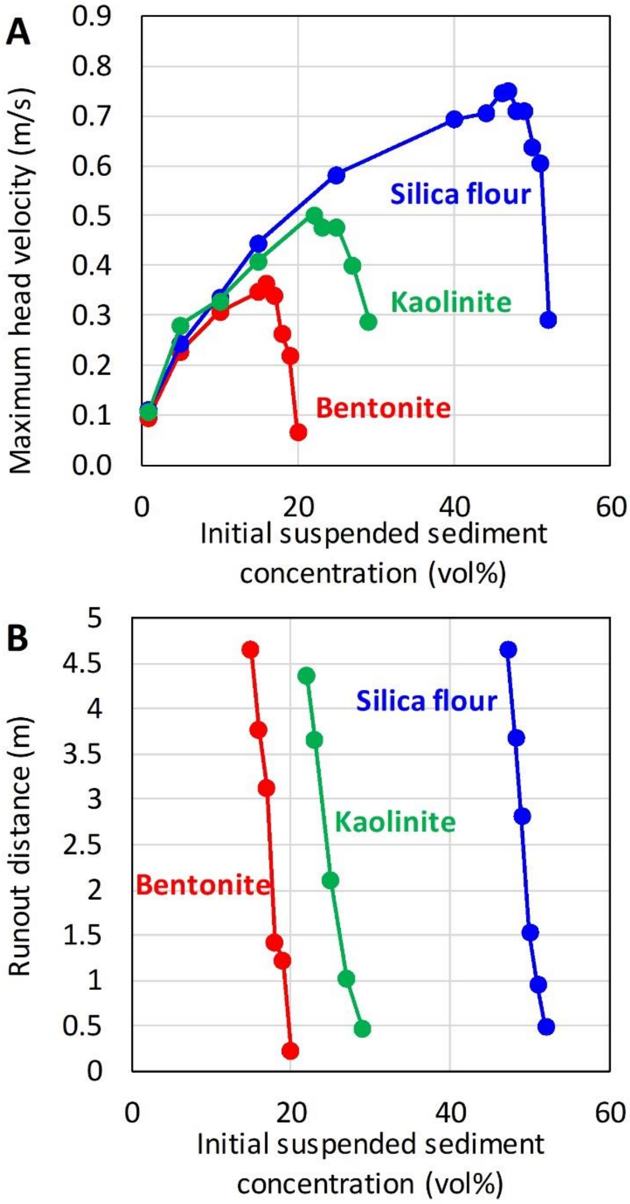

Figure 3.9: (A) Maximum head velocity and (B) deposit runout distance against suspended-sediment concentration for the three sediment types. The lower concentration flows that reflected off the end of the tank do not have a measurable runout distance.

3.4 Process interpretations of the flows and deposits

3.4.1 Silica-flour flows

Silica flour is composed of ground quartz and is generally assumed to be non-cohesive as it does not have a surface charge (Parker *et al.*, 1987; Baas *et al.*, 2005; Felix & Peakall, 2006; Kane *et al.*, 2010). However, Pashley and Karaman (2004) found that silica-flour particles may have a weak negative surface charge owing to the disassociation in water of some of the silanol (SiOH) groups, thus rendering silica flour weakly cohesive. These weak to non-cohesive properties may have caused the silica-flour flows in this study to behave differently from the stronger cohesive kaolinite and bentonite flows, particularly at high initial suspended-sediment concentration values. However, frictional interaction between grains, dispersive pressure, and hindered settling may have also controlled the flow behaviour of the silica-flour suspensions, as discussed below.

3.4.1.1 Visual observations

The flows laden with $C \leq 44\%$ silica flour behaved in a manner similar to that of experimental turbidity currents in other studies (Fig. 3.1A, B; *e.g.,* Kuenen & Migliorini, 1950; Middleton, 1966; Marr *et al.*, 2001); they were fully turbulent, thus allowing the sediment particles to be supported by the upward velocity component of fluid turbulence (Middleton & Hampton, 1973; Kneller & Buckee, 2000). This behaviour renders these flows low-density turbidity currents (LDTC; Table 3.2), following the definition of Lowe (1982). These flows remained fast-moving with pronounced Kelvin-Helmholtz instabilities at the upper boundary up to $C = 44\%$, owing to the large density difference with the ambient water and the small particle size ($D_{50} = 18.2$ µm). Consequently, turbulent energy in the flows was able to outcompete the particle settling velocity, and keep the particles in suspension. High dispersive pressure and hindered settling may also have helped the particles remain suspended (Middleton & Hampton, 1973).

The $46\% \leq C \leq 50\%$ silica-flour flows were classified as high-density turbidity currents (HDTC; *sensu* Lowe, 1982; Table 3.2), as these flows comprised a dense lower zone 1 separated from a dilute upper zone 2 by a break in density (Fig. 3.1C). Zone 1 formed from the accumulation of particles near the base of the flow, and zone 2 resulted from shear-induced mixing of sediment with the ambient water. The $C = 51\%$ silica-flour flow is classified as a non-cohesive mud flow (NCMF) due to its strong to full turbulence suppression and limited mixing at the upper boundary (Table 3.2). Finally, the $C = 52\%$

silica-flour flow is classified as a slide, following the definition of a high-density SGF that moves as a coherent mass without significant internal deformation (Fig. 3.1D; Table 3.2; Martinsen, 1994; Mohrig & Marr, 2003). At $C \geq 48\%$ the flow mobility decreased progressively, and the flow density approached the cubic-packing density of clastic sediment (*c.* 52%). It is therefore inferred that frictional interactions between particles prevented the development of turbulence in these flows, thus outcompeting the effect of excess density, encouraging bulk settling and slowing down the flows (Iverson, 1997). The flows with $C \geq 47\%$ showed a dilute suspension cloud that outran the main body of the flow (Fig. 3.1D). While the dense main body of the 47% to 50% HDTCs slowed and stopped, as the frictional forces outcompeted the excess density, the dilute suspension cloud was driven by turbulence and still had enough momentum to continue flowing. Minor erosion at the top of the 51% and 52% silica-flour flows helped in producing the dilute turbidity current, which was then able to travel slowly along the entire length of the tank.

In contrast to the kaolinite and bentonite flows herein and other high-density clay-laden SGFs described in the literature, none of the silica-flour flows hydroplaned (Fig. 3.1; Marr *et al.*, 2001; Elverhøi *et al.*, 2005). Hydroplaning occurs when the dynamic pressure generated in the ambient fluid just below the head of the flow approaches or exceeds the weight per unit area of the material in the head of the flow (Mohrig *et al.*, 1998). Another requirement for hydroplaning is that the permeability of the base of the flow is low enough to prevent mixing of the overridden water into the flow above (Talling, 2013). This permeability requirement may not have been achievable for the silica-flour flows because of the lack of cohesive strength in these flows. In the LDTCs and HDTCs in particular, the high turbulent energy and small particle size meant that any water forced underneath the head was rapidly mixed into the flow. The NCMF and slide may have had a permeable base as well, but these dense flows were probably also too heavy and did not travel quickly enough to allow water to be forced underneath the head of the flow.

The pointed semi-elliptical shape of the head of the silica-flour flows with $C \leq 48\%$ is commonly seen in turbidity currents of relatively low density and low internal strength, in which the head is shaped into a streamlined form to minimize the pressure force at the front of the flow (Fig. 3.1A-C; Hampton, 1972; Middleton, 1993). Although the 46% and 48% flows behaved as HDTCs, the heads of these flows apparently did not have enough internal strength to resist being shaped by the hydrodynamic pressures (Britter & Simpson, 1978; Kneller & Buckee, 2000). Only the silica-flour flows with $C \geq 49\%$ had enough internal strength to produce rounded-shaped heads. This strength may result from a variety of mechanisms: high dispersive pressure, hindered settling, frictional interaction between grains, and weak negative surface charge of silica flour (Middleton & Hampton, 1973; Iverson, 1997; Pashley & Karaman, 2004). The flows with $C \geq 49\%$ also had relatively low head velocities, which reduced the hydrodynamic pressure on the heads of these flows, and thus the ability to streamline the head (Mohrig *et al.*, 1998).

3.4.1.2 Flow velocities

The silica-flour flows reached a progressively higher maximum head velocity as the initial suspended-sediment concentration was increased from 1% to 47%, because increasing the concentration increased the density difference between the sediment suspension and the ambient fluid, and it is this difference that drives the flow. However, increasing C above 47% reduced the maximum velocity to which the flows accelerated, which is interpreted as a further expression of the effect of friction between the sediment grains on the mobility of these high-concentration flows, mentioned above.

The rate of decrease of the head velocity of the silica-flour-laden flows increased as C was increased. At $C \leq 25\%$, the head velocity decreased relatively slowly, driven by resistive shear forces, along the length of the tank (Fig. 3.2A; Kneller & Buckee, 2000). At higher concentrations, the flows slowed more quickly, especially at $C \geq 47\%$, where all the flows showed a rapid spatial decrease to zero velocity (Fig. 3.2B; *cf.* Hallworth & Huppert, 1998). This process is attributed to frictional freezing (Mutti *et al.*, 1999; Mulder & Alexander, 2001; Kane *et al.*, 2009). As the flow starts to slow down, the vertical settling velocity of the grains becomes greater than the horizontal movement, and the flow contracts vertically. This contraction process brings the particles into closer proximity, resulting in greater frictional forces, which further reduces the forward momentum of the particles. This positive feedback thus leads to a rapid decline in head velocity. The origin of the velocity fluctuations superimposed on the general trend of slowing head velocity is unclear. These fluctuations might be attributable to the formation of elongate packets of sediment with contrasting velocity within lobes and clefts at the base of the flow, and interaction of the flow with waves on the water surface, produced by the displacement of ambient water upon release of the suspension from the reservoir.

3.4.1.3 Deposits

All flows of $C \geq 47\%$ silica flour produced a measurable runout distance which decreased in length as the suspended-sediment concentration increased, because frictional freezing occurred closer to the point of release (Figs 3.2B and 3.3). The HDTCs, NCMF, and slide with $C \geq 47\%$ deposited all or most of the silica flour within *c*. 1 m of the lock gate, forming steeply inclined, wedge-shaped sediment bodies

(Fig. 3.3). This is further testament to the dominance of frictional forces over turbulent forces at these high suspended-sediment concentrations. However, part of the sediment in the HDTCs was transported beyond x = 1 m, suggesting that the remaining turbulent forces were able to keep part of the silica flour in suspension until frictional freezing commenced. The blocky shape of these deposits agrees well with the shape of deposits formed by high-density SGFs in the Marnoso-arenacea Formation, Italy (Amy *et al.*, 2005, their figure 3B). The depression in the deposits of the 50% and 51% flows (Fig. 3.3) resembles those that Elverhøi *et al.* (2005) associated with flow "stretching" due to hydroplaning, which causes the head of a dense flow to accelerate away from the body. However, the silica-flour flows in the present study did not hydroplane, suggesting that other mechanisms may also create these depressions. Internal velocity measurements are needed to ascertain how these features form in non-hydroplaning flows. The 52% flow did not produce a deposit with a depression, possibly because of a lack of internal velocity gradients, which is typical for a slide moving as a rigid plug.

3.4.2 Kaolinite and bentonite flows

3.4.2.1 Visual observations

The kaolinite and bentonite flows of $C \leq 15\%$ and $C \leq 10\%$, respectively, behaved as LDTCs (Table 3.2), with a streamlined semi-elliptically shaped head and fully dominated by turbulent mixing in the head and body (Middleton, 1966; Middleton & Hampton, 1973; Lowe, 1982; Sumner *et al.*, 2009). The flows that carried between 22% and 25% for kaolinite and between 15% and 17% for bentonite showed HDTC behaviour, where a typically distinct colour difference between the dense zone 1 and the dilute zone 2 and the presence of interfacial waves suggest the presence of a break in density (Table 3.2; Fig. 3.4B, E, F; Kuenen, 1951; Britter & Simpson, 1978; Lowe, 1982; Middleton, 1993; Baas *et al.*, 2004). These clay-laden HDTCs can be classified as transitional flows (*sensu* Wang & Plate, 1996; Baas & Best, 2002; Kane & Pontén, 2012). Herein, the high concentration of clay particles in zone 1 of these flows caused the transient-turbulent behaviour. In this near-bed flow layer, the probability for particles to collide, flocculate, and form gels was high, which made the flows viscous, attain a higher cohesive strength, and thus become subjected to turbulence suppression (Baas *et al.*, 2009; Cartigny *et al.*, 2013). The 22% kaolinite flow and the 17% bentonite flow produced a three-part structure along part of their flow path (Fig. 3.4B, F). The horizontal sheets of water in the basal zone 1a of the 17% bentonite flow appeared to form by injection of water at the flow front. The formation of coherent fluid entrainment structures in zone 1b of both flows suggests that this zone had a slightly lower cohesive strength than zone 1a. The flows were probably too slow, and therefore too cohesive, to develop the three-part structure in the early and late flow stages. Instead, the two-part structure, discussed above, prevailed. Alternatively, the two-part flow structures may have remained after deposition of clay from basal zone 1a in the final flow stages (*cf.* Cartigny *et al.*, 2013). Although it cannot be ruled out that the formation of the coherent fluid entrainment structures in zone 1 of the HDTCs was limited to the side wall of the flume, the presence of coherent fluid entrainment structures implies that the flows had a high enough yield stress to limit turbulent mixing of the entrained water into the flow.

The 15% and 16% bentonite flows carried packets of cohesive sediment, which formed when small sections of cohesive sediment were torn off zone 1 by ambient water forced over the front of the flows (Fig. 3.4E). This suggests that the shear force imposed by this ambient water at times exceeded the yield stress of the sediment suspension. These packets of bentonite were cohesive enough to resist mixing with the ambient water, as they were thrown over the top of the head. Yet, these packets were seen to disintegrate and become incorporated into the dilute mixing zone 2 under the influence of high turbulence. Packets that were carried along at the base of the head survived for longer, presumably because the shear forces at the base of zone 1 were weaker than near the top of zone 2.

The clay concentration in the flows with $C \geq 25\%$ kaolinite or $C \geq 17\%$ bentonite appeared high enough to form clay gels, *i.e.*, pervasive, volume-filling networks of clay particle bonds, throughout the flow (Fig. 3.4C, D, G, H; Baas *et al.*, 2009). These gels are inferred to have had a high enough yield stress to form rigid-plug flows without internal turbulence, typical of debris flows (Middleton & Hampton, 1973; Baas *et al.*, 2009). The 27% kaolinite flows and the 18% and 19% bentonite flows are classified herein as cohesive mud flows (CMF; Table 3.2). The high yield stress of these CMFs is further supported by the sharply reduced mixing with the ambient water, although the relatively weak water flow across the upper flow boundary at these high C values may also have prevented the bonds between the clay particles from breaking on a large scale. Likewise, mixing at the top of the 29% kaolinite flow and 20% bentonite flow was negligible as a consequence of the particularly high cohesive strength and low head velocity. These flows were arrested in the sliding phase soon after the gate was lifted in a manner similar to that of the 52% silica-flour flow, and are therefore classified as slides (Table 3.2).

The presence of tension cracks on the tops of the 27% kaolinite flow and the 19% bentonite flow suggests that these flows were cohesive enough to have tensile strength and were placed under flow-parallel tension (Fig. 3.4C; Marr *et al.*, 2001). Small spatio-temporal variations in flow velocity, partly related to hydroplaning, may have put these flows under tension. The 20%-bentonite slide exhibited tension cracks oriented parallel to the direction of slide movement. These cracks formed because the flow moved slightly faster in the centre of the flume than at the sidewall, thus placing it under tension perpendicular to the flow direction.

As in the silica-flour flows, the shape of the head of the clay flows with high *C* values can be related to their rheological properties as well as the hydrodynamic pressure at the front of these flows (Mohrig *et al.*, 1998). The 25% kaolinite flow attained a rounded shape for part of its flow path, the 27% kaolinite flow had a particularly thin, pointed semi-elliptically shaped head, and the 29% kaolinite flow had a blunt, semi-circular shaped head. It is inferred that these high-density flows were cohesive enough to withstand streamlining by ambient water swept over the fronts and tops of these flows (Fig. 3.4C, D). The roller waves in the heads of the 18% and 19% bentonite flows were particularly striking (Fig. 3.4G). Hampton (1972) also observed "blunt snouts with a sharp-tipped crest curled back over the top of the flow" in debris flows with a low water content (below 70% by weight). Hampton (1972) attributed this shape to the high yield stress of the flows, which allowed the water pushed back over the top of the head to create a fold that was able to resist erosion and maintain the sharp-tipped crest.

The kaolinite flows with 22% ≤ *C* ≤ 27% and the bentonite flows with 15% ≤ *C* ≤ 19% hydroplaned along parts of their flow path, thus meeting the criteria for hydroplaning discussed above (Fig. 3.4B, E, F, G). It is assumed that the permeability and the turbulence forces at the base of the lower-clay-concentration flows were high enough to allow water to be mixed straight into the flows. In the 29% kaolinite and 20% bentonite flows, the weight per unit area of the sediment in the head is inferred to have been too large to allow hydroplaning to develop (Fig. 3.4D, H). Hydroplaning did not take place either in the initial or in the final stages of the kaolinite flows with 22% ≤ *C* ≤ 27% and the bentonite flows with 15% ≤ *C* ≤ 19%. Near the reservoir, the hydrodynamic pressures at the front of the head needed time to support the downward-directed weight of the flow and force a thin layer of water underneath the head (Mohrig *et al.*, 1998; Talling, 2013). As the flows slowed during their final stages, the hydrodynamic pressure at the front of the head decreased and might not have been able to support the weight of the flows any longer, thus causing hydroplaning to end (Mohrig *et al.*, 1998).

3.4.2.2 Flow velocities

The balance between turbulent forces and cohesive forces can also be used to explain the observed trends in head velocity of the clay flows (Figs 3.5 and 3.6). As in the silica-flour LDTCs, the progressive increase in head velocity with increasing concentration in the *C* ≤ 15% kaolinite and *C* ≤ 10% bentonite

LDTCs resulted from the density difference driving these flows (Figs 3.5A and 3.6A). It is concluded that at these concentrations the cohesive forces did not influence the flow dynamics. This is further confirmed by the relatively slow decrease in the head velocity of these flows along the length of the tank, which is inferred to result from effective particle support by shear turbulence and minor particle settling (Figs 3.5A and 3.6A).

In the flows with C > 22% kaolinite and C > 16% bentonite, U_h decreased as C was increased, because the cohesive forces became stronger than the turbulent forces in these flows, despite the large density difference with the ambient water. This lack of turbulent support, combined with bulk settling of the clay gel, resulted in a rapid decrease in head velocity as the flows travelled along the tank (Figs 3.5B and 3.6B). These flows slowed particularly quickly in the final stage, which may have resulted from "cohesive freezing" (Mulder & Alexander, 2001). As the flow slows down, lower turbulent forces and flow contraction due to bulk settling allow the clay particles to form a greater number of electrostatic bonds and increase the cohesive strength of the flows. In turn, this further reduces the turbulence and encourages even greater cohesive strength. This positive-feedback mechanism allows the clay flow velocities to decrease very quickly. Jacobson and Testik (2013) also produced laboratory flows composed of kaolinite with abrupt transitions, defined as a process in which the bulk of the suspended sediment in the propagating sediment gravity flow quickly deposits. This was attributed to the presence of a lutocline, which, combined with the non-Newtonian rheology of the clay, suppressed the turbulence. As with the silica-flour flows, the high-frequency fluctuations in head velocity in the clay flows could have been related to the formation of lobes and clefts, and waves on the water surface.

3.4.2.3 Deposits

For flows with $C \geq$ 15% bentonite and $C \geq$ 22% kaolinite, suspended-sediment concentration shows an inverse, linear relationship with runout distance (Figs 3.7 and 3.8). Similarly to the deposits of the silica-flour flows, the deposits of the clay flows changed from wedge-shaped with a block-shaped extension to wedge-shaped without an extension, as the flow type changed from HDTC via CMF to slide (Figs 3.7 and 3.8; Table 3.2). Strong cohesive forces caused rapid bulk settling of clay gels in the reservoir and down to x = 1 m, and turbulent forces in the HDTCs were able to move part of the clay into the flume and form block-shaped deposits with an abrupt termination associated with cohesive freezing. The deposits of the 25% and 27% kaolinite flows and the 18% and 19% bentonite flows showed distinct depressions (Figs 3.7 and 3.8; Table 3.2). Since all of these flows hydroplaned, the aforementioned flow-stretching mechanism of Elverhøi *et al.* (2005) may explain the depression. Interestingly, hydroplaning in the 25% kaolinite flow encouraged the head to detach completely from the body and form an outrunner block. This zero-thickness depression was found 1.37 m behind the front of the deposit, implying that the detached head stretched after separating from the body. The slides laden with kaolinite and bentonite had such a strong network of clay particle bonds that they flowed only a short distance from the reservoir.

Table 3.2: Summary of flow and deposit properties. Dimensional height is relative to the maximum thickness of the deposit. Dimensionless distance is relative to the runout distance.

	Low-density turbidity current (LDTC)	**High-density turbidity current (HDTC)**	**Cohesive and non-cohesive mud flow (CMF/NCMF)**	**Slide**
Visual flow properties	Fully turbulent; uniform colour; mixing with ambient water	Dense lower layer and dilute upper layer; mixing with ambient water	Weak to no internal turbulence; some sediment entrained at top, producing dilute sediment cloud	Coherent mass without significant internal deformation
Flow shape and internal structures	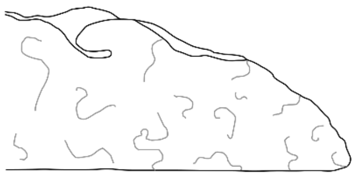	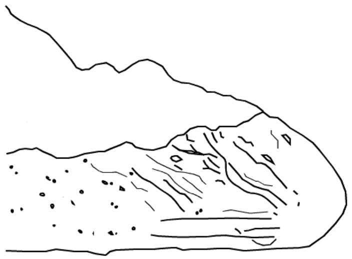	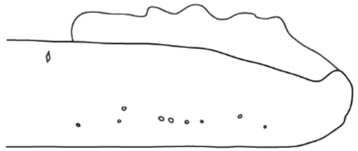	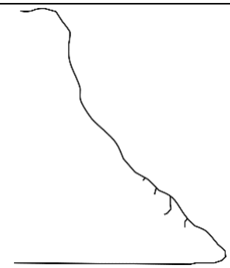
Deposit shape	Not measured, but probably elongate, thin and wedge-shaped (*cf.* Amy *et al.*, 2005)	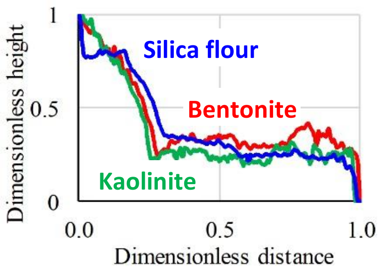	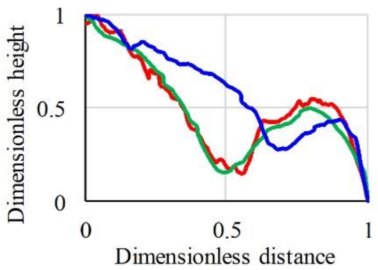	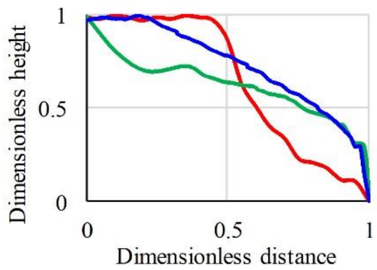
Range of *C*-values	Silica flour: $C \leq 44\%$ Kaolinite: $C \leq 15\%$, Bentonite: $C \leq 10\%$	Silica flour: $46\% \leq C \leq 50\%$ Kaolinite: $22\% \leq C \leq 25\%$ Bentonite: $15\% \leq C \leq 17\%$	Silica flour: $C = 51\%$ Kaolinite: $C = 27\%$ Bentonite: $18\% \leq C \leq 19\%$	Silica flour: $C = 52\%$ Kaolinite: $C = 29\%$ Bentonite: $C = 20\%$
Yield stress boundaries	Lower boundary: 0 Pa Upper boundary: 16–22 Pa	Lower boundary: 16–22 Pa Upper boundary: 67–94 Pa	Lower boundary: 67–94 Pa Upper boundary: 119–141 Pa	Lower boundary: 119–141 Pa Upper boundary: 268 Pa

3.4.3 Effect of sediment type on maximum head velocity and runout distance

Figure 3.9A shows that at $C \leq 10\%$, U_h increased with increasing sediment concentration in a similar way across the three sediment types, suggesting that these flows were driven purely by the density difference. However, at $C > 10\%$, the maximum head velocities diverge, as cohesive forces in the clay flows started to attenuate turbulence. U_h kept increasing at a decreasing rate until a maximum was reached, which is inferred to indicate the stage where flow deceleration by gelling exceeds flow acceleration by density difference. The experimental data also show that once the maximum U_h value is exceeded the cohesive forces strongly dominate, producing a rapid reduction in U_h with increasing C (Fig. 3.9A). The shape of the curve in Figure 3.9A corresponds well with the theoretical curve of velocity against clay concentration of Talling (2013). The U_h of the bentonite flows was consistently lower than that of the kaolinite flows for $C \geq 15\%$. Bentonite clay is more cohesive than kaolinite clay (Yong *et al.*, 2012) and can therefore create a stronger network of particle bonds and resists stronger turbulent forces than kaolinite at similar C values. The silica flour also produced a convex-upward curve in Figure 3.9A, but frictional forces, rather than cohesive forces, started to outcompete the excess density at much higher concentrations than for kaolinite and bentonite. The same trend can be seen for the runout distances of the flows, where from silica flour via kaolinite to bentonite a progressively smaller suspended-sediment concentration is required to produce a comparable runout distance because of the contrasting rheological properties of the sediments (Fig. 3.9B).

3.5 Discussion

3.5.1 Dimensional analysis of maximum head velocity and runout distance

Figure 3.9A reveals that the bentonite, kaolinite, and silica-flour flows reacted in a similar way to changes in initial suspended-sediment concentration, driven by density difference at low C values and by cohesive and frictional forces at high C values. It should therefore be possible to describe the changes in flow behaviour in terms of differences in rheological properties. Below, is it shown that the initial yield stress of the clay suspension in the reservoir can be used to delineate flow type, determine a dimensionless maximum head velocity, and determine a runout distance largely independent of clay type. It is hypothesized that the initial yield stress governs the ability of the clay suspension to leave the reservoir after lifting the lock gate. If the suspension is able to move out of the reservoir, this yield stress then controls the spatial evolution of the head velocity and the runout distance of the flow related to the conversion from potential energy to kinetic energy. Testing this hypothesis required several analytical steps: (a) nondimensionalising the velocity curves in Figure 3.9A, so that the data collapse onto a single curve; (b) determining functional relationships between sediment concentration and initial-yield-stress ranges, based on the available rheometrical data for bentonite and kaolinite; (c) converting the collapsed curve for head velocity from dimensionless sediment concentration to yield stress; (d) delimiting initial yield stress ranges for LDTCs, HDTCs, CMFs, and slides, and; (e) establishing a functional relationship between initial yield stress and runout distance.

The maximum head velocities of the experimental bentonite, kaolinite, and silica-flour flows (Fig. 3.9A) were collapsed using the following best-fit equations (Fig 3.10):

$$\frac{U_h}{U_{h,m}} = \left(\frac{C}{C_m}\right)^{0.466}, \text{for } 0 < C \leq C_m \tag{3.1a}$$

$$\frac{U_h}{U_{h,m}} = 1 - \left(\frac{C - C_m}{C_0 - C_m}\right)^{2.82}, \text{for } C_m < C \leq C_0 \tag{3.1b}$$

where U_h is the maximum head velocity of the flow, $U_{h,m}$ is the highest value of U_h for the sediment type under consideration (*i.e.*, 0.75 m s^{-1} for silica flour, 0.50 m s^{-1} for kaolinite, and 0.37 m s^{-1} for bentonite; Table 3.1), C_m is the suspended-sediment concentration at $U_{h,m}$ (47% for silica flour, 22% for kaolinite, and 16% for bentonite), and C_0 is the threshold concentration above which the flow is not mobile enough to leave the reservoir (U_h = 0). The C_0 values were derived by extrapolation of the experimental data to U_h = 0, yielding 20.5% for bentonite, 30.5% for kaolinite, and 53% for silica flour.

The best-fit Equations 3.1a and 3.1b have high R^2 values (probability value, $p << 0.05$; Fig. 3.10), confirming that the head-velocity curves for the bentonite, kaolinite, and silica-flour flows have a similar profile. Equation 3.1a describes the effect of density difference on head velocity in flows where turbulence is dominant and cohesive and frictional forces have a small influence on flow dynamics, or no influence at all. The power in Equation 3.1a is similar to the power of 0.5 in the well-known relationship between density difference and head velocity for experimental density currents by Keulegan (1957, 1958) and Middleton (1966):

$$U_h = 0.75 \left[\frac{(\rho_f - \rho_a)gH}{\rho_a}\right]^{0.5} \tag{3.2}$$

where ρ_f is the flow density, ρ_a is the density of the ambient water, g is the acceleration due to gravity, and H is the flow thickness. Here, $\rho_f = \rho_s C + \rho_a(1-C) = \rho_a[C(s-1)+1]$, where ρ_s is the sediment density and s is the specific density of the sediment, ρ_s/ρ_a. The square-bracketed term in Equation 3.2 is equal to $(g'H)^{½}$, where $g' = g_s'C$ is the reduced gravity of the sediment, where $g_s' = (1-s)g$. Since the densimetric Froude number is defined by $\mathrm{Fr}' = U_h/(g'H)^{½}$, Equation 3.2 states that the head velocity is governed by a densimetric Froude number of 0.75. This dimensional expression controls the approximate size of $U_{h,m}$ in Equations 3.1a and 3.1b. Assuming that C remains constant during the run and the volume per unit width is conserved $H = A/(0.31+x_h)$, where A = 0.1085 m^2 is the cross-sectional area of the reservoir, and 0.31 m refers to the length of the reservoir, respectively, $U_{h,m}$ = 0.79 m s^{-1} for silica flour, 0.41 m s^{-1} for kaolinite, and 0.24 m s^{-1} for bentonite.

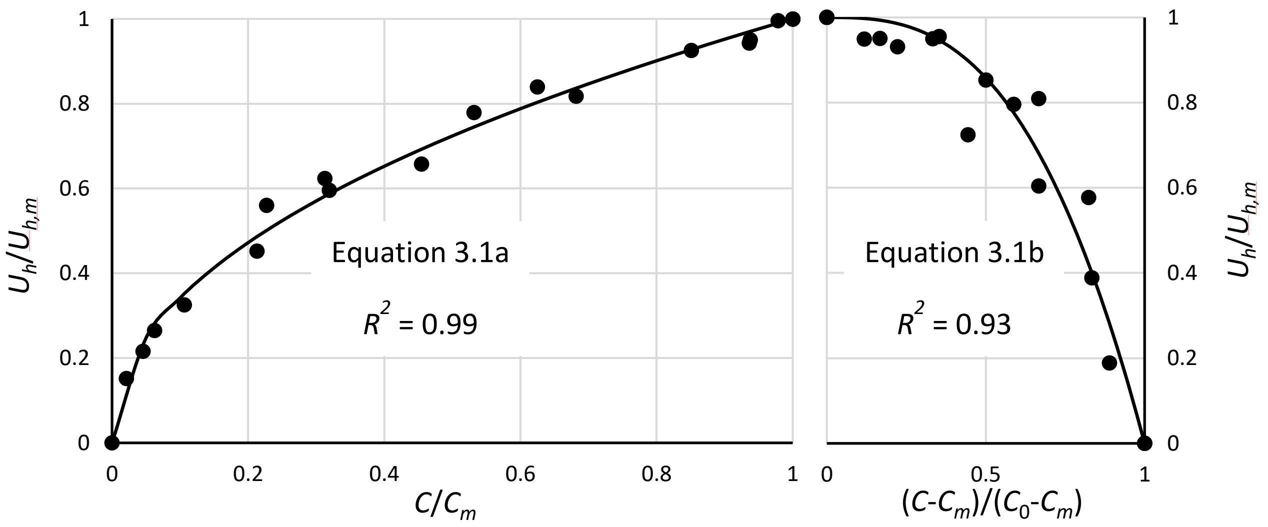

Figure 3.10: Nondimensional relationship between C and U_h for the kaolinite, bentonite, and silica-flour flows. Dots represent experimental data. Solid lines denote best-fit curves (Equations 3.1a and 3.1b).

Equation 3.1b describes the flows where the cohesive and frictional forces outbalanced the density difference and reduced the head velocity. The effect of these forces on head velocity is exponential, probably because the clay gelling and frictional interaction also caused rapid loss of turbulent particle support. Below, the exponents in Equations 3.1a and 3.1b are rounded to 0.5 and 3, respectively. These approximations do not cause a significant reduction in the R^2 values.

In the next step of the dimensional analysis, the dimensionless maximum head velocity, $U_h/U_{h,m}$, was related to the initial yield stress, τ_y, by using the dependence of yield stress on suspended-clay concentration, summarised in Table 3.1. These rheometrical data are available for kaolinite and bentonite clay only at concentrations greater than 1% (Table 3.1). The yield stresses for the bentonite and kaolinite suspensions that produced the flows with U_h values driven by the density difference with the ambient water ($C \leq C_m$) collapse well if plotted against C/C_m (Fig. 3.11A). This relationship can be described by a power law:

$$\tau_y = \tau_{y,m}\,(C/C_m)^3\text{ , for } 0 < C \leq C_m \qquad (3.3a)$$

with R^2 = 0.94 (p << 0.05) and $\tau_{y,m}$ = 37.9 Pa. $\tau_{y,m}$ is the yield stress at $U_h = U_{h,m}$ and $C = C_m$. Hence, 37.9 Pa is the estimated initial yield stress at which U_h changed from being dominated by the density difference with the ambient water to being dominated by cohesive forces, independently of clay type. The yield stresses of the bentonite and kaolinite suspensions that produced the flows with U_h dominated by cohesion ($C > C_m$) collapse if plotted against $(C-C_m)/(C_0-C_m)$ (Fig. 3.11B):

$$\tau_y = \tau_{y,m} + \left(\tau_{y,0} - \tau_{y,m}\right)\left(\frac{C - C_m}{C_0 - C_m}\right)^3\text{ , for } C_m < C \leq C_0 \qquad (3.3b)$$

with R^2 = 0.96 (p << 0.05) and $\tau_{y,0}$ = 271 Pa. $\tau_{y,0}$ is the estimated yield stress at $C = C_0$ and $U_h = 0$, thus representing the yield stress above which the clay suspensions did not leave the reservoir, regardless of clay type.

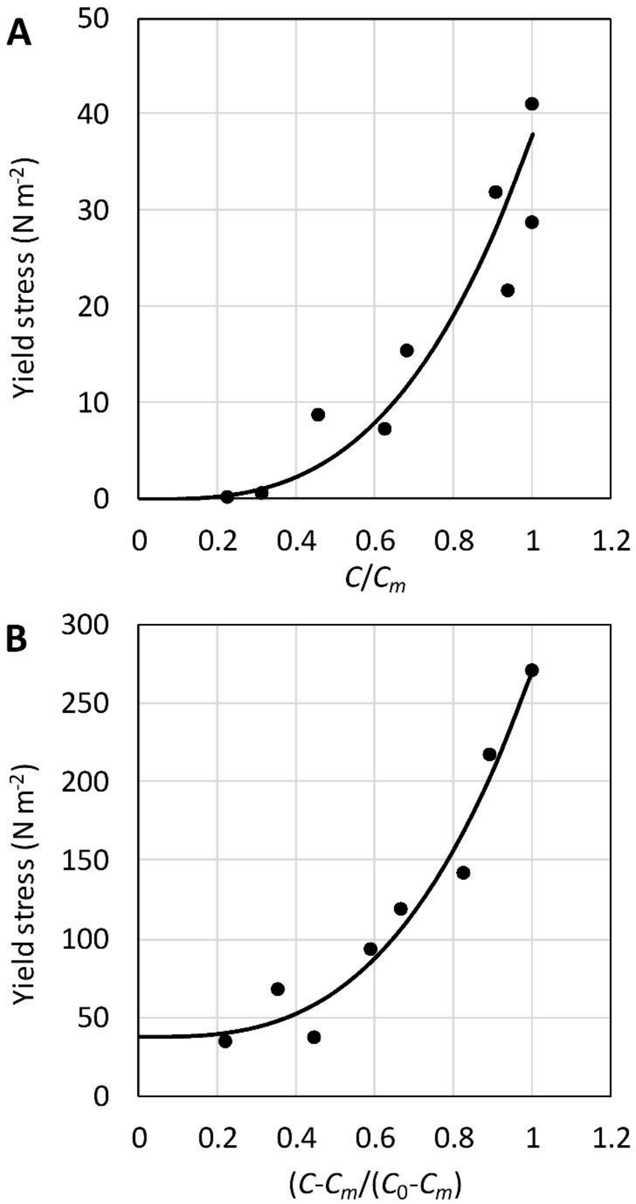

Figure 3.11: (A) C/C_m against yield stress for bentonite and kaolinite. (B) $(C-C_m)/(C_0-C_m)$ against yield stress for bentonite and kaolinite. Dots represent experimental data. Solid lines denote best-fit curves (Equations 3.3a and 3.3b).

Equations 3.1a, 3.1b, 3.3a, and 3.3b can now be combined to derive relationships between τ_y and $U_h/U_{h,m}$ with $R^2 = 0.82$ ($p << 0.05$; Fig. 3.12):

$$\frac{U_h}{U_{h,m}} = \left(\frac{\tau_y}{\tau_{y,m}}\right)^{\frac{1}{6}}, \text{for } 0 < \tau_y \leq \tau_{y,m}, \qquad (3.4a)$$

$$\frac{U_h}{U_{h,m}} = \frac{\tau_{y,0} - \tau_y}{\tau_{y,0} - \tau_{y,m}}, \qquad \text{for } \tau_{y,m} < \tau_y \le \tau_{y,0} \qquad (3.4b)$$

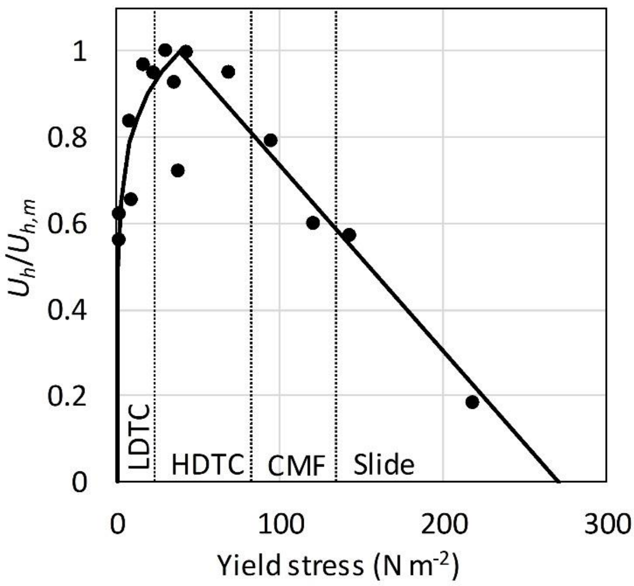

Figure 3.12: $U_h/U_{h,m}$ against yield stress for kaolinite and bentonite. Dots represent experimental data. Solid line denotes best-fit curve (Equations 3.4a and 3.4b). LDTC = low-density turbidity current; HDTC = high-density turbidity current; CMF = cohesive mud flow. Boundaries between flow types are average yield-stress values based on the ranges in Table 3.2.

In experiments where the runout distance was beyond the end of the tank, Hallworth *et al.*'s (1998) box model was used to estimate the expected runout distance. This model, which is for non-cohesive flows, assumes that the Froude number at the head of the flow is constant, the volume is conserved, and the settling is unhindered. The runout distance, x_0, corresponding to the time for all the sediment to settle out, is

$$x_0 = QC^{\frac{1}{5}} \qquad (3.5)$$

where Q is a constant for each sediment type, which is dependent on the sediment density, grain diameter, settling velocity, and the cross-sectional area of the reservoir. Hallworth and Huppert (1998) demonstrated that Hallworth *et al.*'s (1998) model predicts the runout distance well, provided that C < 15%. Based on fitting to the velocities for the 1% and 5% runs for each sediment (Figs 3.2A, 3.5A and 3.7A), x_0 for the 1% and 5% runs can be estimated following Hallworth *et al.*'s (1998) model. This is now described.

According to Hallworth *et al.* (1998), by defining a characteristic timescale, T, given by $T = (x_0^3/Fr^2 g_s' C)^{0.5}$, the nondimensional velocity, $\chi = TU_h/x_0$, can be expressed as

$$\chi = \xi^{-0.5} - \xi^{2} \tag{3.6}$$

where $\xi = x/x_0$. When ξ is close to 1, the functional form of Equation 3.6 can be approximated by a simpler linear function:

$$\chi = 2.5(1 - \xi) \tag{3.7}$$

provided that $\xi > 0.288$ ($x > 0.288x_0$). Thus, the dimensional velocity can be fitted to a functional form given by $U_h = B_1x^{-0.5} - B_2x^2$ or $U_h = B_1 - B_2x$, if the linear approximation can be applied, and $x_0 = (B_1/B_2)^{0.4}$ or B_1/B_2. The 1% and 5% cases for silica flour are shown in Figure 3.13. Since Equations 3.6 and 3.7 result in the velocity decreasing with increasing distance, only the part of the curve given by $x > x_s$, where $x_s = 2.5$ m, is included in the fit. For $x < x_s$, the current can be considered to be slumping and the assumption of a constant Froude number is not valid (Huppert & Simpson, 1980). Thus, the linear fit can be used only if $x_s > 0.288x_0$. This criterion is satisfied for the 1% flows, but not for the 5% flows, so the nonlinear functional form must be used. Of the 1% and 5% flows, the 1% flow is considered the more reliable, because it requires less extrapolation and is likely to have the least cohesive behaviour. The fit to the preferred runout distance for C = 1% on the basis of a $C^{1/5}$ dependence results in Q = 21 m in Equation 3.5. Figure 3.13B shows this $C^{1/5}$ dependence. Using a similar approach for kaolinite and bentonite, Q was determined to be 20 m for both clay types. There is little evidence of dependence on sediment grain size, density, or settling-velocity (all reservoir cross-sectional areas are the same), since all three values of Q are similar. For concentrations in the range 1% ≤ C ≤ 15% and using these Q values, Equation 3.5 correctly predicts runout distances that are greater than 4.69 m (*cf.* Fig. 3.14A). The preferred extrapolated runout distances for all 1% and 5% flows are listed in Table 3.3.

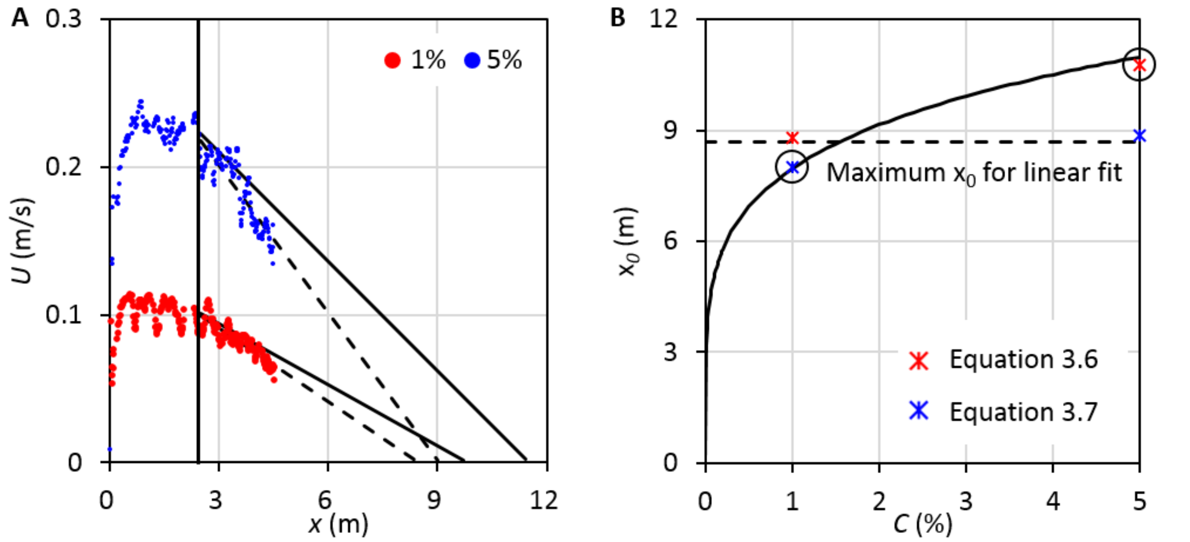

Figure 3.13: (A) Determination of runout distance, x_0, for the 1% and 5% silica-flour flows for $x > x_s$, using both Equation 3.6 (solid line) and Equation 3.7 (dashed line). (B) Determination of the $C^{1/5}$ dependence for x_0, based on the curve passing through the preferred x_0 at C = 1%. The preferred x_0, with circle around symbol, is determined by the $x_0 \leq x_s/0.288$ condition for linear fitting.

Table 3.3: Extrapolated runout distances (m).

Material	1%	5%
Silica flour	8.47	11.48
Kaolinite	7.87	10.00
Bentonite	8.00	10.76

The dependence of runout distance on concentration for the high-concentration flows in Figure 3.9B is approximately linear. Therefore, anticipating that there is a crossover between this straight-line fit and the runout distance of the low-concentration flows, predicted by Equation 3.5, a composite best-fit equation for $x_0/x_{0,m}$ can be defined as

$$\frac{x_0}{x_{0,m}} = \left(\frac{C}{C_{m1}}\right)^{\frac{1}{5}}, \text{for } 0 < C \leq C_{m1} \tag{3.8a}$$

$$\frac{x_0}{x_{0,m}} = \frac{C_0 - C}{C_0 - C_{m1}}, \text{for } C_{m1} < C \leq C_0 \tag{3.8b}$$

where C_{m1} is the concentration at which the maximum runout distance, $x_{0,m}$, is reached. Using Equation 3.5, $x_{0,m} = QC_{m1}^{1/5}$, C_{m1} was calculated as 29.8% for silica flour, 5.9% for kaolinite and 6.5% for bentonite. These values of C_{m1} are consistent with the assumption that C = 1% and 5% behave non-cohesively and show $C_{m1} < C_m$. The maximum runout distance for silica flour is largest, $x_{0,m}$ = 16.5 m, and the maximum runout distances for kaolinite and bentonite are smaller and similar, $x_{0,m}$ = 11.4 m and 11.3 m, (Fig. 3.14A). The linear fit to the data based on Equation 3.8b yielded $R^2 = 0.97$ ($p << 0.05$; Fig. 3.14B).

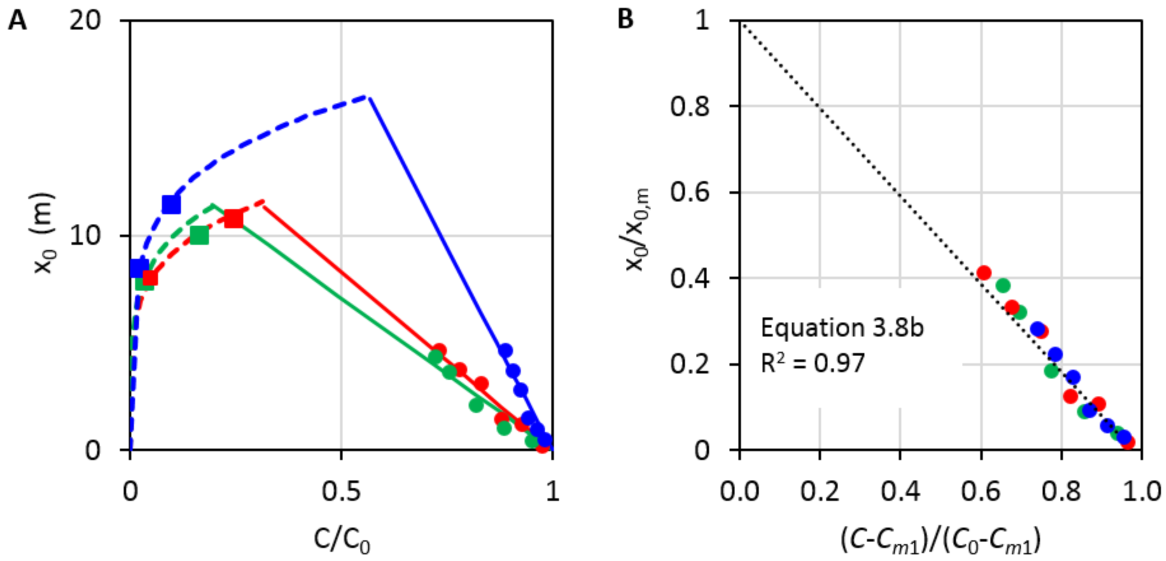

Figure 3.14: (A) Runout distance, x_0, against dimensionless concentration, C/C_0 for all flows. Circles denote the measured values given in Table 3.1. Squares are the extrapolated values given in Table 3.3. Solid lines represent fit to the data (Equation 3.8b), and dashed lines represent predictions by Hallworth and Huppert (1998) for low-concentration flows (Equation 3.5). The cross-over between these lines denotes the predicted maximum runout distance, $x_{0,m}$. (B) Fit of $x_0/x_{0,m}$ to $(C-C_{m1})/(C_0-C_{m1})$ for all the experimental data, where $C > C_{m1}$.

Equations 3.3 and 3.8 can now be combined to derive relationships between τ_y and $x_0/x_{0,m}$:

$$\frac{x_0}{x_{0,m}} = \begin{cases} \left(\frac{\tau_y}{\tau_{y,m1}}\right)^{1/15}, & \text{for } 0 < \tau_y \leq \tau_{y,m1}, \\ \frac{C_0 - C_m(\tau_y/\tau_{y,m})^{1/3}}{C_0 - C_{m1}}, & \text{for } \tau_{y,m1} < \tau_y \leq \tau_{y,m}, \\ \left(\frac{C_0 - C_m}{C_0 - C_{m1}}\right)\left[1 - \left(\frac{\tau_y - \tau_{y,m}}{\tau_{y,0} - \tau_{y,m}}\right)^{1/3}\right], & \text{for } \tau_{y,m} < \tau_y \leq \tau_{y,0}, \end{cases} \tag{3.9}$$

where $\tau_{y,m1} = \tau_{y,m}(C_{m1}/C_m)^3$, with $\tau_{y,m1}$ = 0.74 Pa for kaolinite and $\tau_{y,m1}$ = 2.52 Pa for bentonite. Equation 3.9 for kaolinite and bentonite is compared with the data in Figure 3.15 ($R^2 = 0.71$; $p << 0.05$). It can be seen that there are only slight differences between the curves for the two sediments. Since $\tau_{y,m1}$ for kaolinite and bentonite are small compared to $\tau_{y,m}$, Equation 3.9 for $0 \leq \tau_y \leq \tau_{y,m}$, can be approximated by

$$\frac{x_0}{x_{0,m}} = 1 - \left(\frac{C_m - C_{m1}}{C_0 - C_{m1}}\right)\left(\frac{\tau_y}{\tau_{y,m}}\right)^{\frac{1}{2}} \tag{3.10}$$

where the 1/2 power is based o^{n} ^{m}atching the slope of x_0 at $\tau_y = \tau_{y,m}$ in Equation 3.9. Use of this approximation must be with the understanding that x_0 ultimately tends to zero as τ_y tends to zero. For kaolinite and bentonite, $(C_m{-}C_{m1})/(C_0{-}C_{m1})$ = 0.654 and 0.679 and $(C_0{-}C_m)/(C_0{-}C_{m1})$ = 0.346 and 0.321, such that $x_0/x_{0,m}$ can be approximated from Equations 3.9 and 3.10 and by

$$\frac{x_0}{x_{0,m}} = 1 - \frac{2}{3}\left(\frac{\tau_y}{\tau_{y,m}}\right)^{\frac{1}{2}}, \qquad \text{for } 0 \leq \tau_y \leq \tau_{y,m}, \qquad (3.11a)$$

$$\frac{x_0}{x_{0,m}} = \frac{1}{3}\left[1 - \left(\frac{\tau_y - \tau_{y,m}}{\tau_{y,0} - \tau_{y,m}}\right)^{\frac{1}{3}}\right], \quad \text{for } \tau_{y,m} \leq \tau_y \leq \tau_{y,0} \qquad (3.11b)$$

which is also shown in Fig. 3.15 (R^2 = 0.68; p << 0.05). In Equation 3.11, only $x_{0,m}$ is dependent on the box model (since $x_{0,m}$ = 11.4 m and 11.3 m for kaolinite and bentonite, an average of these $x_{0,m}$ values could reasonably be taken). Equation 3.11 thus supports the hypothesis that the yield stress of the clay suspensions in the reservoir governs the variation in the runout distance of the clay flows after lifting the lock gate.

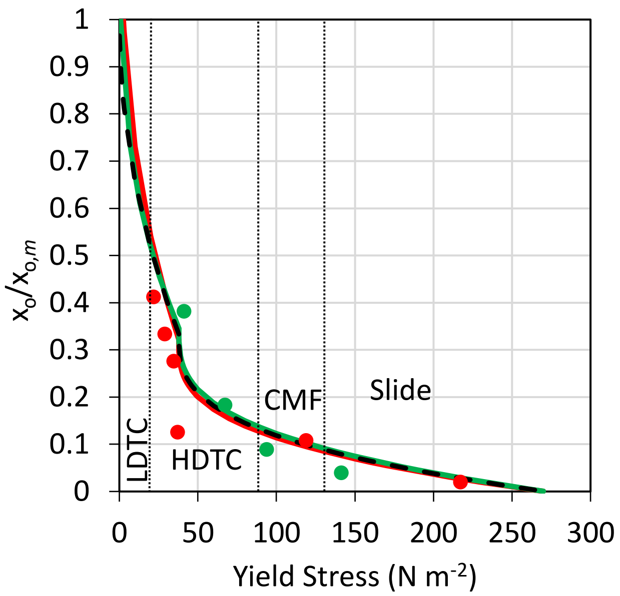

Figure 3.15: Dimensionless deposit runout distances of the clay flows against yield stress for kaolinite and bentonite. Dots represent experimental data. Solid lines denote curves according to Equation 3.9 for kaolinite (green) and bentonite (red) (for clarity, yield stresses where $\tau_y < \tau_{y,m1}$ have not been plotted) and the dashed line denotes the curve according to Equation 3.11. LDTC = low-density turbidity current; HDTC = high-density turbidity current; CMF = cohesive mud flow. Boundaries between flow types are average yield stress values based on the ranges in Table 3.2.

3.5.2 Yield stress as an independent parameter to describe flows and deposits

The above dimensional analysis demonstrates that fine-grained SGFs go through similar stages of flow dynamics and deposit properties with increasing initial suspended-sediment concentration. The differences in the cohesive properties of the clay suspensions were accounted for by converting suspended-sediment concentration to yield stress. This indicates that yield stress is a primary control on the head velocity and the runout distance. Equation 3.4 allows $U_h/U_{h,m}$ of a cohesive SGF to be estimated from the initial yield stress in a straightforward manner, independent of clay type. In addition, Equation 3.11 provides a simple tool for computing the runout distance of a cohesive SGF from its initial yield stress, also independent of clay type. At present, however, the determination of the maximum head velocity requires knowledge of $U_{h,m}$, which is dependent on clay type. The dimensional analysis is based on the initial τ_y value of the suspensions in the reservoir. Once these suspensions flow out of the reservoir, the yield stress of the SGFs can be expected to vary in space and time as a result of mixing with ambient water and sediment deposition, as clay bonds break and reform under the changing flow stresses. However, the results of the dimensional analysis imply that these variations have little effect on the nondimensional maximum head velocity and the runout distance of these experimental flows, if the yield stress of the bentonite and kaolinite clay in the reservoir is identical.

Table 3.2 summarises the properties of the LDTCs, HDTCs, mud flows, and slides, and their deposits. Despite the large differences in initial suspended-sediment concentration of the three types of sediment, these flow types have similar shapes, internal dynamics, and deposit shapes. The HDTCs produced deposits that were wedge-shaped with a block-shaped extension, the CMFs and NCMF produced wedge-shaped deposits with outrunner blocks, and the slides produced wedge-shaped deposits without extension (Table 3.2). These deposit shapes were clearly linked to the flow behaviour of the fine-grained SGFs and the balance between the processes that promote and impede flow. The properties of the four flow types and their deposits are bracketed by yield stress in Table 3.2. LDTCs change to HDTCs at $\tau_y \approx$ 16-22 Pa, the boundary between HDTCs and CMFs is at $\tau_y \approx$ 67-94 Pa, and slides are stable between $\tau_y \approx$ 119-141 Pa and $\tau_y \approx$ 271 Pa.

3.5.3 Wider implications

The present laboratory experiments are a suitable starting point for determining the dynamic properties, runout distance, and deposit geometry of fine-grained SGFs in the natural environment, based on differences in rheology. However, quantitative scaling of the experimental results to natural flows and their deposits is not possible at present, principally because the best-fit coefficients in Equations 3.1 and 3.3-3.11 and the value of $\tau_{y,m}$ might be dependent on the experimental setup. For example, the experiments were limited to flows carrying a single sediment type and moving across a horizontal bed with a low bed roughness, and to a single set of potential energies, controlled by the height of the suspension column in the reservoir.

Notwithstanding these limitations, the experimental data can be used to make a qualitative comparison with full-scale flows in nature. The laboratory flows with $C \leq 10\%$ behaved in a similar manner for the three sediment types, with turbulence dominating these flows and the sediment particles unable to form high enough frictional forces or electrostatic forces of attraction to limit flow mobility. It is expected that the shape of the deposits of these LDTCs is also independent of the cohesive properties of the sediment, although a longer lock-exchange tank is needed to test this hypothesis. Based on previous work (*e.g.,* Middleton, 1967; Lüthi, 1981; Bonnecaze *et al.*, 1993; Amy *et al.*, 2005), these turbidite deposits should be elongate, thin, and wedge-shaped. The threshold concentration of 10% might be higher for natural flows, since full-scale turbidity currents are often more turbulent (Talling *et al.*, 2013), and therefore more likely to break the bonds between clay particles, than laboratory-scale turbidity currents. For practical purposes, this outcome implies that the deposits of clay-size and fine-silt size LDTCs can be interpreted in terms of turbulence properties and density difference with the ambient water, and that the type of sediment and yield stress can be ignored, even if these flows carry strongly cohesive clay minerals, such as bentonite. In other words, clay- and silt-laden LDTCs have similar flow efficiencies (*sensu* Mutti *et al.*, 1999).

In contrast, the type of sediment and the yield stress need to be taken into account for most HDTCs, mud flows, and slides. These high-density SGFs should generally transport weakly cohesive kaolinite over a greater distance than strongly cohesive bentonite, whilst non-cohesive fine-grained SGFs are inferred to travel the greatest distance from the origin. Hence, the flow efficiency of HDTCs, mud flows, and slides is generally lower for bentonite than for kaolinite (Mutti *et al.*, 1999). The high efficiency of the laboratory flows laden with up to 47% silica flour is remarkable, and the anticipated implications for natural flows are significant. These laboratory flows were driven by a high density difference with the ambient water, high turbulence intensity, and low particle settling velocity. Natural turbidity currents may be at least one or two orders of magnitude faster than in the laboratory (Talling *et al.*, 2013). Since turbulence intensity increases with increasing flow velocity (*e.g.,* Baas *et al.*, 2009), natural turbidity currents should be able to carry large volumes of silt-size particles over long distances. This high sediment flux and long transport distance may even extend to sand-size particles (*cf.* Talling *et al.*, 2007), if turbulent forces are sufficiently strong to keep the sand particles in suspension and frictional forces between the sand particles are weak. It is clear that the runout distance of SGFs also depends on other factors, such as flow volume, basin-floor morphology, and the ratio of cohesive to non-cohesive sediment (Talling, 2013). However, it is concluded here that fine-sediment type is a major control above suspended-sediment concentrations that are equivalent to the laboratory threshold of 10%, and that flow efficiency reaches a maximum value at which frictional and cohesive forces become dominant over density difference and particle support by turbulence. Once past this maximum, the flow efficiency rapidly decreases.

The rheological control on flow properties may also have significant implications for the geometry of the deposits of high-density SGFs. It is expected that, at similar C values, the deposits of high-density SGFs laden with weakly cohesive clay cover a larger surface area and have a smaller bed thickness than the deposits of high-density SGFs laden with strongly cohesive clay. Conversely, weakly cohesive clay beds may be thicker than their strongly cohesive equivalents, if these beds were formed by flows with the same initial yield strength, because flows laden with strongly cohesive clay carry a smaller volume of sediment, and were predicted to have approximately the same runout distance as the flows laden with weakly cohesive clay (Fig. 3.15; Equation 3.11).

Kaolinite and bentonite are the weakly and strongly cohesive end members of a suite of clay minerals that are common in nature. Illite and chlorite are clay minerals of intermediate cohesive strength. Further work is needed to verify if the rheological model for kaolinite and bentonite SGFs presented in this study is also valid for chlorite and illite SGFs, and also stretches to SGFs that carry mixtures of clay minerals. This study covered the entire spectrum from non-cohesive to strongly cohesive sediment, so it is appropriate to hypothesize that measuring the relationship between yield stress and suspended-sediment concentration for, for example, illite, chlorite, and mixed clay minerals is sufficient to determine the flow dynamics, runout distance, and deposit shape of SGFs laden with these types of sediments, notwithstanding the limitations described above. This hypothesis assumes that other clay minerals do not have more complex rheological properties than kaolinite and bentonite.

With time, recurring SGF events build the architecture of larger-scale sediment bodies, such as channel fills, levees, and lobes in submarine fans. It follows from the above discussion that this architecture may be different for flows that carry different types of clay minerals and non-cohesive fine sediment, especially if HDTCs, mud flows, and slides constitute a major portion of this architecture. Other potential geological applications of this study include: (i) a better delineation of the rheological properties of SGFs that form LDTC deposits, HDTC deposits, debris flows, and slides in core and outcrop, and; (ii) rheological characterization of modern turbidity currents in lakes and oceans, based on novel techniques for measuring flow velocity and suspended-sediment concentration (*e.g.,* Sumner & Paull, 2014).

3.6 Conclusions

The present laboratory experiments show that both sediment type and suspended-sediment concentration control the flow properties and the deposits of fine-grained SGFs. At low concentrations, the dominant turbulent forces prevent electrochemical binding and frictional interaction between the particles, and the density difference with the ambient water drives the flow, thus producing similar behaviour between flows laden with sediment of contrasting cohesive properties. At high concentrations, however, cohesive and frictional forces outbalance turbulent forces, leading to decreased particle support in the flow. Consequently, non-cohesive silica-flour flows produce a greater runout distance and a higher maximum head velocity, U_h, than weakly cohesive kaolinite flows of similar density. This difference in flow behaviour is even greater for strongly cohesive bentonite flows, which have the shortest runout distances and the lowest U_h. The change in flow behaviour controlled by density difference and turbulent forces to flow behaviour controlled by cohesive or frictional forces increased from 16% for bentonite via 22% for kaolinite to 47% for silica flour. This threshold concentration for the silica-flour flows is close to the cubic packing density of clastic sediment, which supports the idea that non-cohesive fine-grained SGFs are turbulent and highly mobile up to very high densities, and friction between particles in an extremely dense suspension is required to impede flow.

The SGFs laden with silica flour, kaolinite, and bentonite changed from LDTCs via HDTCs and mud flows to slides as C was increased. Within the limits of the experimental setup, these flow types have similar flow properties and produce similar deposit shapes. The initial yield stress of the pre-failure suspension defines the transition between these flow types, and τ_y also governs the dimensionless maximum head velocity and the runout distance of these SGFs, independently of clay type. In other words, the present study demonstrates that yield stress is a primary control on the momentum and the runout distance of fine-grained SGFs.

This laboratory study provides an exciting platform for increasing the understanding and the predictive ability of the shape and the runout length of the deposits of natural fine-grained SGFs. The effect of the cohesive properties of the suspended sediment on deposit geometry can be ignored only at $C \leq$

10%. Above this concentration, the runout length of the deposits increases, as the cohesive properties of the suspended sediment decrease. However, it should be noted that this threshold concentration is probably higher for natural flows, because these are often more turbulent than the laboratory flows. The differences in the geometry of deposits from flows laden with fine-grained sediment of contrasting cohesive strength may be reflected in differences in the architecture of stacked fine-grained SGF deposits.

4. Using rheological properties to understand mixed-clay sediment gravity flows and their deposits

4.1. Introduction

The varying cohesive strength of different clay minerals means that the type of clay minerals within cohesive sediment gravity flows (SGFs) is an important control on their flow behaviour and deposit properties (Marr *et al.*, 2001; Baker *et al.*, 2017). For example, Chapter 3 contrasted cohesive SGFs composed of weakly cohesive kaolinite and strongly cohesive bentonite. For high-density SGFs of the same concentration, kaolinite flows had a higher maximum head velocity and a longer runout distance than bentonite flows. This is because the bentonite flows were able to form a stronger network of particle bonds, of greater rheological strength, than kaolinite flows of the same concentration. The rheological properties of the starting suspension describe their cohesive strength. In Chapter 3, the yield stress was used to predict the dimensionless maximum head velocity and the runout distance of the SGFs, demonstrating that the rheology of single clay SGFs can aid understanding and predict their flow behaviour and deposits.

Current understanding on how the rheological properties, flow behaviour, and deposits of mixed-clay SGFs change with varying proportions of different clay minerals is limited. Yet in the natural environment, the deposits of clay-rich SGFs are usually composed of a variety of different clay minerals (*e.g.*, Kolla *et al.*, 1980; Alonso & Maldonado, 1990; Zhang *et al*., 2015; France-Lanord e*t al.*, 2016). The formation of clay minerals is primarily dependent on parental material, topography, time and climate (Chamley, 1981; Evans, 1992; Thiry, 2000; Fagel, 2007). In nature, these competing controls can generate different clay minerals that are transported to the source area of SGFs. SGFs are therefore expected to be composed of mixtures of the most common clay minerals, which are, in order of increasing cohesive strength, kaolinite, chlorite, illite, and smectite (which includes bentonite) (Griffin *et al.*, 1968; Yu *et al.*, 2014). Because of these contrasting cohesive strengths, different proportions of clay minerals can change the cohesive and rheological properties of mixed-clay SGFs, which in turn can influence the dynamics of these flows.

The rheology of mixed-clay SGFs may provide simple parameters to predict the behaviour of the flows, rather than having to measure their clay mineral composition. It is hypothesised here that the rheology of the suspensions forming mixed-clay SGFs can be predicted from the sum of the rheologies of the pure clay components. This would be a powerful approach, as potentially the rheological properties of any clay mixture could be predicted. However, this assumes the clay minerals do not interact and change the rheology when mixed together.

This chapter presents experiments aiming to improve our understanding of the effect of different clay mineral mixtures on the suspension rheology, flow behaviour, and deposit properties of mixed-clay SGFs. SGFs of varying proportions of kaolinite and bentonite were generated at a fixed volume concentration and data on the flow behaviour, head velocity and deposits were collected. Rheological tests were also conducted on the starting suspensions of the flows. This chapter aims to answer the following specific questions:

1. At a fixed volume concentration, how does changing the proportion of kaolinite and bentonite influence the flow behaviour, flow velocity, runout distance, and deposit geometry of mixed-clay SGFs?
2. Can the rheological properties of the pre-failure suspension be used to understand the behaviour of the flows?
3. Can the yield stress of the mixed-clay suspensions be accurately predicted from the sum of the yield stresses of the pure clay components?
4. Can the predictive equations presented in Chapter 3 correctly calculate the dimensionless maximum head velocity and the runout distance of the mixed-clay SGFs?
5. How can the results be used to improve our interpretation of the flow dynamics and deposit properties of natural mixed-clay SGFs?

4.2 Methods

4.2.1 Lock-exchange experiments

Ten sediment gravity flow experiments were conducted using the experimental methods described in Chapter 2. The SGFs had a fixed volume concentration of 20%, whereas the proportion of strongly cohesive bentonite to weakly cohesive kaolinite varied. A velocity-distance series was obtained from analysis of the high-definition video camera, which tracked the head of the flow. The video recordings were also used to analyse how the behaviour of the head of the flows changed visually for the different proportions of kaolinite and bentonite, and as the flows travelled along the tank. The SGF deposits were measured along the centre line of the flume to produce deposit height-distance plots and runout distances recorded for all flows that stopped before reaching the end of the flume. The experimental data presented in this chapter are summarised in Table 4.1.

4.2.2 Rheology experiments

Rheological tests with the rheometer were conducted on samples with the same composition as in the laboratory flows. A full explanation of the rheometer rheology method is provided in Chapter 2.4.1. The rheological results presented in this chapter include the yield stress and the complex shear modulus, measured via the oscillatory test, the strain-controlled test, and the stress-controlled test. In addition, the apparent viscosity as a function of strain rate from the stress-controlled test is presented.

Table 4.1: Experimental data. Oscillatory, strain and stress refer to the different rheological tests. HDTC = high-density turbidity current.

Run number	Bentonite proportion (%), C_b	Kaolinite proportion (%), C_k	pH	Runout distance (m)	Maximum head velocity (m s^{-1})	Flow type	Yield stress (Pa)			Complex shear modulus (Pa)		
							Oscillatory	Strain	Stress	Oscillatory	Strain	Stress
1	0	100	4.3	-	0.43	HDTC (weak)	31.95	3.05	2.74	15.04	1.18	1.79
2	10	90	7.1	-	0.45	HDTC (weak)	17.85	2.72	2.48	8.00	1.01	1.74
3	20	80	7.3	-	0.45	HDTC (weak)	17.85	3.85	3.86	8.21	1.96	2.74
4	35	65	7.4	4.11	0.41	HDTC (strong)	21.25	7.39	7.44	12.11	3.56	5.59
5	45	55	7.6	3.46	0.38	HDTC (strong)	26.20	12.3	12.6	17.68	6.13	7.36
6	55	45	7.6	2.45	0.35	HDTC (strong)	28.42	17.8	19.4	23.76	10.41	11.61
7	65	35	7.8	1.80	0.32	Mud flow	50.80	30.6	36.8	39.57	18.44	17.09
8	75	25	7.9	1.07	0.25	Mud flow	71.60	47.6	52.7	51.80	24.64	28.74
9	85	15	8.0	0.78	0.17	Mud flow	106.90	65.6	71.4	69.57	29.58	37.41
10	100	0	8.2	0.21	0.04	Slide	217.12	102	104	122.34	39.63	63.30

4.3 Flume results of mixed kaolinite-bentonite flows

The behaviour of the mixed kaolinite-bentonite SGFs altered as the proportion of bentonite in the flows, C_b, increased from 0% to 100% and the percentage of kaolinite in the flows, C_k, correspondingly reduced from 100% to 0%. Visual changes in the flow dynamics of the head of the flows, and variation in the flow head velocity and deposit properties along the flow paths are presented below in terms of increasing bentonite concentration.

4.3.1 Visual observations

Video recordings show that the C_b = 0% to C_b = 20% flows had pointed, semi-elliptically shaped heads, which hydroplaned from distance from the lock gate, x, of *c.* 1 m to *c.* 4 m. The heads of the C_b = 0% and C_b = 10% flows initially had a uniform colour and were visually dominated by turbulent mixing (Fig. 4.1A). However, by x = *c.* 1.80 m the $C_b \leq$ 10% flows could be divided into two zones: a dark lower zone 1 without visible internal mixing and a lighter upper zone 2, where ambient water mixed into the flow and Kelvin-Helmholtz instabilities developed. The boundary between zone 1 and zone 2 became clearer as the flows travelled along the tank and contained interfacial waves. The head of the C_b = 20% flow was only dominated by turbulent mixing at the start; from $x \approx$ 0.9 m the flow could be divided into the two layers described above (Fig. 4.1B). Between x = *c.* 1.5 m and x = *c.* 3.5 m, linear features of clear ambient water, termed coherent fluid entrainment structures, were observed in zone 1 of the heads of the $C_b \leq$ 20% flows (Fig. 4.1B). The coherent fluid entrainment structures were larger and more numerous in the C_b = 20% flow compared to flows containing $C_b \leq$ 10%. Packets of cohesive sediment could be seen detaching from the heads of the $C_b \leq$ 20% flows, before being thrown over or under the head (Fig. 4.1A).

The heads of the C_b = 35% to C_b = 65% flows had a rounded shape with a blunt nose. These flows also produced the two-layer flow structure, but interfacial waves between the two zones and hydroplaning were observed only up to C_b = 55% (Fig. 4.1C-F). An increasing colour difference between the two layers made the boundary between the zones more distinct as C_b increased, whilst mixing with the ambient water in zone 2 reduced.

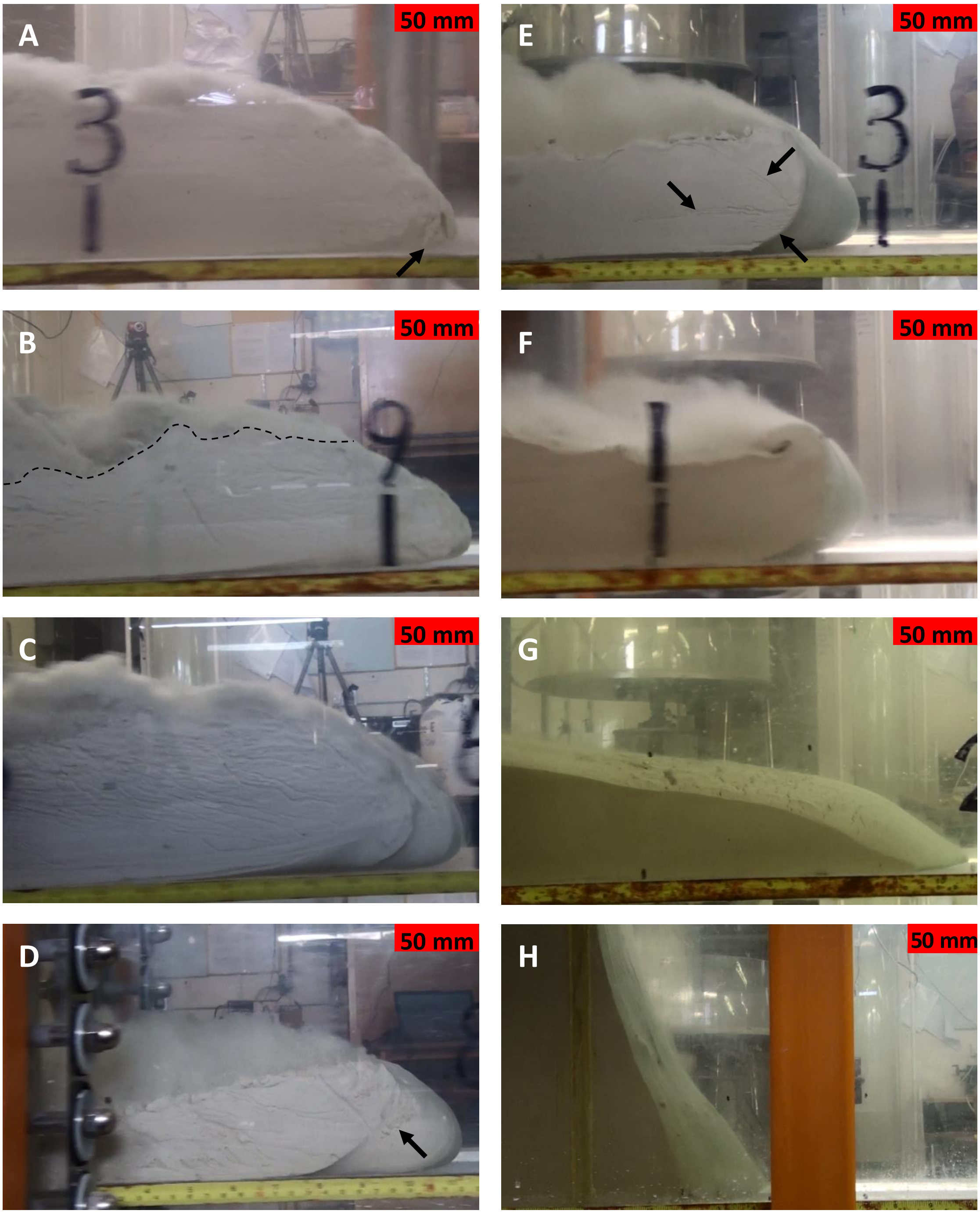

Figure 4.1: Video snapshots of the heads of the mixed-clay flows. (A) Fully turbulent C_b = 0% flow at t = 3.24 s and x = 1.10 m; a packet of cohesive sediment is shown by the arrow. (B) Pointed head of the C_b = 20% weak high-density turbidity current, which can be divided into two parts shown by the dotted line at t = 7.00 s and x = 2.81 m; coherent fluid entrainment structures are visible in the lower layer. (C) C_b = 35% flow at t = 4.63 and x = 1.79 m; this strong high-density turbidity current can be divided into three parts (see accompanying text). (D) Rounded head of the C_b = 45% flow at t = 6.80 s and x = 2.39 m; mixing in the upper layer is reduced and the arrow points to bubbles in zone 1. (E) Hydroplaning head of the C_b = 55% flow with a few thin coherent fluid entrainment structures shown by arrows at t = 2.80 s and x = 0.89 m. (F) Mud flow at C_b = 65% at t = 1.57 s and x = 0.43 m; the head of the flow is curled back on itself. (G) Featureless, wedge-shaped head of the C_b = 85% mud flow with tension cracks on the surface at t = 3.73 s and x = 0.58 m. (H) Front of the C_b = 100% slide at t = 5.06 s and x = 0.11 m.

The head of the C_b = 35% flow initially had a two layer structure, but from x = 1.06 m to x = 2.30 m the flow could be divided into three layers: (i) a thin, dense lower zone 1a, which contained horizontal coherent fluid entrainment structures; (ii) a thick, dense middle zone 1b with many angled coherent fluid entrainment structures; and (iii) a thin, dilute upper zone 2, dominated by mixing with the ambient water (Fig. 4.1C). Zone 1a became featureless after x = 2.30 m and the coherent fluid entrainment structures in zone 1b started to reduce and thin until by x = 3.20 m the flow reverted to a two-layer structure with a featureless zone 1.

Within the bipartite structure of the C_b = 45% flow, striking horizontal coherent fluid entrainment structures formed in the dense lower layer at x = 0.75 m, which were angled from x = 1.10 m to x = 3.05 m, after which the coherent fluid entrainment structures ceased to exist (Fig. 4.1D). From x = 3.43 m, bubbles appeared in the head of the C_b = 45% flow. During the final flow stage, the bubbles became elongate as the head of the flow stretched. In the head of the C_b = 55% flow the dense lower layer was mostly featureless apart from a few, thin coherent fluid entrainment structures from x = 0.60 m to x = 1.65 m (Fig. 4.1E).

Upon leaving the reservoir the top of the head of the C_b = 65% flow curled back on itself producing a rounded head with a curl at the top until x = 1.20 m when the curl became indistinct from the rest of the head (Fig. 4.1F). The head of the C_b = 65% flow did not hydroplane. The dense lower zone was featureless until x = 0.90 m, when bubbles developed in the head of the flow which lasted for the flow duration. In the final flow stages, small tension cracks perpendicular to the flow direction appeared.

The C_b = 75% and C_b = 85% flows had pointed, wedged-shaped heads without internal features (Fig. 4.1G). The C_b = 75% flow hydroplaned at the start and produced a weak suspension cloud as it travelled along the tank. In contrast, the front of the head of the C_b = 85% flow did not hydroplane or mix with the ambient water (Fig. 4.1G). Tension cracks developed during the final flow stages of both flows; the tension cracks were greater in size and number for the C_b = 85% flow than for the C_b = 75%. The highest proportion bentonite flow, C_b = 100%, left the reservoir *en-masse* without discernible head, mixing, or hydroplaning (Fig. 4.1H). Vertical tension cracks, parallel to the flow direction developed at the front of the flow.

4.3.2 Flow velocities

The head of the flows accelerated rapidly once the lock gate was lifted (Fig. 4.2). The maximum head velocity of the flows increased slightly from U_h = 0.43 m s^{-1} for the C_b = 0% flow to U_h = 0.45 m s^{-1} for the C_b = 10% and C_b = 20% flows. Thereafter, further increasing the proportion of bentonite in the flow reduced the maximum head velocity of the flows, reaching a minimum of U_h = 0.04 m s^{-1} for C_b = 100%. As the flows travelled down the flume, velocity fluctuations of the order of 1 second duration were observed. These fluctuations were most apparent in the $C_b \leq 55\%$ flows, and the maximum velocity fluctuations of *c.* 0.06 m s^{-1} recorded in the $C_b = 20\%$ flow correspond to 13% of U_h.

After the initial flow acceleration the C_b = 0% to C_b = 20% flows maintained a fairly constant head velocity until *c.* 3 m; thereafter these flows started to decelerate to *c.* 50% of their maximum U_h before reflecting off the end of the flume. In contrast, the flows of $C_b \geq 35\%$ showed a shorter period of steady flow velocity before starting to decelerate. These flows exhibited a rapid decrease in velocity in the final flow stages to produce measurable runout distances. As C_b was increased, the location of the reduction in head velocity occurred progressively closer to the lock gate. The head velocity of the C_b = 100% increased rapidly to 0.04 m s^{-1}, before reducing to zero within 0.21 m.

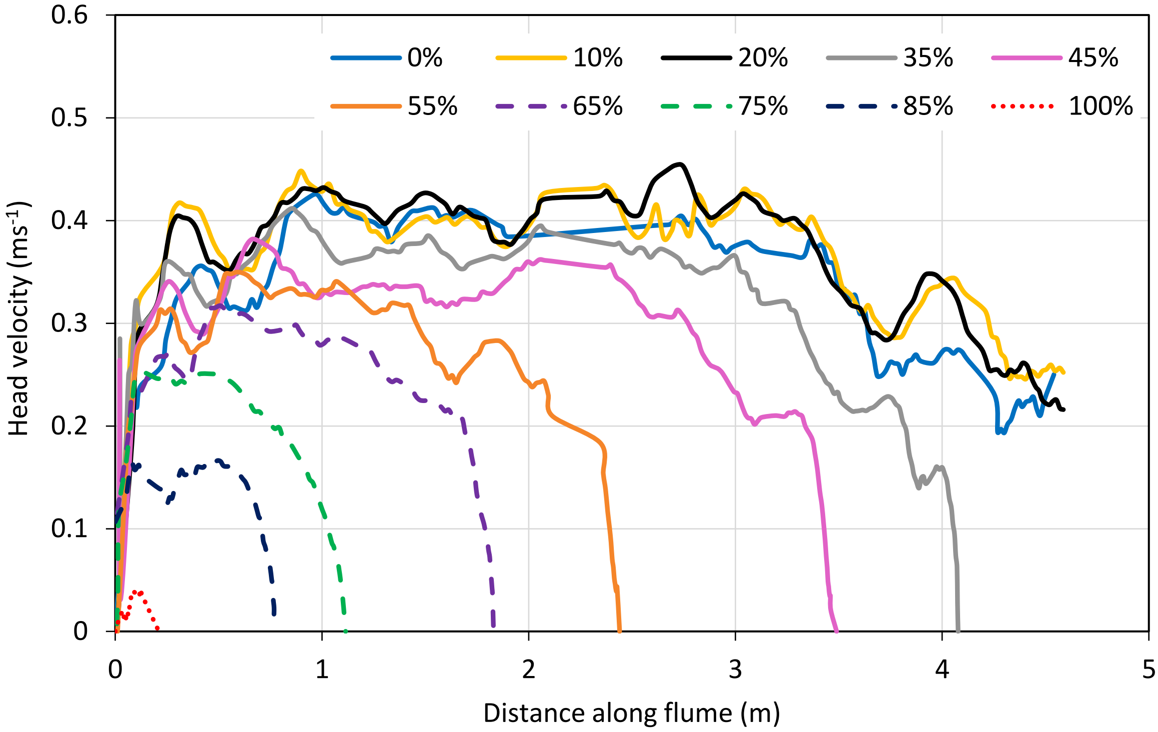

Figure 4.2: Changes in the head velocity of the mixed-clay flows. The different colours denote different C_b values. The dotted, dashed and continuous lines indicate slides, cohesive mud flows and high-density turbidity currents, respectively.

4.3.3 Deposits

All flows with $C_b \geq 35\%$ produced deposits with measurable runout distances that reduced in length from 4.07 m for $C_b = 35\%$ to 0.21 m for $C_b = 100\%$ (Fig. 4.3). The flow deposits were thickest at the back of the reservoir, and the maximum deposit thickness increased with increasing C_b. The deposits of the C_b = 35% and C_b = 45% flows thinned gradually from the back of the reservoir to $x \approx 0.8$ m; hereafter the deposits maintained a constant thickness before terminating with a pronounced leading edge. The 55% $\leq C_b \leq$ 75% flows show pronounced depressions that were 0.01 m to 0.03 m deep between

x = 0.6 m to x = 0.8 m, and thick fronts that ended abruptly. The C_b = 85% deposit reduced steadily in height from the back of the reservoir, but with a rapid reduction in height at the front of the deposit. In contrast, the majority of the C_b = 100% flow deposit stayed within the reservoir rapidly reducing in thickness over 0.21 m to produce a block-shaped deposit (Fig. 4.3).

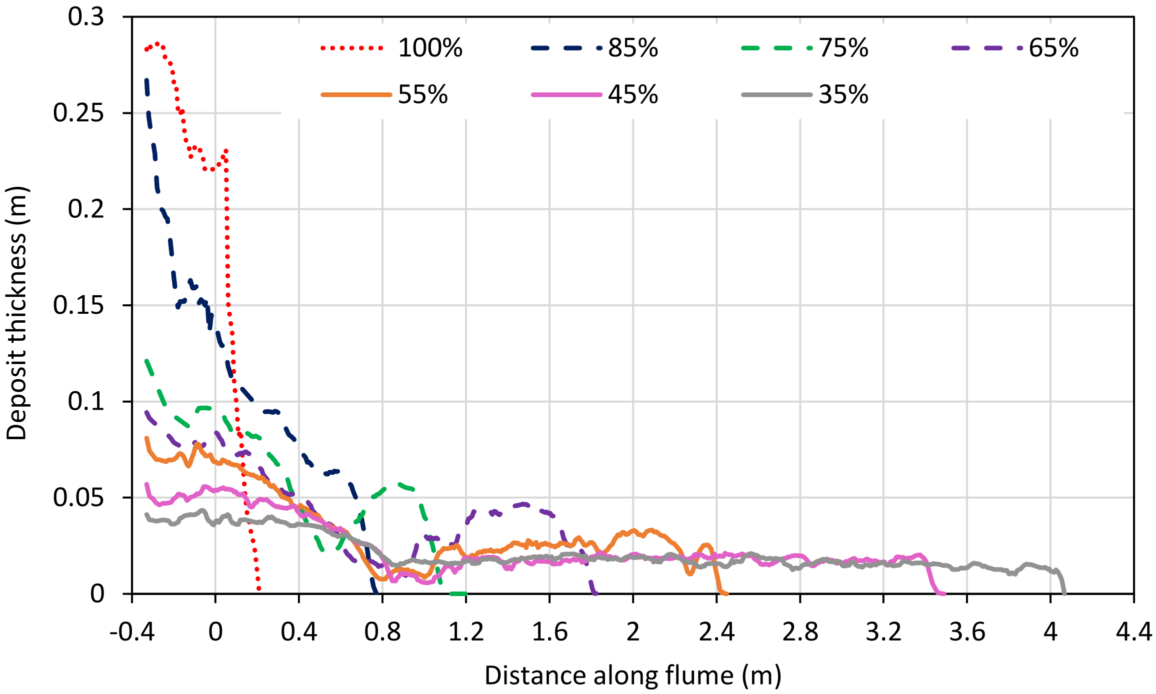

Figure 4.3: Deposit thickness against the distance along the tank for the mixed-clay flows that had measurable runout distances. The dotted, dashed and continuous lines indicate slides, cohesive mud flows and high-density turbidity currents, respectively.

4.4 Rheology results of mixed kaolinite-bentonite suspensions

The rheological characteristics of mixtures of the same composition as the starting suspensions used in the lock-exchange experiments were measured using the oscillatory test, the strain-controlled test, and the stress-controlled test. All three tests produce the yield stress, τ_y, and complex shear modulus, G, of the suspensions. In addition, the stress-controlled test provides the apparent viscosity of the suspensions as a function of strain rate.

All three tests show that τ_y and complex shear modulus reduce from C_b = 0% to C_b = 10%, with the greatest reduction for both variables shown in the oscillatory test (Figs 4.4 and 4.5). The stress- and strain-controlled tests then show a slight increase in the values of τ_y and complex shear modulus from C_b = 10% to C_b = 20%, and for C_b > 20% the two variables increase exponentially with increasing proportion of bentonite in the suspension. In contrast, the τ_y-values from the oscillatory test are constant for C_b = 10% and C_b = 20% and increase only slightly for 20% ≤ C_b ≤ 55%. The τ_y-values do not exceed the yield stress value at $C_b = 0\%$ until $C_b \geq 55\%$. Thereafter, τ_y increases exponentially with increasing proportion of bentonite. The G-values from the oscillatory tests are similar for $C_b = 10\%$ and $C_b = 20\%$. The complex shear modulus then increases exponentially as C_b increases in the same manner as in the stress- and strain-controlled tests (Fig. 4.5).

Figure 4.6 shows the apparent viscosity of the suspensions for a full range of strain rate values. The precision of the measurements is low for shear rates from 10^{-5} to 10^{-4} s^{-1}, creating a lot of scatter on the trend of increasing apparent viscosity with increasing strain rate. At strain rates > 10^{-4} s^{-1}, the apparent viscosity peaks and then reduces at a constant rate with increasing strain rate. The curves for apparent viscosity versus strain rate for $C_b = 0\%$ and $C_b = 10\%$ plot on top of each other, although the maximum apparent viscosity is greater for $C_b = 0\%$ than for $C_b = 10\%$ (Table 4.1). For $C_b \geq 20\%$, increasing the proportion of bentonite in the suspension increases the apparent viscosity at all strain rates (Fig. 4.6). The maximum apparent viscosity increases exponentially with increasing C_b (Fig. 4.7).

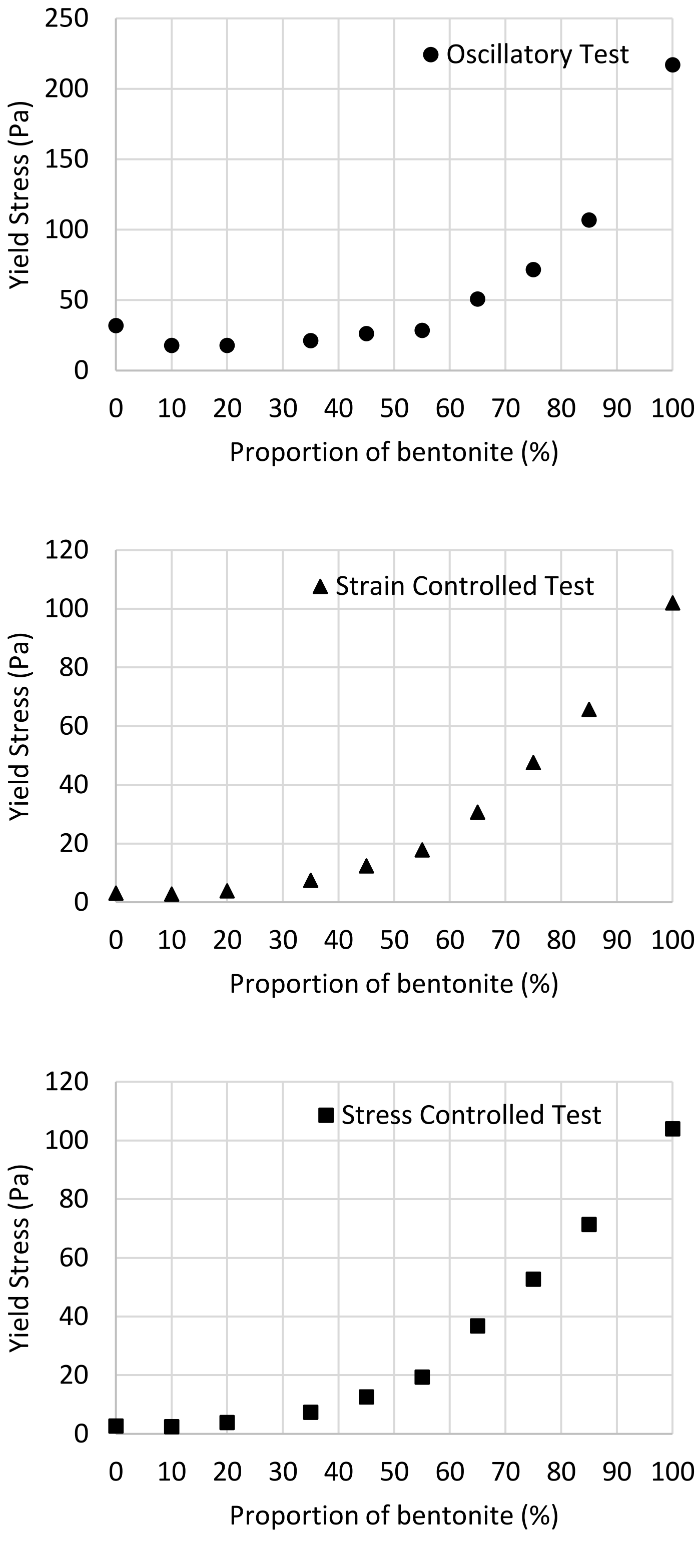

Figure 4.4: Yield stress of the suspensions against the proportion of bentonite in the suspension obtained from the three rheological tests.

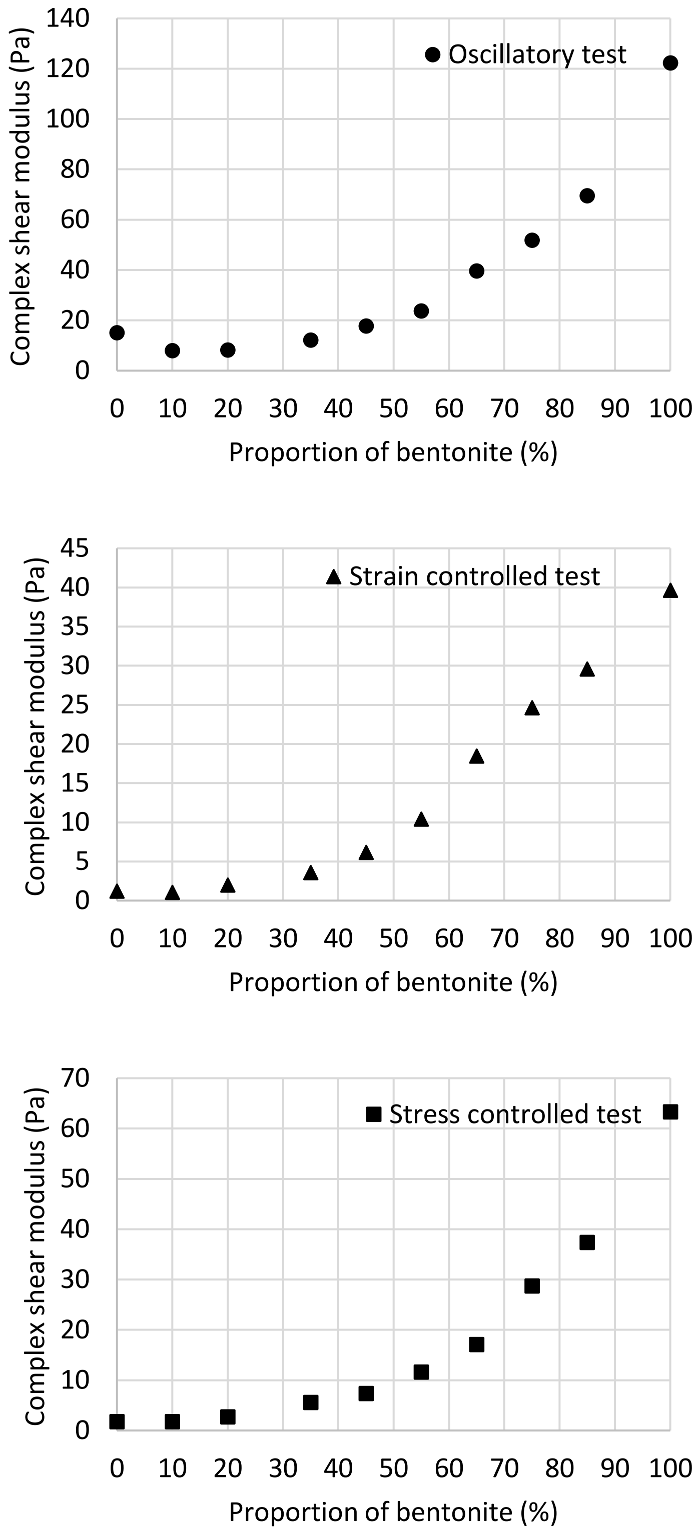

Figure 4.5: Complex shear modulus against increasing proportion of bentonite in the suspension derived from the three rheological tests.

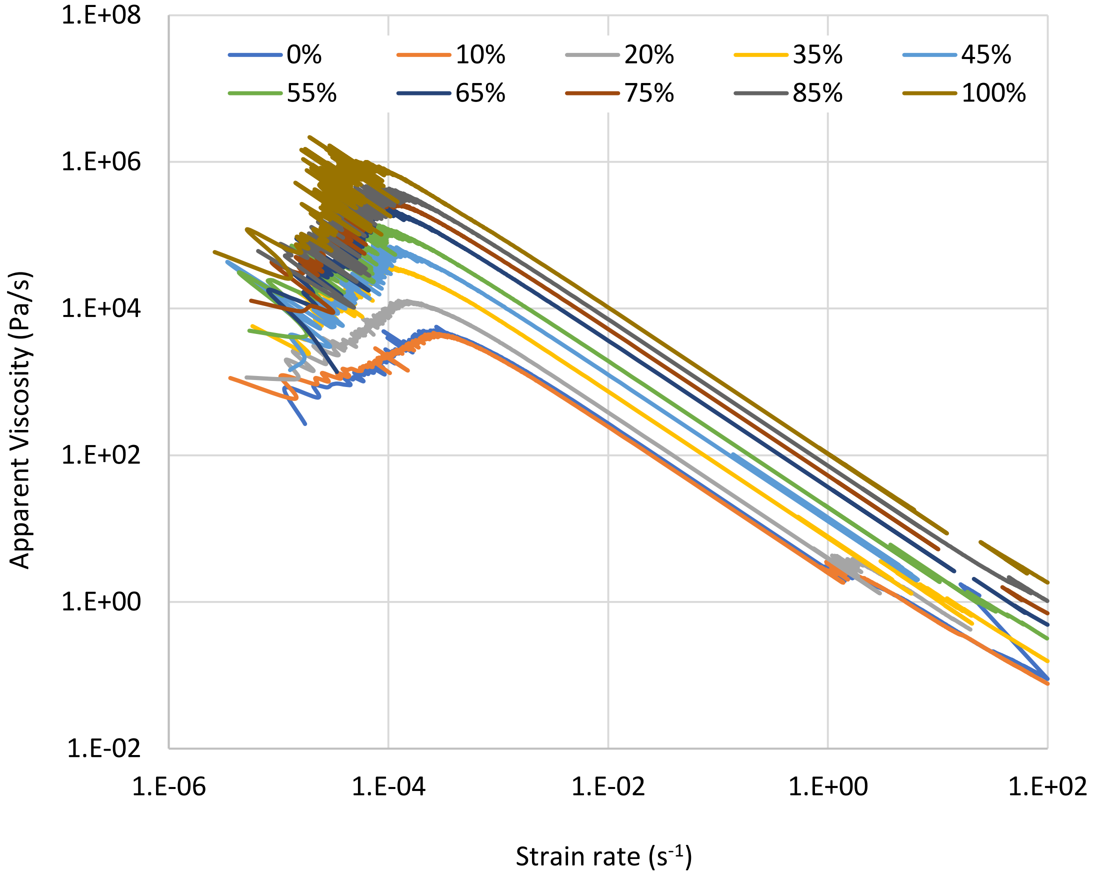

Figure 4.6: Apparent viscosity versus strain rate for the different proportions of bentonite in the suspension, obtained from the stress-controlled test. Line colours indicate different C_b values.

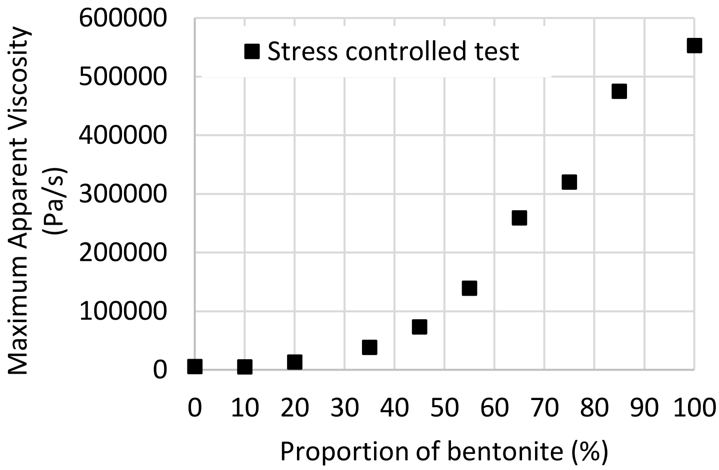

Figure 4.7: The maximum apparent viscosity for the different proportions of bentonite in the suspension obtained from the stress-controlled test.

4.5 Process interpretation of the mixed kaolinite-bentonite flows and deposits

4.5.1 Visual observations

As in Chapter 3, the SGFs can be subdivided into low-density turbidity currents, high-density turbidity currents, mud flows, and slides, all of which have distinctive flow behaviour. The 0% ≤ C_b ≤ 55% flows contained a dense lower zone 1 and a dilute upper zone 2 and are classified as high-density turbidity currents (*sensu* Lowe, 1982). The darker zone 1 has a high concentration as a result of the settling of clay particles near the base of the flow. At these concentrations, the clays can collide, flocculate and form a gel, which supresses the turbulence in this lower zone. The dilute, upper zone 2 forms as a result of shear-induced mixing of sediment with the ambient water. The difference in colour and presence of interfacial waves between the two layers suggests a break in density. As C_b was increased to 55%, the boundary between the two zones became more distinct as zone 2 became progressively lighter, this is because the increasing cohesive forces in zone 1 prevented the bonds between the clay particles from breaking on a large scale.

For the purpose of this study, the high-density turbidity currents can be further subdivided into weak high-density turbidity currents at 0% ≤ C_b ≤ 20% and strong high-density turbidity currents at 35% ≤ C_b ≤ 55% flows. This classification is based on several aspects of the flow behaviour linked to the cohesive strength of the flows. The C_b ≤ 20% flows had semi-elliptically shaped heads, suggesting that these flows did not have enough cohesive strength to resist being streamlined by the hydrodynamic pressure at the front of the flows (Middleton & Hampton, 1973; Britter & Simpson, 1978; Kneller & Buckee, 2000). In contrast, the 35% ≤ C_b ≤ 65% flows had rounded heads and had enough cohesive strength to maintain their shape. The weak high-density turbidity currents did not have enough cohesive strength to initially develop the two-layer structure. The flows containing a proportions of 35% to 55% bentonite had a high enough cohesive strength to resist turbulent mixing from the onset of flow as they formed the two-layer structure upon leaving the reservoir.

All the high-density turbidity currents contained coherent fluid entrainment structures in zone 1. Although these structures might be confined to the sidewall of the flume, their presence suggests zone 1 had a yield stress great enough to limit turbulent mixing of water entrained into the flow. The coherent fluid entrainment structures became more distinct and increased in number from C_b = 0% to C_b = 35%, signifying that the turbulence in zone 1 decreased and water was less readily mixed into the flow. In the strong high-density turbidity currents with C_b = 45% to C_b= 55%, the coherent fluid entrainment structures were thin and scarce, which suggests that the cohesive strength of zone 1 was strong enough to limit their formation. The orientation of the coherent fluid entrainment structures in the high-density turbidity currents is interpreted to mimic dominant flow patterns. Hence, horizontal flow in the strongly cohesive part of zone 1 formed horizontal coherent fluid entrainment structures, and the angled coherent fluid entrainment structures occurred in slightly weaker parts of zone 1 where the water can escape in an upward direction. The featureless zone 1 observed along most of the transport path of the C_b = 55% flow, and in the final flow stages of all the flows with $C_b \leq$ 55%, suggests the cohesive strength of zone 1 was too great for the formation of coherent fluid entrainment structures. The presence of bubbles in the head of the C_b = 45% indicates that water entrained into the flow cannot escape because of the high yield stress of the suspension.

The 0% ≤ $C_b \leq$ 55% and C_b = 75% flows all hydroplaned along part of their flow path. This suggest that: 1) the dynamic pressure of the ambient fluid below the head of the flow exceeded the weight of the flow head (Mohrig *et al.*, 1998); and 2) the permeability at the base of the flow was high enough to stop mixing of the overridden water into flow (Talling, 2013). The C_b = 85% and C_b = 100% flows lacked hydroplaning, presumably because either the flow velocity was too low or the flow weight was too large for the hydrodynamic pressure at the front of the flows to support the head of the flows. It is not clear why the C_b = 65% did not hydroplane, as it was faster and less dense than the C_b = 75% flow which did hydroplane.

The 65% ≤ $C_b \leq$ 85% flows are classified as mud flows. At these bentonite proportions, a strong clay gel is interpreted to have formed. The yield stress of these gels was high enough to fully suppress the turbulence and produce a plug flow. The limited mixing at the upper boundary further confirms that these flows had a high yield stress, which prevented the clay minerals from breaking away from the main body of the flow. The bubbles in the head of the C_b = 65% flow suggests the gel was weak enough to allow some entrainment of water but too strong for the water to mix further into the flow. As described in Chapter 3, the curled head of the C_b = 65% flow may have been shaped by the ambient water moving backward over the top of the head. This created a fold that could be maintained along the flow path because of the high cohesive strength of the flow. The thin, pointed heads of the flows with C_b = 75% and C_b = 85% were cohesive enough to also resist the hydrodynamic forces. Tension cracks formed in all of the cohesive mud flows, and the size and number of the tensions cracks increased as C_b increased. The formation of tension cracks implies that the flows had a high enough yield stress to have tensile strength, and that the flows were placed under tension. The flow containing C_b = 100% is classified as a slide, as the flow left the reservoir as a coherent mass without substantial internal deformation (Martinsen, 1994; Mohrig & Marr, 2003). The vertical tension cracks parallel to flow direction suggests the flow was placed under tension perpendicular to the direction of the flow, as the flow travelled faster in the centre than at the sidewalls of the tank.

4.5.2 Flow velocities

The fixed volume concentration mixed-clay flows had a constant density difference between the suspended sediment and the ambient water upon leaving the reservoir, which controls the flow velocity. Thus, the changes in head velocity can be explained by the balance between the turbulent forces and cohesive forces, which in turn promote and reduce the mobility of the flow. The maximum head velocity increased slightly from C_b = 0% to C_b = 10% and then remained constant from C_b = 10% to C_b = 20% (Fig. 4.8A). This suggests that the turbulence forces driving the flow increased marginally from C_b = 0% to C_b = 10% and remained constant for the flows carrying C_b = 10% and C_b = 20%. The flows with C_b > 20% showed a reduction in the maximum head velocity as the proportion of bentonite in the flow increased (Fig. 4.8A). This reduction in maximum head velocity is interpreted to result from the cohesive forces increasingly dampening the turbulent forces, resulting in the bulk settling of the clay gel and reducing the head velocity. Flows with C_b = 35% to C_b = 100% all exhibited a rapid deceleration to zero velocity in their final flow stages (Fig. 4.2). This can be attributed to the positive feedback mechanism described as "cohesive freezing" by Mulder and Alexander (2001) and introduced in Chapter 3. Cohesive freezing is interpreted to occur in these experiments because of a reduction in the head velocity, which decreases the turbulent forces and allows the clay minerals to form a greater number of electrostatic bonds and increase the cohesive strength of the flows. This in turn further reduces the turbulence and results in a rapid further reduction in the head velocity of the flows. This deceleration process repeats itself until the flow swiftly comes to a halt.

4.5.3 Deposits

The runout distance of the $C_b \geq 35\%$ flows show an inverse, linear relationship with the proportion of bentonite in the flow (Fig. 4.8B, R^2 = 0.97). This agrees with the above-mentioned increasing dominance of cohesive forces as the percentage of bentonite in the flow increased, causing the bulk settling of the flows to occur progressively closer to the lock gate. As in Chapter 3, the high-density turbidity currents, mud flows and slides produced different deposit shapes. The $35\% \leq C_b \leq 45\%$ high-density turbidity currents deposits were wedge-shaped with a block-shaped extensions (Fig. 4.3). This shape is interpreted to have resulted from cohesive forces encouraging rapid settling of the flow close to the reservoir, whilst the turbulent forces were able to move part of the flows further into the flume to produce the consistent block-shaped extension. The $65\% \leq C_b \leq 75\%$ mud flow deposits contained characteristics depressions (Fig. 4.3), most likely resulting from the head of the flow hydroplaning and accelerating away from the body of the flow, as observed by Elverhøi *et al*. (2005). However, the head of the C_b = 65% did not hydroplane, suggesting another mechanism may have produced these deposits. The C_b = 55% flow behaved as a high-density turbidity current, but the deposit of this flow contained a depression as well as a block-shaped extension, demonstrating components of both high-density turbidity current deposits and mud flow deposits and thus a sliding scale between SGF deposit characteristics. The C_b = 85% and C_b = 100% flows travelled only a short distance from the reservoir as rigid plugs and thus produced the wedge-shaped deposits observed (Fig. 4.3).

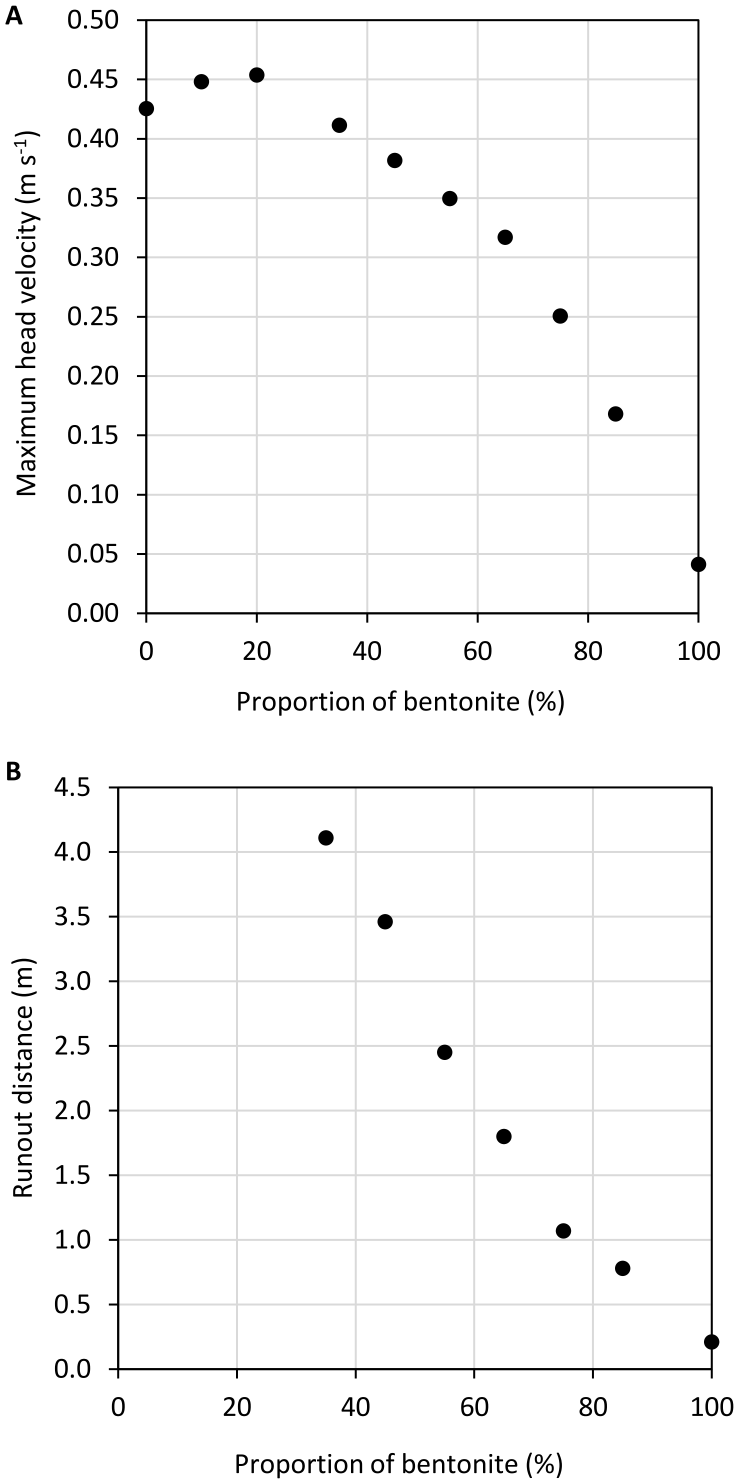

Figure 4.8: (A) Maximum head velocity and (B) runout distance against the proportion of bentonite within the flow.

4.6 Discussion

4.6.1. Effect of clay mineral mixture on suspension rheology, flow behaviour, head velocity and runout distance

In general, the experimental data show that the flow mobility reduces as C_b is increased. This is expressed by a progressive reduction in maximum head velocity at $C_b > 20\%$ and progressively shorter runout distances at $C_b \geq 35\%$ (Fig. 4.8). The flow type also changed from weak HDTC, via strong HDTC and mud flow, to slide, as C_b increased, suggesting an increasing dominance of cohesive forces over turbulent forces. All these high-density clay flows formed a gel in their dense lower layer, defined as a volume-filling network in which all the clay minerals are connected by attractive bonds (Lowe & Guy, 2000; Baas *et al.*, 2009; Ali & Bandyopadhyay, 2016). The observed reduction in flow mobility, as progressively more kaolinite is replaced by bentonite, results from the ability of the strongly cohesive bentonite minerals to increase the cohesive forces in the clay gel and dampen the turbulent forces that drive the flow. The rheological data provide direct evidence for increasing cohesive strength in the starting suspensions with greater C_b, demonstrated by the increasing yield stress, complex shear modulus, and apparent viscosity of the $C_b \geq 20\%$ suspensions in the strain- and stress-controlled tests and of the $C_b \geq 55\%$ suspensions in the oscillatory test (Figs 4.4 to 4.7). These rheological trends match previous work on mixed kaolinite-bentonite suspensions at fixed volume concentrations. At low volume concentrations of *c.* 2% and 0.1%, Kasperski *et al.* (1986) and Keren (1989) found that replacing kaolinite with bentonite increased the apparent viscosity of the suspensions. At the other extreme of very high volume concentrations, replacing kaolinite with bentonite in kaolinite-bentonite pastes increases the liquid limit, defined as the water content at which material changes from plastic to liquid state (Lagaly, 1989; Grabowska-Olszewska, 2003; Karunaratne *et al.*, 2014). At volume concentrations of *c.* 6% Au and Leong (2013) found increasing the proportion of bentonite increased the yield stress of the suspensions.

Increasing the proportion of bentonite in the suspensions increases their cohesive strength by increasing the strength and number of inter-particle bonds within the clay gels. Bentonite is a strongly cohesive clay mineral owing to its small size, large specific surface area and high cation exchange capacity (Yong *et al.*, 2012). Thus, when bentonite is added to the suspension in place of weakly cohesive kaolinite, the strength of the inter-particle forces increases, producing larger yield stress values of the suspensions (Lagaly, 1989; Au & Leong, 2013). Adding bentonite also increases the number of inter-particle bonds in the gels as bentonite swells and delaminates, increasing the particle concentration. The distinctive swelling of bentonite occurs because of adsorption of water into the interlayer space in the clay minerals. This allows the minerals to expand and swell to 10 times their dry volume (Murray, 1991; Au & Leong, 2013). If the interlayer spacing expands greatly, the bentonite layers are able to delaminate into individual or thin packets of silicate layers (Fig. 4.9; Lagaly & Ziesmer, 2003). The increased particle concentration by delamination of the bentonite will result in a greater number of particle-particle bonds within the gel structure, strengthening it and increasing the yield stress (Au & Leong, 2013). Delamination will also increase the strength of the particle-particle interaction, as delamination reduces the particle size and increases the specific surface area (Au & Leong, 2013). The replacement of weakly cohesive kaolinite by strongly cohesive bentonite may also strengthen the microstructure arrangements of the suspensions. The microstructure of bentonite-kaolinite mixtures has been inferred to change from a "card-house" structure to a "card-pack" structure, as bentonite is increased (Lagaly, 1989). This change in the microstructure is expected to increase the yield stress of the suspension (Lagaly, 1989; Nasser & James, 2009; Ndlovu *et al.*, 2011).

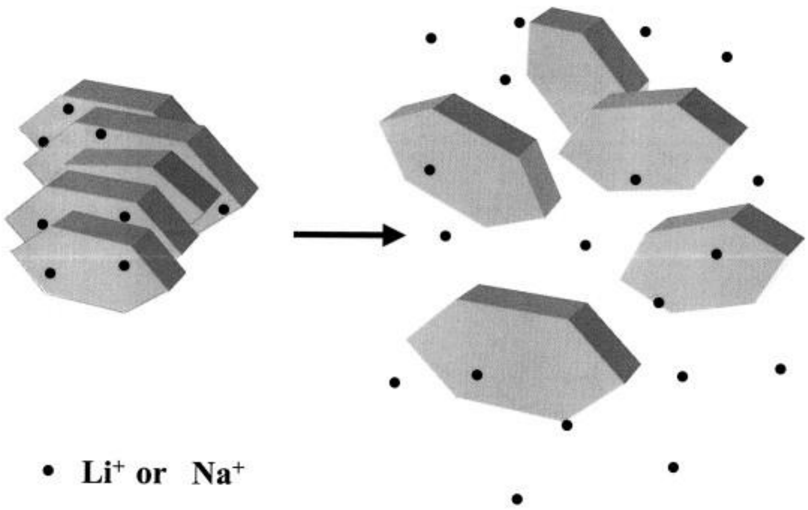

Figure 4.9: Example of bentonite delamination. From Lagaly and Ziesmer (2003).

It is unexpected that the maximum head velocity of the SGFs increases as the proportions of kaolinite and bentonite change from C_b = 0% to C_b = 10% and only starts to decrease at C_b > 20% (Fig. 4.8). This is matched by a reduction in the yield stress, complex shear modulus, and apparent viscosity from C_b = 0% to C_b = 10% for all three rheology tests (Figs 4.4 to 4.7). These two independent tests on the strength of the clay suspension suggest that adding a small amount of bentonite to a kaolinite-dominated suspension reduces the strength of the clay gel, which was unexpected given the strongly cohesive properties of bentonite. The strength of a clay gel is controlled not only by the strength of the particle-particle interactions but also by the microscopic arrangements of the platelets in the gel (Laxton & Berg, 2006; Ndlovu *et al.*, 2011; Ali & Bandyopadhyay, 2016). These experimental results suggest that a small amount of bentonite within a predominately kaolinite gel reduces the gel strength by either reducing the strength or number of the inter-particle forces or changing the microstructure arrangement of the platelets. More research is needed to verify the particle configuration and inter-particle forces within mixed kaolinite and bentonite suspensions (Au & Leong, 2013).

The reduction in yield stress as the proportions of kaolinite and bentonite change from C_b = 0% to C_b = 10% may be related to the change in the pH of the suspensions from an acidic pH of 4.3 at C_b = 0% to a neutral pH of 7.1 at C_b = 10% (Table 4.1). The pH further increases as bentonite replaces kaolinite and the pure bentonite suspension had a pH of 8.2. These pH changes from pure kaolinite to pure bentonite match those cited in the literature (Keller & Matlack, 1990; Kaufhold *et al.*, 2008; Au & Leong, 2013). The pure kaolinite suspension has an acidic pH because of deprotonation reactions on the octahedral Al-OH sites and the tetrahedral Si-OH sites (Tombácz & Szekeres, 2006) . In contrast, the pure bentonite suspension has an alkaline pH because of two processes: 1) the hydrolysis of bentonite causes an exchange of Na^+ for H^+, which leaves an OH^- in solution and thus increases the pH, and 2) adsorption of H^+ onto the surfaces of the bentonite laminae (Kaufhold *et al.*, 2008).

The pH of clay suspensions is an important control on the clay mineral interaction, particularly for kaolinite because the surface charge on kaolinite particle faces is pH dependent (Cruz *et al.*, 2013). The faces of the kaolinite particles are permanently negative, whereas the charge on the edges of kaolinite particles are positive under acidic conditions and negative under neutral to alkaline conditions, because of the adsorption of hydrogen ions and hydroxyl groups, respectively (Tombácz & Szekeres, 2006; Au & Leong, 2013). The increase in pH of the suspension from pure kaolinite to mixed kaolinite-bentonite at C_b = 10% could cause some or all of the kaolinite edges to become negatively charged. This could change the dominant particle interactions from strong Coulomb attraction between the positive edges and the negative faces of the kaolinite particles to weaker van der Waals attraction between the fully negatively charged kaolinite particles, thus reducing the yield stress of the C_b = 10% suspension (Nasser & James, 2009). Further increasing the proportion of the bentonite in the suspension above C_b = 10% may then increase the yield stress of the suspension via increasing the strength and number of inter-particle forces, as described above. This change in the dominant particle interactions for kaolinite particles needs to be confirmed by scanning electron microscopy (Ali & Bandyopadhyay, 2016).

4.6.2 Predictive equations for pure-clay flows applied to the mixed-clay flows

In Chapter 3, dimensional analysis of the pure-clay flows showed that the yield stress of the suspensions can be used to predict the dimensionless maximum head velocity and the runout distance of the flows. Below, it is investigated if the yield stress of the pure-clay suspensions can be used to predict the yield stress of the mixed-clay suspensions. The predicted and measured yield stress values of the mixed-clay suspensions are then used to test the accuracy of the predictive equations for maximum head velocity and runout distance of the mixed-clay flows.

4.6.2.1 Predicting the yield stress of the mixed-clay suspensions

For the individual clay flows, the yield stress, τ_y, was calculated from the suspended-clay concentration, C

$$\tau_{y,i} = \tau_{y,m} \left(\frac{C_i}{C_{m,i}}\right)^3, \qquad \text{for } 0 < C_i \leq C_{m,i} \tag{4.1a}$$

$$\tau_{y,i} = \tau_{y,m} + \left(\tau_{y,0} - \tau_{y,m}\right)\left(\frac{C_i - C_{m,i}}{C_{0,i} - C_{m,i}}\right)^3, \qquad \text{for } C_{m,i} < C_i \leq C_{0,i} \tag{4.1b}$$

Where C_m is the concentration at which the flows reach their maximum head velocity, $U_{h,m}$. Subscript i represents either kaolinite, k, or bentonite, b, and $C_{m,k}$ = 22% and $C_{m,b}$ = 16% (see Chapter 3 for details). Below C_m and $U_{h,m}$ the flows are driven by the density difference with the ambient fluid. Flows with C-values above C_m are driven by the cohesive forces in the flow. $\tau_{y,m}$ is the estimated yield stress where the head velocity, U_h, equals $U_{h,m}$ and the concentration, C, equals C_m, and has a value of 37.9 Pa, as shown in Chapter 3. $\tau_{y,0}$ and $C_{0,i}$ are the yield stress and the concentration above which the clay suspensions do not leave the reservoir: $\tau_{y,0}$ = 271 Pa, $C_{0,k}$ = 30.5%, and $C_{0,b}$ = 20.5%.

To investigate if the yield stress values of the mixed-clay suspensions can be predicted from the yield stress values of the pure-clay suspensions, two different methods were explored. Method 1 assumes no interaction between the clay minerals, comprising of the linear addition of the yield stress of the kaolinite fraction and the bentonite fraction of the mixed-clay suspension. For example, the yield stress of a 20% flow with 85% kaolinite and 15% bentonite is calculated as the yield stress of a 17% kaolinite suspension plus the yield stress of a 3% bentonite suspension. Method 1 is simple, but it underestimates the yield stress of the mixed-clay suspension, especially at 20% < C_b ≤ 90% (Fig. 4.10). The yield stress of a suspension is determined by the strength, number, and microstructure arrangement of attractive forces between particles (Laxton & Berg, 2006). The linear addition method might not capture all attractive forces in the suspension, because it does not account for the non-linear increase in the number of inter-particle bonds with concentration. This is demonstrated by the fact that the addition of 17% bentonite suspension yield stress and 3% bentonite suspension yield stress does not equal the yield stress of a 20% bentonite suspension. It is encouraging in this respect that for kaolinite-rich suspensions (C_b ≤ 10%) and pure bentonite suspensions (C_b = 100%) the linear method predicts the yield stress more accurately than for 20% ≤ C_b ≤ 90% (Fig. 4.10).

Method 2 uses a non-linear method to predict the yield stress of the mixed-clay suspension. This method uses Equation 4.1 to calculate a new total concentration for each clay mineral mixture equivalent to either a pure kaolinite or a pure bentonite suspension. This “equivalent concentration” method requires several computational steps. To calculate an equivalent bentonite concentration of a mixed-clay flow, first the yield stress for the kaolinite fraction in the mixture is determined using Equation 4.2 (taken from Equation 4.1)

$$\tau_{y,k} = \tau_{y,m} \left(C_k/C_{m,k}\right)^3 , \qquad \text{for } 0 < C_k \leq C_{m,k} \tag{4.2a}$$

$$\tau_{y,k} = \tau_{y,m} + \left(\tau_{y,0} - \tau_{y,m}\right)\left(\frac{C_k - C_{m,k}}{C_{0,k} - C_{m,k}}\right)^3 , \qquad \text{for } C_{m,k} < C_k \leq C_{0,k} \tag{4.2b}$$

Equation 4.1 can then be rearranged to determine the bentonite concentration, $C_{b=k}$, equivalent to $\tau_{y,k}$

$$C_{b=k} = C_{m,b}\left(\frac{\tau_{y,k}}{\tau_{y,m}}\right)^{\frac{1}{3}} , \qquad \text{for } 0 < \tau_{y,k} \leq \tau_{y,m} \tag{4.3a}$$

$$C_{b=k} = C_{m,b} + \left(C_{0,b} - C_{m,b}\right)\left(\frac{\tau_{y,k} - \tau_{y,m}}{\tau_{y,0} - \tau_{y,m}}\right)^{\frac{1}{3}} , \qquad \text{for } \tau_{y,m} < \tau_{y,k} \leq \tau_{y,0} \tag{4.3b}$$

Subsequently, a new total concentration, $C_{b,total}$, is determined by adding the calculated equivalent bentonite concentration to the original bentonite concentration

$$C_{b,total} = C_{b=k} + C_b \tag{4.4}$$

Finally, the yield stress of the flow is determined using Equation 4.1 and the new concentration of the mixed-clay flow calculated as if it is a pure bentonite flow, using $C_{0,b}$ and $C_{m,b}$. Equivalent kaolinite concentrations were calculated in a similar way.

Figure 4.10 demonstrates that at low proportions of bentonite the equivalent bentonite concentration and equivalent kaolinite concentration methods produce similar yield stresses, which are above the measured yield stresses. For $C_b \geq 55\%$, the predicted yield stresses diverge slightly and the equivalent bentonite concentration method gives slightly higher yield stresses, and the equivalent kaolinite concentration slightly lower yield stresses, than the yield stress values measured with the rheometer. The differences between the equivalent bentonite concentration and equivalent kaolinite concentration methods are due to the kaolinite and bentonite specific constants ($C_{0,i}$ and $C_{m,i}$). Both equivalent concentration methods do a good job of predicting the measured yield stress values. The slight differences between the measured yield stress and the equivalent concentration method yield stress values may be because this method does not capture the interaction between the kaolinite and bentonite particles. The bentonite-kaolinite interactions are complex and the effect these interactions may have on the yield stress is not fully understood (Au & Leong, 2013).

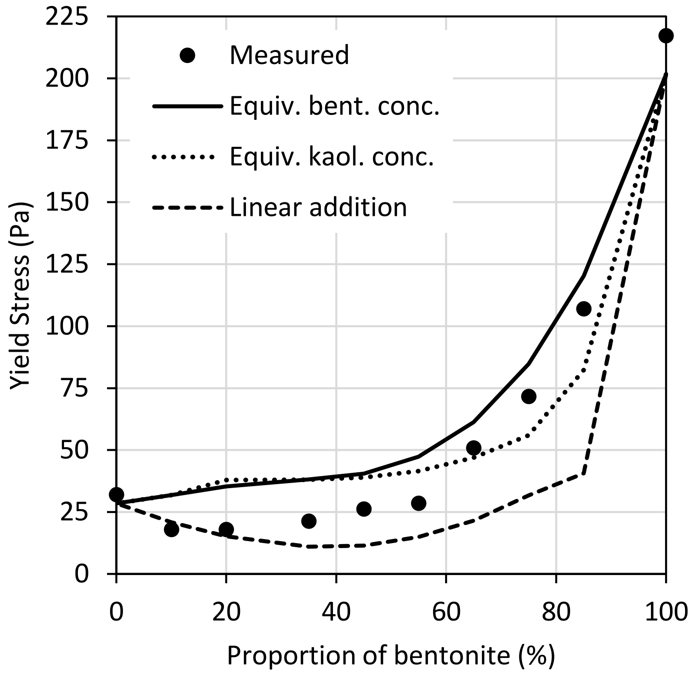

Figure 4.10: Predicted yield stress of the mixed-clay suspensions (curves) compared to measured yield stress (black dots). The dashed line is based on the linear addition of the yield stress values of the constituent clay minerals of the mixture. The solid and dotted lines show the yield stresses calculated from equivalent bentonite concentrations and equivalent kaolinite concentrations, respectively. See text for full explanation of the predictive yield stress methods.

4.6.2.2 Predicting the maximum head velocity and runout distance of the mixed-clay flows

The yield stress values calculated from the linear and non-linear methods described above can be used to predict the maximum head velocity and the runout distance of the mixed-clay flows, using Equations 3.4 and 3.9 presented in Chapter 3. The maximum head velocity calculations require the highest maximum head velocity, $U_{h.m,i}$, where *i* denotes kaolinite, *k*, or bentonite, *b*: $U_{h.m,k}$ = 0.50 m s^{-1} and $U_{h.m,b}$ = 0.37 m s^{-1}. The highest maximum head velocity for the mixed-clay flows, $U_{h.m,w}$, was estimated as a weighted sum, based on the volume concentration of kaolinite, C_k, and bentonite, C_b, in the mixed-clay flows

$$U_{h,m,w} == \frac{U_{h,m,k}C_k + U_{h,m,b}C_b}{20} \tag{4.5}$$

$U_{h.m,w}$ was then used in the following equations to calculate maximum head velocity, $U_{h,m}$, from the yield stresses

$$U_h = U_{h,m,w}\left(\frac{\tau_y}{\tau_{y,m}}\right)^{\frac{1}{6}}, \text{ for } 0 < \tau_y \le \tau_{y,m} \tag{4.6a}$$

$$U_h = U_{h,m,w}\frac{\tau_{y,0} - \tau_y}{\tau_{y,0} - \tau_{y,m}}, \text{ for } \tau_{y,m} < \tau_y \le \tau_{y,0} \tag{4.6b}$$

The runout distances of the flows, x_0, were calculated using:

$$x_0 = x_{0,m}\left(1 - \frac{2}{3}\left(\frac{\tau_y}{\tau_{y,m}}\right)^{\frac{1}{2}}\right), \text{ for } 0 \le \tau_y \le \tau_{y,m}, \tag{4.7a}$$

$$x_0 = \frac{1}{3}x_{0,m}\left[1 - \left(\frac{\tau_y - \tau_{y,m}}{\tau_{y,0} - \tau_{y,m}}\right)^{\frac{1}{3}}\right], \text{ for } \tau_{y,m} \le \tau_y \le \tau_{y,0}, \tag{4.7b}$$

where $x_{0,m}$ = 11.35 m is the maximum runout distance of the experimental flows, based on the average of 11.4 m for the pure kaolinite flows and 11.3 m for the pure bentonite flows, as in Chapter 3.

The predicted maximum head velocities and runout distances are compared to the measured maximum head velocities in Figure 4.11 to assess the suitability of Equations 4.6 and 4.7 for the mixed-clay flows. This comparison uses four relationships between yield stress and C_b, based on the linear addition method, the equivalent bentonite and kaolinite concentration methods, and the measured data (Fig. 4.10). Figure 4.11 shows that the linear addition method poorly predicts the maximum head velocity of the mixed-clay flows, probably because this method underpredicts the yield stress of the mixed-clay suspensions, causing anomalously high maximum head velocities in the bentonite-rich flows.

The nonlinear methods of equivalent bentonite and equivalent kaolinite concentration correctly predict the shape of the curve of maximum head velocity against proportion of bentonite, except from C_b = 0% to C_b = 20%, where the nonlinear methods fail to predict the increase in maximum head velocity. Both methods overpredict the yield stress at $C_b \le$ 55% and this results in overprediction of the maximum head velocity values, because these yield stresses are close to $\tau_{y,m}$= 37.9 Pa, where U_h = $U_{h,m,w}$. The predictive equations are particularly sensitive to the weighted sum method used to estimate $U_{h,m,w}$ in Equation 4.5, as this value can change the shape and height of the curve. For $C_b \ge$ 45%, the $U_{h,m}$-values predicted by the equivalent bentonite concentration method remain closer to the measured $U_{h,m}$-values than for the equivalent kaolinite concentration method, because the larger yield stresses for the equivalent bentonite concentration method result in lower predicted head velocities (Equation 4.6B). Both equivalent concentration methods predict the runout distances of the mixed-clay flows reasonably well, but the gradient of the C_b-x_0 curves are somewhat lower than for the measured runout distances.

The measured yield stresses poorly predict the runout distances for $C_b < 65\%$ (Fig. 4.11). The yield stresses from the oscillatory test are low at $20\% \leq C_b \leq 55\%$, but not much lower than the yield stresses predicted by the equivalent concentration methods (Fig. 4.10), which produce much better runout distance predictions (Fig. 4.11). Critically, the measured yield stress values for $C_b < 65\%$ are lower than $\tau_{y,m}$, which equals 37.9 Pa, defined as the yield stress below which the flows are driven by their density difference with the ambient fluid (see Chapter 3). This means that for the measured yield stress values at $C_b < 65\%$ the runout distance is calculated using Equation 4.7a, which inherently assumes the flows are primarily controlled and driven by their excess density from its derivations. The results from these experiments imply that at $\tau_y < 37.9$ Pa the mixed-clay flows are still mainly controlled by the cohesive forces in the flow. Perhaps more importantly, the predicted runout distances at these low τ_y values are based on extrapolations (Fig. 3.14), in which runout distance is predicted to rapidly increase with increasing clay concentration. Consequently, small variations in the yield stress may cause large variations in the runout distance predictions for the $C_b < 65\%$ flows. This limitation does not apply to the maximum head velocity predictions. Therefore, the difference in the curves between the maximum head velocity predicted from the measured yield stress values and the maximum head velocity predicted from the equivalent concentration yield stress values for $C_b < 65\%$ may be caused only by the fact that the measured yield stress values predict the maximum head velocity via Equation 4.6a and the equivalent concentration predictions calculate the maximum head velocity via Equation 4.6b (Fig. 4.11A).

When comparing the predictive models, it is evident that the linear addition of the yield stress of the kaolinite fraction and bentonite fraction of the mixed-clay suspension poorly predicts the yield stress, the maximum head velocity, and the runout distance of the flows. In comparison, the equivalent concentration method, where a new total concentration for each clay mineral mixture equivalent to either a pure kaolinite or a pure bentonite suspension is calculated, provides better results. The shapes of the curves for the predicted yield stress and maximum head velocity match the measured data and the runout distance predictions are also in line with the measured runout distances. It appears that the method calculating the equivalent bentonite concentration is slightly closer to the measured data than the equivalent kaolinite concentration. This suggests the bentonite constants ($C_{0,b}$ and $C_{m,b}$) are more appropriate for this dataset. This seems logical as it is apparent that from $C_b > 55\%$ the flow behaviour is strongly controlled by the bentonite proportion. The results derived from using the measured yield stress to predict the maximum head velocity and flow runout distance highlight a shortcoming in the method used in Chapter 3 to predict runout distance at low yield stress values, as well as the sensitivity of the analysis to the method used to divide the predictive equations between density-driven flows and cohesion-driven flows. This shows a limitation of the predictive equations produced in Chapter 3; they utilised the changing relationship between flow concentration and yield stress, but for experiments where the concentration is constant, the yield stress where the flows were interpreted to change from density driven to cohesion driven may not be fully appropriate.

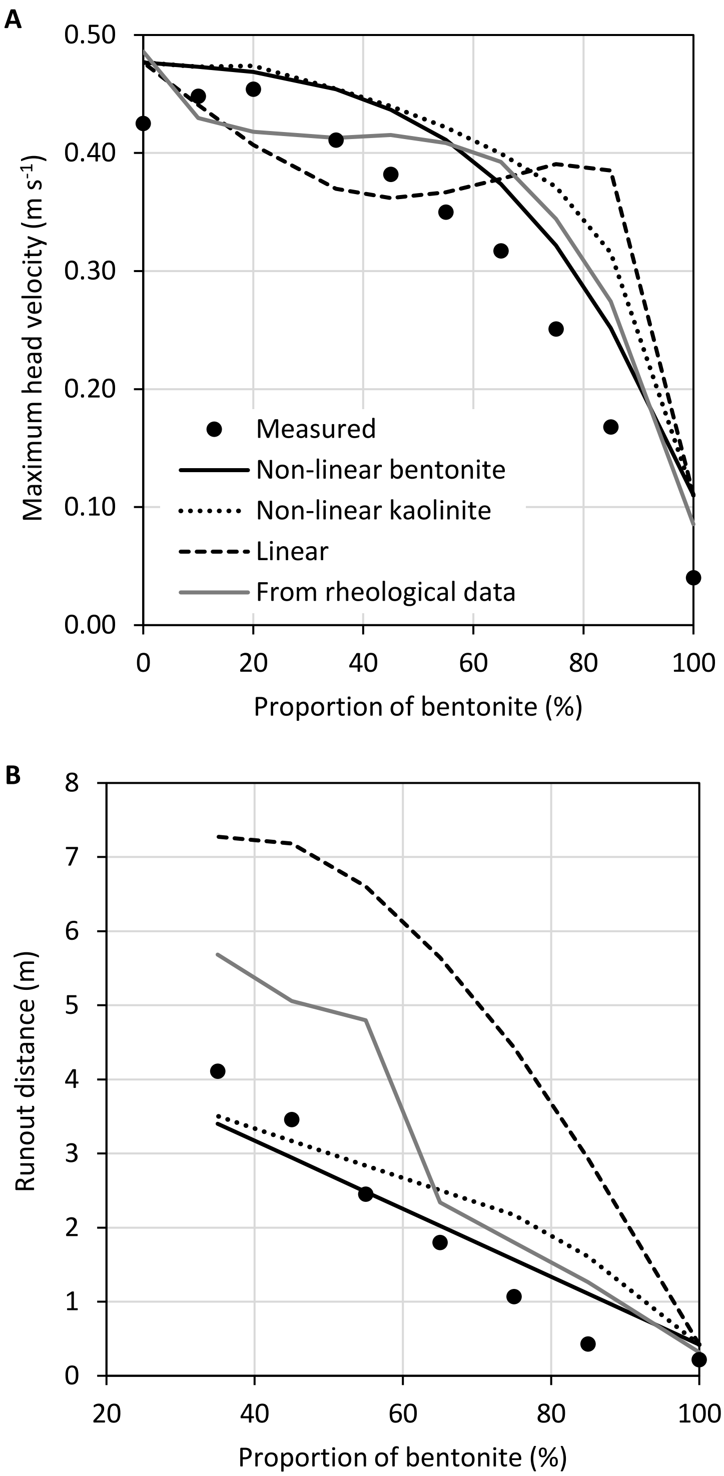

Figure 4.11: (A) Predicted maximum head velocity against the proportion of bentonite (Equation 4.6) and (B) runout distance against the proportion of bentonite (Equation 4.7) for the mixed-clay flows. The different lines represent the different methods for calculating the yield stress explained in Figure 4.10.

4.6.3. Wider implications

This study provides an exciting platform from which the interpretation of the flow dynamics and deposit properties of mixed-clay, high-density cohesive SGFs in the natural environment can be improved. Unfortunately, the experimental results cannot be scaled up quantitatively to predict the flow and deposit characteristics of natural flows, because natural flows can travel at least one or two orders of magnitude faster than the SGFs generated in the laboratory (Talling *et al.*, 2013). Faster flows will generate greater amounts of turbulence. These stronger turbulent forces may break the clay bonds and limit the cohesive forces at the clay concentrations and proportions of clay mineral types shown in these experiments. Thus, the dominance of cohesive forces over turbulent forces is predicted to occur at higher clay concentrations in many natural flows. However, the trends observed in these experiments should still be valid in the natural environment and a qualitative comparison can be made to full-scale, natural SGFs.

The flume experiments presented herein support and expand the results from Chapter 3 in that clay mineral type, as well as clay concentration, control the flow properties and deposits of high-density cohesive SGFs. The rapid transformation in flow behaviour as the proportion of bentonite and kaolinite was changed in the laboratory flows of fixed total volume concentration is additional evidence that knowledge of the clay mineral composition within natural SGFs may be vital for the correct interpretation of the flow and deposit properties.

The experimental mixed kaolinite-bentonite flows highlight how the different cohesive strengths of the clay minerals and the effect of mixing the clay minerals can result in non-linear changes in flow behaviour, when proportions of clay minerals change within the flow. Under the experimental conditions, increasing the bentonite proportion above 35% dramatically reduced the runout distance and head velocity of the flows. When the flows were dominated by kaolinite, changing the bentonite proportion from 0% to 20% had a small effect on the flow behaviour. These results suggest that for suspended-clay concentrations that are equivalent to 20%, once the proportion of strongly cohesive bentonite is 35%, further replacement of weakly cohesive clay by bentonite could result in large changes in flow behaviour. More generally, the results also suggest that mixed-clay flows are sensitive to the most cohesive clay mineral within the flow, once that clay mineral has reached a proportion within the flow that is well below 50%. The second most cohesive clay mineral after bentonite (which is part of the smectite group of clay minerals) is illite. It is likely that illite will have to reach a higher proportion in the flow compared to bentonite to start dominating the flow behaviour. In contrast, chlorite and kaolinite have low cohesive strength, and will reduce the cohesive strength of the flow if they replace bentonite or illite. Future assessment of clay mineral assemblages of submarine fans should focus on full clay mineral assemblages, instead of on the dominant clay type within these assemblages, as the relative proportion of the different clay minerals has a non-linear influence on the cohesive properties of a suspension. Particular attention should be paid to the concentration of strongly cohesive bentonite, as even low proportions of this clay mineral may have a large effect on the flow behaviour.

Changes in the rheology of the mixed-clay suspensions correlated well to changes in the flow behaviour of the mixed-clay cohesive SGFs in the laboratory. It is expected that there will also be a relationship between the rheological properties of natural cohesive SGF suspensions and their flow behaviour. SGFs with high rheological strength are expected to behave as strong high-density turbidity currents, mud flows and slides and have lower mobility than flows of lower rheological strength that behave as weak high-density turbidity currents and low-density turbidity currents. Direct monitoring campaigns may soon allow yield stress to be measured directly from sediment samples of natural SGFs, which would be extremely powerful. For example, direct monitoring of cohesive SGFs at one location – for example, using acoustic backscatter techniques – may record cohesive flows with similar suspended-sediment concentrations, but vastly different flow velocities and runout distances. Hence, suspended-sediment concentration alone may often not be sufficient to predict flow behaviour and deposit properties, the important missing link being yield stress. Sediment samples from within the flows may reveal that different clay mineral compositions, and hence different flow yield stress values, are responsible for the different flow behaviours and deposit styles. Currently, direct monitoring work of SGFs is more likely to sample the deposits of the flows. Reconstructing the flow yield stress from the deposits is challenging as the flow concentration is unknown. It may be possible to interpret the flow type from the deposit style and then construct a flow concentration and yield stress range based on the clay mineral assemblage. This requires further studies across a wider range of mixed clay flow behaviours.

The results in Chapter 4.6.2 demonstrate that the linear addition of the individual yield stresses of the clay minerals within the clay mineral assemblages underestimates the yield stress, as the component concentrations do not properly account for the increased number of interparticle bonds within the full mixed flow. Calculating a new equivalent concentration was more successful, and although this method still requires constants and best-fit coefficients that may be dependent on the experimental setup, predictive equations of natural, mixed clay SGFs using the yield stress of single-clay type suspensions should be possible. This would be powerful, because once the relationship between yield stress and maximum head velocity and runout distance has been understood for natural, cohesive SGFs of a certain clay type, this knowledge may be able to be used to predict the behaviour of mixed clay flows. This would be particularly relevant for geohazard assessment on seafloor networks of cables, pipelines, and other infrastructure, which may be vulnerable to dense, fast cohesive SGFs (Piper *et al.*, 1999; Anthony *et al.*, 2008; Hsu *et al.*, 2008; Zakeri, 2008). Improved equations could be used to predict the maximum head velocity and runout distance of flows within deep-marine basins with sea-floor infrastructure. The deposits of mixed-clay flows may act as seals for reservoir sands. The runout distance of such flows thus govern the areal extent of these deposits. The present experiments show that proportions of highly cohesive clay, such as bentonite, well below 50% may dramatically limit the areal extent of these deposits. However, highly cohesive clay may also increase the areal extent of mixed-clay deposits, if this clay type is present in small proportions (up to 20% of the total assemblage in this study).

4.6.4 Future research

The present experiments can be viewed as the starting point for many additional directions of research related to mixed-clay SGFs. Future experiments ought to include illite and chlorite, which are also common on the modern seafloor (Biscaye, 1965; Griffin *et al.*, 1968). Illite and chlorite are of intermediate cohesive strength between strongly cohesive bentonite and weakly cohesive kaolinite. The present experiments should be repeated with mixed illite and chlorite to determine if the changes in flow behaviour are smaller than for mixed kaolinite and bentonite, which are further apart in terms of cohesive behaviour. Mixtures of three or four clay mineral types may produce nonlinear changes in the flow behaviour and rheology that are different from the changes found in the present study.

The different chemical and physical properties of clay minerals may mean that certain combinations of clay minerals may have a higher or lower yield stress than expected. In some combinations, clay minerals may be able to “work together” and form a greater number or stronger inter-particle bonds, or a stronger microstructure arrangement. Other combinations clay minerals may work against each other and reduce the strength and number of attractive bonds or weaken the gel microstructure. Future work should focus on understanding the yield stress of a larger combination of clay mineral mixtures than presented in this study. Cryogenic scanning electron microscopy should be used to visualise the microscopic structures formed, and may help interpret the rheological data (Ali & Bandyopadhyay, 2016).

Direct monitoring of SGFs is a new method that can directly link the flow behaviour to the deposit properties. As technological advances in this field continue to improve, equipment will soon be able to record the velocity, concentration, mineralogical composition, and grain-size profiles of natural SGFs and collect sediment cores of the corresponding deposits (Talling *et al.*, 2015). These types of data are vital to understanding the balance of turbulent and cohesive forces within natural, cohesive SGFs. Direct monitoring will help understanding of how laboratory experiments of clay-rich SGFs scale up to the natural environment. Future direct monitoring studies of mud-rich SGFs should focus on trying to collect suspended sediment samples, from which the yield stress and the mineralogical composition of the flow can be measured. This information may be key in understanding mud-rich SGF behaviour.

4.7 Conclusions

The present experiments show that increasing the proportion of strongly cohesive bentonite above 20% in a mixed kaolinite-bentonite sediment gravity flow with a fixed 20% volume concentration reduces the flow mobility. This was demonstrated by an increase in the yield stress, complex shear modulus, and apparent viscosity of the starting suspension, a reduction in the head velocity, and a reduction in measurable runout distance. The flow behaviour also changed from weak high-density turbidity current, via strong high-density turbidity current and cohesive mud flow to slide as the bentonite proportion was increased from 0% to 100%. These changes in flow behaviour and rheology are interpreted to result from a greater number and strength of inter-particle bonds within the clay gels. At bentonite proportion of 10%, the yield stress, complex shear modulus, and apparent viscosity measurements of the suspension reduced slightly, and the flow had a higher maximum head velocity, than the pure kaolinite flow. This suggests that adding a small amount of bentonite reduces the cohesive strength of the mixed-clay suspension by either reducing the strength or number of the inter-particle bonds or changing the microstructure arrangement.

The changes in the rheology of the mixed-clay suspensions correlate with the changes in the maximum head velocity and runout distance. This suggests that rheological parameters may be powerful for predicting the flow behaviour and deposit properties of natural cohesive sediment gravity flows. For the laboratory flows, the method of predicting the yield stress of the mixed-clay flows by calculating the yield stress of an equivalent pure-clay suspension produced good predictions of the yield stress, maximum head velocity and runout distance of the mixed-clay flows. A full understanding of how the cohesive forces within natural cohesive sediment gravity flows change with clay mineral assemblage is important for the correct interpretation of the deposits of these flows in the modern environment and in the geological record.

5. Flow mobility of mixed sand-clay sediment gravity flows

5.1. Introduction

Chapter 3 considered the changes in flow behaviour, rheology and deposit properties for pure-clay flows in terms of increasing clay concentration, but in the natural environment sediment gravity flows (SGFs) commonly consist of a mixture of sand, silt and clay (Reading & Richards, 1994; Marr *et al.*, 2001; Talling *et al.*, 2004; Amy *et al.*, 2006). It is therefore relevant and interesting to consider how pure-clay flows may change with the addition of non-cohesive sediment, such as sand. For low-density cohesive SGFs dominated by turbulence, it is expected that the addition of sand will increase the density difference and therefore the flow velocity, provided the sand can be kept in suspension (Middleton, 1966). However, for high-density cohesive SGFs controlled by cohesive forces *e.g.*, high-density turbidity currents, mud flows and slides, the addition of sand to the flow is expected to be more complex as it is not known how the dynamic balance between turbulent and cohesive forces may change.

The purpose of this chapter is to investigate how the addition of non-cohesive sand changes the behaviour of high-density cohesive SGFs, to help better understand their flow dynamics and deposits in the natural environment. Specifically, this work contrasts how increasing the volume concentration of a bentonite-laden cohesive SGF by 25% from adding either fine sand or bentonite clay changes the flow rheology, flow behaviour and deposits, via laboratory experiments. Two flows classified as high-density turbidity currents from Chapter 3 and containing 14.4% and 16% bentonite were selected as the pure clay controls to which 3.6% and 4% of fine sand or clay were added. These control high-density turbidity currents are at the top of the maximum head velocity against flow concentration curve (Fig. 5.1), where the turbulent forces driving the flow and the cohesive forces limiting flow mobility are finely balanced. The experiments investigated how increasing the volume concentration by adding 25% of sand or clay changes the balance between the turbulent and cohesive forces in these flows. This chapter aims to answer the following specific questions:

1. How does increasing the volume concentration by 25% from the addition of sand change the flow behaviour, flow velocity, runout distance, and deposit geometry of high-density cohesive SGFs, compared to adding an equal amount of clay?
2. How does the addition of 25% volume concentration of sand change the yield stress of the 14.4% and 16% bentonite suspensions, and what are the physical explanations for any observed changes?
3. Based on these experiments, what are the inferred changes in flow mobility from the addition of 25% volume concentration of sand or clay to cohesive SGFs across the full range of flow concentrations?
4. What are the potential implications of these results for natural sediment gravity flows and their deposits?

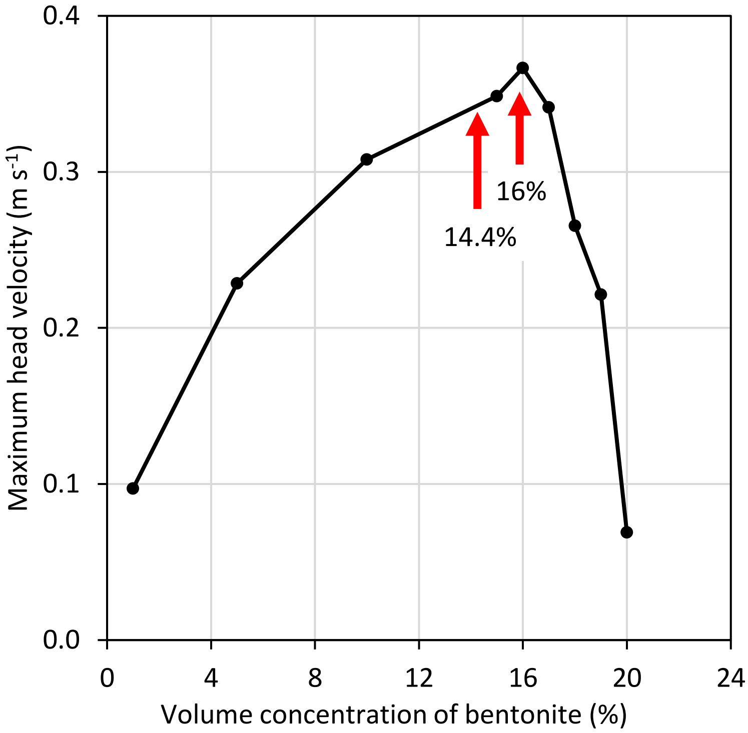

Figure 5.1: Maximum head velocity against the volume concentration of bentonite from the laboratory experiments in Chapter 3. The arrows point to 14.4% and 16% volume concentration, which were the initial flow concentrations to which the new flows with a 25% increase in volume concentration from the addition of fine sand were compared to.

5.2 Methods

5.2.1 Lock-exchange experiments

Two mixed bentonite-sand SGFs were generated using the methods described in Chapter 2.1. The SGFs had a fixed ratio of bentonite to sand of 80:20 and two volume concentrations were contrasted:

18% bentonite-sand and 20% bentonite-sand. Fine-sand sized ballotini was used to represent sand; specifications of these spherical quartz grains are given in Chapter 2.3.4. Video camera recordings were used to measure the head velocity of the flows, describe the flow behaviour, and define the flow type as both flows travelled along the tank. The deposit height and the runout distance were recorded using the laser bed scanner. In addition, sediment cores were taken from the deposits and analysed for grain-size distributions, as described in Chapter 2.2. Yield stress measurements of sediment mixtures with the same composition as the suspensions used in the lock-exchange experiments were calculated using the dam break method outlined in Chapter 2.4.2. Table 5.1 presents the experimental data.

Table 5.1: Experimental data. Bold text indicates new data with all other flows presented in Chapter 3. TC = turbidity current.

Total volume concentration	Bentonite (%)	Sand (%)	Runout distance (m)	Maximum head velocity (m s^{-1})	Yield stress (Pa)	Flow type
15% bentonite	15	0	4.66	0.35	1.8	High-density TC
18% bentonite-sand	**14.4**	**3.6**	**3.52**	**0.36**	**5.0**	**High-density TC**
18% bentonite	18	0	1.42	0.27	21.3	Mud flow
16% bentonite	16	0	3.77	0.37	4.6	High-density TC
20% bentonite-sand	**16**	**4**	**1.79**	**0.31**	**11.8**	**Debris flow**
20% bentonite	20	0	0.22	0.07	67.5	Slide

5.3 Flume results of bentonite-sand flows

5.3.1 Visual observations

The video recordings show that the 18% bentonite-sand flow had a rounded head that hydroplaned from x = 0.3 m to x = 2.20 m, where x is the distance from the lock gate (Fig. 5.2A). Upon leaving the reservoir, the flow formed a two-part structure consisting of a dense lower zone 1 without visible mixing and a dilute upper zone 2 where ambient water was mixed into the flow. Kelvin-Helmholtz instabilities were observed at the top of the flow. Small interfacial waves were present between zones 1 and 2 until x = *c.* 1.5 m. Cohesive packets of material formed at the top of the head as soon as the flow started; these packets then sat at the interface between the two zones and slowly disintegrated (Fig. 5.2A). Within the dense lower zone, linear features of clear ambient water termed coherent fluid entrainment structures were observed from x = 1.2 m to x = 3.2 m (Fig. 5.2B). The head and body of the flow thinned as it travelled along the tank. Bubbles were observed from x = 2.5 m, and in the final flow stages the head of the flow and the bubbles within the head stretched (Fig. 5.2C).

The head of the 20% bentonite-sand flow had a similar two-layer structure as the 18% bentonite-sand flow described above. However, the upper zone was a lot lighter in colour, less mixing with the ambient water was observed, and no interfacial waves between the two zones were present (Fig. 5.2D). Once the lock gate was lifted, the head of the flow curled back on itself before attaining a rounded shape at x = 0.6 m (Fig. 5.2D). The head of the flow did not hydroplane. Faint coherent fluid entrainment structures were observed from x = 0.5 to x = 1.5 m, but these were not as numerous as in the 18% bentonite-sand flow (Fig. 5.2E). Instead, a large number of bubbles were observed in the head of the 20% bentonite-sand flow from x = 1 m (Fig. 5.2F).

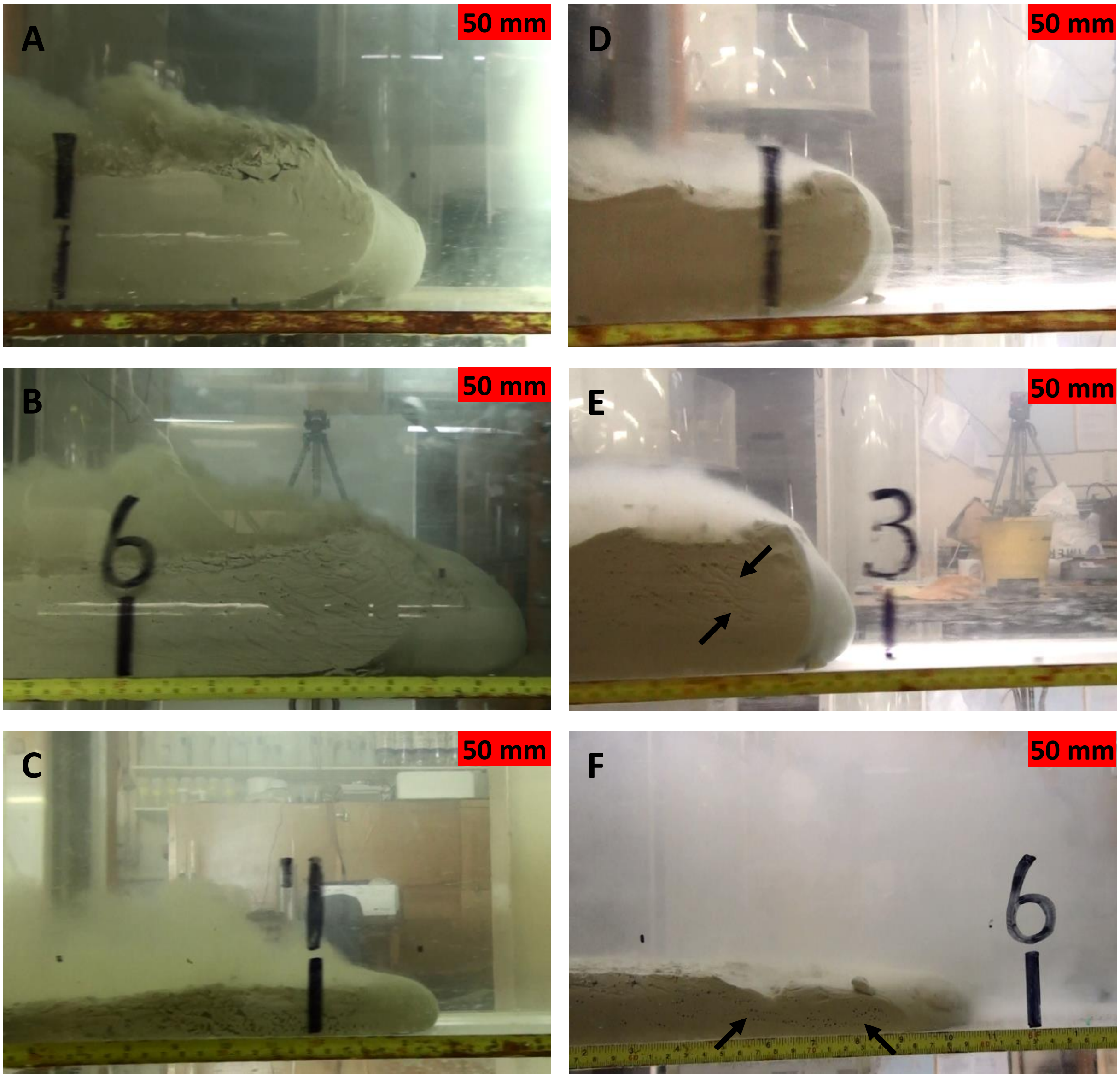

Figure 5.2: Head of the 18% bentonite-sand flow: (A) At time, t = 1.90 s and distance from the lock gate, x = 0.51 m, the flow had a two layer structure and cohesive packets of sediment can be seen forming at the top of the head; (B) At t = 6.30 s and x = 2.05 m, coherent fluid entrainment structures can be seen in the lower layer; (C) At t = 11.70 s and x = 3.42 m the head of the flow and the bubbles within the flow stretch during the final flow stages. Head of the 20% bentonite-sand flow: (D) At t = 1.47 s and x = 0.38 m, the head is curled back on itself to make a small roller wave; (E) At t = 3.07 s and x = 0.90 m, the flow has a rounded head and faint coherent fluid entrainment structures shown by arrows are observed in the lower layer; (F) At t = 13.5 s and x = 1.79 m, the flow has stopped and arrows point to bubbles that can be seen trapped in the head of the flow.

5.3.2 Flow velocities

Figure 5.3 shows the head velocity data for the mixed bentonite-sand flows and also for specific pure-bentonite flows from Chapter 3, to which the mixed bentonite-sand flows will be compared in the Discussion Chapter 5.7.1. Both mixed bentonite-sand flows accelerated rapidly after the lock gate was lifted (Fig. 5.3). The 18% bentonite-sand flow accelerated to a maximum head velocity of 0.36 m s^{-1} compared to a maximum head velocity of 0.31 m s^{-1} for the 20% bentonite-sand flow. After the initial acceleration, the 20% bentonite-sand flow gradually decelerated until x = 1.5 m, whereas the 18% bentonite-sand flow maintained a fairly constant head velocity until x = 2.5 m. Both flows exhibited a rapid decrease in velocity in the final flow stages to produce measurable runout distances. The 20% bentonite-sand flow travelled 1.79 m, whereas the 18% bentonite-sand flow travelled 3.52 m.

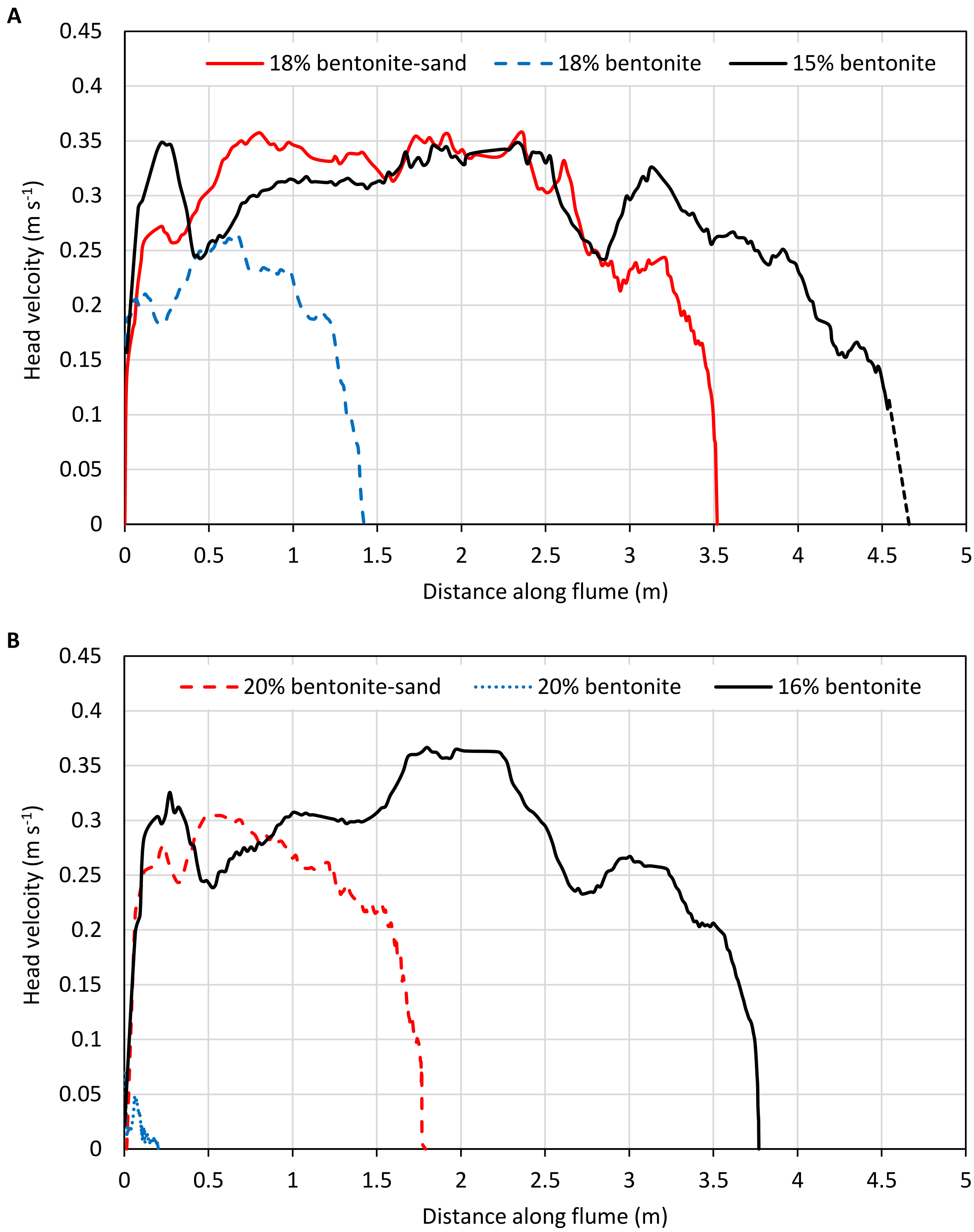

Figure 5.3: Head velocity against distance along the flume for the mixed bentonite-sand flows and the pure-bentonite flows from Chapter 3. (A) Shows the effect of increasing the volume concentration from 15% clay (black line; a 15% bentonite flow is used to represent the 14.4% bentonite flow) by 25% sand (red line) or 25% clay (blue line). (B) Demonstrates the effect of head velocity on a 16% bentonite flow (black line) by adding 25% sand (red line) and 25% clay (blue line). The solid line, dashed, and dotted lines represent a high-density turbidity current, mud flow or debris flow, and slide, respectively. Black dotted part of the 15% bentonite line denotes extrapolated velocity to the recorded runout distance.

5.3.3 Deposits

Figure 5.4 presents the mixed bentonite-sand flow deposits, as well as selected pure-bentonite flow deposits from Chapter 3 that will be discussed in Discussion Chapter 5.7.1. Both the mixed bentonite-sand flows produced deposits which were thickest at the back of the reservoir (Fig. 5.4). The deposit of the 18% bentonite-sand flow decreased steadily in thickness from the back of the reservoir to $x = 0.9$ m; thereafter, the deposit maintained a fairly constant thickness. The deposit of the 20% bentonite-sand flow also thinned from the back of the reservoir, to a thickness of 0.018 m at $x = 0.7$ m. The deposit then increased in thickness producing a clear depression with a distinct, thick front. Both deposits ended abruptly with pronounced leading edges.

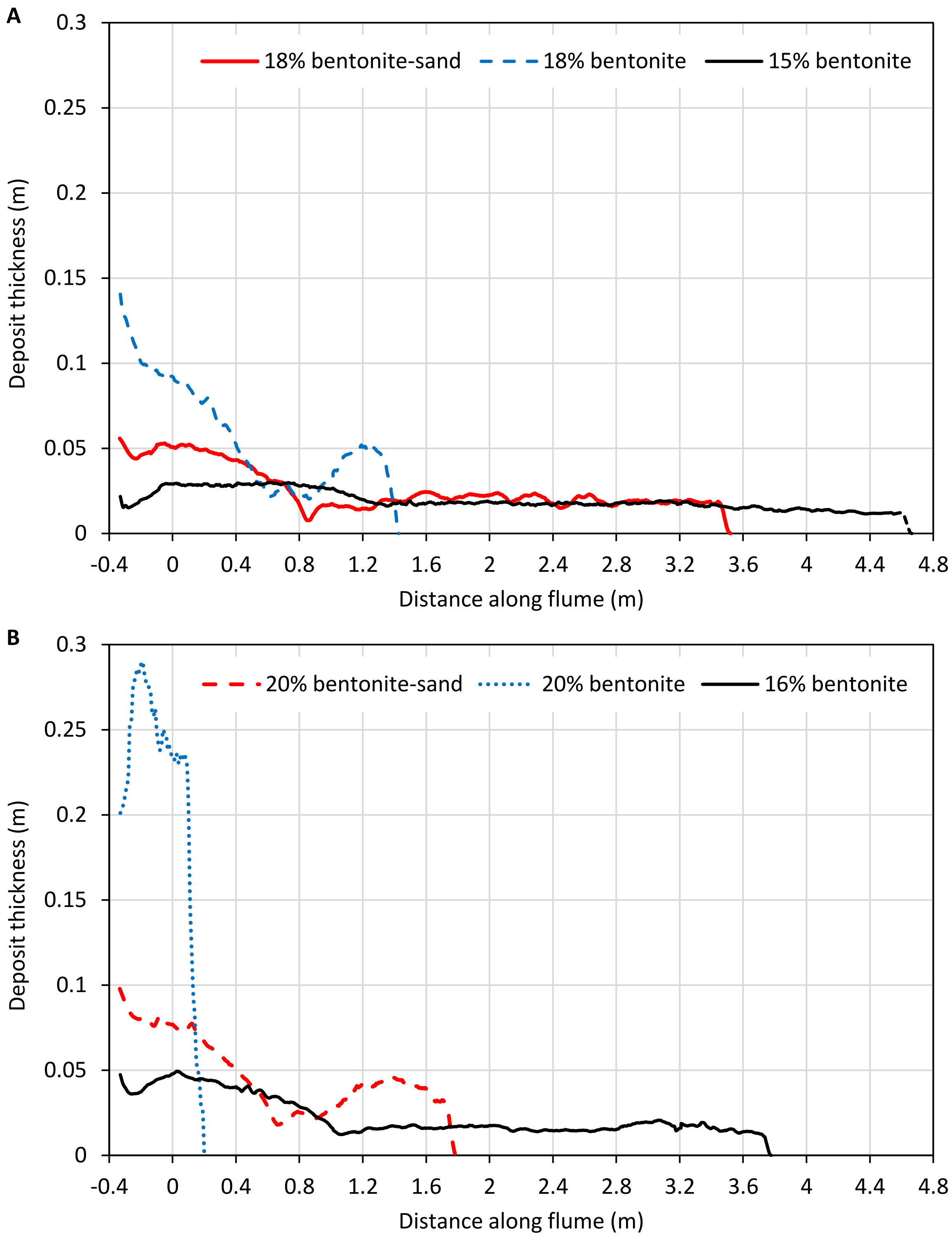

Figure 5.4: Changes in deposit thickness with distance along the tank for the (A) 18% mixed bentonite-sand flow (red), 15% bentonite flow (black; as a proxy for a 14.4% bentonite flow deposit) and 18% bentonite flow (blue). (B) the 20% bentonite-sand flow deposit (red) can be compared with the 20% bentonite flow deposit (blue) and the 16% bentonite flow deposit (black). The solid line, dashed, and dotted lines represent a high-density turbidity current, mud flow or debris flow, and slide, respectively. Dotted end of the deposit for the 15% flow was beyond the reach of the Ultrasonic Ranging System and was measured by hand instead.

5.3.4 Grain-size variations in the deposits of the bentonite-sand flows

Figure 5.5 demonstrates the vertical and horizontal changes in bentonite percentage within the deposits of the 18% bentonite-sand and the 20% bentonite-sand flows. The 20% bentonite-sand deposit lacks horizontal and vertical changes in bentonite percentage (Fig. 5.5B). The maximum variation between subsequent data points is 1.6%, which is within the error range. In contrast, the 18% bentonite-sand deposit shows both horizontal and vertical changes in the percentage bentonite (Fig. 5.5A). All three cores have a similar bentonite percentage in the lowermost sample and they all show a vertical increase in bentonite percentage, which signifies a fining upward trend. The core at 0.20 m along the deposit fines gradually upwards until 22.5 mm above the bed. In contrast, the cores at 1.40 m and 3.20 m from the lock gate fine upwards quickly to 6.35 mm above the bed. Above the fining upward layer, all the sediment cores show a consistently high bentonite percentage. The two most distal sediment cores have a higher percentage bentonite in the lowest 11.25 mm above the bed than the most proximal core.

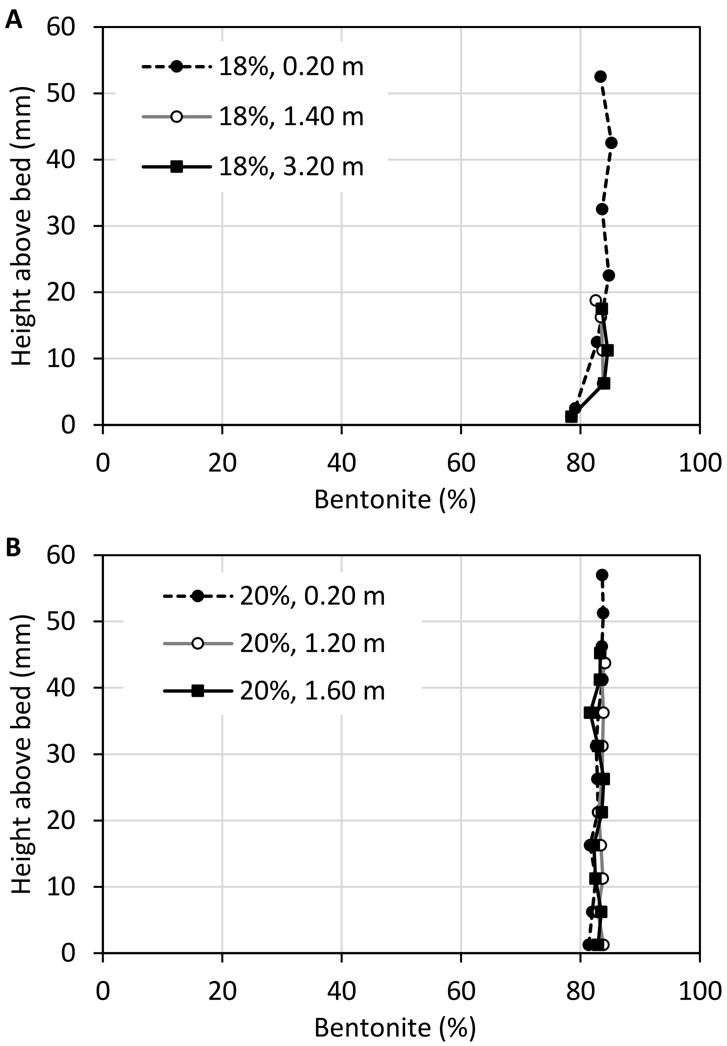

Figure 5.5: Changes in grain size with height above the bed at different locations in the deposits for (A) the 18% bentonite-sand flow, and (B) the 20% bentonite-sand flow.

5.4 Rheology results of bentonite-sand suspensions

The yield stress values of the pure-bentonite suspensions and the mixed bentonite-sand suspensions are given in Table 5.1 and Figure 5.6. The yield stress of the 14.4% pure-bentonite suspension was calculated as 1.8 Pa. In contrast, the yield stress of the 18% bentonite-sand suspension was 5.0 Pa, whereas the 18% bentonite suspension had a yield stress of 21.3 Pa. The 20% bentonite-sand suspension had a yield stress of 11.8 Pa. This is 2.5 times greater than the yield stress of the 16% bentonite suspension which equals 4.6 Pa. The 20% pure-bentonite suspension had a yield stress of 67.5 Pa.

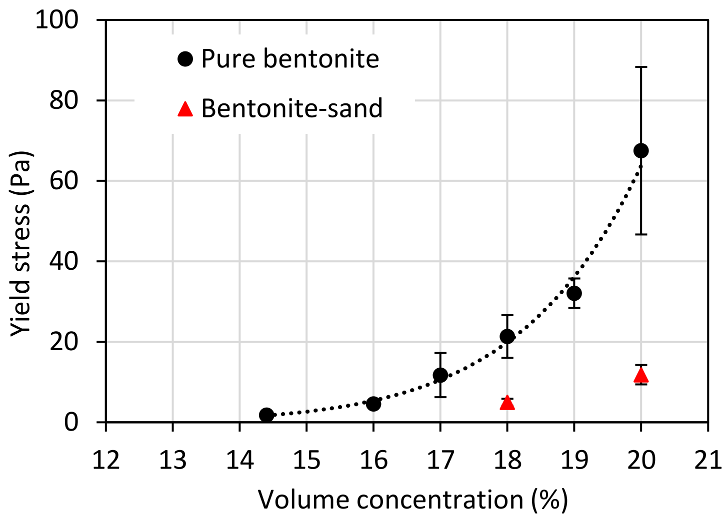

Figure 5.6: Yield stress of the pure-bentonite suspensions (black circles) and mixed bentonite-sand suspensions (red triangles) measured by dam break experiments. Error bars are the 95% confidence intervals.

5.5 Process interpretation of the mixed bentonite-sand flows and deposits

5.5.1 Visual observations

The two mixed bentonite-sand flows can be classified using the flow classification scheme described in Chapter 3. The 18% bentonite-sand flow is interpreted as a high-density turbidity current, as the flow can be divided into a dense lower zone 1 without visible mixing and a dilute upper zone (*sensu* Lowe, 1982). The two-layer structure of the 18% bentonite-sand flow was also observed in the 15% to 17% pure-bentonite flows and in the 22% to 25% pure-kaolinite flows, which were also interpreted as high-density turbidity currents (Chapter 3). The interpretation for the two-layer structure is the same for the pure-clay flows and the mixed bentonite-sand flows. The lower zone is darker than the upper zone because it has a higher sediment concentration as a result of particle settling. The high clay concentration in zone 1 also explains the lack of visible turbulent mixing, because the clay minerals collided, flocculated and produced a gel with high cohesive strength. The lighter and more dilute zone 2 formed from sediment mixing with the ambient water.

The 20% bentonite-sand flow also formed a two-layer structure, but the colour of zone 1 was darker and mixing with the ambient water was weaker. This flow is classified as debris flow because of its strong to full turbulence suppression in zone 1 and limited mixing at the upper boundary. This flow behaviour matches the 18% and 19% pure-bentonite flows and the 27% pure-kaolinite flow (Chapter 3), but these flows were described as mud flows because they did not contain sand. As for the pure-clay mud flows, the limited mixing in the 20% bentonite-sand flow occurred because the stronger clay gel prevented the clay bonds from breaking. In addition, the lower flow velocity resulted in a weaker flow of water over the head, which may have prevented the clay from breaking away from the upper layer of zone 1.

Both flows contained pathways of clear water, termed coherent fluid entrainment structures, in zone 1. These structures were also observed in the pure-clay high-density turbidity currents and mud flows in Chapter 3, and are again interpreted to form as water is injected into the flow but not mixed in as a result of the high yield stress. The coherent fluid entrainment structures were larger, and more numerous in the 18% bentonite-sand flow than in the 20% bentonite-sand flow, presumably because the higher cohesive strength of the 20% bentonite-sand flow limited their formation. The disintegration of the coherent fluid entrainment structures at the end of the 18% bentonite-sand flow and the formation of bubbles indicates that the flow became too cohesive for water to escape.

The curled back head of the 20% bentonite-sand flow that was generated upon departure from the lock gate behaved in the same manner as in the 18% and 19% pure-bentonite mud flows (Chapter 3). For all these flows, the unique roller-wave shaped head formed as ambient water pushed the flow back on itself at the top, and the flow had enough cohesive strength to maintain the shape. The rounded head of both flows suggests that the cohesive strength of the head was high enough to resist being streamlined by the hydrodynamic forces. The 18% bentonite-sand flow hydroplaned but the 20% bentonite-sand flow did not. As for the pure-clay flows, the head of the 20% bentonite-sand flow was most likely too slow and too heavy for the hydrodynamic pressures at the front of the flow to support the head. In contrast, the 18% bentonite-sand flow was lighter and faster enabling water to be forced underneath the flow.

5.5.2 Flow velocities

As was observed for the pure-clay flows in Chapter 3, both mixed bentonite-sand flows accelerated upon leaving the gate, driven by the density difference between the flows and the ambient water. However, despite the 20% bentonite-sand flow having a greater density than the 18% bentonite-sand flow, it accelerated to a lower maximum head velocity. Most likely, the higher clay concentration allowed a greater number of electrostatic bonds to form, which dampened flow turbulence in the 20% bentonite-sand flow more effectively than in the 18% bentonite-sand flow. The 20% bentonite-sand flow started to decelerate almost immediately because the cohesive forces dampened the turbulent forces, resulting in the bulk settling of the clay gel. In contrast, the 18% bentonite-sand flow was able to maintain a constant flow velocity until approximately 2.5 m, driven by the density difference of the flow. This interpretation matches that of the pure-clay flows (Chapter 3), which changed from turbulence-driven to cohesion-driven at 16% bentonite and 22% kaolinite, respectively. The rapid reduction in the head velocity of both bentonite-sand flows was caused by cohesive freezing, whereby a reduction in flow velocity starts a positive feedback loop. As described in Chapter 3 for the pure-clay flows, the reduction in the head velocity allows the clays to form more electrostatic bonds and increase the cohesive strength of the flow, which in turn reduces the flow velocity (Mulder & Alexander, 2001).

5.5.3 Deposits

Both flows produced measurable runout distances. The 20% bentonite-sand flow had a shorter runout distance than the 18% bentonite-sand flow because the greater cohesive forces caused bulk sediment settling closer to the point of release. The 18% bentonite-sand high-density turbidity current produced a deposit that matched the deposits of the pure-clay high-density turbidity currents (Chapter 3), and a similar interpretation is used to explain the deposit shape. The thick proximal part of the deposit results from cohesive forces encouraging the flow to settle rapidly near the lock gate, whereas the extension of uniform thickness is associated with turbulent forces driving the flow along the tank. The 20% bentonite-sand flow produced a deposit in keeping with the mud flow deposits described in Chapter 3. The depression and thick front are thought to result from the head stretching away from the body of the flow (Elverhøi *et al.*, 2005), as described in Chapters 3 and 4.

The grain-size variations in the 18% bentonite-sand and 20% bentonite-sand deposits provide additional evidence for the flow classification of the bentonite-sand flows. The lack of horizontal and vertical changes in bentonite or sand percentage for the 20% bentonite-sand flow (Fig. 5.5B) is typical of a debris flow, where the sand is held by the cohesive matrix strength of the flow (Mulder & Alexander, 2001). In contrast, the upward and downflow fining of the deposit of the 18% bentonite-sand flow implies that some sand was able to settle out of suspension as the flow travelled along the tank. This suggests that the cohesive strength of dense lower layer of the 18% bentonite-sand flow was lower than that of the 20% bentonite-sand flow.

5.6 Process interpretation of the rheological data

The results described in Chapter 5.4 demonstrate that increasing the volume concentration of the suspension by 25% from the addition of sand increases the yield stress. This is in line with other work on the yield stress of mixed clay-sand suspensions (Coussot & Piau, 1995; Ancey & Jorrot, 2002; Paulsen, 2007). Limited work has been done to clarify the mechanisms that result in the increase in yield stress of a non-Newtonian suspension when non-cohesive particles are added (Paulsen, 2007). Below, the several mechanisms for increasing the yield stress are outlined and the most relevant mechanisms for the present dataset are suggested:

Hydrodynamic interactions. These can be divided into excluded volume and additional hydrodynamic effects. The excluded volume mechanism describes how the particles take up volume which cannot be occupied by the interstitial fluid, thus reducing the volume of the fluid and increasing the rheological strength of the suspension (Sengun & Probstein, 1989; Coussot & Piau, 1995). Additional hydrodynamics effects have not been fully explored, but the main effect discussed is the wake effect. The wake effect occurs when movement of a particle produces a flow field which influences neighbouring particle motion, increasing the forces required to maintain flow and consequently increasing the fluid rheology (Paulsen, 2007).

Particle interactions. Suspended non-cohesive particles may contact, collide and jam, increasing the rheological strength of the suspension (Sengun & Probstein, 1989; Ancey & Jorrot, 2002). For non-cohesive particles in a Newtonian fluid, particle interactions are only considered to change the rheology at volume concentrations greater than 10% (Paulsen, 2007). It is not known if this concentration value applies also to non-cohesive particles in a non-Newtonian fluid.

Increase in dry solids surface. When non-cohesive particles are added to the suspension, water molecules may be immobilised on their surface. This results in a reduction of "free" water and the effective water concentration in the suspension is reduced, in turn increasing the clay volume concentration and the yield stress of the suspension (Paulsen, 2007).

Cohesive and non-cohesive particle interactions. It is possible that a net attractive force occurs between the non-cohesive and the cohesive particles. A greater number of attractive bonds between the particles in the suspension would increase the yield stress (Paulsen, 2007).

Change in floc or gel structure. Sumner *et al.* (2000) suggested that non-cohesive particles could become incorporated into, and change, the clay floc structure, thus reducing the distance between the flocs and increasing the yield stress. Ancey and Jorrot (2002) have also suggested that non-cohesive particles could become surrounded by clay particles and interact with each other as clay flocs, thus increasing the rheological strength of the suspension.

The mechanisms presented above are all likely to play a role in increasing the rheological strength of a cohesive suspension to which non-cohesive sediment are added. However, the relative importance of these processes is not currently known (Paulsen, 2007). Hydrodynamic interactions are hypothesised to be the most important mechanism responsible for the increased yield stress of the bentonite-sand flow presented here (*cf.* Sengun & Probstein, 1989; Coussout & Piau, 1995). The experimental data show that the strongly cohesive bentonite clay is more effective at increasing the yield stress than the non-cohesive sand (Table 5.1). This suggest that clay particle interactions were dominant in determining the rheology of the clay-sand mixtures. It follows that the excluded volume effect is likely to be important, as, when sand is added to the suspension, the volume of seawater is reduced, which causes an increase in the effective clay concentration. This increase in effective clay concentration may increase the number and strength of interparticle bonds, thus increasing the yield strength. This excluded volume effect could be compensated by vertical expansion of the flow, thus annulling the theoretical increase in yield strength. However, this is unlikely to have occurred in the present experiments, because the visibly strong cohesive nature of the 18% and 20% bentonite-sand flows precludes rapid entrainment of water at the front and top of the flow. Moreover, seawater that did manage to get incorporated into the flow probably did not contribute much to breaking clay particle bonds, given the common occurrence of coherent fluid entrainment structures and water bubbles.

The other mechanisms proposed above for increasing the yield stress are considered inappropriate for this dataset. The effect of particle interactions is likely to be negligible since the 3.6% and 4% volume concentrations of sand used in these experiments are far below the 10% boundary for non-Newtonian fluids at which particle interactions are thought to change the yield stress. In addition, particle interactions are expected to be rarer and weaker in the viscous clay flows. Cohesive and non-cohesive particle interactions are considered to be unlikely as the ballotini used in the experiments is inert with no surface charge. The ability for the sand particles to change the gel structure in a manner that makes the gel more cohesive is also doubtful. Within the gel structure the sand is likely to encourage clay particles closer together and increase the distance between clay particles by its presence in equal measure. Finally, for an increase in dry solids surface water needs to be immobilised into nooks and crevasses on the non-cohesive particles, this process is improbable for the spherical and smooth ballotini particles.

5.7 Discussion

5.7.1 Comparison of pure-bentonite and bentonite-sand flows in the laboratory

Using the pure-bentonite flows presented in Chapter 3, it is possible to compare how increasing the volume concentration by 25% with sand or clay changes the suspension yield stress, flow velocities and runout distance (Fig. 5.7). A 14.4% bentonite flow is compared to an 18% bentonite and an 18% bentonite-sand flow, and a 16% bentonite flow is compared to a 20% bentonite and 20% bentonite-sand flow. It should be noted that for this discussion a 15% bentonite flow is used instead of a 14.4%

bentonite flow. However, the difference in flow behaviour between a 14.4% bentonite and 15% bentonite is likely to be small and within the error range of the experiments.

Increasing the volume concentration of the suspension by 25% by adding sand or clay increases the yield stress, and this increase is greater with the addition of clay than sand (Fig. 5.7A, D). Adding bentonite raises the number of inter-particle bonds within the clay gel by a greater amount compared to non-cohesive sand. However, the addition of sand does increase the yield stress by a non-trivial amount. From the line of best fit applied to the yield stress against bentonite concentration data in Figure 5.6, the yield stress of the bentonite-sand suspensions can be compared to the yield stress of pure-bentonite suspensions. The yield stress of the 14.4% bentonite suspension increased by a factor of 2.8, from 1.8 Pa to 5.0 Pa, by adding 25% sand. A yield stress of 5.0 Pa is equivalent to a 15.7% pure-bentonite flow. Thus, the rise in yield stress from the addition of sand is comparable to increasing concentration of bentonite by 9%. This trend is similar for the 20% bentonite-sand suspension, whose yield stress is equivalent to a 17% pure-bentonite flow (Fig. 5.7A, D). This increase in yield stress corresponds to increasing the volume concentration by 6% bentonite.

The runout distances of the bentonite-sand flows are considerably reduced compared to the original pure-bentonite flows, and can be compared to the pure-bentonite flows by applying a line of best fit to the runout distance against bentonite concentration data in Figure 3.9 (Fig. 5.7B, E). The 18% bentonite-sand flow's 3.52 m runout distance is reduced by a factor of 1.3 compared to the 14.4% pure-bentonite flow, which is equivalent to the runout distance of a 16.3% pure-bentonite flow (Fig. 5.7B). This means that increasing the volume concentration by adding 25% sand is akin to increasing the volume concentration by 13% clay, for the runout distance of the 14.4% bentonite flow. The runout distance of the 20% bentonite-sand flow was reduced by a factor of 2.5 compared to the 16% bentonite flow (Fig. 5.7E). This runout distance is equivalent to an 18.2% pure-bentonite flow and comparable to increasing the volume concentration of the 16% bentonite flow by 14% clay. This reduction in runout distance by adding sand potentially has important consequences for SGF mobility predictions, as discussed in Chapter 5.7.3.

The change in flow behaviour from the addition of either 25% sand or clay is only partly represented by the maximum head velocity (Fig. 5.7C, F). Since the maximum head velocities are based on single points on the head velocity versus distance curves (Fig. 5.3), it is beneficial to compare the entire velocity profiles in this chapter. For the 14.4% bentonite flow, the maximum head velocity did not change with the addition of 3.6% sand, because both the 14.4% bentonite and 18% bentonite-sand flows accelerated to similar maximum head velocity values. This similarity may be because the enhanced excess density of the 18% bentonite-sand flow (compared to the 14.4% bentonite flow) was counteracted by the greater cohesive forces in the flow (Fig. 5.3). The 18% bentonite-sand flow decelerated rapidly from 2.5 m to produce a shorter runout distance than the 14.4% bentonite flow (Fig. 5.3). This suggests that the greater cohesive forces in the 18% bentonite-sand flow were only able to outcompete the density difference in the later part of the flow. The maximum head velocity in the 20% bentonite-sand flow was lower than in the 16% bentonite flow, as the increased cohesive forces reduced the flow velocity, despite the larger density difference (Fig. 5.7F).

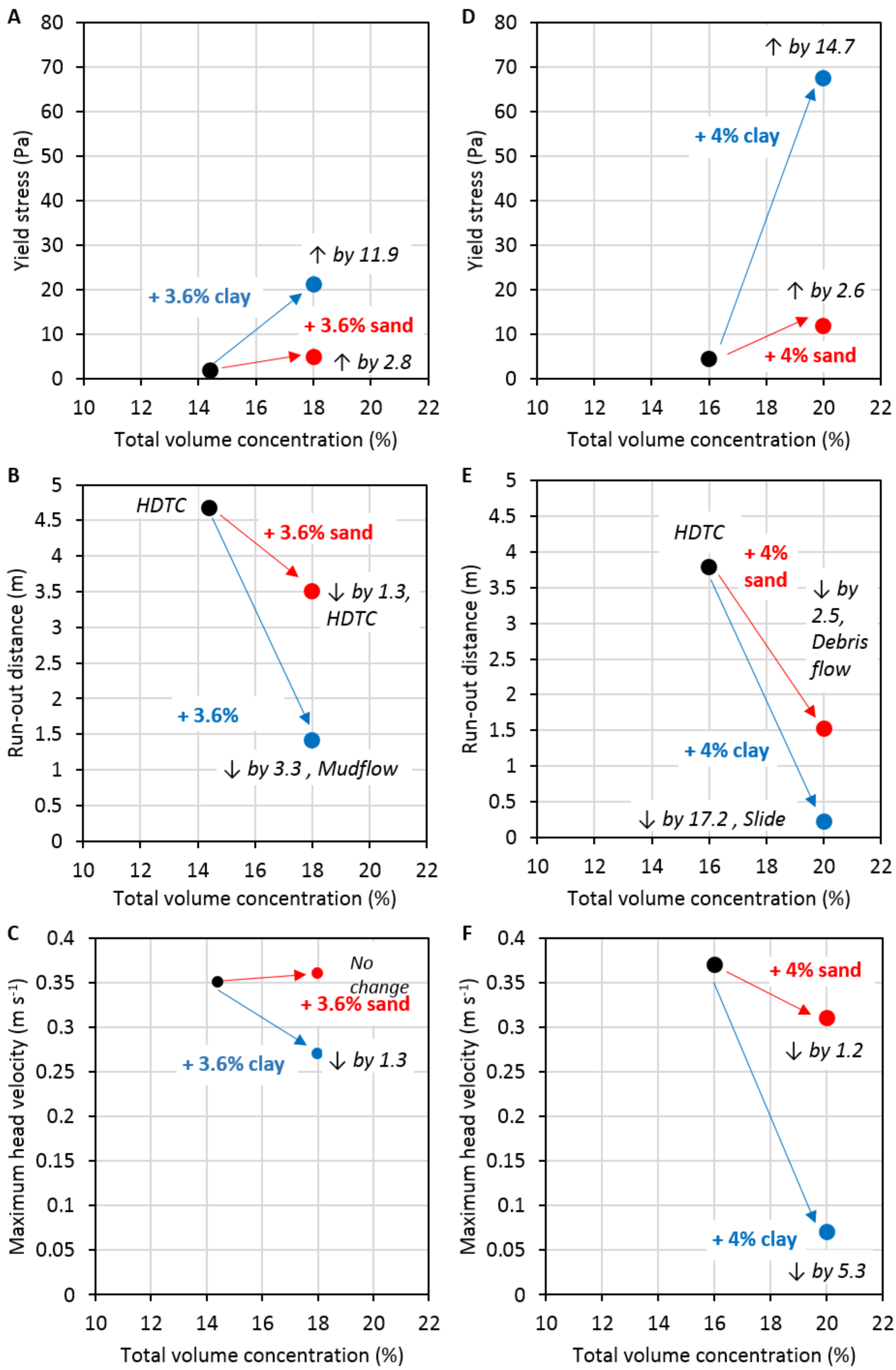

Figure 5.7: Summary of changes in yield stress, runout distance and maximum head velocity for the (A) to (C) 14.4% bentonite flow and (D) to (F) 16% bentonite flow when the volume concentration of the suspension is increased by 25% from the addition of sand (red arrows and data points) or bentonite (blue arrows and data points). Factors of change in yield stress, runout distance and maximum head velocity from the original 14.4% or 16% bentonite flows are shown in italics. In (B) and (E), the flow types are also displayed, HDTC = high-density turbidity current.

5.7.2 Comparison of adding sand and clay across a full range of clay concentrations

The two bentonite-sand flows presented in this chapter can be used to predict the effect of adding 25% volume concentration of clay or sand for the full range of clay concentrations, by considering the balance between the turbulent and cohesive forces in the flow. This is schematically shown in Figure 5.8, which compares changes in flow mobility as a function of flow concentration for pure-clay flows and flows containing a ratio of 20:80 of sand to clay. This conceptual model allows the following comparisons between the pure-clay and the mixed sand-clay flow curves to be made:

- At low clay concentrations, where the flows behave as low-density turbidity currents, the clay and clay-sand curves are very similar. Increasing the concentration of the flows increases the density difference between the flows and the ambient fluid. With turbulent forces dominating the flow behaviour and limiting the cohesive forces, the density difference drives the flow. The curve for clay-sand flows may lie below the curve for pure-clay flows, as the sand has a higher settling velocity than the clay.
- The transition from low-density turbidity current to high-density turbidity current is expected to occur at a lower concentration for the pure-clay flows than for the clay-sand flows, because the cohesive forces are greater in the pure-clay flows.
- The apex of the mobility curve likely occurs at a higher mobility and at a higher total concentration for the clay-sand flows than for the pure-clay flows, because the inclusion of sand causes the concentration at which the cohesive forces becomes strong enough to prevent the density difference from increasing the flow mobility to be higher.
- Once the maximum mobility is reached, the mobility of both the pure-clay flows and the clay-sand flows starts to reduce rapidly, with a shift in the boundaries between high-density turbidity current and mud/debris flow, and between mud/debris flow and slide to higher concentrations for the clay-sand flows. The clay-sand flows are inferred to reach the point where they are too cohesive to flow at a higher concentration than the pure-clay flows.

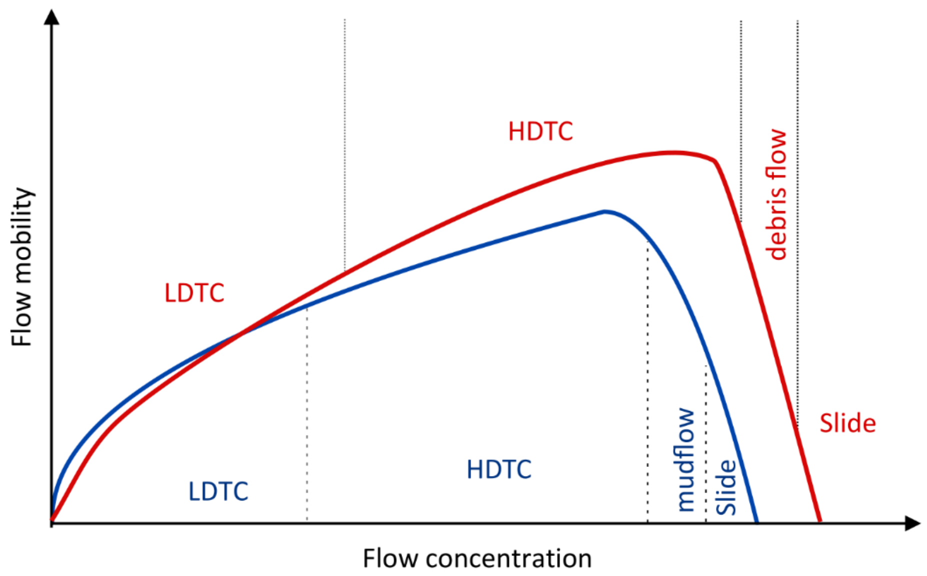

Figure 5.8: Conceptual diagram of flow mobility against concentration for pure-clay flows (blue) and mixed clay-sand flows at a ratio of 20:80 of sand to clay (red). The addition of a small amount of sand allows the flows to reach a higher maximum flow mobility before the cohesive forces start to counteract the excess density and reduce the flow mobility. The addition of sand also shifts the transition between flow behaviours. LDTC = low-density turbidity current; HDTC = high-density turbidity current.

Figure 5.8 only considers a clay-sand mixture with a clay-to-sand ratio of 80:20. Predicting what will happen at different clay-to-sand ratios across the full range of flow concentrations without a more comprehensive set of experimental data is challenging. The yield stress of mixed clay-sand suspensions increased as progressively more sand was added in the experiments of Ancey and Jorrot (2002; Fig. 5.9). However, there is a disconnect between the yield stress of a suspension and the flow behaviour of that suspension, since rheology experiments use a fixed volume and natural flows can expand by entraining water. Ilstad *et al.* (2004) produced experimental debris flows at a fixed volume concentration of 41% – equivalent to 65 weight % (wt %) – and varied the ratio of medium sand to kaolinite clay. In the 'clay-rich flow' of Ilstad *et al.* (2004) that carried 32.5 wt % clay and 32.5 wt % sand, mixing with the ambient water was limited (Fig. 5.10A) and these flows had the lowest head velocities of all the debris flows produced (their figure 10). In contrast, the head of debris flow with 20 wt % clay and 45 wt % sand rapidly broke up, resulting in flow transformation into a turbidity current (Fig. 5.10B). The sand-rich flow that carried 5 wt % clay and 60 wt % sand had a high head velocity and the head of this flow fluidised even more rapidly and intensively.

The experiments of Ilstad *et al.* (2004) took place at a fixed concentration, but the results should be similar if different volume concentrations of sand are added to fixed-concentration clay flows. It is likely that this sand only increases the yield stress of the flow if the flow has enough cohesive strength to resist breaking up under the dynamic stresses of the flow. Once a critical volume concentration of sand is reached, the enhanced density difference and flow velocity force the head of the flow to break up and increase the flow mobility. The amount of sand that can be added and still increase the yield stress and reduce the flow mobility is expected to be different depending on the initial clay concentration in the flow. It is likely that for weakly cohesive flows, only a small amount of sand is needed for the flow to break up, the yield stress to decrease, and the flow mobility to increase. For strongly cohesive flows, the experiments of Ilstad *et al.* (2004) suggest that a larger amount of sand can be added. Using the main outcomes of Chapter 3, high-concentration bentonite flows should break up and gain mobility at larger concentrations of added sand than equivalent high-concentration kaolinite flows.

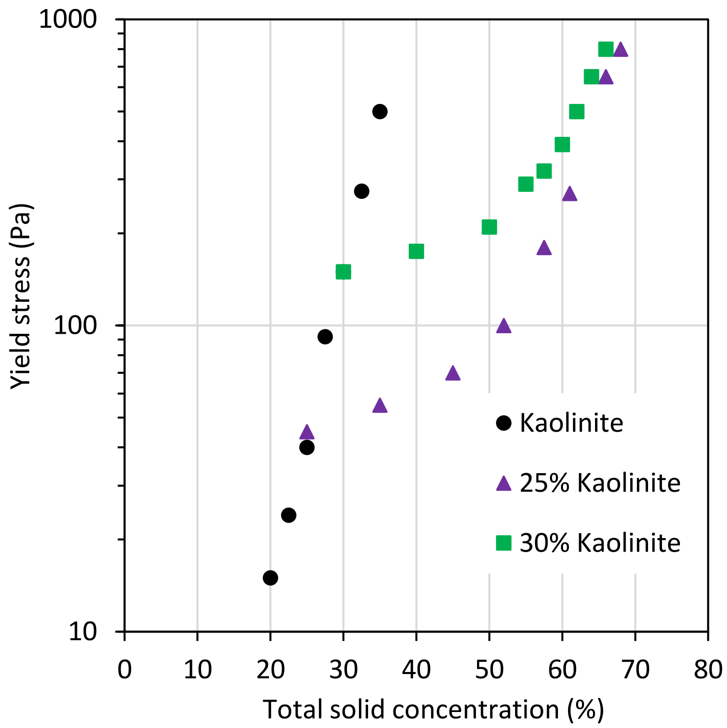

Figure 5.9: Yield stress as a function of total solid concentration for pure kaolinite (black circles), 25% kaolinite with increasing amounts of added sand (purple triangles), and 30% kaolinite with increasing amounts of added sand (green squares). The yield stress of the mixed sand-kaolinite suspensions increases with solid concentration of sand. The sand was fine-grained and poorly-sorted. Modified from Ancey and Jorrot (2002).

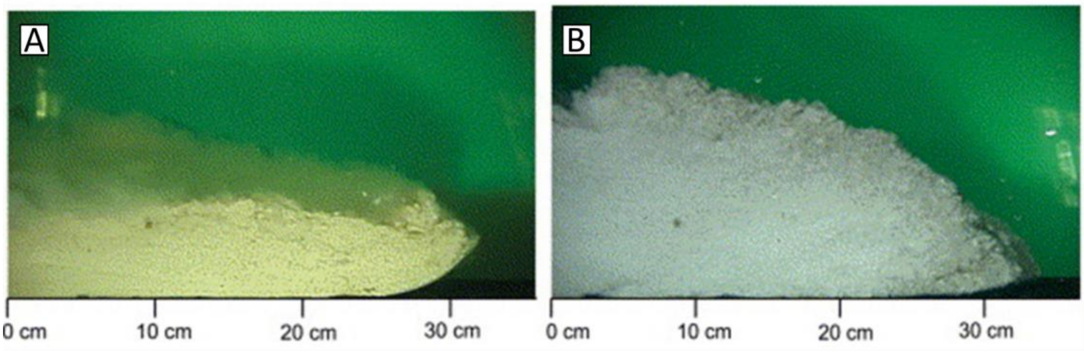

Figure 5.10: Pictures from the heads of the: (A) 50:50 clay to sand flow (35 wt % of each) and (B) 30:70 clay to sand flow (20 wt % clay and 45 wt % sand) of Ilstad et al. (2004). In (A) the high clay concentration allowed sand to stay within the clay gel. In (B) the low clay content produced a weaker clay gel that was not able to prevent the flow from breaking up. Both flows have a fixed volume concentration of 41%. From Ilstad et al. (2004).

5.7.3 Wider implications

These experiments further extend the evidence that the yield stress of high-density cohesive SGFs is an important control on their flow mobility. The yield stress of cohesive SGFs containing sand and silt, which are expected to be common in the natural environment, cannot be considered only in terms of the clay concentration. The present experiments show that the yield stress of these mixed flows has a significant non-cohesive component. Thus, calculating the yield stress of high-density cohesive SGFs using equations which relate yield stress to clay concentration, *i.e.,* the equation of Wan (1982), is not appropriate. The non-cohesive component of the yield stress was large enough to change the flow type and limit the flow mobility of the mixed sand-clay laboratory flows compared to pure-clay flows with the same clay content. This is likely to be important also for natural high-density cohesive SGFs.

As SGFs travel across the distal region of mud-rich submarine fans, these flows are thought to transform from turbulent to laminar as the cohesive forces increasingly dominate the turbulent forces. This results in the formation of transitional flow deposits and hybrid event beds (Barker *et al.*, 2008; Haughton *et al.*, 2009; Kane & Pontén, 2012). The mechanisms for causing flow transformation are the entrainment of mud from the substrate into the flow (Hodgson, 2009) and the deceleration of the flows allowing the cohesive forces in the flow to dampen turbulence (Kane *et al.*, 2017). The results from these experiments suggest that the presence of sand in high-density cohesive SGFs can also increase the yield stress of the flow and encourage flow transformation. The addition of sand to clay-rich SGFs , for example via scouring of sandy SGF deposits, and the ensuing increase in the likelihood of flow transformation, may further explain the large number of hybrid event beds and transitional flow deposits in the distal margins of submarine fans.

The change in SGF behaviour from the addition of sand is complex, as the experimental data presented here and those of Ilstad *et al.* (2004) suggest that increasing the volume concentration by adding sand can both increase and decrease the mobility of the SGF. The effect of adding sand on the dynamic behaviour of SGFs depends on, amongst others, clay concentration, clay type, initial flow properties and amount of added sand. Adding sand to natural cohesive SGFs dominated by turbulence and behaving as low-density turbidity currents is likely to increase the flow mobility as it will increase the density difference and the turbulent forces. In contrast, adding sand to natural cohesive SGFs dominated by transitional or laminar flow behaviour, such as high-density turbidity currents, mud flows, and slides, is hypothesised to increase the yield stress and reduce the flow mobility, if the sand can be held within the matrix strength of a plug layer. This could result in a change in flow behaviour from high-density turbidity current to debris flow, or from debris flow to slide. However, if more sand is added than can be held within the plug layer, the flow is likely to break up and debris flows could transition to high-density turbidity currents and high-density turbidity currents may change to low-density turbidity currents. For dense slides, it is suggested that adding any amount of sand reduces the flow mobility and promotes bulk settling. Baas *et al.* (2011) described turbulence-attenuated transitional flows, in which both the turbulent and the cohesive forces are not large enough to hold the sand within the plug layer. Consequently, this sand rapidly falls out of suspension. The turbulence-attenuated transitional flows of Baas *et al.* (2011) may be equivalent to weak high-density turbidity currents in nature. It is hypothesised that adding sand will make these flow more turbulent and increase their mobility. This could change the flow behaviour from high-density turbidity current to low-density turbidity current. However, the fact that these flows are susceptible to rapid settling of sand particles suggests that such weakly turbulent and weakly cohesive mixed-sand-mud flows are unstable in the natural environment.

5.7.4 Future research

These experiments have shown significant changes in the flow mobility and yield stress of high-density cohesive SGFs to which small amounts of sand were added. Further experiments should be conducted to test the effect of adding sand over the full range of flow clay concentrations, from low-density turbidity currents to slides. There is also potential to compare how increasing the volume concentration by adding different volumes of sand changes the flow behaviour and the suspension rheology. At what increase in volume concentration of sand in high-density cohesive SGFs does the flow mobility swap from decreasing to increasing? Observing the suspension microstructure directly would allow the mechanisms responsible for the decrease and increase in yield stress as a function of sand content to be better understood (Coussot & Piau, 1995). Finally, the results from these laboratory experiments cannot be directly compared to deposits in the field because of the different scales. Robust scaling relations, such as using Reynolds and Froude numbers as in the recent paper by

Hermidas *et al.* (2018), could facilitate quantitative comparison between the laboratory and field scales.

5.8 Conclusions

These experiments demonstrate that increasing the volume concentration of high-density cohesive sediment gravity flows by adding 25% sand increases the yield stress of the suspension and reduces the runout distance and the maximum head velocity of these flows. Thus, accounting only for the clay concentration when considering the cohesive properties of a SGF is incorrect. The comparison of the effect of increasing the volume concentration by adding 25% sand or 25% clay established that clay is more effective at increasing the yield stress of the suspension and reducing the flow mobility of the high-density cohesive sediment gravity flow, because its cohesive properties. However, adding 25% sand still reduced the flow mobility significantly, despite the non-cohesive properties of the sand particles. The theoretical mechanisms by which sand could increase the yield stress of clay suspensions include: hydrodynamic interactions; particle interactions; increase in dry solid surface; cohesive and non-cohesive particle interactions; and change in floc or gel structure. The relative importance of the different mechanisms has not been established, but hydrodynamic interactions are argued to have had the largest influence on the sand-bentonite flows in the present experiments. The change in flow behaviour and rheology from the addition of sand has important implications for flow transformation, particularly in the distal region of mud-rich submarine fans. It is hypothesised that sand only increases the yield stress and reduces the flow mobility if it can be held within the matrix strength of the plug region of a flow. If the sand cannot be held in a cohesive plug it is likely to promote turbulence mixing in the flow and increase the flow mobility.

6. Formation of mixed sand-mud bedforms by transient turbulent flows in the fringe of submarine fans

6.1. Introduction

The fringe of fine-grained deep marine systems often exhibit complex sedimentary facies and facies associations, as the presence of clay promotes the development of transient turbulent flows with complex depositional properties. The deposits of these transient turbulent flows have been termed 'hybrid event beds' by Haughton *et al.* (2009) and this term now covers a wide range of deposit and process types (Kane *et al.,* 2017). Hybrid event beds have been reported from many medial to distal lobe settings (Haughton *et al.*, 2003; Talling *et al.*, 2004; Barker *et al.*, 2008; Haughton *et al.*, 2009; Hodgson, 2009; Kane & Pontén, 2012; Talling *et al.*, 2012; Fonnesu *et al.*, 2015; Southern *et al.,* 2015; Kane *et al.*, 2017; Spychala *et al.*, 2017; Pierce *et al.,* 2018). However, little work has been done to understand if the bedforms in these fringe environments differ from those found in more proximal locations of fine-grained systems.

Previous laboratory experiments on bedforms produced under rapidly decelerated, mixed sand-mud flows have shown a strong link between flow type and bedform type (Baas *et al.,* 2011, 2013, 2016). These experiments identified a number of unique, cohesive, mixed sand-silt-clay bedforms. A new bedform phase diagram was proposed that defined the boundaries between the mixed sand-mud bedform types based on the cohesive and turbulent forces within the flow (Baas *et al.*, 2016). Fieldwork in the fringe of the mud-rich submarine fan that makes up the Aberystwyth Grits Group and Borth Mudstone Formation (Wales, U.K.) was undertaken to try to identify and interpret mixed sand-mud bedforms in the natural environment. The principal aims of this research were:

1. To fully describe and classify the bedform types observed in the field based on their shape, size, texture, and internal stratification

2. Use the strong link between transitional flow type and bedform type, summarised in the extended bedform phase diagram of Baas *et al.* (2016), to interpret the flow processes that formed the different bedform types identified in the field
3. Interpret the observed spatial distribution of these bedforms in terms of flow transformation from the fringe to the distal fringe of the fan.
4. To assess the applicability of mixed sand-mud bedforms in the fringe of other deep marine systems.

6.2 Geological setting of the Aberystwyth Grits Group and Borth Mudstone Formation

The Silurian Aberystwyth Grits Group (AGG) and Borth Mudstone Formation (BMF) are exposed in coastal cliffs between Cwmtydu and Borth in west-central Wales, United Kingdom (Fig. 6.1). These outcrops are part of a 50-km long open synclinal structure, in which palaeoflow directions have been found to be subparallel to the NE-trending cliff lines (Wood & Smith, 1958; Wilson *et al.*, 1992; Smith, 2004; Talling *et al.*, 2004; Cherns *et al.*, 2006; Fig. 6.1A). The highly wave-polished nature of the outcrops has allowed for detailed analysis of sedimentary structures, sedimentary facies, and facies associations (*e.g.*, Wood & Smith, 1958; Talling *et al.*, 2004).

The AGG and BMF formed during a major phase of extensional faulting in the Welsh Basin and its margins in the upper Llandovery, related to collision of Avalonia with Laurentia at low latitude (Cherns *et al.*, 2006). The extensional faulting accompanied major uplift of the hinterland, which became a source of sediment for the Welsh Basin. This coincided with major subsidence of the Welsh Basin, thus providing accommodation space for the accumulation of sediment gravity flow deposits, including the AGG and BMF (Cherns *et al.*, 2006). In the Llandovery, the Welsh Basin was bound by NE-striking normal faults, which instigated physiographic confinement of the sediment gravity flow deposits (Wilson *et al.*, 1992; Smith, 2004). Previous studies have proposed that most sediment was supplied from the south-west by sediment gravity flows into a linear upper crustal fault trough that was confined to the east and south-east by the Bronnant Fault (Cherns *et al.,* 2006; Gladstone *et al.,* 2018; Fig. 6.1A). Lovell (1970) subdivided the AGG into the Trefechan and Mynydd Bach Formations, which are primarily exposed in the southern and northern part of the coastal outcrops, respectively (Davies *et al.*, 1997; Fig. 6.1A). The average grain size and the bed thickness of the AGG decrease both north-eastward down the sub-basin and stratigraphically upward (McClelland *et al.*, 2011). The mudstone-rich facies of the BMF have been interpreted to extend laterally and distally beyond the limits of the more sandstone-prone facies of the AGG (Wilson *et al.*, 1992). The present study comprises field observations from the fringe part of the AGG between Aberystwyth and Harp rock and the proximal part of the BMF from Harp Rock to Borth (Fig. 6.1A).

Two distinct types of deposits have been found in the AGG and BMF: i) sandy and muddy sediment gravity flow deposits; and ii) interbedded mudstone. The sediment gravity flow facies in the proximal AGG, between Cwmtydu and Aberarth, are a combination of medium- to thick-bedded massive sandstones, muddy sandstones and classical, Bouma-type turbidites (Bouma, 1962; Wilson *et al.*, 1992). Moving distally, north of Aberarth and around Clarach Bay, the massive sandstone units thin and the turbidites primarily contain T_b-T_e or T_c-T_e Bouma-type divisions with occasional, thin T_a divisions, and the interbedded mudstones increase in thickness (Wilson *et al.,* 1992; Fig. 6.1B). In addition, hybrid event beds are present north of Aberarth (Talling *et al.,* 2004). South of Borth, in the fringe of the system, the BMF contains medium- to thin-bedded, muddy, T_d-T_e turbidites with thick interbedded mudstones (Wilson *et al.,* 1992; Fig. 6.1B).

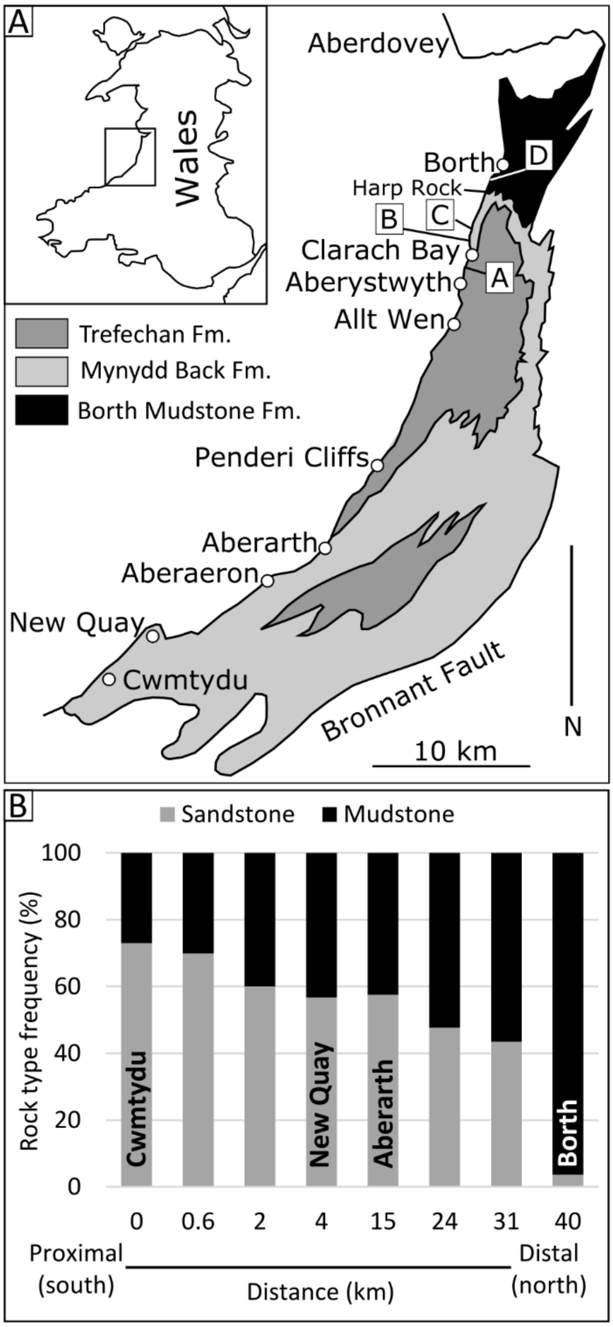

Figure 6.1: (A) Geological map of the Aberystwyth Grits Group and Borth Mudstone Formation in Wales (inset). Letters denote position of logs A-D. Modified after Davies et al. (1997) and McClelland et al. (2011). (B) Changes in the sandstone and mudstone frequency from South to North through the system.

6.3 Methods

Four sedimentary sections were logged in detail at a scale of 1:5 between Aberystwyth and Borth across the transition from the AGG to the BMF (Fig. 6.1A). These logs record a characteristic set of muddy, mixed sandstone-mudstone, and sandy sedimentary facies and facies transitions. Particular attention was given to the vertical and horizontal distribution of heterolithic stratification, mixed sandstone-mudstone bedforms, and couplets of mudstone and underlying thin siltstones. Because of the complex structural deformation within the AGG and BMF, it was not possible to correlate individual beds among the logs. Post-compaction thicknesses of beds normal to bedding were measured using a standard tape measure at an accuracy of 1 mm.

The sedimentary logs were accompanied by detailed descriptions of current-generated bedforms and primary current stratification along the entire outcrop between Aberystwyth and Borth. These descriptions included common bedform types in pure sandstone and novel bedform types in mixed sandstone-mudstone, where cohesive forces were hypothesised to have affected bedform development. The total record consists of 99 mixed sandstone-mudstone bedforms and 59 sandy bedforms. The descriptions and interpretations of the mode of formation of these bedforms are based on high-resolution field photographs, detailed field drawings, granulometric data, and bedform height and length measurements. Grain-size was estimated in the field using a hand lens and grain-size comparator. The colour of the deposits gave an additional indication of the typical grain-size, as increasing mud content produced darker coloured rock, with black deposits corresponding to mudstone. Strike and dip orientations of bedding planes as well as independent palaeoflow directions from, for example, flute and groove casts were measured using a standard geological compass. If required, these data were used to convert apparent bedform lengths to true bedform lengths using a stereonet. The bedform heights were not corrected for compaction, as the primary porosity of muddy and mixed sandy-muddy sediment is highly variable and cannot easily be reconstructed from sedimentary rocks. However, the angle of cross lamination observed in the bedforms was close to the angle-of-repose, suggesting that the amount of compaction for the bedforms was small. The measured heights of the bedforms may slightly underestimate the heights of the bedforms upon their formation.

Markov chain analysis was conducted to obtain the common facies transitions in the sedimentary logs. Each type of vertical facies transition in the logs was counted to produce a table of observed facies transition counts (Table 6.1). The probability of the facies transitions was then calculated by dividing the number of occurrences of a facies transition by the sum of all the facies transitions for that facies.

The wide range in facies counts for the various facies meant that methods to remove the random probability from the observed probability were unsuitable (*e.g.,* Gingerich, 1969).

6.4 Sedimentary facies

The sedimentary rocks found within the AGG and BMF are described using a facies scheme, with representative photographs of each facies shown in Figure 6.2. Many of the facies observed in this study correspond to facies described in other deep-water sediment gravity flow systems (*e.g.,* Pickering *et al.*, 1986). Figure 6.3 provides the key to sedimentary logs A, B, C and D (Figs 6.4 to 6.7), which demonstrate progressive changes in facies from the fringe to the distal fringe of the fan. Below, each facies is described and their mode of formation is interpreted.

Massive sandstone (Sma)

Observations

The massive sandstone (Sma) facies comprises structureless, very-fine grained to medium-grained sandstone, which is light blue-grey in colour (Fig. 6.2A). Most beds lack grading, but some beds show weak to strong normal grading. The massive sandstone facies is further characterised by sharp, flat bases and sharp tops or gradually fining upward transitions. Bed tops are sometimes wavy.

Interpretation

Deposits of massive sand may be formed by rapid suspension fallout from high-concentration sandy gravity flows that are fully turbulent (Arnott & Hand, 1989; Kneller & Branney, 1995; Talling *et al.*, 2012) or transient turbulent (Baas *et al.*, 2009, 2011). The presence of normal grading in the massive sandstone facies is interpreted to represent suspension settling of sand from waning flows (Kneller, 1995). Massive sand may also be generated by *en-masse* deposition from sandy gravity flows dominated by laminar flow behaviour, which does not produce normal grading (Shanmugam & Moiola, 1995; Talling *et al.*, 2012). The sharp bed bases suggest an abrupt change in depositional conditions from those producing the underlying bed, as well as possible erosion, which supports the interpretation of rapid input of sediment into the basin by a sediment gravity flow. The sharp tops of the massive sandstone facies indicate another abrupt change in depositional process; in contrast, the fining upward transitions suggest a more gradual change in depositional process. The wavy tops of the massive sandstone facies are interpreted to have resulted from post-depositional deformation, possibly involving dewatering after rapid deposition of the sand.

Structured sandstone (Ss)

Observations

The structured sandstone (Ss) facies consists of light blue-grey, mud-poor, very-fine grained to medium-grained, stratified sandstone (Fig. 6.2B). Horizontal, plane-parallel lamination is the most common primary current structure, with subordinate occurrences of wavy and convoluted lamination, and angle-of-repose ripple-cross lamination. Individual laminae are typically up to 3 mm thick. The beds are visually ungraded or normally graded; all beds with convolute lamination lack grading. Bed bases and tops are nearly always sharp and mostly flat, with occasional wavy boundaries. In some instances, the top of structured sandstone facies fine upward and are diffuse.

Interpretation

The presence of primary current lamination in the structured sandstone facies suggests deposition from fully turbulent sandy gravity flows with a lower rate of suspension fall-out than for the massive sandstone facies. Current velocity varied, allowing bedload transport to generate upper-stage plane beds and plane-parallel lamination at high velocities, and ripple cross-lamination at low velocities (Allen, 1982; Best & Bridge, 1992). Temporal reduction in flow velocity, and hence flow competence, produced the normally graded beds, whereas ungraded beds suggest a more constant flow velocity or the settling of well-sorted sand. The wavy lamination observed in the structured sandstone facies may have formed by soft sediment deformation of plane-parallel laminae. Some occurrences of wavy lamination also resemble the “sinusoidal ripple lamination” or “draped lamination” described by Jopling and Walker (1968) and Ashley *et al.* (1982). These structures have been experimentally shown to form under a flow with high rates of suspension settling depositing over inactive bedforms (Ashley *et al.*, 1982). The convoluted laminae in the Aberystwyth Grits Group formed from deformation of sediment during or shortly after deposition (Gladstone *et al.*, 2018). The observed bed bases and tops in the structured sandstone facies, as well as in all other facies described below, are interpreted in a similar way to the massive sandstone facies.

Clast-rich sandstone (Sc)

Observations

The clast-rich sandstone facies (Sc) is light blue-grey, very-fine grained to fine-grained sandstone with dispersed mudstone and matrix-supported black mudstone clasts or light blue-grey, medium-grained sandstone clasts (Fig. 6.2C). The clast-rich sandstone facies consists of structureless and ungraded beds with sharp, flat bases and tops. The clasts are well-rounded and have a high aspect ratio with an average length and height of 75 mm and 22 mm, respectively. The clasts were found to have a strong preferred alignment parallel to the bed base.

Interpretation

This facies resembles the deposit of a laminar debris flow or an upper-transitional plug flow, in which clay provides the cohesive forces required to support the sand grains and the sand and mud clasts (Iverson, 1997; Baas *et al.*, 2009, 2011; Talling *et al.*, 2012). *En-masse* freezing is interpreted to have produced the ungraded, structureless character of these clast-rich beds (Iverson, 1997; Talling *et al.*, 2012). The horizontal alignment of the clasts and their matrix-supported texture provides further evidence that the flow was laminar and cohesive, rather than dominated by turbulence, at the site of deposition. However, the flows could initially have exhibited turbulent behaviour to give the mud and sand clasts a rounded shape after erosion of these clasts from the substrate (Fonnesu *et al.*, 2017). This abrasion process could have helped the change from turbulent flow to laminar flow by the release of clay minerals (Fonnesu *et al.*, 2017). The high aspect ratio of the mud clasts may result from compaction of the bed.

Structured muddy sandstone (Smu)

Observations

The structured muddy sandstone facies (Smu) consists predominantly of mixtures of light blue-grey, very-fine grained to fine-grained sandstone, darker blue-grey mixed sandstone-mudstone, dark blue-grey siltstone, and black mudstone. The structured character of structured muddy sandstone comprises two bedform types: (1) asymmetric current ripples with angle-of-repose cross-lamination, generally larger in height and length than the current ripples in facies Ss, termed *large current ripples* herein (Fig. 6.2D); and (2) thin and long bedforms with low-angle cross-lamination (*c.* 12°), termed *low-amplitude bed-waves* (LABWs) herein. The large current ripples often climb supercritically, *i.e.*, with climbing angles sufficiently high to preserve the full ripple profiles. Most large current ripples are encased in siltstone or mudstone, with this fine-grained sediment thickly deposited at the base and lee side of the bedforms, as well as draping their crest and stoss side. The basal mudstone was found to coarsen upward and upstream to sandstone. The LABWs contain varying proportions of sandstone and mudstone, and occasionally climb on top of muddy surfaces. These large current ripples and LABWs are described and compared with 'classic' current ripples in more detail in Chapter 6.6. The bed bases are always sharp and mostly flat, but occasionally wavy. The bed tops are sharp or fine upward as well as flat and occasionally wavy.

Interpretation

The large current ripples in the structured muddy sandstone facies resemble the large bedforms formed below rapidly decelerated turbulence-enhanced transitional flow and lower transitional plug flow in the laboratory, in which high near-bed turbulence causes the height and length of the bedforms to increase compared to sandy current ripples (Baas *et al.,* 2016). The large current ripples climbed supercritically because of high sedimentation rates (Allen, 1971), here including clay, silt, and sand particles. This agrees with the behaviour of the rapidly decelerated turbulence-enhanced transitional flows and lower transitional plug flows of Baas *et al.* (2016). The muddy and silty bedform fronts, basal sections, and drapes are attributed to fine particles settling out of suspension during flow. To produce the muddy and silty basal division, the bedforms are inferred to have migrated across muds and silts that settled continuously in the troughs of these bedforms (Baas *et al.,* 2016). The fine-grained front of the bedforms resembles sediment-starved ripple profiles, suggesting that the bedform troughs were passively filled with mud or silt during the final phase of bedform migration and after the ripples stopped moving altogether. This was likely associated with a progressive decrease in flow velocity to below the threshold of sediment motion. The presence of the fine-grained drapes confirms that mud kept settling out of suspension after the ripples had stopped moving.

The low-amplitude bed-waves are interpreted to have been formed under lower transitional plug flows and upper transitional plug flows that contained varying proportions of sand and mud. In the laboratory, these flows have a high yield strength and reduced turbulence at the base, which limits the bedforms to long, thin shapes (Baas *et al.,* 2016). The low-angle cross-lamination forms as the gently inclined front of the bedforms migrates in the flow direction. Fine-grained sediment settling from suspension in front of the migrating bedforms is interpreted to generate the climbing muddy basal surfaces.

Heterolithic sandstone-mudstone (SMh)

Observations

The heterolithic sandstone-mudstone facies (SMh) is characterised by alternating bands and laminae of light blue-grey, very-fine grained to fine-grained sandstone and black mudstone, in which individual bands are up to 4 mm thick (Fig. 6.2E). The bands and laminae are plane-parallel or wavy. Most commonly, the thickness of the mudstone bands increases upwards in the beds. The heterolithic sandstone-mudstone facies has flat and either sharp or diffuse bases, and mostly flat and sharp tops. The bed tops occasionally fine upward.

Interpretation

The origin of the heterolithic character of heterolithic sandstone-mudstone is unclear. Previous explanations include: (a) phases of waxing and waning of mixed sand-mud gravity flows, where sand and mud are deposited at high and low velocity, respectively (Kneller, 1995); (b) individual, dilute turbidity currents deposit the sand layers and suspension settling of hemipelagic mud between turbidity current events produces the mudstone layers; (c) rapidly decelerated and highly depositional transitional sand-mud gravity flows of constant velocity, involving cannibalisation of bed material shortly after deposition as a result of reinstated turbulence at decreased flow density (Baas *et al.,* 2016); (d) a combination of slowly migrating, sandy low-amplitude bed-waves (Best & Bridge, 1992) and continuous suspension settling of fine sediment (Baas *et al.*, 2016); and (e) slurry flows that experience near-bed shear sorting (Lowe & Guy, 2000). The upward increase in mudstone band thickness may indicate an increase in mud content within the flow and a gradual temporal decrease in flow velocity.

Siltstone (Si)

Observations

The siltstone facies (Si) is composed of dark blue-grey siltstone, often structureless, but also with plane-parallel lamination. Individual laminae are less than 3 mm thick (Fig. 6.2F). Beds in facies siltstone are normally graded, producing gradual tops, or ungraded, with sharp tops. Almost all bed boundaries are flat and the base of the beds are always sharp.

Interpretation

The siltstone facies were formed by fine-grained, fully turbulent sediment gravity flows or lower transitional plug flows (Baas *et al.*, 2011), from which silt settled out of suspension. The plane-parallel lamination suggests the presence of tractional forces (Piper *et al.*, 1984; Talling *et al.*, 2012).

Silty-mudstone (Msi)

Observations

The silty-mudstone facies (Msi) consists of very dark grey, structureless mudstone with dispersed silt particles, marking it as an intermediate between the siltstone and mudstone facies (Fig. 6.2G). Slight variations in colour show variations in silt content. Bed bases and tops are sharp and flat.

Interpretation

The silty-mudstone facies is interpreted to have formed by fine-grained sediment gravity flows, in which silt particles were not segregated from clay particles during deposition. This suggests that the flows were sufficiently cohesive to prevent vertical segregation of silt and clay. In the laboratory, these flows included upper transitional plug flows and quasi-laminar plug flows (Baas *et al.*, 2011).

Mudstone (M)

Observations

The mudstone facies (M) comprises black uniform mudstone without primary current lamination (Fig. 6.2F). Bed bases and tops are usually flat and sharp, with a few examples of wavy tops and bases.

Slight variations in colour in the form of swirly textures are associated with variations in silt content in thick mudstone facies directly above silty and sandy event beds.

Interpretation

The mudstone facies was generated by hemipelagic settling between events or from the fine-grained components of sediment gravity flows (Bouma, 1962; Talling *et al.*, 2012). The swirly textures are interpreted to have been contained within the plug region of mud-rich, turbulence-attenuated gravity flows, undergoing *en-mass*e deposition (Baas *et al*., 2011; Stevenson *et al.,* 2014; their figure 16).

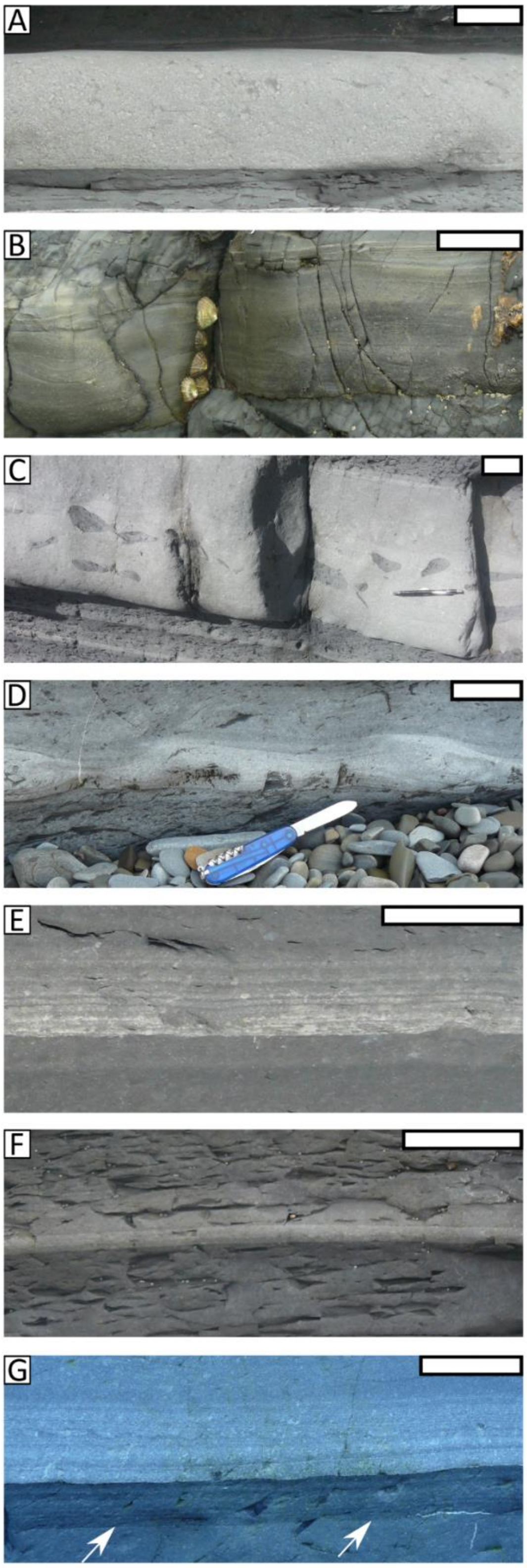

Figure 6.2: Representative outcrop photographs of the observed sedimentary facies: (A) massive sandstone, Sma; (B) structured sandstone, Ss; (C) clast-rich sandstone, Sc; (D) structured muddy sandstone, Smu, here with large current ripples; (E) heterolithic sandstone-mudstone, SMh; (F) siltstone, Si, within mudstone, M; (G) silty-mudstone, Msi (arrows point to the base of the bed). Scale bar is 50 mm long.

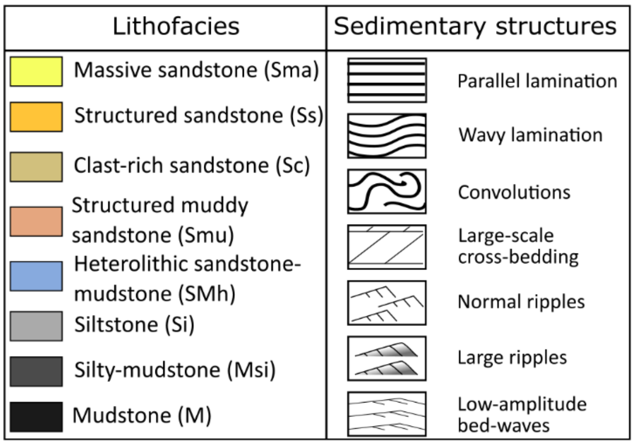

Figure 6.3: Key to lithofacies (with abbreviations) and sedimentary structures, shown in Figures 6.4 to 6.8.

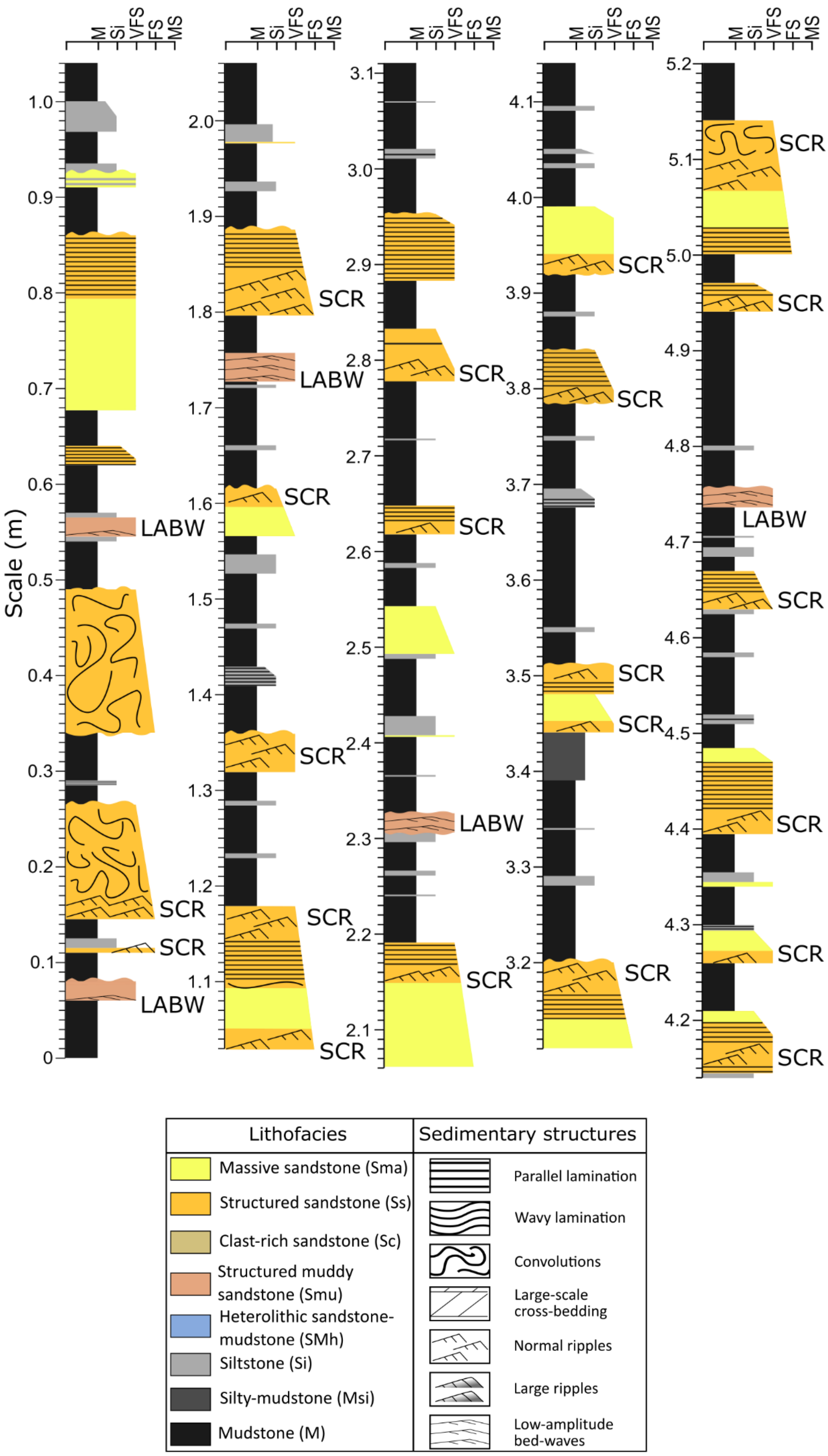

Figure 6.4: Sedimentary log A. Position is shown in Figure 6.1. SCR = sandy current ripples, LABW = low-amplitude bed-waves. Scale is in metres. Key to lithofacies shown below log.

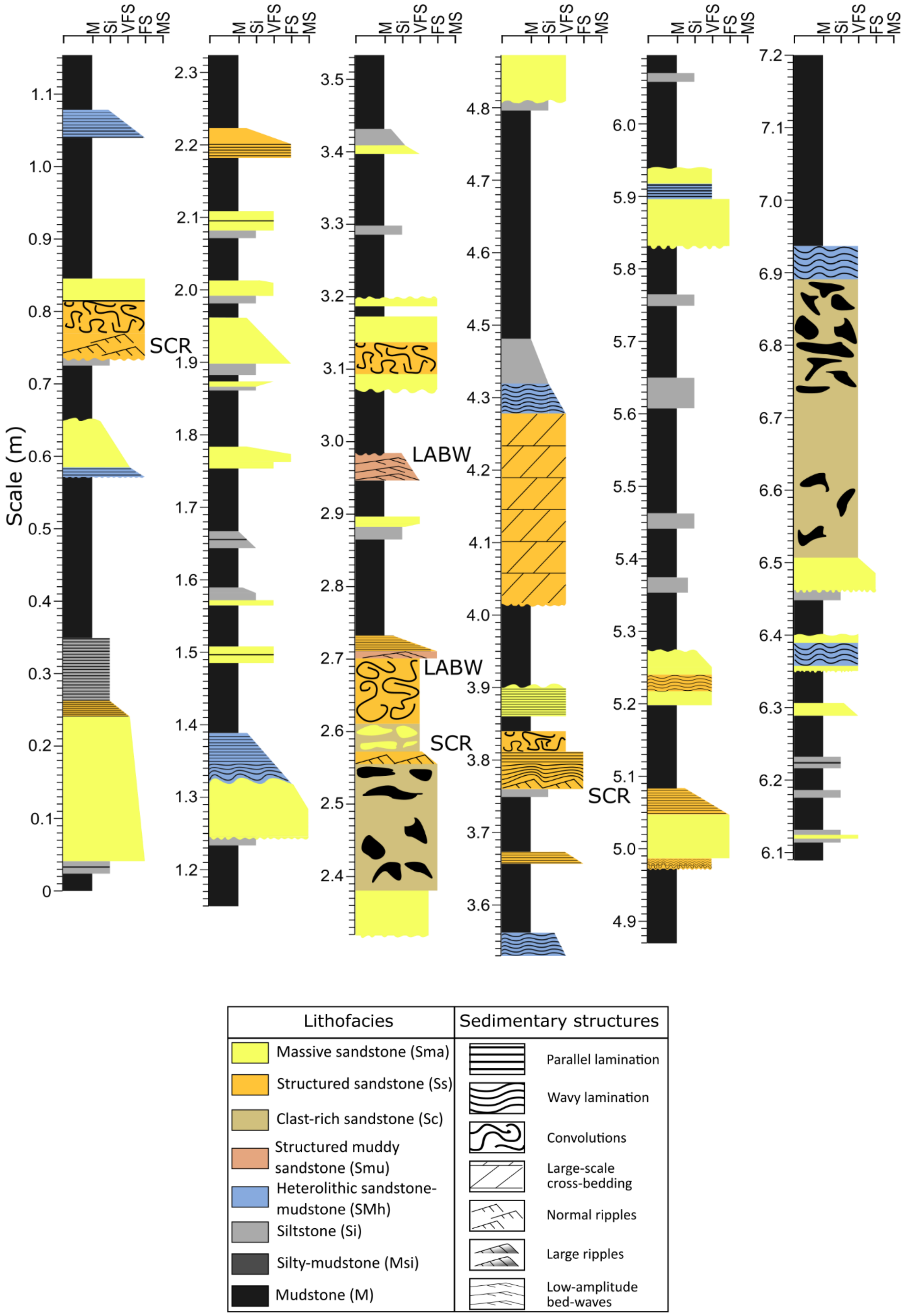

Figure 6.5: Sedimentary log B. Position is shown in Figure 6.1. SCR = sandy current ripples, LABW = low-amplitude bed-waves. Scale is in metres. Key to lithofacies shown below log

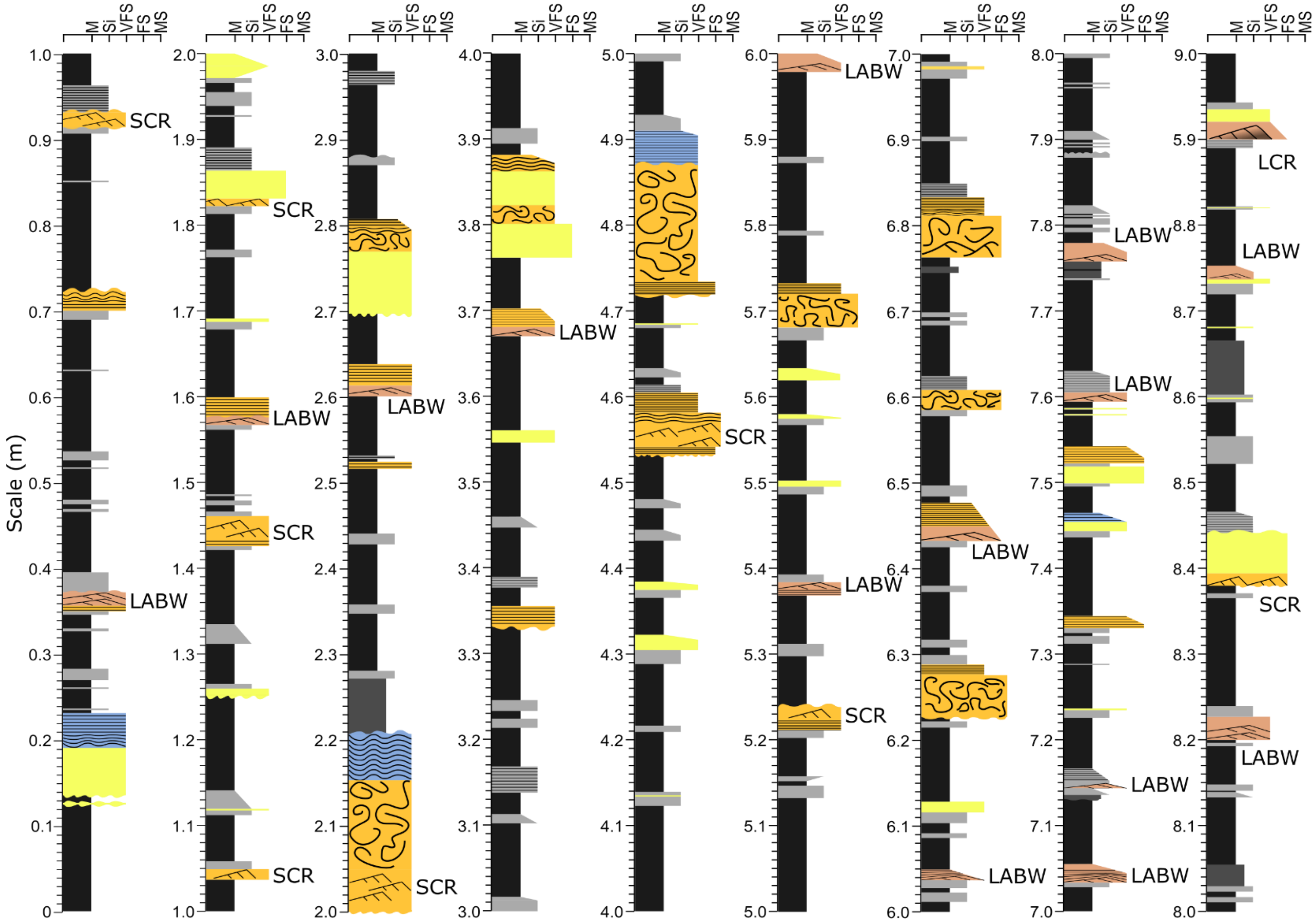

Figure 6.6: Sedimentary log C. Position is shown in Figure 6.1. SCR = sandy current ripples, LCR = large current ripples, LABW = low-amplitude bed-waves. Scale is in metres.

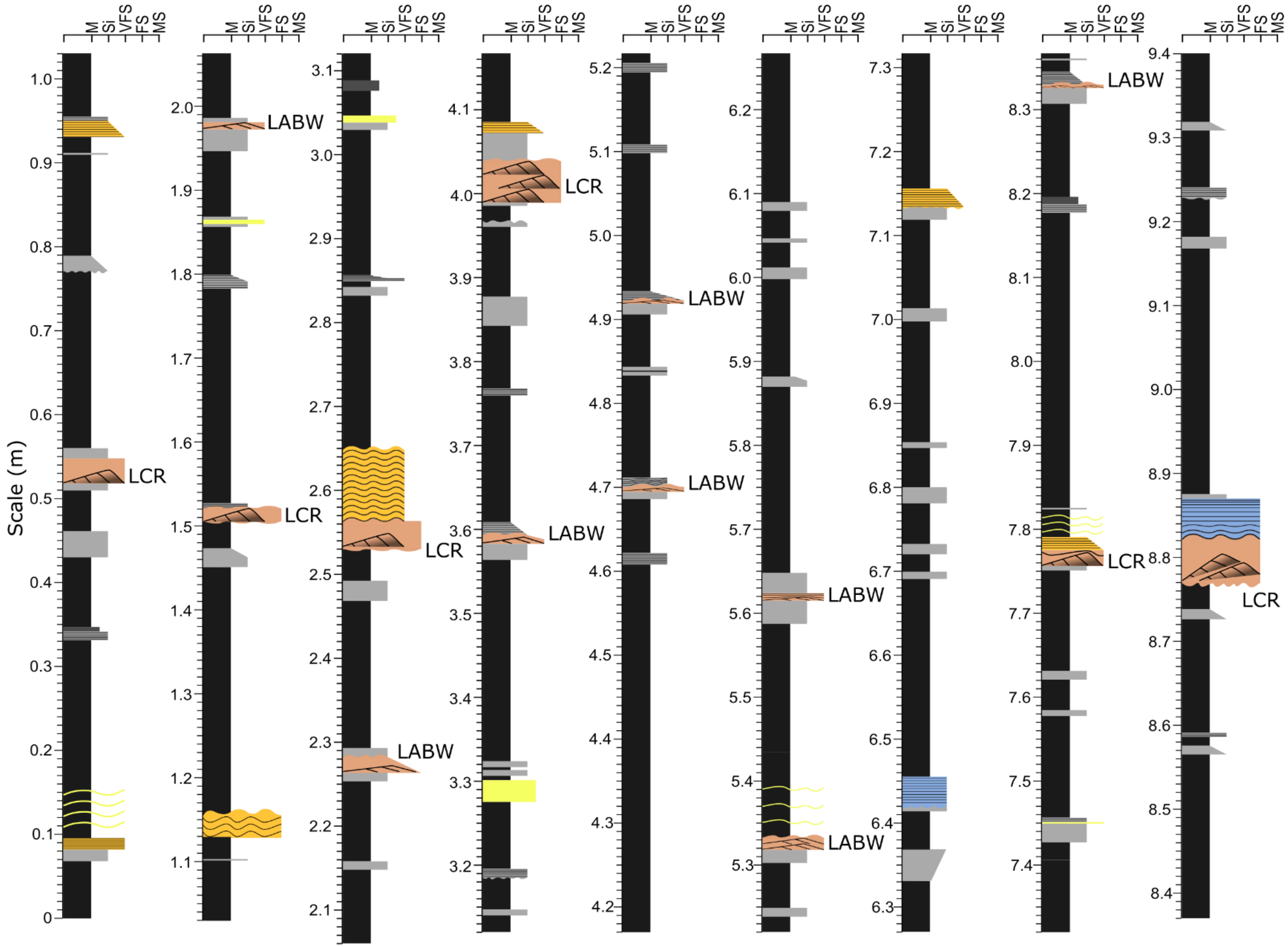

Figure 6.7: Sedimentary log D. Position is shown in Figure 6.1. LCR = large current ripples, LABW = low-amplitude bed-waves. Scale is in metres.

6.5 Facies associations

A total number of 762 vertical transitions between the different facies in the sedimentary logs (Figs 6.4 to 6.7) were analysed using Markov chain analysis. The observed counts and probabilities of the vertical transitions are given in Table 6.1, and the facies relationship diagram in Figure 6.8A shows the three most common vertical facies transitions for each facies type. The outcomes of the Markov chain analysis in combination with observations of the logs were used to construct common facies associations, which were then interpreted in terms of temporal changes in flow behaviour. It was assumed that the mudstone facies separated event beds.

Table 6.1: Results of the vertical facies transition analysis for the four logs. Facies in the columns overlie the facies in each row. The top value in each cell denote the probability of the vertical facies transitions. The number in brackets underneath represents the number of transitions of that pair. Sma = massive sandstone; Ss = structured sandstone; Sc = clast-rich sandstone; Smu = structured muddy sandstone; SMh = heterolithic sandstone-mudstone; Si = siltstone; Msi = silty-mudstone; M = mudstone.

	M	***Msi***	***Si***	***SMh***	***Smu***	***Sc***	***Ss***	***Sma***	***TOTAL***
M		0.01 (4)	0.73 (223)	0.01 (3)	0.03 (10)	0.00 (0)	0.11 (35)	0.10 (30)	305
Msi	0.56 (5)		0.22 (2)	0.00 (0)	0.00 (0)	0.00 (0)	0.22 (2)	0.00 (0)	9
Si	0.74 (200)	0.02 (5)		0.00 (1)	0.05 (14)	0.00 (0)	0.08 (21)	0.11 (30)	271
SMh	0.57 (8)	0.07 (1)	0.14 (2)		0.00 (0)	0.00 (0)	0.00 (0)	0.21 (3)	14
Smu	0.31 (8)	0.00 (0)	0.42 (11)	0.04 (1)		0.00 (0)	0.23 (6)	0.00 (0)	26
Sc	0.00 (0)	0.00 (0)	0.00 (0)	0.33 (1)	0.00 (0)		0.67 (2)	0.00 (0)	3
Ss	0.53 (38)	0.00 (0)	0.19 (14)	0.04 (3)	0.01 (1)	0.01 (1)		0.21 (15)	72
Sma	0.51 (39)	0.00 (0)	0.21 (16)	0.06 (5)	0.00 (0)	0.03 (2)	0.19 (15)		77

FA1: Fine-grained, thin-bedded turbidites and transitional flow deposits (Fig. 6.8B)

The Markov chain analysis highlights that the mudstone facies is most commonly overlain by the siltstone facies (probability, $p = 0.73$), and that siltstone is most frequently overlain by mudstone ($p = 0.74$). These isolated siltstone beds are always thin-bedded (< 0.05 m) and are interpreted to have been deposited by suspension settling from fine-grained turbidity currents. The presence of swirly textures in the mudstone facies overlying the siltstone facies, observed at Borth, suggests that the flows may have been cohesive; in these cases, FA1 could represent transitional flow deposits.

FA2: Thin-bedded turbidites (Fig. 6.8C)

This facies is mainly composed of massive sandstone or structured sandstone encased within mudstone, or within siltstone which then transitions upwards or downwards to mudstone. FA2 also includes isolated heterolithic sandstone-mudstone facies encased in mudstone. FA2 with the massive and structured sandstone facies is interpreted as the product of sandy turbidity currents. FA2 with heterolithic sandstone-mudstone may have involved turbulent flow or transient turbulent-laminar flow behaviour. FA2 is the only facies association appropriate for the interpretation that heterolithic sandstone-mudstone facies is formed by multiple turbidity currents separated by hemipelagic mud.

FA3: Medium-bedded turbidites (Fig. 6.8D)

Facies association FA3 is made up of thin- to medium-bedded (0.05 m to 0.30 m) structured sandstone, massive sandstone, and heterolithic sandstone-mudstone, as well as siltstone and mudstone facies. These facies are most commonly organised in partial Bouma sequences denoting waning turbidity currents (Bouma, 1962) and in sequences that represent waxing turbidity currents (*cf.* Kneller & Buckee, 2000). FA3 is interpreted as the depositional product of high-density turbidity currents if massive sandstone is the lowermost division. In the absence of massive sandstone, FA3 represents the deposits of low-density turbidity currents. The heterolithic sandstone-mudstone facies is mainly present near the top of FA3 and might therefore represent the T_d-division formed when the flow had waned and possibly attained transitional behaviour.

FA4: Clast-rich hybrid event beds (Fig. 6.8E)

The clast-rich sandstone facies was interpreted as an upper transitional plug flow or debris flow deposit and it forms the central division of facies association FA4. In FA4, clast-rich sandstone facies is typically underlain by massive sandstone, and overlain by either structured sandstone ($p = 0.67$) or heterolithic sandstone-mudstone ($p = 0.33$). These vertical sequences of facies resemble the products of hybrid flows *sensu* Haughton *et al.* (2009) and Baas *et al.* (2011), where the same flow event exhibits both laminar and turbulent flow behaviour. Here, a debris flow followed a forerunner high-density turbidity current or transient turbulent flow, and the tail of the event consisted of a low-density turbidity current (structured sandstone) or a transitional plug flow (heterolithic sandstone-mudstone).

FA5: Transitional flow deposits (Figs 6.8F and 6.8G)

Facies association FA5 includes a variety of distinctive facies successions that include the structured muddy sandstone facies, which was interpreted to be formed by flows with transient turbulent-laminar behaviour. These facies successions are therefore called transitional flow deposits *sensu* Kane & Pontén (2012).

Of the 25 upward transitions to structured muddy sandstone in the logs, 14 are from siltstone and ten are from mudstone, suggesting that the structured muddy sandstone facies are often near, or at, the base of an event bed. The structured muddy sandstone beds are overlain directly by mudstone (p = 0.31) or by the following facies in order of decreasing p-values: siltsone (p = 0.41), structured sandstone (p = 0.23), and heterolithic sandstone-mudstone (p = 0.04).

The structured muddy sandstone facies is the primary facies of interest in this study. Therefore, additional analysis was undertaken using a combination of logs and photographs to investigate the most common sequences of vertical facies transitions that include the structured muddy sandstone beds (Fig. 6.8H). These sequences were all bounded by mudstone or siltstone. At 42% probability, a single structured muddy sandstone facies between the fine-grained facies was most common. A quarter of the structured muddy sandstone beds transitioned to structured sandstone or heterolithic sandstone-mudstone. The final sequence, with a probability of 20%, was structured muddy sandstone, to clast-rich sandstone, via either heterolithic sandstone-mudstone or structured sandstone.

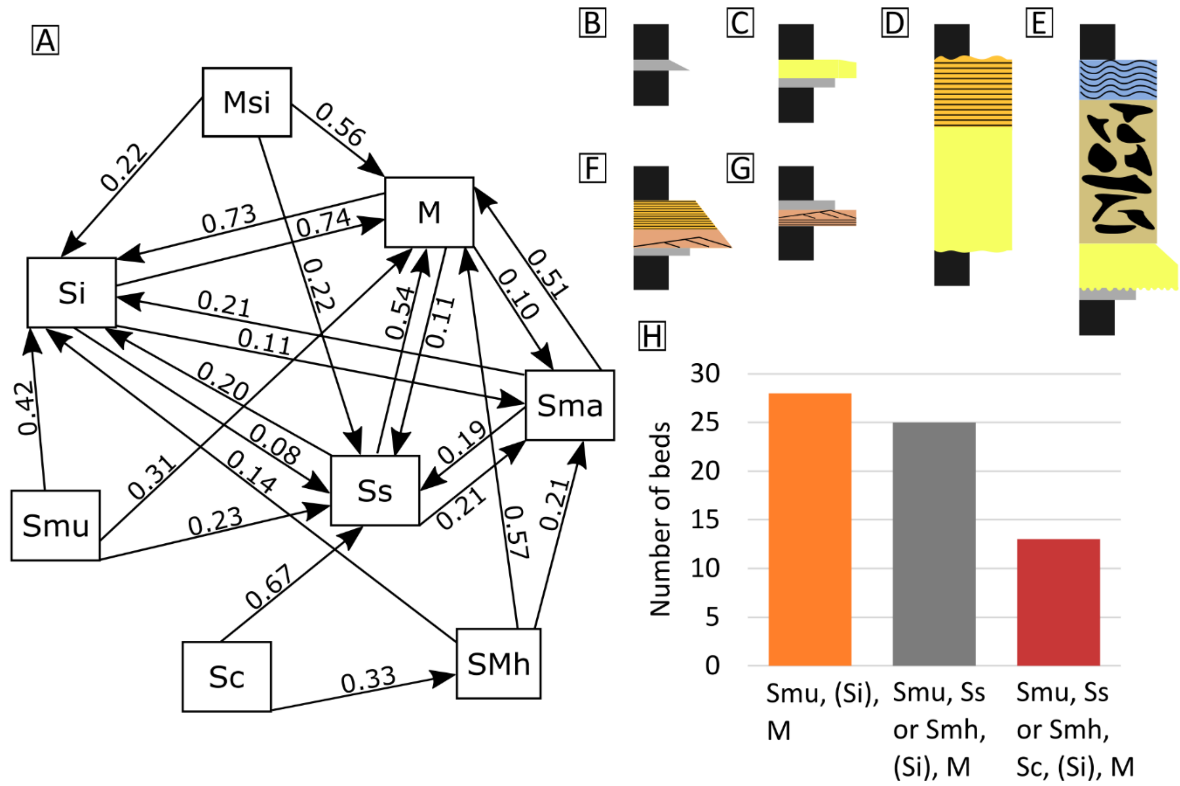

Figure 6.8: Results from the Markov chain analysis. (A) Transition tree showing the three most common vertical facies transitions for each facies type with the probability values. Sma = massive sandstone; Ss = structured sandstone; Sc = clast-rich sandstone; Smu = structured muddy sandstone; SMh = heterolithic sandstone-mudstone; Si = siltstone; Msi = silty-mudstone; M = mudstone. (B) to (G) show the facies associations identified from the transition tree: (B) Fine-grained thin-bedded turbidites and transitional flow deposits, FA1; (C) thin-bedded turbidites, FA2; (D) medium-bedded turbidites, FA3; (E) clast-rich hybrid event beds, FA4; and (F) and (G) transitional flow deposits, FA5. (H) Plot of the three common vertical facies transitions that include the structured muddy sandstone facies, based on logs and photographs. All structured muddy sandstone beds are above either a mudstone or siltstone. Siltstone at the top of the event beds is not always present and thus shown in brackets. The most common transition is from structured muddy sandstone directly to mudstone, or to mudstone via siltstone (in orange), which corresponds to facies association FA5, shown in (G). The second most likely transition is structured muddy sandstone to either structured sandstone or heterolithic heterolithic sandstone-mudstone to either mudstone, or siltstone to mudstone (in grey), which corresponds to facies association FA5, shown in (F). The final 20% of the structured muddy sandstone facies were in the following sequence: structured muddy sandstone - heterolithic sandstone-mudstone or structured sandstone - clast-rich sandstone - siltstone - mudstone, or directly from clast-rich sandstone to mudstone (in red).

6.6 Sand-mud sedimentary structures

The sedimentary logs, as well as other outcrops in the study area, revealed bedforms in mixed sandstone-mudstone that have not been described in detail in outcrop and core before. The large current ripples (Figs 6.11 and 6.12) and low-amplitude bed-waves (Figs 6.13 and 6.14) in the structured muddy sandstone facies of FA5 stand out as having shapes, dimensions, and textural and structural properties that are different from the ‘classical’ sandy current ripples in the structured sandstone facies of FA2 and FA3 (Figs 6.9 and 6.10). Figure 6.15 shows the average height and length of the sandy current ripples, the large current ripples and the low-amplitude bed-waves. The diagnostic properties of each bedform type are described below.

6.6.1 Sandy current ripples

The sandy current ripples (facies Ss) in the study area have an asymmetrical shape with a steep lee slope angle of up to 30° and a gentle, longer, stoss slope angle. These bedforms contain high-angle cross lamination with little variation in grain size (Figs 6.9 and 6.10). The sandy current ripples are between 4 and 19 mm high (average height, H = 11 mm; standard deviation, σ = 3 mm) and between 89 and 216 mm long (average length, L = 141 mm; σ = 31 mm; Fig. 6.15). These heights and lengths are within the range of current ripples defined by Baas (1999, 2003). The aspect ratio, defined as the bedform height divided by bedform length, of the sandy current ripples ranged from 0.041 mm to 0.141 mm (average aspect ratio, A = 0.076 mm, σ = 0.024 mm).

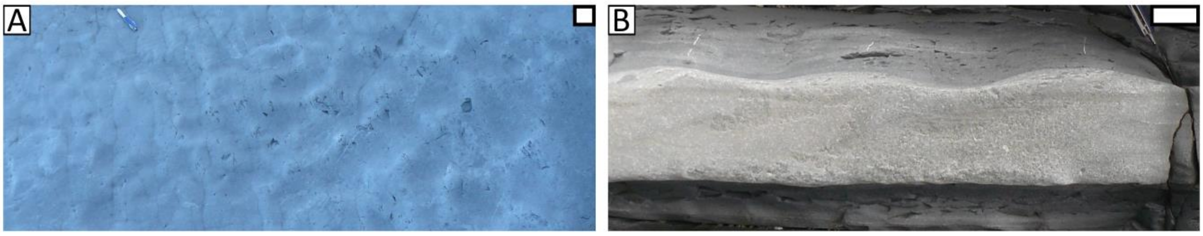

Figure 6.9: Examples of sandy current ripples found in the field. (A) ripples in bedding plane, predominantly with a three-dimensional structure, but with some linearity of the crests in the bottom right of the photo. (B) sand-dominated ripples with angle-of-repose cross-lamination. Scale bar is 50 mm long.

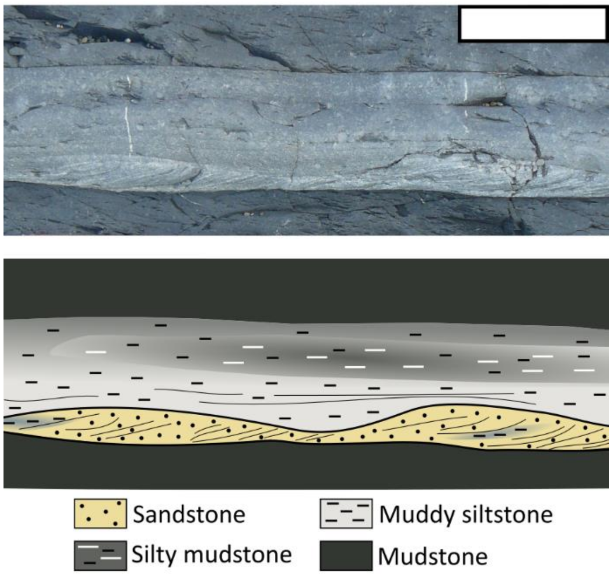

Figure 6.10: Schematic drawing of sandstone-dominated sandy current ripples, note the high-angle cross lamination. Scale bar is 50 mm long.

6.6.2 Large current ripples

The large current ripples in the structured muddy sandstone facies have heights ranging from 13 mm to 31 mm (H = 19 mm; σ = 4 mm) and lengths ranging from 145 mm to 433 mm (L = 274 mm, σ = 60 mm). These dimensions are significantly greater than those of the sandy current ripples in the field area (Fig. 6.15). The aspect ratio of the large current ripples ranged from 0.042 mm to 0.102 mm (A = 0.070 mm, σ = 0.016 mm). The large current ripples have a variety of forms and textural and structural properties. Many large current ripples have a muddy or silty front, which coarsens to sand in an upstream direction within the bedform (Fig. 6.11B). Muddy and silty bases that coarsen vertically upward to sand within the bedform were also common (*e.g.*, Figs 6.11A and 6.12). Some large current ripples had loaded into mud below (Fig. 6.11C). Thin mudstone layers commonly drape the surface of the large current ripples. These mud drapes tend to extend into the bedform trough and therewith contribute to the trough fill (Fig. 6.12). Many large current ripples in the field area are climbing bedforms (Figs 6.11A and 6.11B) with clear high-angle cross lamination (Fig. 6.12) and occasional plane-parallel lamination at the base or top of the co-sets (Fig. 6.11A). Some of the lamination consists of alternating sandstone and mudstone (Fig. 6.12). When observed on the bedding plane, the large current ripples have pronounced sharp high crests and nearly linear, two-dimensional crest lines (Fig. 6.11D).

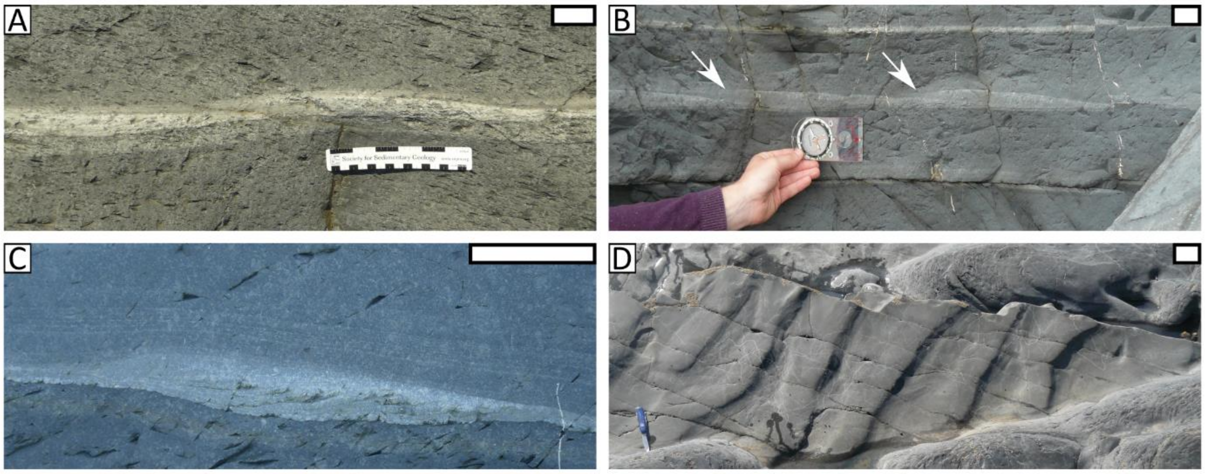

Figure 6.11: Examples of large current ripples found in the field. (A) Climbing bedforms with a muddy base. (B) Climbing bedforms with muddy fronts shown by the arrows. (C) Large ripple loaded into the bed below. (D) In the bedding plane, large ripples show prounounced, almost linear, two-dimensional crest lines. Scale bar is 50 mm long.

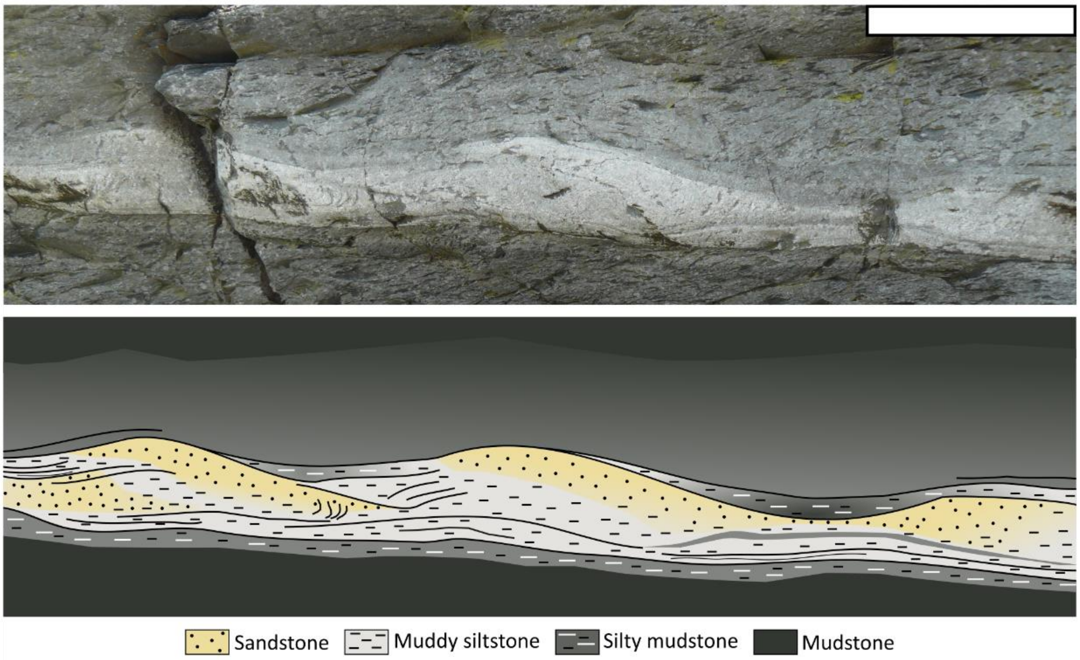

Figure 6.12: Schematic drawing of large current ripples with muddy bases and fronts that coarsen upward and upstream to sandstone. Bedforms contain high-angle cross lamination, occasionally of alternating sandstone and mudstone. Scale bar is 50 mm long.

6.6.3 Low-amplitude bed-waves

The low-amplitude bed-waves (LABWs) are bedforms with unusually long lengths of 140 mm to 818 mm (L = 354 mm, σ = 92 mm) and relatively short heights of 4 mm to 16 mm (H = 10 mm, σ = 3 mm) (Fig. 6.15). The LABWs had aspect ratios ranging from 0.013 mm to 0.046 mm (A = 0.028 mm, σ = 0.008 mm). These bedforms resemble the bed-waves in sand identified under upper-stage plane bed flow conditions by Bridge and Best (1988), who defined the term LABW, and similar bedforms generated under a range of flow velocities and flow yield strengths in the experiments of Baas *et al.* (2016). The LABWs in the field are composed of clean sandstone, or, more commonly, mixed sandstone-mudstone. The mixed sandstone-mudstone LABWs often have muddy or silty fronts and bases which coarsen upward and upstream to sandstone; this can make the front of the bedforms hard to distinguish (Figs 6.13A and 6.14). These fine-grained bases and fronts are particularly clear in climbing LABWs, whose climbing surfaces are therefore mudstone-rich (Figs 6.13A and 6.14). The sandy LABWs are frequently isolated within mudstone, giving the bedforms a lenticular appearance (Fig. 6.13B). Internally, the LABWs contain low-angle cross lamination of *c.* 12° and infrequently plane-parallel lamination near the upflow end of the bedforms (Fig. 6.14). In the mixed sandstone-mudstone LABWs, these stratification types consist of alternations of sandstone and mudstone (Fig. 6.14).

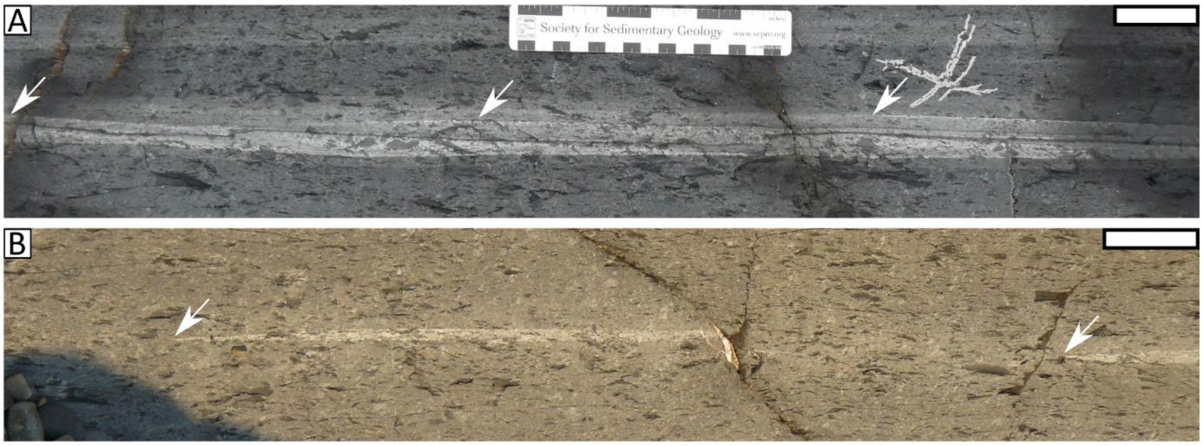

Figure 6.13: Examples of LABWs found in the field. (A) Climbing, mixed sandstone-mudstone LABWs with muddy fronts; arrows point to the crests of the LABWs. (B) Lenticular shaped, sandstone-dominated LABWs isolated in mudstone; arrows point to front of bedforms. Scale bar is 50 mm long.

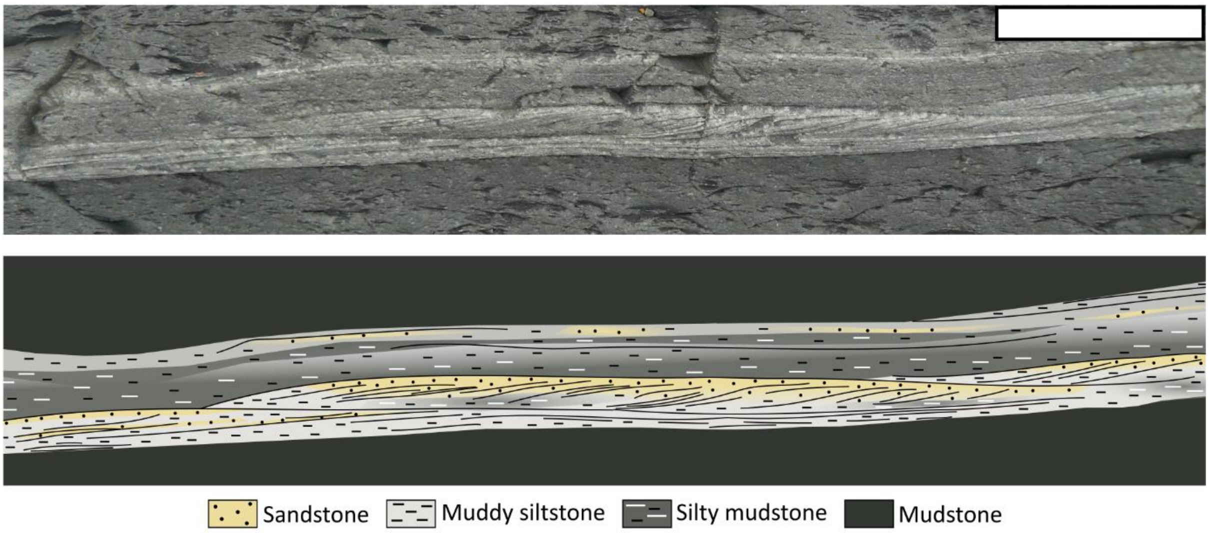

Figure 6.14: Schematic drawing of climbing, mixed sandstone-mudstone LABWs with muddy bases and fronts, that coarsen upward and upstream to sandstone and low-angle cross-lamination. Scale bar is 50 mm long.

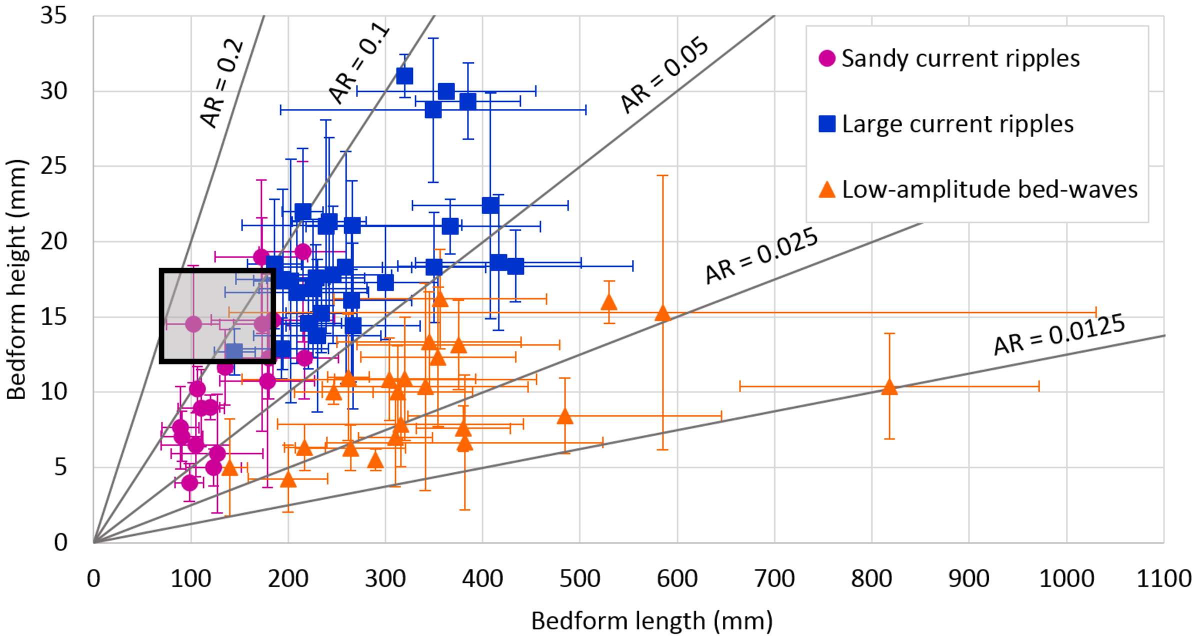

Figure 6.15: Height and length of the different bedform types throughout the field area. AR = aspect ratio. Black box represents the expected height and lengths of ripples composed of grain sizes from 20 µm to 700 µm predicted by Baas et al. (1993).

6.6.4 Process interpretation of the bedforms

The laboratory experiments of Baas *et al.* (2011, 2016) demonstrated that flows carrying sand, silt and clay change from turbulent via transitional (*sensu* Baas *et al.*, 2009) to laminar as the proportion of cohesive clay is increased. The transitional flows produced different types of bedform and primary current stratification that were delimited in a bedform phase diagram based on the cohesive forces in the flow (via the yield strength) and the turbulent forces (via a grain-related mobility parameter, defined in equation 3 by Baas *et al.,* 2016). It is proposed that the balance between these forces also controls the properties of natural sediment gravity flows and their deposits, and the bedform phase diagram can therefore be used to interpret the mixed sandstone-mudstone bedforms in the AGG and BMF. Figure 6.16 shows a schematic summary of the bedform phase diagram of Baas *et al.* (2016).

Sandy current ripples were produced in the laboratory under mixed sand-mud flows with low yield strength (≤ 0.03 Pa) and grain-related mobility parameters of up to 1.1 (turbulent flow of Baas *et al.,* 2016; Fig. 6.16). The low yield strength of these flows implies that the turbulent fluctuations in flow velocity were strong enough to prevent the clay minerals from forming bonds. The dynamics of these flows were therefore interpreted to be similar to clearwater flows, where the frictional forces between the flow and substrate shaped the bed into 'classical' current ripples, which are typically <20 mm high and <200 mm long, with aspect ratios of <0.1 mm (Baas, 2003). The average height (H = 11 mm), length (L = 141 mm), and aspect ratio (A = 0.076 mm) of the sandy current ripples in the AGG are within this range. These ripples are therefore interpreted to have formed under fully turbulent conditions, *i.e.*, by turbulent sandy gravity flows (equivalent to turbulent flow of Baas *et al.* (2016); Fig. 6.16).

Another type of current ripple produced in the laboratory by decelerated mixed sand-mud flows was characterised by heights and lengths that were greater than the dimensions of sandy current ripples (Baas *et al.,* 2011). These so-called large ripples contained sand, silt and clay that were distributed differently within the bedform as a function of ripple development stage. Initially, the bedforms had a muddy core below cross-laminated sand which then developed into cross-laminae consisting of alternating mud and sand, and finally into mixed sand-mud cross-laminae (Baas *et al.,* 2011; their figure 14).

The bedforms classified as large current ripples in the study area are comparable to the large current ripples of Baas *et al.* (2011) in their mixed sand-mud composition, large size, muddy base, and alternating sand-mud cross-laminae. In the laboratory, the large current ripples formed under the same range of mobility parameters as the sandy current ripples, but the flows had greater yield strengths (0.03-3 Pa; Fig. 6.16). These flows were classed as turbulence-enhanced transitional flows and lower transitional plug flows (Baas *et al.,* 2016), in which near-bed turbulence was enhanced because the cohesive strength of the flows promoted the development of an internal shear layer. This increased turbulence caused stronger erosion in the lee of the bedforms, thus increasing their height and length compared to sandy current ripples (Baas *et al.,* 2011). It is therefore inferred that the large current ripples in the AGG and the BMF were formed by sediment gravity flows with turbulence-enhanced transitional flow and lower transitional plug flow behaviour. The fact that the large ripples observed in the field area were dominated by muddy bases and alternating sandstone-mudstone cross-laminae suggests that these bedforms were in a relatively early stage of development, as in the experiments of Baas *et al.* (2011). This agrees with the generally short migration distance of the climbing large ripples (*e.g.*, Fig. 6.12), which is typical of rapidly decelerated and highly depositional sediment gravity flows.

The laboratory experiments of Baas *et al.* (2016) also produced long, thin bedforms – low-amplitude bed-waves (LABWs) – with heights of 3 mm to 16 mm and lengths of 70 mm to 5000 mm. These bedforms consisted of sand or mixed sand-mud, where the sand and mud were either uniformly mixed or heterolithic. Low-angle cross-lamination in the LABWs was often composed of alternating laminae of sand and mud. The lowest 20-30% of the mixed sand-mud LABWs was usually rich in mud. These properties are analogous to those observed in the field. Although found in lower transitional plug flow, the experimental LABWs were most typically produced by upper transitional plug flows at a wide range of mobility parameters, covering flows that would form upper-stage plane bed, washed-out ripples and sandy current ripples in clay-poor turbulent flow (Baas *et al.,* 2016; Fig. 6.16). These LABWs formed at yield strength between ~1 to 4 Pa in plug flows with attenuated turbulence at the base (Baas *et al*., 2009). The LABWs in the AGG and BMF are inferred to have formed under similar flow conditions.

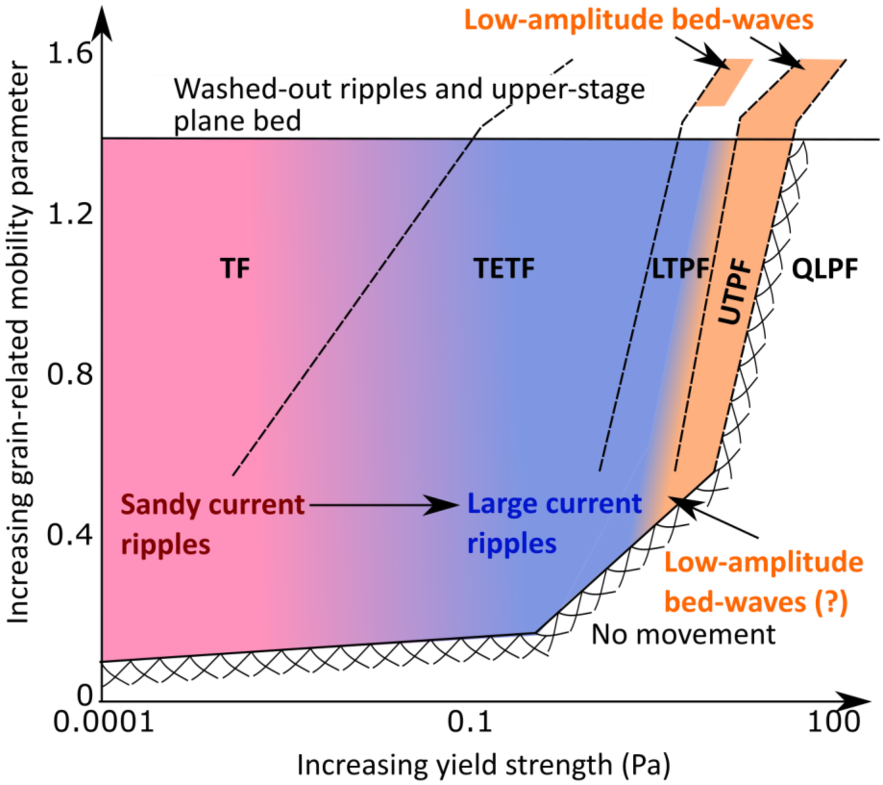

Figure 6.16: Schematic summary of the bedform phase diagram of Baas et al. (2016) for rapidly decelerated mixed sand-mud flows, based on grain-related mobility parameter and yield strength of the suspension. The colours represent the stability fields of the three bedform types mentioned in this study. The dashed lines represent the boundaries between the different flow types. Note that this diagram is based on a limited range of boundary conditions; in particular, the field boundaries of the low-amplitude bed-waves are approximate at present. TF = turbulent flow, TETF = turbulence-enhanced, LTPF = lower transitional plug flow, UTPF = upper transitional plug flow, QLPF = quasi-laminar plug flow.

6.6.5 Spatial distribution of the bedforms in the field area

Figure 6.17 shows the spatial distribution of the sandy current ripples, large current ripples, and LABWs throughout the study area, subdivided into four sections of the coastal outcrops from the fringe to the distal fringe of the fan. In the most proximal part of the study area, between Aberystwyth and Clarach Bay, sandy current ripples are the most common bedform type, followed by LABWs, with only a few examples of large current ripples (Fig. 6.17). Moving north and more distally, the number of sandy current ripples decreases, and no sandy current ripples are present at Borth. Large current ripples are the most common bedform type in the two central sections of the study area, although

LABWs are also widespread (Fig. 6.17). At Borth, LABWs account for the largest proportion of bedform types, with subordinate occurrences of large current ripples.

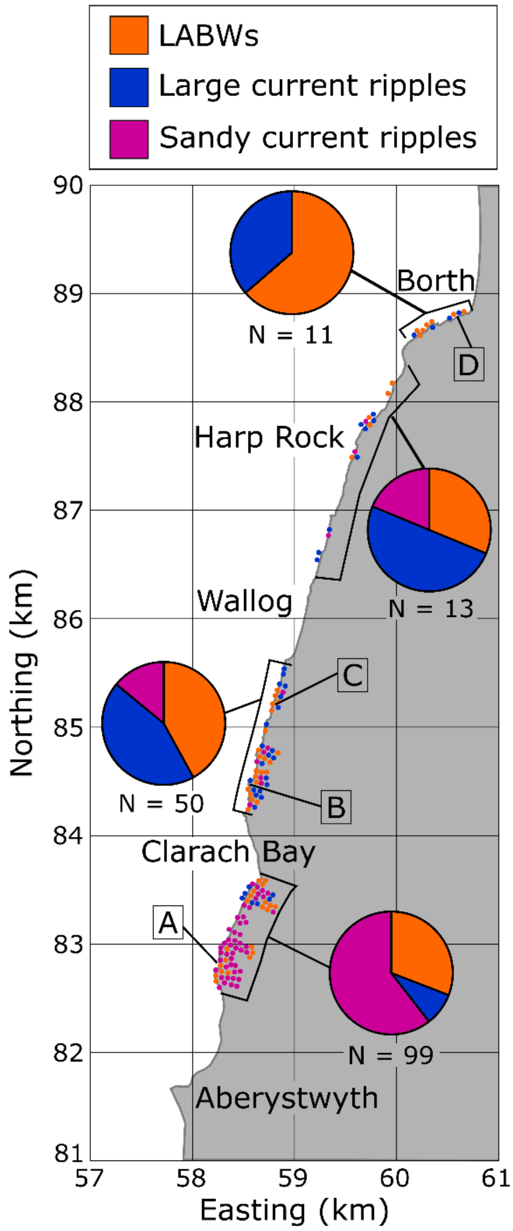

Figure 6.17: Spatial distribution of the bedforms in the field area. Each dot represents a bedform observation. Pie charts show proportion of bedform types for each section of accessible outcrop. Letters A to D show locations of the logs. N = number of bedforms for the pie chart, LABWs = low-amplitude bed-waves.

6.7 Discussion

6.7.1 Using bedforms to infer flow processes in the fringe regions of the AGG and BMF

Baas *et al.* (2016) showed that flow type and bedform type are closely linked. In the laboratory, increasing the clay concentration caused turbulence modulation and changed turbulent flow via transitional flow to laminar flow, which in turn produced sandy current ripples, large current ripples, and LABWs (Fig. 6.16). In the AGG and BMF, the dominant bedform type changed from sandy current ripples via large current ripples to LABWs from the fringe of the system near Aberystwyth to the distal fringe of the system at Borth. However, it is important to note that for each of the four sections of outcrop an assemblage of bedforms was observed, which attests to a variety of flow types reaching individual locations. The observed change in the prevailing bedform type from Aberystwyth to Borth indicates that many of the flows transformed from turbulent flow, via turbulence-enhanced transitional flow and lower transitional plug flow, to upper transitional plug flow as they travelled through the fringe to the distal fringe of the fan, this is summarised in Figure 6.18.

Flow transformation has been shown to be key in interpreting spatial trends in deposit type in the fringe of other deep-marine systems, such as Late Jurassic fans in the northern North Sea (Haughton *et al.*, 2003) and in the Tanqua Karoo system (Kane *et al.*, 2017). Flow transformation occurs when flows react to changing boundary conditions. Consequently, the flow may alter its velocity, deposit or erode sediment, incorporate water and increase the flow height, or dewater and reduce the flow height. The Reynolds number, *Re*, can be used to describe flow behaviour and transformation, representing the ratio of inertial and viscous forces:

$$Re = \frac{Uh}{\nu} \tag{6.1}$$

where *U* is the depth-averaged current velocity, *h* is the flow height, and ν is the apparent kinematic viscosity. Apparent viscosity is used for non-Newtonian suspensions, such as shear thinning clay-laden flows, where the viscosity parameter changes with shear rate. *Re* can be used to differentiate flow types: high *Re* values represent fully turbulent flows and low *Re* values characterise laminar flows, with transitional flow behaviour found between these two end members. In the experiments of Baas *et al.* (2009), the boundary between laminar flow and transitional flow was at *Re* = 7,000 and the boundary between turbulent flow and transitional flow was at *Re* = 55,000.

To produce the observed changes in dominant bedform type from Aberystwyth to Borth, the inferred flow transformation from turbulent flow to upper transitional plug flow, via turbulence-enhanced transitional flow and lower transitional plug flow, requires *Re* to decrease from the fringe to the distal fringe of the basin. Below, *Re* is used to interpret which flow parameters in Equation 6.1 altered as the flows transformed through the study site and prompted the observed trend in dominant bedform type. In our *Re*-based analysis, it is assumed that the sediment gravity flows were predominantly depositional and did not erode sediment from the bed in the studied part of the fan. This is supported by the fact that the log data and other observations in the field area lack evidence for deep erosion (Figs 6.4 to 6.7) and demonstrate that the flows progressively lost sand and silt, and thus the relative proportion of mud in the flow increased, from the fringe to the distal fringe of the system. These textural changes are expressed by thickening mudstone facies, decreasing frequency and thinning of massive sandstone and structured sandstone facies, and an increase in the number of structured muddy sandstone and heterolithic sandstone-mudstone facies. In turn, these facies changes provide further evidence for the inferred transformation from turbulent via transitional to laminar flows, resulting from the decrease in *Re*.

The progressive loss of sand and silt between the fringe to the distal fringe of the fan implies that the density difference between the flow and the ambient fluid was reduced, thus leading to the deceleration of the sediment gravity flows. The thick mudstone caps at Borth suggest that large amounts of clay were carried to the fringe of the fan (see Chapter 6.7.2, Mudstone cap analysis). It is therefore unlikely that the viscosity of the flows decreased as a result of clay deposition along the transport path. Instead, we expect the viscosity to have increased because of the shear thinning nature of the clay-rich flows. Shear thinning behaviour enables the viscosity to increase at a constant clay concentration when a reduction in flow velocity, and hence shear rate, enables a network of cohesive bonds between clay particles to develop (Coussot, 1997; Talling, 2013). Equation 6.1 demonstrates that the deceleration of the cohesive sediment gravity flows between Aberystwyth and Borth, and the increased viscosity due to shear thinning, both contribute to a reduction of *Re*, thus aiding the flow transformation.

The flow height term in *Re* is difficult to interpret from the rock record, as the deposits of only quasi-laminar plug flows, *i.e.,* debris flows, can be related to the original flow thickness (Kneller & Branney, 1995; Talling *et al.*, 2012). However, laboratory experiments have shown that the amount of mixing at the upper boundary of sediment gravity flows decreases as the flow viscosity increases (Marr *et al.*, 2001; Mohrig & Marr, 2003; Baker *et al.*, 2017). Increasing the stability of the upper boundary reduces the ability of the flow to incorporate water. Given the inferred increase in viscosity from the fringe to the distal fringe of the fan, it is therefore unlikely that flow height was able to increase much along this transect. Numerical models and numerical simulations constrained by field data also suggest that steady state turbidity currents form stratified flows with a lower layer of consistent flow height that contains the majority of the suspended sediment (Kneller *et al.,* 2016; Luchi *et al.,* 2018). It is also unlikely that the flow height decreased due to radial spreading of the flows, as the flows were confined within a linear upper crustal fault trough (Cherns *et al.,* 2006; Gladstone *et al.,* 2018). In addition, the deposition of sand and silt between Aberystwyth and Borth induced by flow deceleration could have decreased the flow thickness (Kneller & Branney, 1995). A constant or decreasing flow height in combination with flow deceleration and increasing flow viscosity, as the flows travelled from the fringe to the distal fringe of the fan, would further reduce *Re*, promote flow transformation, and explain the observed trend in dominant bedform type (Fig. 6.18).

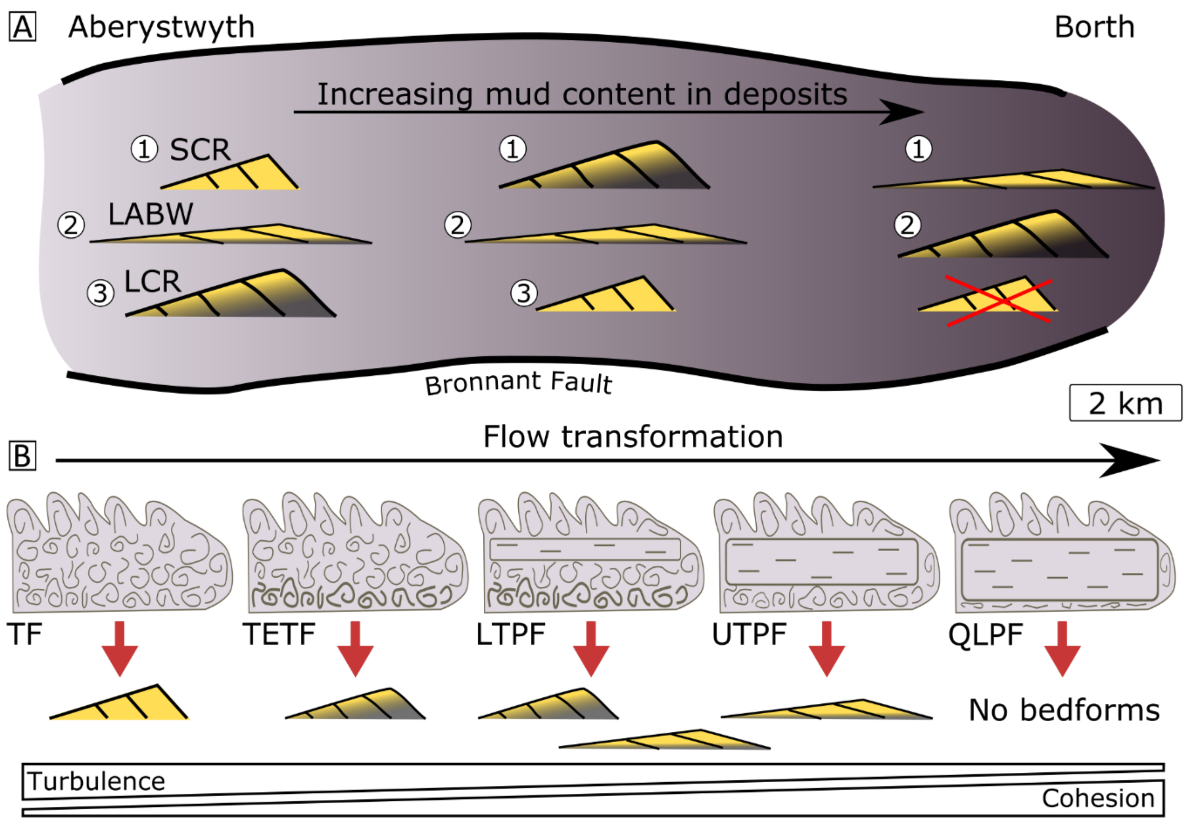

Figure 6.18: (A) Schematic plan view of the fringe to distal fringe of the fan within the AGG and BMF, confined within an elongate sub-basin of the Welsh Basin, with the different bedform assemblages found throughout the studied part of the fan. Numbers in (A) denote observed bedform type in order of decreasing frequency. SCR = sandy current ripples, LCR = large current ripples, LABW = low-amplitude bed-waves. (B) Model of flow transformation from the fringe to the distal fringe of the fan, and the link between sediment gravity flow dynamics and the bedforms produced.

6.7.2 Mudstone cap analysis

Turbiditic and hemipelagic mudstone cannot be visually distinguished from each other in the AGG and BMF (Talling, 2001). However, part of the mudstone facies in the fringe of the system around Borth contained slight variations in colour in the form of swirly textures, associated with coherent variations in silt content. These swirly textures are interpreted to have been confined within the plug region of a mud-rich, turbulence-attenuated upper transitional plug flow or quasi-laminar plug flow, which underwent *en-masse* deposition enabling the structures to be preserved (Stevenson *et al.,* 2014). Hemipelagic settling is unlikely to produce these swirly textures. Moreover, the thickness of mudstone facies of hemipelagic origin are not expected to correlate with the thickness of underlying event beds. Instead, it was hypothesised that larger events produce thicker flow-derived mudstone caps. To determine if an event bed and the mudstone facies above it were indeed formed by the same flow, linear regression analysis was undertaken comparing the thickness of the event beds and the overlying mudstone facies in the four sedimentary logs. The best-fit line between event bed and mudstone cap thickness was forced through the (0,0) intercept.

No statistically significant correlation between event bed thickness and mudstone cap thickness was found for logs A to C. However, for log D located at Borth, these thicknesses correlate positively, with an $R^2 = 0.27$ ($P < 0.01$; Fig. 6.19). This supported our hypothesis that a statistically significant number of the mudstone caps were flow derived. These mudstone caps were partly formed by *en masse* freezing of upper transitional plug flows and quasi-laminar plug flows, which led to the preservation of the swirly silt textures. The lack of correlation between the thickness of the event beds and their mudstone caps in logs A to C is interpreted to result from the mud dominantly bypassing in faster, more turbulent flows. This finding supports the spatial distribution of the bedform types through the system, which was interpreted above to indicate longitudinal flow transformation to increasingly cohesive transitional flows at the fringe of the fan at Borth.

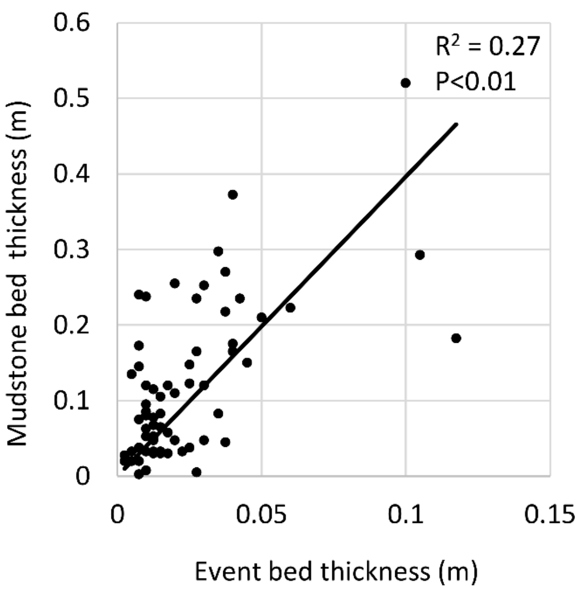

Figure 6.19: Event bed thickness and overlying mudstone bed thickness for log D. Black line denotes least-squares linear fit to data.

6.7.3 Hybrid event beds in the fringe region of a mud-rich submarine fan

Figure 6.8H shows that structured muddy sandstone facies can be part of the following facies sequence: structured muddy sandstone - heterolithic sandstone-mudstone - clast-rich sandstone - siltstone - mudstone, or directly from clast-rich sandstone to mudstone. This sequence resembles the hybrid event bed model of Haughton *et al.* (2009), where: (i) heterolithic sandstone-mudstone is equivalent to the H2 division of banded mud-poor sandstone and mud-rich sandstone, formed by transitional flow; (ii) facies clast-rich sandstone fits the H3 section of argillaceous sandstone rich in sandstone and mudstone clasts, formed by debris flow; and (iii) siltstone and mudstone resemble the H4 and H5 divisions, formed by low-density turbidity current and mud suspension fallout (*cf.* Fig. 6.20). The structured muddy sandstone facies at the base of these event beds diverges from the basal H1 division in the model of Haughton *et al.* (2009) by being structured and consisting of mixed sandstone-mudstone instead of comprising massive and structureless sandstone (Fig. 6.20). In the Haughton *et al.* (2009) model, the H1 division was interpreted to have formed by a non-cohesive, high-density turbidity current. An alternative explanation for the AGG and BMF is proposed below.

Hybrid event beds have been defined as deposits produced by flows which transform from poorly cohesive, turbulent to cohesion-dominated (Haughton *et al.*, 2009; Fonnesu *et al.*, 2015; Pierce *et al.,* 2018). Based on the observations in the AGG and BMF, we propose that mud-rich hybrid event beds at the fringe of a system may contain argillaceous H1 divisions with mixed sandstone-mudstone bedforms. The H1 division in these mud-rich hybrid event beds need not be formed by a high-density turbidity current, but could result from transitional flow, in which flow turbulence is modulated by cohesive forces throughout deposition, as also previously suggested by Baas *et al.* (2011). By analogy to the laboratory experiments of Baas *et al.* (2009), these flows could include turbulence-enhanced transitional flow, lower transitional plug flow, and upper transitional plug flow. If hybrid event beds with large current ripples and LABWs in basal mixed sandstone-mudstone are also present in other deep-marine systems, this extended model for the origin of hybrid event beds could help interpret their formation by including an increased range of turbulence-modulated flow types.

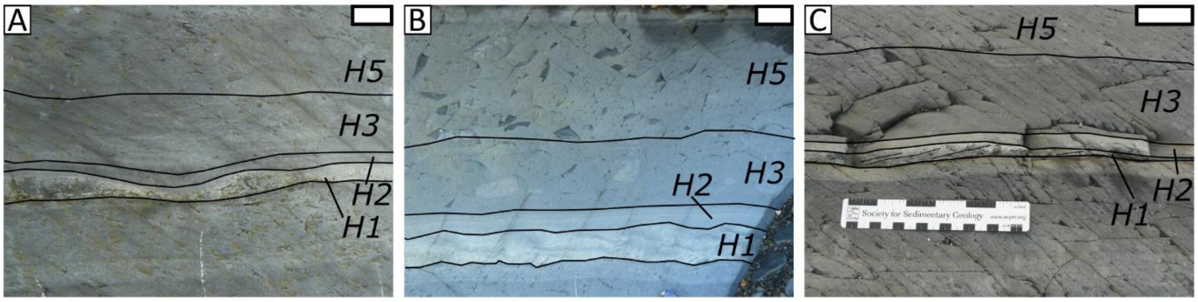

Figure 6.20: Examples of bedforms within the H1 division of hybrid event beds: (A) Large current ripples, (B) climbing sandy current ripples, and (C) LABWs with low-angle cross lamination outlined.

6.7.4 Mixed sand-mud bedforms in other deep-marine systems

The identification of large current ripples and low-amplitude bed-waves, in addition to sandy current ripples, shows that a diverse range of bedforms may be present in the mud-rich outer part of a submarine fan. Since these mixed sand-mud bedforms are formed by transitional to laminar flows, the deposits of which have been shown to be common in many fine-grained submarine fans (*e.g.*, Haughton *et al.*, 2009; Kane & Pontén, 2012; Kane *et al.*, 2017), it is likely that mixed sand-mud bedforms are present in the fringe to the distal fringe of other mud-rich deep marine systems. It is proposed herein that mixed sand-mud bedforms are valuable as an additional indicator for the outer margins of mud-rich systems, in combination with hybrid event beds, thin sandy turbidites, and mud-rich turbidites, thus aiding the interpretation of the deep-marine sedimentary record. These bedforms may also be present in the fringe region of more sand-dominated systems, in which deposition has also been shown to be controlled by cohesive clay, *e.g.,* the sandy Late Jurassic deep-water fans in the North Sea (Haughton *et al.*, 2003).

The spatial trend in dominant bedform type is attributed to flow transformation from the fringe to the distal fringe of the system, informed by the strong relationship between the flow type and bedform type found in laboratory experiments. Flow transformations have been shown to occur in the fringe of other submarine fans, such as the Ross Formation (Pyles & Jennette, 2009) and the Skoorsteenberg Formation (Kane *et al.*, 2017). Thus, assemblages of sandy current ripples, large current ripples and LABWs could be used as an additional predictive tool to determine a more precise location within the fringe and, in particular, the distal fringes of other deep-marine systems. The results of this study show that the distal fringes of a system may be dominated by turbulence-modulated flows that form large current ripples, and in particular LABWs, whereas more proximal portions of the fringe part of the system may show a majority of sandy current ripples formed by fully turbulent flows (Fig. 6.18).

The exceptional exposure of the AGG and BMF aided the identification of the mixed sandstone-mudstone bedforms based on texture, internal composition, bedform dimensions, and style of cross-lamination. It may not be possible in outcrops with poor exposure to determine bedform types based on all of the diagnostic criteria, but bedform size and angle of cross-lamination, using the quantitative data detailed herein, should enable differentiation between sandy current ripples, large current ripples, and LABWs. Recognising LABWs and large current ripples need not be confined to outcrop studies. A powerful aspect of utilising these mixed sand-mud bedforms is that they are small enough to be partly observed in core. Although the full length of large current ripples and LABWs cannot be captured in core, the height of the bedforms and the style of the cross-lamination should enable the interpretation of the mixed sand-mud bedform type. To aid bedform identification in field and core studies, a summary of the diagnostic criteria for the three bedform types is provided in Table 6.2.

Table 6.2: Diagnostic criteria of sandy current ripples, large current ripples and low-amplitude bed-waves to aid identification in the field and in core. Arrows point to cross-lamination of sandy current ripples and the bedform crests of the large current ripples and low-amplitude bed-waves. Scale bar is 50 mm long.

	Sandy current ripples	Large current ripples	Low-amplitude bed-waves
Good photo example	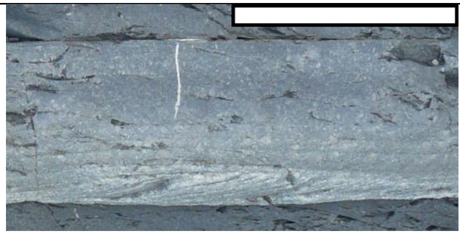		
Poor photo example	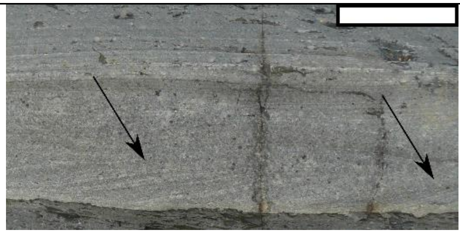	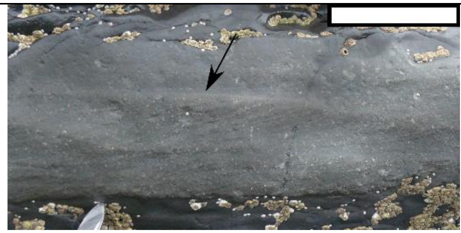	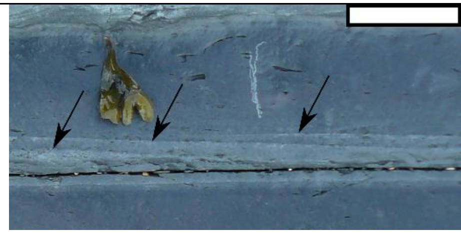
Texture	• Sandstone-dominated • Asymmetric profile	• Mixed sandstone-mudstone • Asymmetric profile • Muddy or silty front and/or base that coarsens upstream and/or upward to sandstone • Climbing and non-climbing • Mudstone layers may drape bedform surface	• Mixed sandstone-mudstone or sandstone dominated • Muddy or silty front and/or base that coarsens upstream and/or upward to sandstone • Climbing and non-climbing • Climbing surfaces often mudstone-rich • Bedforms can be isolated in mudstone
Dimensions	• Heights = < 20 mm • Lengths = < 200 mm	• Heights = *c.* 10 – 30 mm • Lengths = *c.* 140 – 430 mm	• Heights = *c.* 4 – 16 mm • Lengths = *c.* 140 – 820 mm
Cross-lamination	• High-angle cross-lamination of *c.* 30°	• High-angle cross-lamination of *c.* 30° • Plane-parallel lamination at the base or top of co-sets • Laminations may consist of alternating sandstone-mudstone	• Low-angle cross lamination of *c.* 12° • Plane-parallel lamination near the upflow end of the bedforms • Laminations may consist of alternating sandstone-mudstone

6.8 Conclusions

The identification of novel, mixed sand-mud bedforms in the fringe of the mud-rich deep-marine system of the Aberystwyth Grits Group (AGG) and Borth Mudstone Formation (BMF) suggests that the sedimentary structures in the fringe of fine-grained submarine fans may be more diverse than previously thought. The strong link between flow type and bedform type in decelerated mixed sand-mud flows, as previously demonstrated in laboratory experiments, allows the sandy current ripples, large current ripples, and low-amplitude bed-waves to be used to reconstruct formative flow type in the outer part of submarine fans. Sandy current ripples form under fully turbulent flows, large current ripples are generated under turbulence-enhanced transitional flows and lower transitional plug flows, and low-amplitude bed-waves primarily form under upper transitional plug flows.

The downdip trend of dominant bedform type from sandy current ripples, via large current ripples, to low-amplitude bed-waves suggests that the flows in the study area underwent transformation from turbulent via transitional to laminar on their way to the fringe of the fan. This flow transformation can be interpreted as due to a declining flow Reynolds number, mainly caused by flow deceleration following sediment deposition and increasing viscosity related to the shear-thinning nature of the clay-rich suspensions. The strongly cohesive flows at the fringe of the fan produced hybrid event beds with mixed sandstone-mudstone bedforms instead of massive sandstone in the H1 division. This suggests that the hybrid event bed model can be extended to the deposits of mud-rich hybrid events that include H1 divisions formed by cohesive transitional flows, rather than high-density turbidity currents. Moreover, at the fringe of the AGG-BMF system, the positive linear correlation between event bed thickness and the thickness of the overlying mudstone suggests that the mudstone caps may have been formed partly from strongly cohesive transitional and laminar sediment gravity flows.

Large current ripples and low-amplitude bed-waves are likely to be present in the fringe of other deep-marine systems. These bedforms may therefore have value as additional indicators for the outer margins of deep-marine systems and can be used to aid prediction of the depositional processes in these sub-environments.

7. Metadata analysis of the relationships between latitude, clay mineral assemblage, and geometry of modern submarine fans

7.1. Introduction

The latitudinal distribution of clay minerals on the sea bed of the world oceans can be linked to the prevailing climate, which controls the intensity of weathering on the adjacent continents (Chapter 1.6; Biscaye, 1965; Griffin *et al.*, 1968; Chamley, 1989; Fagel, 2007). The laboratory experiments presented in Chapter 3 demonstrate that high-concentration cohesive SGFs composed of weakly cohesive kaolinite have longer runout distances and thinner deposits compared to flows containing strongly cohesive bentonite (part of the smectite group of clay minerals) of the same volume concentration. Therefore, in the natural environment, clay mineral type may be an important control on the kinematic behaviour and deposit properties of cohesive SGFs. It is hypothesised that, if clay mineral type is a first-order control on fan development, in vertical cross-section a fan dominated by strongly cohesive smectite would cover a smaller area and be thicker than fans dominated by weakly cohesive kaolinite. It is also hypothesised that, if the clay mineral assemblages within modern submarine fans are latitudinally controlled, there may be latitudinal trends in the deposit properties of submarine fans because of rheologically distinct, climate-controlled, clay mineral assemblages.

This chapter presents a metadata analysis conducted to determine if there are relationships between the latitude, the clay mineral assemblages, and the geometry of modern submarine fans. The following specific research questions were investigated:

1. Is there a relationship between the clay mineral assemblage in modern submarine fans and their latitude?

2. Can the geometry of modern submarine fans be linked to the clay mineral assemblages within the fans?
3. Is there a relationship between the geometry of modern submarine fans and their latitude?
4. How can these results be used to further our understanding of the clay mineral assemblages within submarine fans and fan geometry?

7.2 Methods

7.2.1 Selection of modern submarine fans

This metadata analysis focuses on modern submarine fans primarily because the clay mineral data collected from these fans is unlikely to have been affected by burial diagenesis, and the clay minerals in these fans are therefore most likely to represent the secondary products of continental weathering (Chamley, 1989; Fagel, 2007). Furthermore, the size, shape, and internal architecture of many modern submarine fans is well known from mapping of the seafloor by remote sensing technology (Fig. 7.1A). In contrast, it is more challenging to reconstruct the morphology of ancient submarine fans, which relies on extensive outcrop exposure or subsurface data. It was decided the large-scale geometry of the fans should be focused on in the metadata analysis, as getting comparable data on the smaller scale architecture of each individual fan from the published literature was unfeasible.

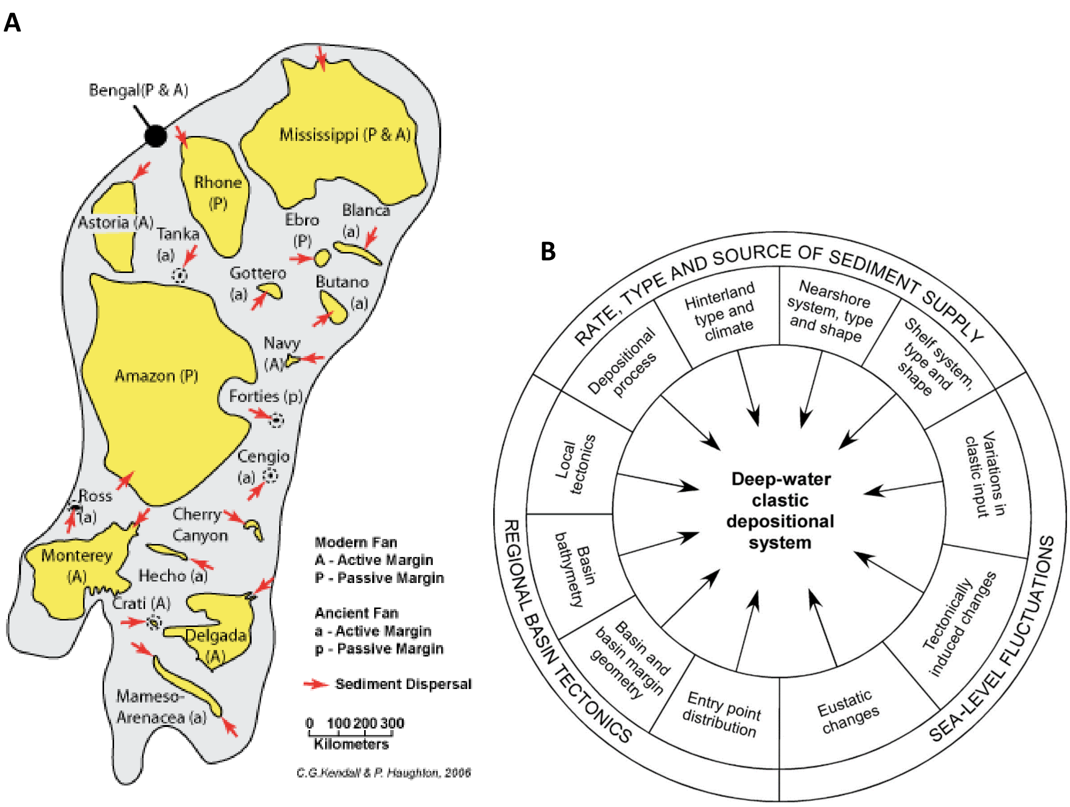

Figure 7.1: (A) Comparison of fan sizes for modern and ancient submarine fans. From Kendall and Haughton (2006). (B) Major controls on the morphology of clastic deep-marine systems. From Stow et al. (1996).

Many factors control the development of deep-marine systems, including climate, tectonics, sea-level, type and source of sediment, and rate of sediment supply (Fig. 7.1B; Stow *et al.*, 1996). These controls can be complex and interdependent. This metadata analysis tried to isolate the effect of clay mineral type by accounting for the most important controls on the depositional properties of deep-marine systems. This involved selecting submarine fans with comparable sediment supply and tectonic regime, but with different climate control, as outlined below.

Sediment Supply

Sediment supply is defined by Stow *et al.* (1996) as the most important control governing the size and depositional style of deep-marine systems. This includes the composition of the sediment being delivered to the fans. Fans dominated by fine-grained sediment are generally of a greater size than fans predominantly composed of sand (Reading & Richards, 1994). For this metadata analysis, only fans classified as mud-rich or mixed sand-mud by Reading and Richards (1994) were considered, as it is in fans dominated by mud where the clay mineral assemblage should have the greatest effect on fan geometry. Sediment supply also comprises the rate sediment is supplied to the fan (Stow *et al.*, 1996). Rate of sediment supply is controlled by the tectonics and morphology of the whole fan source area. The Data analysis chapter (Chapter 7.2.3) outlines how the considerable variations in rate of sediment supply to the fans was accounted for.

Tectonic setting

The tectonic setting of systems is another important control on fan deposition. Tectonics affect the basin size and shape, slope gradients, type and rate of sediment supply, and longevity of an individual fan (Pickering & Hiscott, 2016). To minimise the effect of regional basin tectonics, focus was kept on fans built on passive margins, where the main tectonic process is thermal subsidence, which has little effect on the development of the fans (Pickering & Hiscott, 2016).

In total, sixteen modern, mud-rich and mixed sand-mud fans on passive margins were selected for the metadata analysis, covering a variety of climate zones and geographical locations (Fig. 7.2).

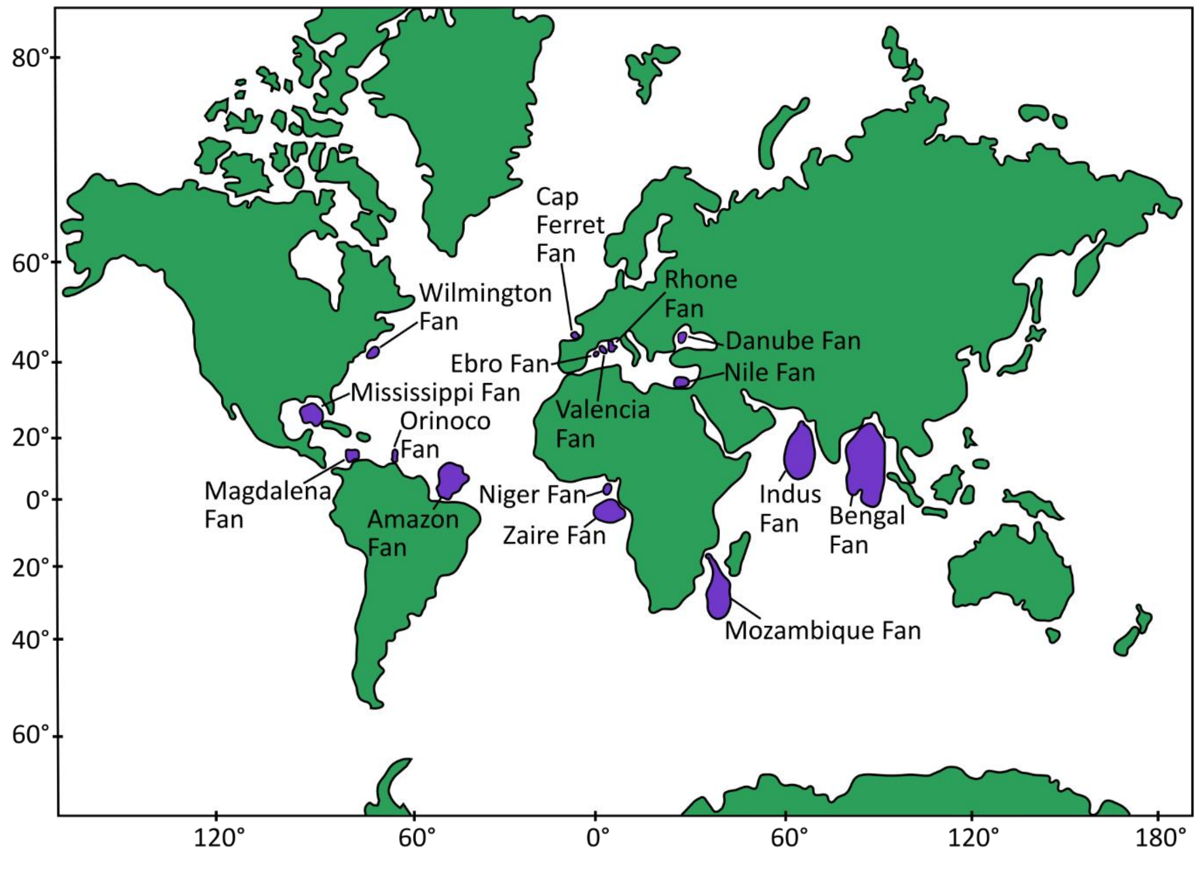

Figure 7.2: Map of the submarine fans used in this study.

7.2.2 Data collection

Data on the geometric parameters, rate of deposition, and latitude were compiled from the published literature for the 16 submarine fans shown in Figure 7.2 (Table 7.1). The fan dimensions – length, width, and volume – were taken from Sømme *et al.* (2009), who studied source-to-sink systems. For these data, when different publications present different values for specific parameters, the most recently published dimensions and/or the dimensions most frequently cited were used (Sømme *et al.*, 2009). This approach was also applied to published data on the fan ages and clay mineral assemblages within the fans.

Establishing the clay mineral assemblages within the deep-marine fans was challenging because of the scarcity of data collected on clay mineral type. Clay mineral assemblage data were obtained from sediment gravity flow (SGF) deposits from between 1 and 25 cores for 14 of the submarine fans. When clay mineral data was available from multiple cores, the average clay mineral assemblage was calculated. The clay mineral types included in the metadata analysis were smectite, illite, chlorite, and kaolinite, as these are the four main clay mineral types found in the World Ocean (Biscaye, 1965; Griffin *et al.*, 1968). When the percentages of the four main clay minerals also included other minerals, *i.e.,* feldspar, the percentages of the four main clay minerals were re-calculated to equal 100% in total. For the Niger fan, only the dominant clay mineral type rather than the full assemblage is known. No clay mineral assemblage data were available for the Rhône and Magdalena fans, but these fans could still be used to test if there is a direct link between the geometry of modern submarine fans and their latitude. Of the 14 fans with clay mineral data, four fans are dominated by smectite (29%), eight fans are dominated by illite (57%) and two fans are dominated by kaolinite (14%).

Four latitudinal controls were considered, as the source to sink systems of some of the fans used in this study were found to span >20° of latitude. The latitude of the fan and the latitude of the catchment were determined by taking the average latitude span of the whole fan and the catchment area, respectively (Fig. 7.3). The latitude of the source of the fan denotes the upper latitudinal extent of the catchment area, whilst the latitude of fan input describes the latitude where terrigenous sediment that feeds the fan enters the sea (Fig. 7.3).

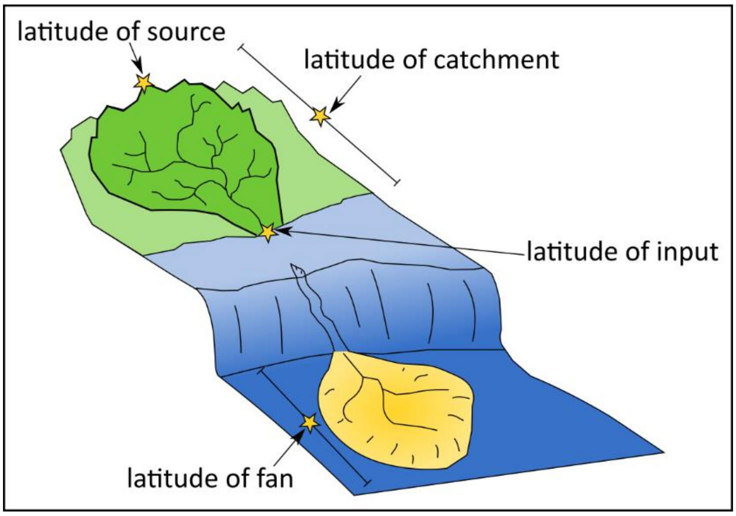

Figure 7.3: Schematic diagram showing the four latitude classes used in this metadata analysis. Latitude of the source is the maximum latitudinal extent of the catchment area, whereas latitude of catchment is the average latitude of the catchment extent. Latitude of input is defined as the latitude where terrigenous sediment enters the marine environment, and latitude of fan is the average of the latitudinal extent of the submarine fan. Modified from Nyberg et al. (2018).

Table 7.1: References (next page): (1) Sømme *et al.* (2009); (2) Wetzel (1993); (3) Barnes and Normark (1985); (4) Reading and Richards (1994); (5) Behl (2011); (6) Figueiredo *et al.* (2009); (7) Curray *et al.* (2002); (8) Winguth *et al.* (2000); (9) Nelson (1990); (10) Govil and Naidu (2008); (11) Clift *et al.* (2001); (12) Fletcher *et al.* (2007); (13) Kolla *et al.* (1980); (14) Zhang *et al.* (2015); (15) Bayon *et al.* (2009); (16) Bonnel *et al.* (2005); (17) Anka and Séranne (2004); (18) Sumner and Westbrook (2001); (19) Maldonado *et al.* (1985); (20) Mattern (2005); (21) Stow *et al.* (1996); (22) Cremer *et al.* (1999) (23) Segall *et al.* (1989); (24) Alonso and Maldonado (1990); (25) France-Lanord *et al.* (2016); (26) Tekiroglu *et al.* (2001); (27) Gonthier *et al.* (2002); (28) Gingele *et al.* (1998); (29) Stow *et al.* (1985); (30) Debrabant *et al.* (1997); (31) Maldonado and Stanley (1981); (32) Popescu *et al.* (2001); (33) Shanmugam and Moiola (1988); (34) Covault *et al.* (2012).

Table 7.1: Data used in this study. Variables: Med. Sea = Mediterranean Sea, p = passive margin, MR = mud rich, M/S = mud and sand rich.

System	Location	Margin type	Dominant sediment type	Latitude of fan (°)	Latitude of source (°)	Latitude of input (°)	Latitude of catchment (°)	Fan volume (km^3)	Fan age (year)	Fan area (km^2)	Length (km)	Width (km)	Dominant clay mineral	Illite (%)	Kaolinite (%)	Smectite (%)	Chlorite (%)
Amazon	Brazil, Atlantic Ocean	P[1]	M[4]	6	10	0	5	700000[1,2,3]	11800000[6]	370000	700	600	S[30]	31	21	36	13
Bengal	Bay of Bengal, Indian Ocean	P[1]	M[4]	5	30	23	26.5	12500000[1,2]	56000000[7]	2900000	3000	1430	I[25]	65	6	6	23
Cap Ferret	France, Atlantic Ocean	P[1]	M[4]	44	42	44	43	1300[1]	23000000[3]	52000	350	150	I[22]	57	11	5	27
Danube	Black Sea	P[1]	M[32]	43	48	45	46.5	30000[1]	900000[8]	16000	150	100	I[26]	40	32	28	0
Ebro	Spain, Med. Sea	P[1]	M/S[4]	40	43	40.5	41.75	1700[1,2]	2580000[9]	5000	50	60	I[24]	35	25		40
Indus	Arabian Sea, Indian Ocean	P[3]	M[4]	15	32	25	28.5	1000000[1,2,3]	23000000[10,11]	1100000	1500	960	I[10]	69	18	4	9
Magdalena	Caribbean Sea, Atlantic Ocean	P[33]	M[4]	26	47	29	38	180000[1,2]	15000000[12]	53000	300	300					
Mississippi	Gulf of Mexico, Atlantic Ocean	P[1]	M[4]	28	11	19	15	290000[1,2]	2400000[2]	300000	540	570	S[29]	12	19	50	19
Mozambique	W Africa, Atlantic Ocean	P[1]	M[4]	3	10	4	7	3000000[1]	23000000[13]	2000000	1800	400	S[13]	30	20	40	10
Niger Fan	W Africa, Atlantic Ocean	P[1]	M[20]	33	2	31	16.5	2000000[1]	66000000[14]	1000000	550	550	K[14]		80		
Nile	Egypt, Med. Sea	P[1]	M[4]	11	2	9	5.5	400000[1,2]	11630000[15]	70000	280	500	S[31]	6	20	73	1
Orinoco	Venezuela, Atlantic Ocean	P	M[21]	36	36	38	37	180000[1,2]	12000000[18]	30000	180	60	I[27]	36	26	25	13
Rhône	France, Med. Sea	P[1]	M/S[4]	6	10	6	8	12000[1,2]	5000000[16]	70000	300	200					
Wilmington	USA, Atlantic Ocean	P[1]	M[4]	41	43	40.5	41.75	50000[1]	23000000[34]	100000	600	190	I[23]	60	6	6	28
Zaire	W Africa, Atlantic Ocean	P[1]	M[4]	6	10	0	5	500000[1]	34000000[17]	1500000	800	400	K[28]	14	62	20	4
Valencia	NW Med. Sea	P[1]	M[4]	5	30	23	26.5	6200[1,2]	2580000[9,19]	11000	350	85	I[24]	35	25		40

7.2.3 Data analysis

7.2.3.1 Clay mineral assemblages

The analysis of the clay mineral assemblages in relation to the latitude classes and the geometrical properties of the fans (Chapters 7.3.1 and 7.3.2) starts by focusing on the dominant clay mineral type within the clay mineral assemblage. Next, the percentages of the individual clay mineral types and the ratio of certain clay mineral types are tested against the latitudinal controls and the fan depositional properties. Clay mineral ratios are the preferred method for palaeoclimate reconstruction, as comparing clay mineral components using their ratios reduces the effect of dilution by other clays (Gingele *et al.*, 1998; Fagel, 2007). To investigate the potential latitudinal control on the clay mineral assemblage, the ratio of two latitudinally and climatically distinct clay minerals is used. The ratio tested in this metadata analysis is kaolinite:chlorite, since kaolinite is expected to dominate equatorial latitudes, whereas chlorite is predominant at high latitudes. High kaolinite:chlorite ratios in samples express a dominance of kaolinite and suggest a low latitude, compared to low kaolinite:chlorite ratios which suggest a dominance of chlorite at high latitude.

Clay mineral ratios are also used to test if a relationship between the clay mineral assemblage and the geometrical properties of the fans exists (Chapter 7.3.2). For this analysis, the most rheologically different clay mineral types were focused on first: weakly cohesive kaolinite and strongly cohesive smectite. Deposits of flows with a low kaolinite:smectite ratio contain a large proportion of strongly cohesive clay compared to weakly cohesive clay. These flows should travel a shorter distance than flows with a high kaolinite:smectite ratio and a large proportion of weakly cohesive clay to strongly cohesive clay. The ratio of kaolinite and chlorite to smectite and Illite, which is the ratio of weakly to strongly cohesive clay minerals using the whole clay mineral assemblage, was also used.

7.2.3.2 Fan geometric properties

If the clay mineral type has a significant effect on the behaviour of SGFs, a signature of this may be preserved in the deposits. Moving from fans dominated by smectite to illite to kaolinite, a fan is expected to become longer and thinner. However, the length of the fans used in this metadata analysis ranges from 50 km to 3000 km, and the fan volumes vary from 1.7 x 10^3 km^3 to 1.25 x 10^7 km^3, spanning three and five orders of magnitude, respectively (Fig. 7.4). It is not possible to directly compare fans of such different sizes, as a fan dominated by smectite may have the same thickness as a fan dominated by kaolinite, if the latter fan is older and thus had more time to grow. To enable comparison of the fan dimensions, the following method was used:

1. Each fan volume was divided by its age, and then multiplied by 1000 to give the volume that represents 1000 years of fan growth. This is termed average volumetric fan growth rate, *V*:

$$V = \frac{Volume}{Age}\ x\ 1000 \tag{7.1}$$

2. Two *V* categories were selected, <100 km^3/ka and 100-350 km^3/ka, in order to facilitate the comparison of fans of similar size.
3. Each *V* value was divided by the fan area to give the average-vertical-fan-growth-rate, *H*:

$$H\ = \frac{V}{Fan\ area} \tag{7.2}$$

4. For each of the two *V* categories, the *H*-values (given in units of m/ka) for fans dominated by different clay mineral types were compared, with the expectation that kaolinite-dominated fans have the thinnest deposits, illite-dominated fans have deposits of intermediate thickness, and smectite-dominated fans have the thickest deposits.

For the analysis of *H* against the clay mineral assemblages within the fans, three fans that do not conform to the typical unconfined fan-shape model (Bouma *et al.*, 1985) were discounted from this test: Cap Ferret, Ebro and Wilmington**.** Cap Ferret fan is formed within a structural trough, which acts as a major channel for sediment transfer and gives the fan an elongate shape (Cremer *et al.*, 1985, 1999). The Ebro fan forms in a restricted basin, limiting the fan's potential runout distance (Nelson *et al.*, 2009). Finally, the distal Wilmington fan is restricted by lower continental rise hills (Cleary *et al.*, 1985).

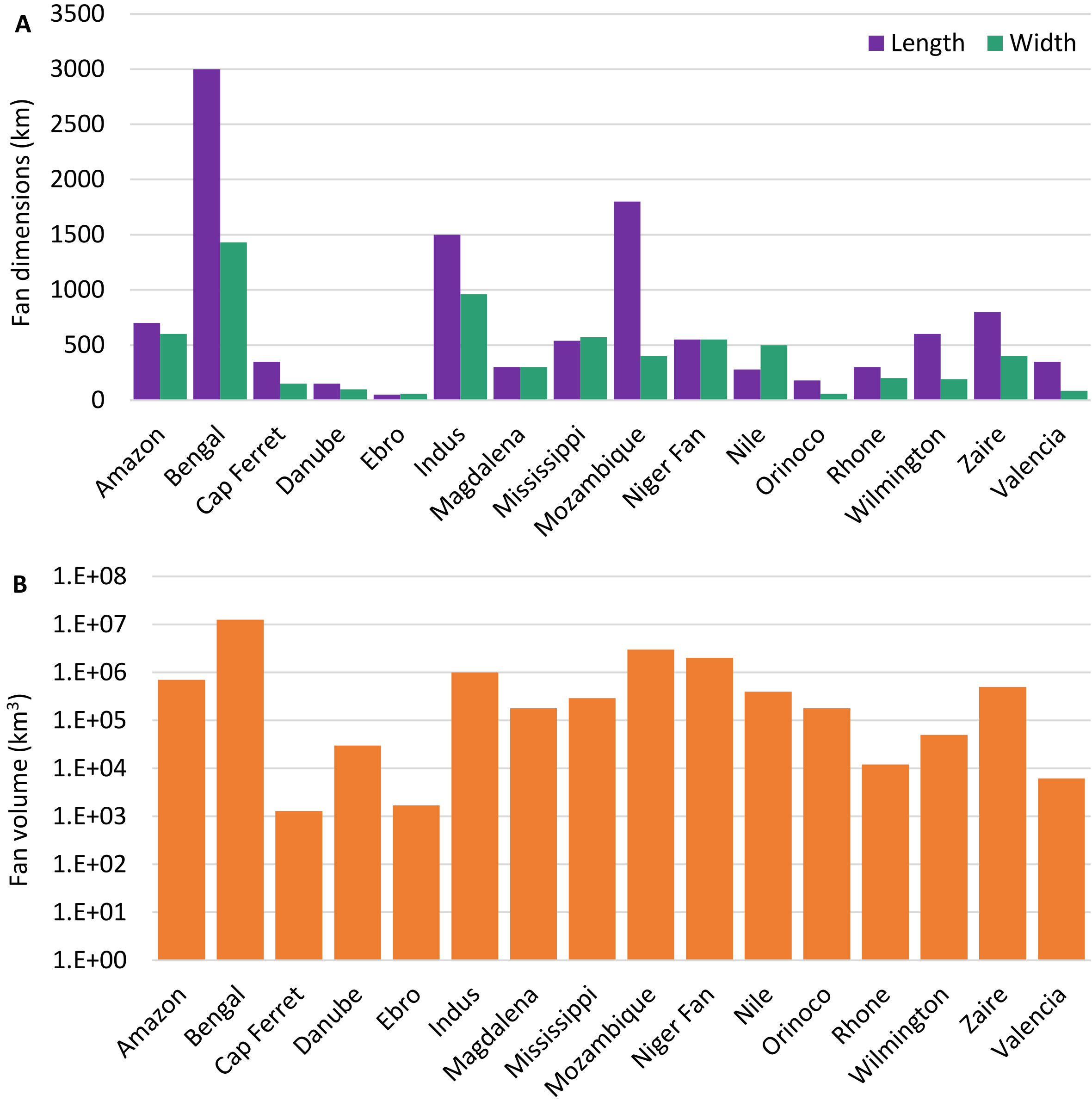

Figure 7.4: (A) Length and width and (B) volume of the submarine fans included in the metadata analysis.

7.2.3.3 Bivariate statistics

Basic bivariate statistical tests were conducted on the continuous data sets to determine the presence and strength of the relationships between: 1) latitude and clay mineral assemblage, 2) clay mineral assemblage and average-vertical-fan-growth-rate, and 3) latitude and average-vertical-fan-growth-rate. For each test the non-parametric Spearman's rank-order correlation coefficient, r_s, was calculated, which represents the strength of the association between the two variables (Dytham, 2011). The values of r_s range from -1 through 0 to 1, indicating perfect negative correlation, no correlation and perfect positive correlation, respectively (Dytham, 2011). Each r_s value has an associated calculated probability (p-value). A critical p-value of 0.05 is used to reject the null hypothesis of no correlation between the variables and represents a statistically significant result. In addition, standard linear regression was conducted to assess the form and strength of each pair of variables and the ability of *x* to predict a value of *y*. Linear regression produces the R^2 value which represents the amount of variation explained by the regression (Dytham, 2011). Linear regressions are only presented when $p < 0.05$, thus indicating that the relationship between *x* and *y* is statistically significant.

For the categorical clay mineral type data, *i.e.,* dominant clay mineral type within the fans, the data are presented in box and whisker plots, which make no assumptions about the distribution of the data (Dytham, 2011). The structure of a box and whisker plot is presented in Figure 7.5. The main box represents the interquartile range, or middle 50%, defined as the difference between the 75th and 25th percentiles. The median value, and the interquartile range, are useful measures as they are unaffected by outliers. The whiskers extend to the largest and smallest values within 1.5 of the interquartile range. Any values greater than 1.5 times the interquartile range are defined as outliers and presented as individual data points (Fig. 7.5; Dytham, 2011).

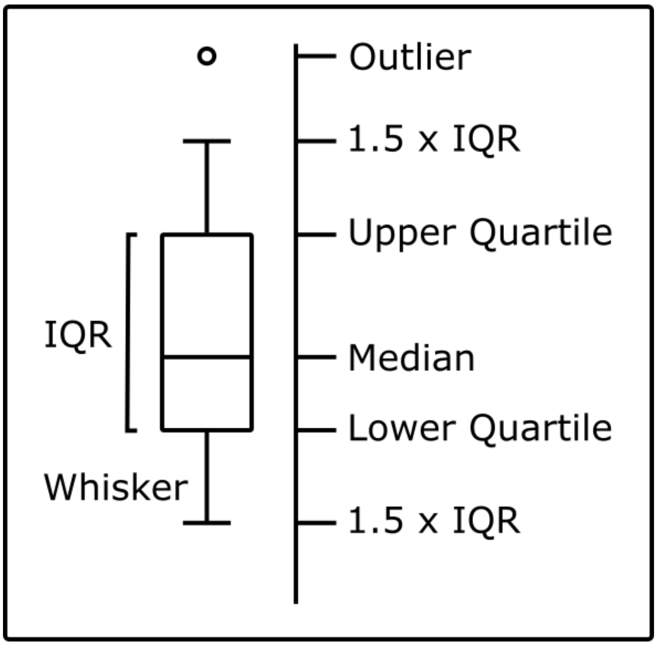

Figure 7.5: Summary of the data presented in a box plot. IQR = interquartile range.

7.2.3.4 Multivariate statistics

Multidimensional scaling plot

To visualize the similarities between the fans based on their clay mineral assemblages, a multidimensional scaling plot was produced using PRIMER analytical software (PRIMER-E Ltd, Plymouth, U.K.). Multidimensional scaling plots present the data in geometric space in which 'similar' data points plot closer together and 'dissimilar' data points plot far apart (Borg *et al.*, 2012). Multidimensional scaling plots were initially developed in psychology, a classic example being the colour-vision experiment of Helm (1962) in which human observers were asked to give the perceived difference between 10 different colours (Vermeesch & Garzanti, 2015). The perceived differences between the colours were plotted in 1D space to reveal the well-known colour circle (Fig. 7.6; Helm, 1962; Vermeesch & Garzanti, 2015). The study of Helm (1962) demonstrated how multidimensional scaling plots can give a simple visual representation of the empirical interrelations, allowing easier exploration of the structure of the data (Borg *et al.*, 2012).

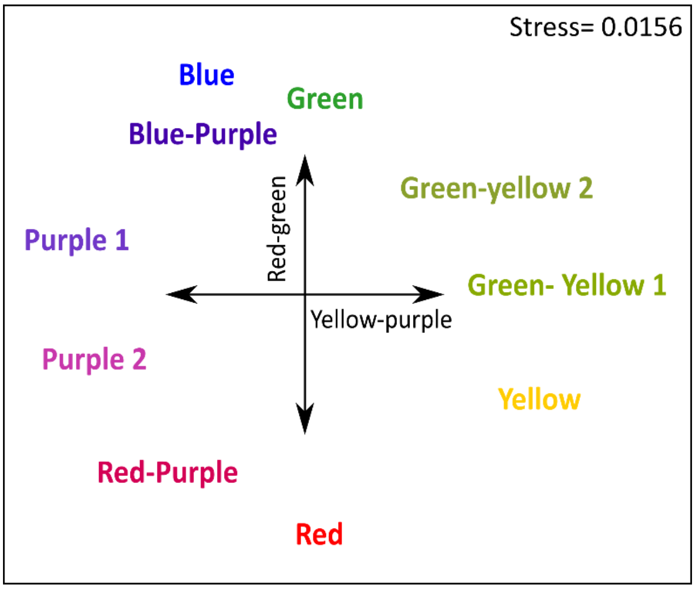

Figure 7.6: Multidimensional scaling plot of Helm's (1964) colour vision data, the principal axes show the drivers causing the variance. Modified from Vermeesch and Garzanti (2015).

To produce a multidimensional scaling plot, the raw data, in this case the clay mineral assemblage of each fan, is converted into a similarity matrix. For the data in this study, the similarity between each pair of fans is given in Euclidian distances. It should be noted that multidimensional scaling calculates the Euclidian distance between the data points in multidimensional space, but the data is then presented in 1D; the 'goodness of fit' of the 1D representation of the data is given by the stress value (Vermeesch & Garzanti, 2015). Principal axes of the variables can be added to the multidimensional scaling plot to show how the variables drive the multidimensional scaling configuration, as demonstrated in Figure 7.6 (Borg *et al.*, 2012).

Similarity Profile Routine

The multidimensional scaling plots are a valuable method to visualise the data, but are not a formal test to see if the data can be grouped. To test the similarities of the clay mineral assemblage between the fans a Similarity Profile Routine was conducted. This is a test for multivariate structure among unstructured samples without *a priori* grouping (Clarke *et al.*, 2008). The Similarity Profile Routine tests the null hypothesis of no meaningful structure within the data set. For the Similarity Profile Routine, similarities are calculated between each pair in the data set; this is the similarity between each fan based on the clay mineral assemblage for this dataset. The sample similarities are then ranked from smallest to largest and plotted against their ranks (Fig. 7.7). This profile is then compared to the similarity profile expected under the null hypothesis, which is calculated from the mean of ≥ 1000 permutated profiles calculated from creating random distribution of values across the dataset. If the real profile falls within the 99% bounds of the profile created from the random similarities, the null hypothesis of no internal structure within the data set cannot be rejected (Fig. 7.7; Clarke *et al.*, 2008).

Similarity Profile Routine test can be used to group the data by conducting a series of Similarity Profile Routine tests on the dataset, to produce a dendrogram illustrating the hierarchical cluster analysis of groups (Fig. 7.8). Starting with the whole data set, progress to the first division of a dendrogram is only permitted if the null hypothesis of no internal structure can be rejected. Progress to each succeeding partition is only permissible if the null hypothesis can be rejected and the data are still deemed to have internal structure. Once a non-significant result is obtained, no tests are performed further down that branch and the data below that point are considered homogenous (Clarke *et al.*, 2008). A limitation of Similarity Profile Routine test is that it can never divide a group of two samples, even if they are extremely dissimilar (Clarke *et al.*, 2008).

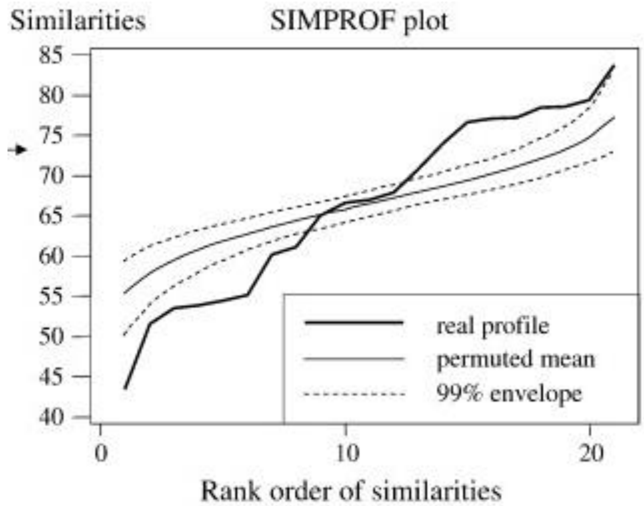

Figure 7.7: Schematic diagram of the result of a Similarity Profile Routine test. The thick black line is the similarity profile of the data, whereas the thin black line is the random similarity profile produced from 1000 permutated profiles of a random distribution of data. If the real profile falls within the 99% bounds of the random similarity profile it is deemed that there is no internal structure in the dataset. From Clark et al. (2008).

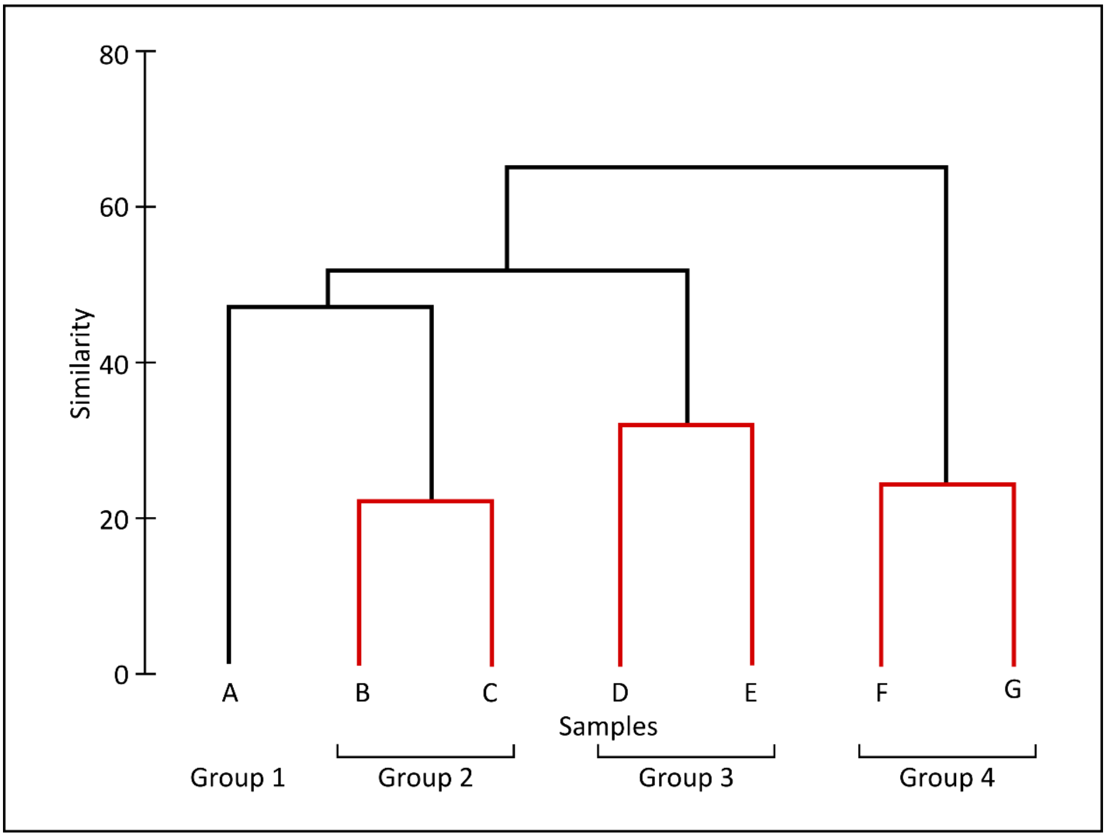

Figure 7.8: Idealised dendrogram produced from a Similarity Profile Routine test showing the similarities between samples. Groups which are significantly different (i.e., separated by Similarity Profile Routine test) are shown in black whereas red denotes samples which do not differ significantly.

Distance-based multivariate multiple regression

To investigate association between the clay mineral assemblages and the latitudinal predictors, a permutational distance-based multivariate multiple regression was used (McArdle & Anderson, 2011; Williams *et al.*, 2011). This non-parametric test is similar to multiple linear regression and can test the significance of single or multiple predictor variables on multivariate response variables (Anderson *et al.*, 2008). For these data, a linear model was built using the latitudinal classes as the predictor variables and the Euclidian distance similarity matrix generated from the clay mineral assemblages within the fans as the response variable. The Euclidian distance similarity matrix is the data used for the multidimensional scaling plot. Pearson's correlation coefficient was used to assess the co-linearity among the latitudinal predictors. Latitude of fan and latitude of source correlated by > 0.80 with latitude of input and latitude of catchment. Latitude of input and latitude of catchment were selected over the other latitudinal predictors because latitude of catchment produced good results when plotted against dominant clay mineral type and latitude of input was considered the easiest latitude class to use for ancient submarine fans. Three models were run with the following predictor variables: latitude of input, latitude of catchment, and latitude of input and latitude of catchment combined. The correlation coefficient, R^2, is a measure of the variation the linear model captured and shows the model performance. Model selection was based on Akaike's Information Criterion, with a second order bias correction applied (termed AICc), where lower values suggest a good balance between the goodness of fit of the model and model simplicity (Akaike, 1973; Burnham & Anderson, 2004).

7.3 Results

7.3.1 Latitude of fans and clay mineral assemblage

7.3.1.1 Multidimensional scaling plot

Figure 7.9 shows the multidimensional scaling plot for the submarine fans, based on their clay mineral assemblage. The figure is based on the similarity matrix between the fans (Table 7.2). Fans closer together are more alike in clay mineral assemblage than those plotted further apart. The principal axes show the four clay mineral types driving the variance. Figure 7.9B shows the results from the hierarchal cluster analysis from the Similarity Profile Routine tests that have been conducted on all nodes of the dendrogram, the resulting groups are superimposed on the multidimensional scaling plot (Fig. 7.9A). This dataset fits the multidimensional scaling plot configuration presented well with a low stress value. Using the multidimensional scaling plot and the Similarity Profile Routine test results, the clay mineral assemblage data between fans can be compared.

A first observation is that few fans are dominated by chlorite, as just the Valencia and Ebro fans are characteristic of high chlorite content and form their own distinct group (Group D in Fig. 7.9). Four fans are dominated by illite, with Cap Ferret, Wilmington and Bengal fans forming a group with no meaningful structure (Group B in Fig. 7.9). The Cap Ferret, Wilmington and Bengal fans are characterised by high illite content, relatively high chlorite content, and low smectite and kaolinite contents. Interestingly, the Indus fan forms its own group distinct from the other fans with a clay mineral assemblage dominated by illite and with subordinate kaolinite (Group A in Fig. 7.9). Group C derived from the Similarity Profile Routine test contains seven of the thirteen fans and has a large amount of variety within the group. This groups is characterised by low chlorite and varying illite, kaolinite, and smectite percentages.

Table 7.2: Euclidian distance between fans based on their clay mineral assemblage. Distance goes from 0 to infinity, the smaller the Euclidian distance the more similar the fans are in terms of clay mineral assemblage. These data are used to create Figure 7.9.

	Amazon	Bengal	Cap Ferret	Danube	Ebro	Indus	Mississippi	Mozambique	Nile	Orinoco	Wilmington	Zaire	Valencia
Amazon													
Bengal	49.497												
Cap Ferret	44.565	10.296											
Danube	21.307	48.104	44.587										
Ebro	45.453	39.825	29.563	49.578									
Indus	50.695	18.974	22.76	41.158	46.712								
Mississippi	23.664	70.214	64.637	42.403	59.211	73.932							
Mozambique	5.099	52.402	48.208	22.091	50.498	53.122	22.494						
Nile	45.717	93.005	89.342	57.671	87.841	93.789	29.833	41.785					
Orinoco	13.491	41.255	35.525	15.166	39.824	40.125	35.861	17.493	58.172				
Wilmington	47.434	7.0711	6.000	48.415	34.147	24.29	67.007	50.754	91.269	39.522			
Zaire	47.686	79.335	72.139	40.694	59.211	72.402	54.571	49.558	68.162	43.428	77.614		
Valencia	45.453	39.825	29.563	49.578	0	46.712	59.211	50.498	87.841	36.824	34.147	59.211	

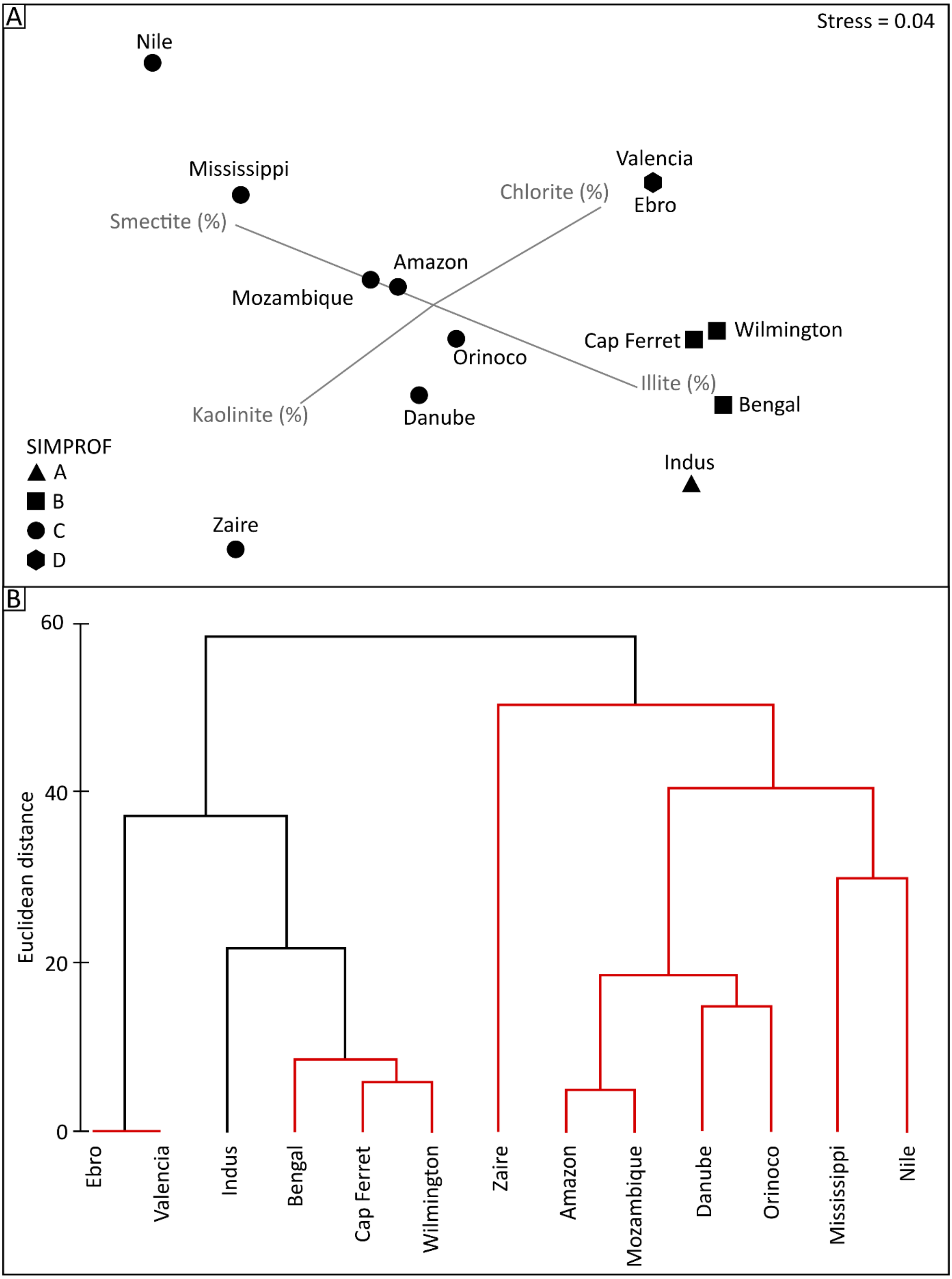

Figure 7.9: (A) Multidimensional scaling plot for the submarine fans based on their clay mineral assemblage. Note that the Valencia and Ebro fans plot on top of each other. The data are grouped according to the Similarity Profile Routine test results shown in (B). (B) Dendrogram produced from Similarity Profile Routine test showing the similarities between fans. Groups which are significantly different are shown in black whereas red represents fans that do not differ significantly.

7.3.1.2 Dominant clay mineral type

Figure 7.10 shows the latitude of fan, latitude of source, latitude of input and latitude of catchment for each fan, as well as the dominant clay mineral type within these fans. The same data are presented in Figure 7.11 and Figure 7.12 as box plots. Fans dominated by illite, smectite, and kaolinite have progressively lower median latitudes of fan, source, input, and catchment (Figs 7.11 and 7.12). The median latitude of the illite-dominated fans is 39° for the latitude of fan, source, input and catchment area, whereas the median latitudes of the kaolinite-dominated fans range from 5° to 7.5° for these latitude classes. The median latitudes for the smectite fans are 10.5° and 15° for the latitude of the source and latitude of catchment, and 24° for the latitude of the fan and latitude of input.

For the fans dominated by illite, smectite, and kaolinite, the full and interquartile ranges vary depending on which latitude class is used. Illite-dominated fans are found at a wide range of latitudes if classified by latitude of fan, latitude of input and latitude of catchment, producing box plots with a large interquartile range that is skewed towards the lower latitudes. For illite fans against latitude of their source, the illite-dominated Orinoco fan is considered an outlier with an abnormally low source latitude of 2° (Fig. 7.11B). Outliers are discounted in the calculations of the interquartile range and whiskers. Thus, by discounting the Orinoco fan the box and whisker plot for the illite fans classified by latitude of source has a small interquartile range and whiskers (Fig. 7.11B). The range of latitudes of fans composed primarily of smectite is larger for latitude of source than for the latitudes of fan, input, and catchment. The size of the interquartile range decreases from smectite-dominated via illite-dominated to kaolinite-dominated fans for all latitude classes apart from latitude of fan, where the illite-dominated fans have a larger interquartile range than the smectite-fans (Figs 7.11 and 7.12). The small number of kaolinite-dominated fans limits the range of the kaolinite box plots.

The interquartile ranges of the kaolinite and illite box plots never overlap for all the latitude classes and the full box plots only overlap for the latitude of fan and catchment, because of the large lower whisker of the box plot for illite. None of the interquartile ranges of the different clay minerals overlap when the fans are sorted by latitude of catchment (Fig. 7.12B). For the latitude of the source, the illite and smectite interquartile ranges do not overlap whilst the kaolinite and smectite interquartile ranges do; this is the opposite for fans sorted by the latitude of fan and input.

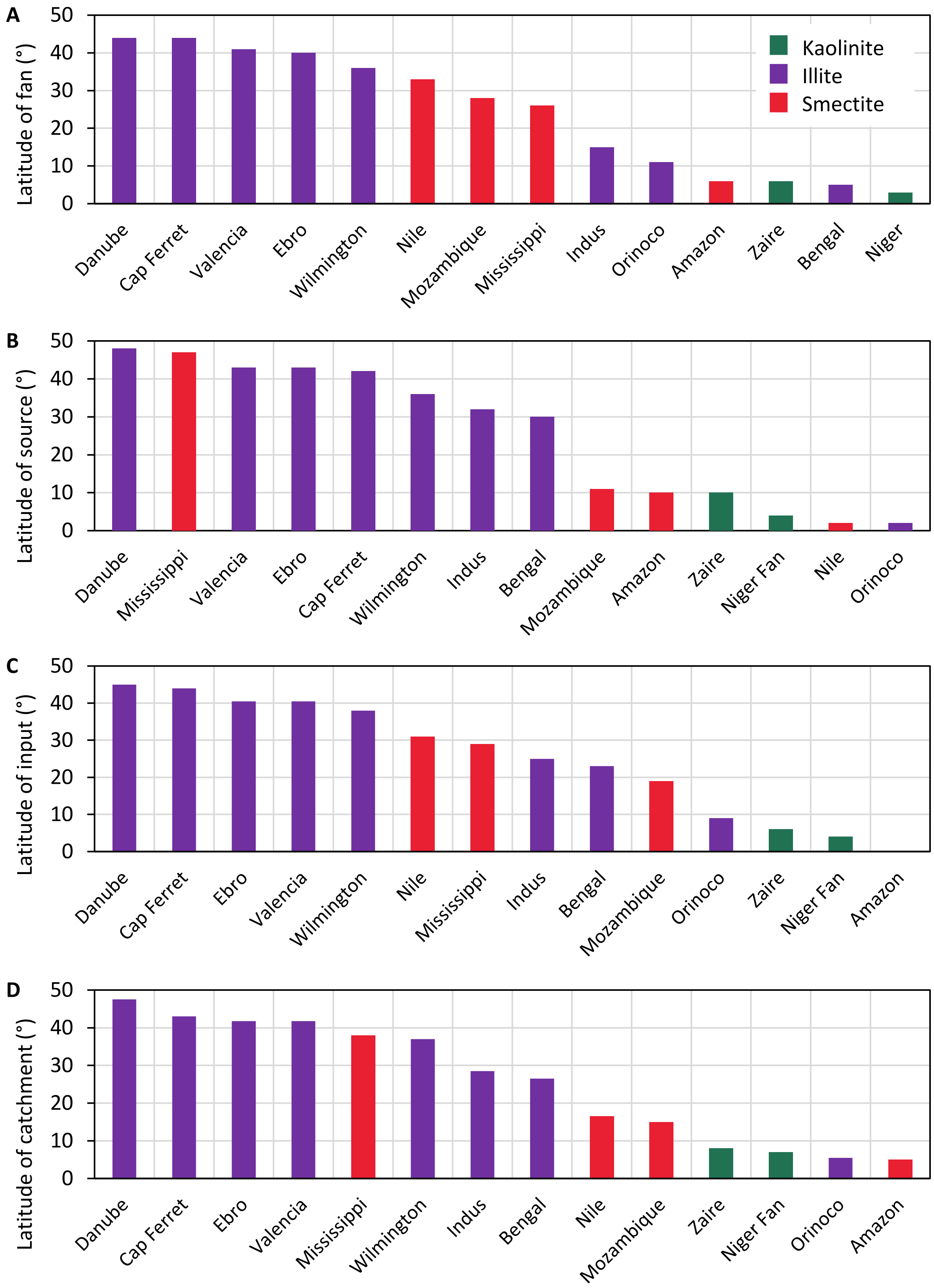

Figure 7.10: (A) Latitude of the fan, (B) latitude of fan source, (C) latitude of fan input, and (D) latitude of fan catchment for the fans used in this study. Colours represent the dominant clay minerals: purple = illite, red = smectite and green = kaolinite.

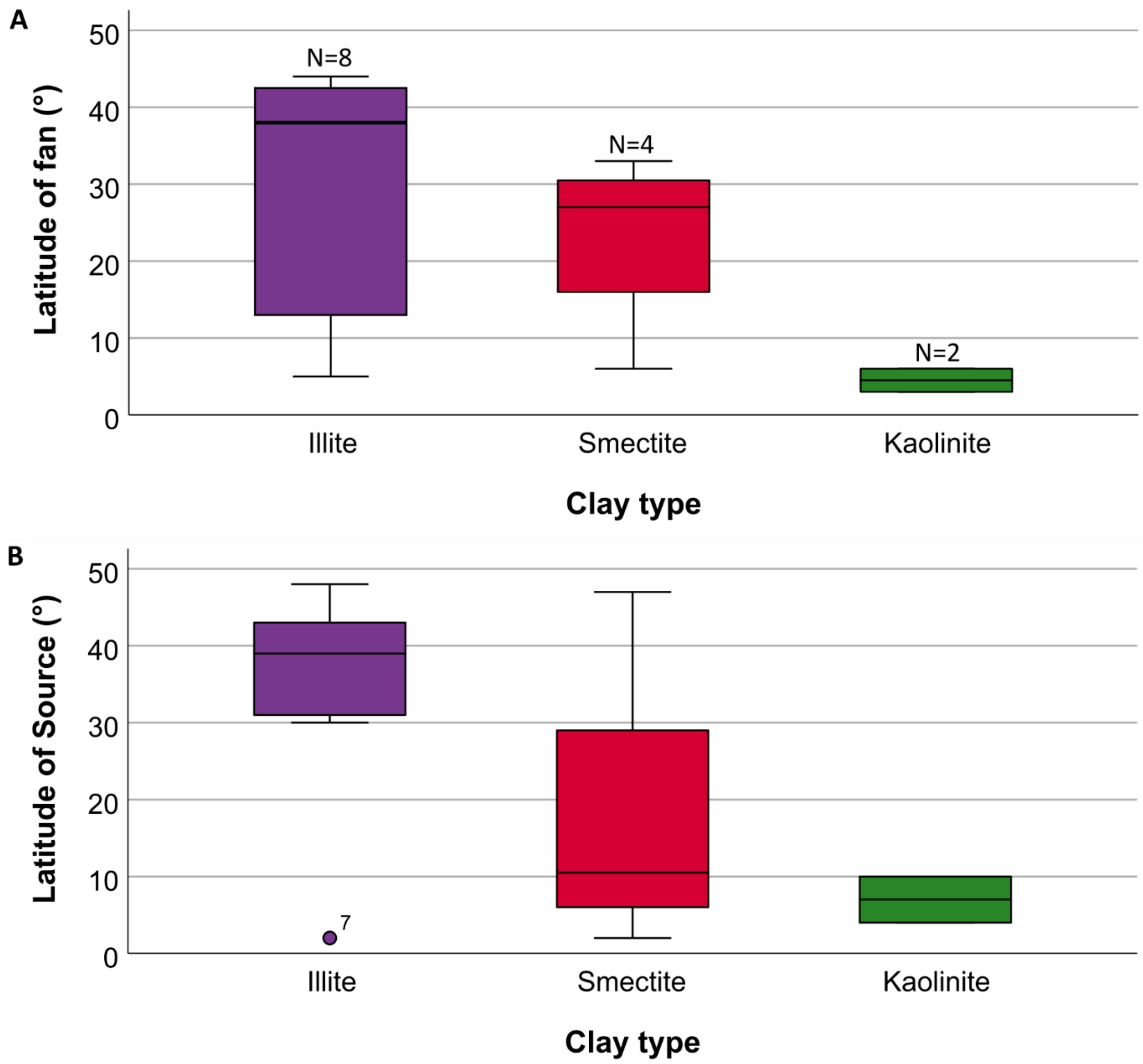

Figure 7.11: Box plots of dominant clay mineral type against (A) latitude of fan and (B) latitude of source. N denotes the number of fans for each box plot.

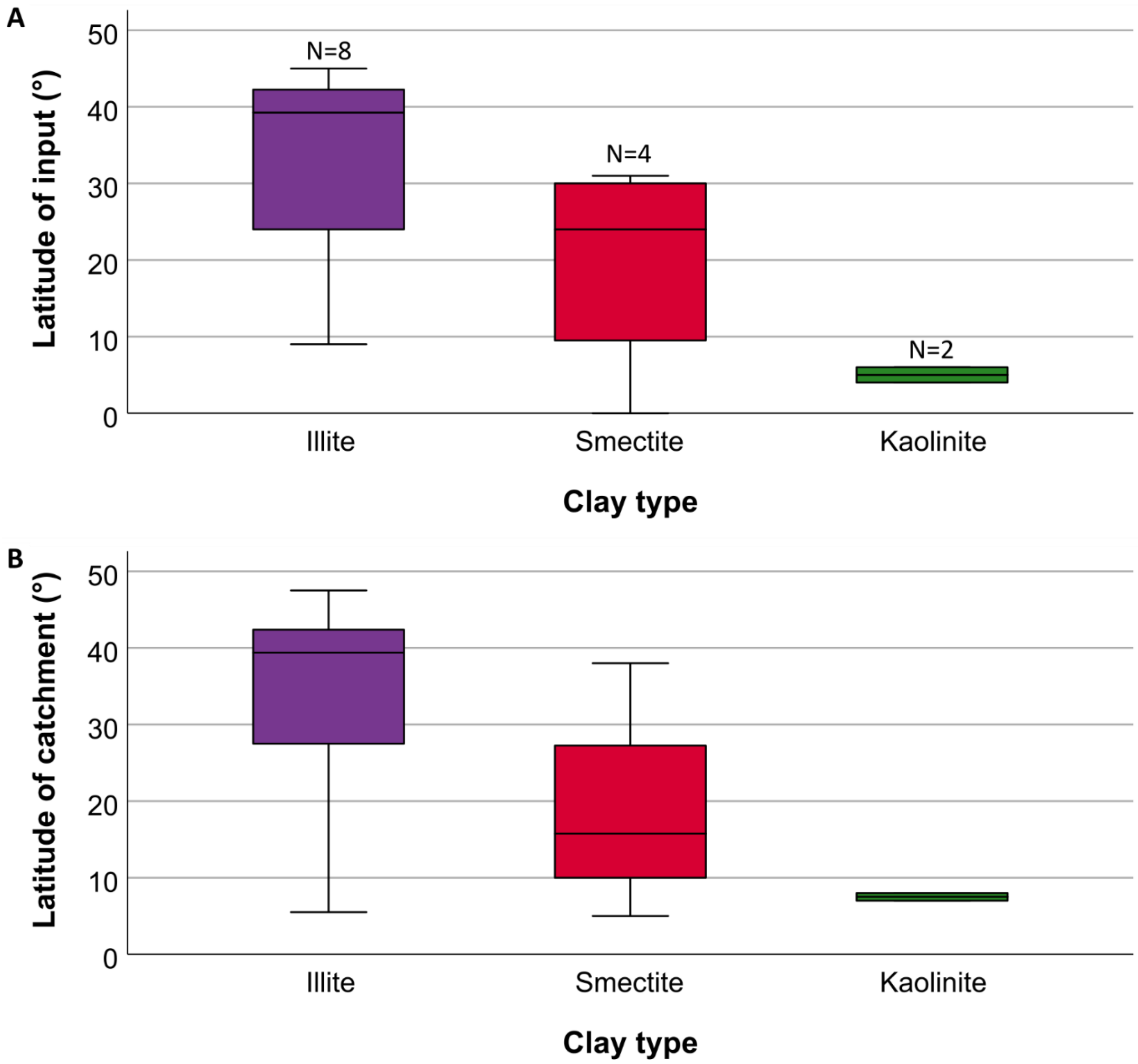

Figure 7.12: Box plots of dominant clay mineral type against (A) latitude of input and (B) latitude of catchment. N denotes the number of fans for each box plot.

7.3.1.3 Clay mineral assemblage

Figure 7.13 and Figure 7.14 present the relative percentages of the different clay minerals against latitude of fan, latitude of source, latitude of input, and latitude of catchment. No statistically significant linear relationships were found for most of these parameters. However, chlorite percentage shows a statistically significant increase with increasing latitude for all the latitudinal classes. In addition, although the kaolinite data are scattered, the two kaolinite-dominated fans are found at low latitudes, for all the latitude classes. Figure 7.15 shows the average clay mineral assemblage for each 10 degrees in latitude for the four latitude classifications. This figure further highlights that for all the latitude classifications the kaolinite percentage is highest at low latitudes of ≤ 20°, and consistently lower at higher latitudes. The opposite trend is observed for chlorite, which increases from low to high latitude for all latitude classifications. Illite and smectite show more complex trends and vary depending on the latitudinal classes. Generally, illite is highest at mid to high latitudes of ≥ 20° for latitude of source, input and catchment, but latitude of fan has high illite proportions at 10-20°. For all the latitude classifications, illite is the dominant clay mineral at 40-50° latitude. Smectite has the largest proportions at low to mid latitudes of ≤ 40°, but shows considerable variation between the latitude classes (Fig. 7.15).

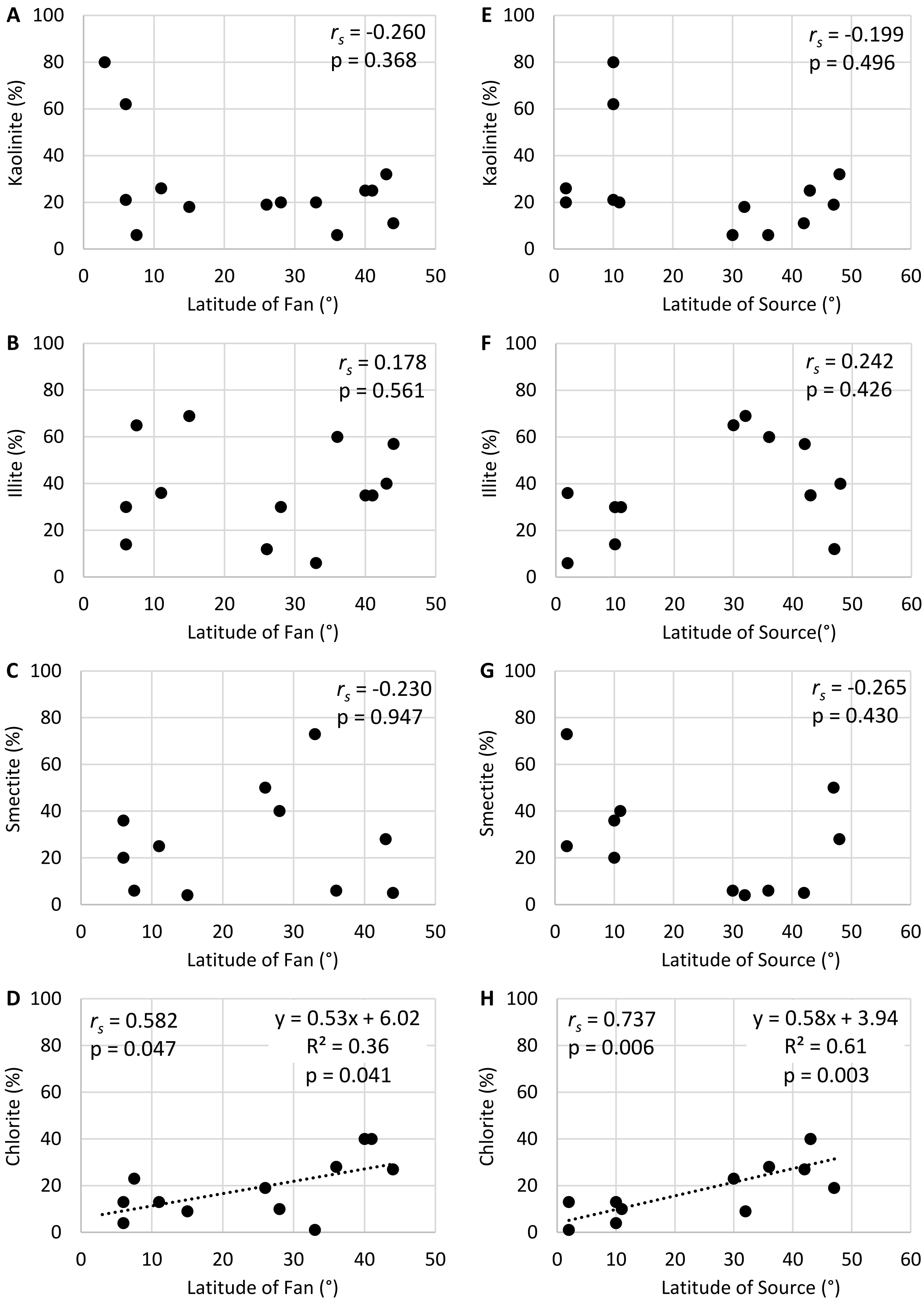

Figure 7.13: Percentage of clay minerals against latitude of fan and latitude of source.

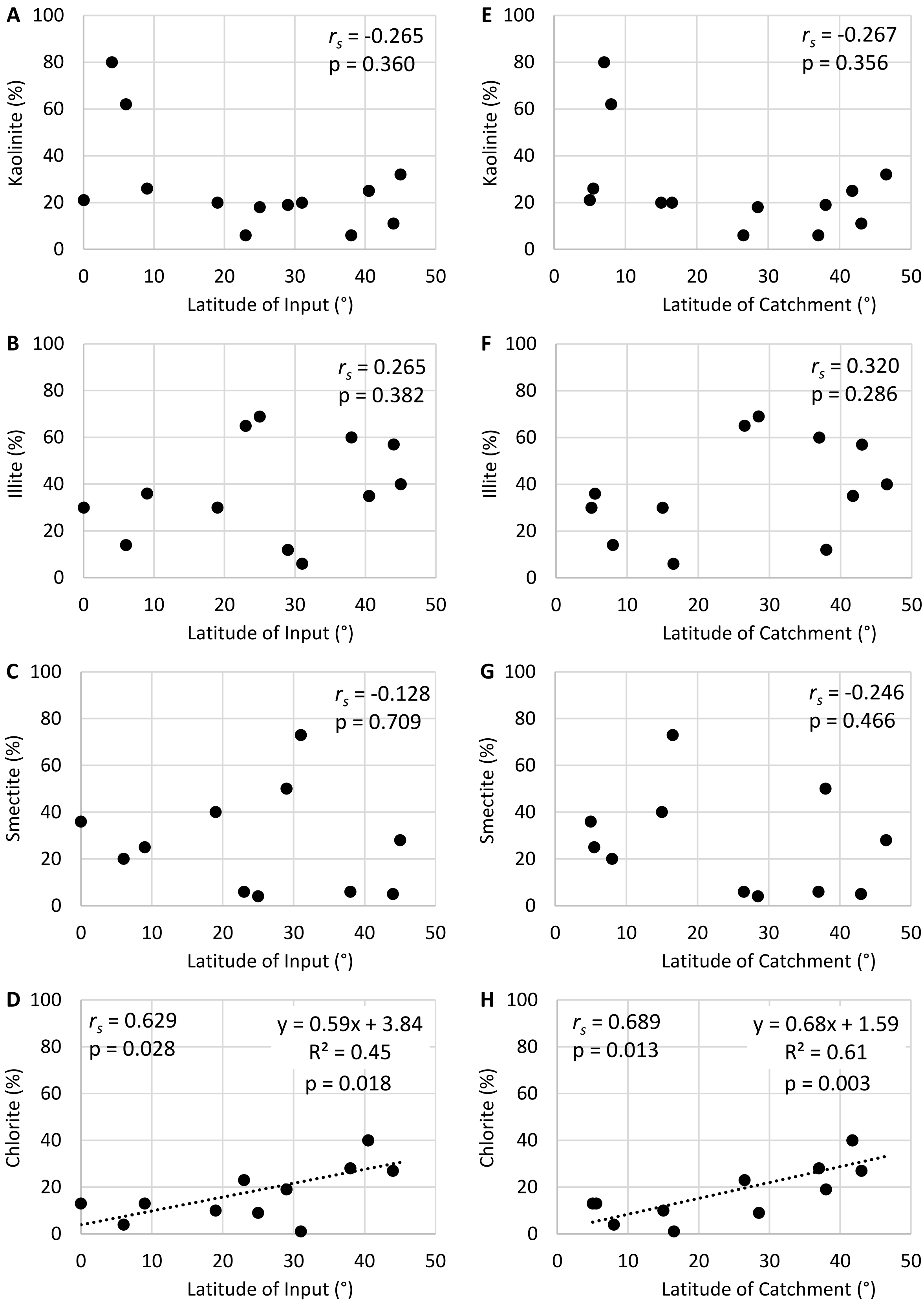

Figure 7.14: Percentage of clay minerals with latitude of fan input and latitude of catchment.

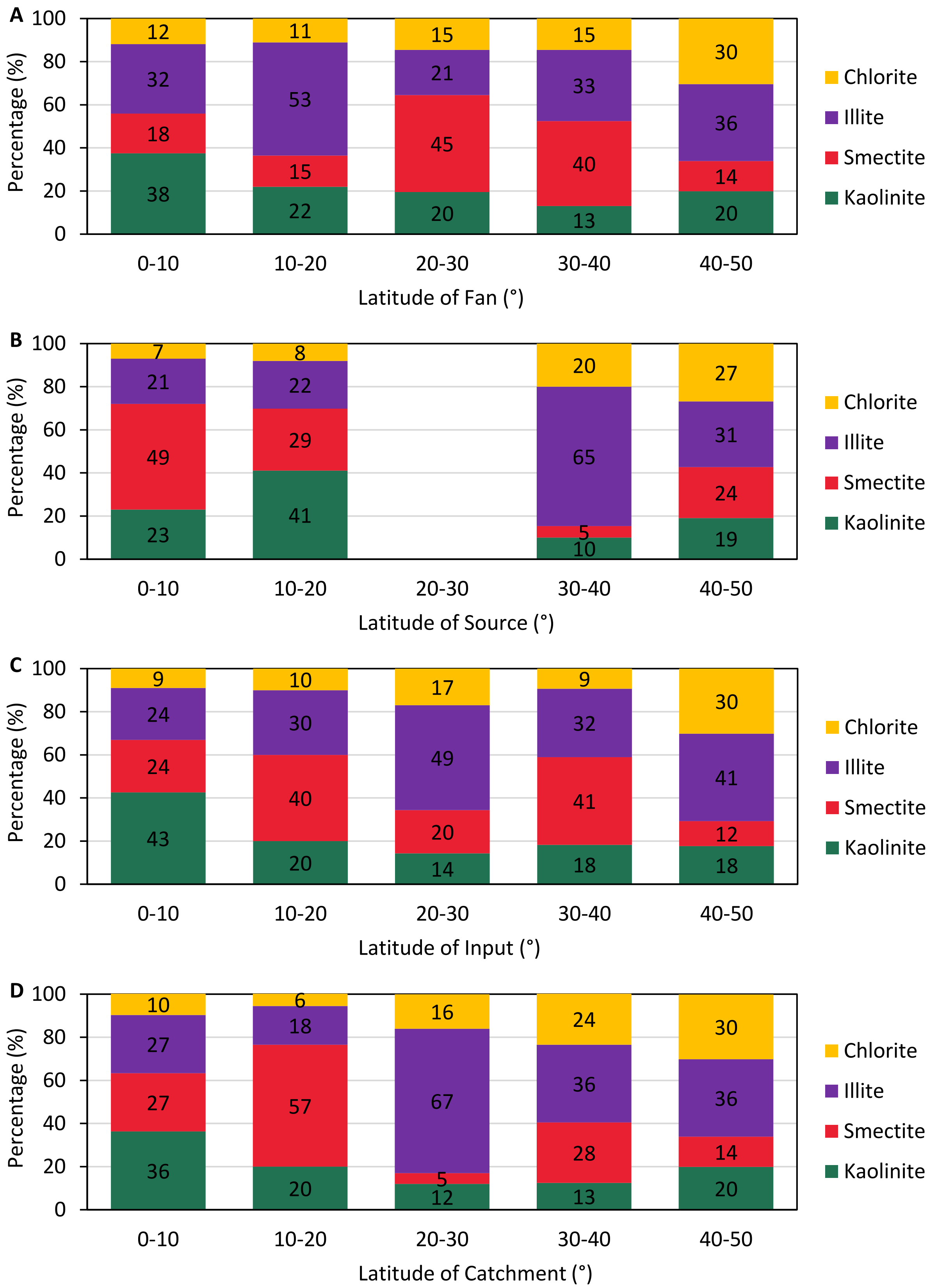

Figure 7.15: Average clay mineral assemblage of the fans in 10-degree bins for the different latitude classifications.

Figure 7.16 shows the kaolinite:chlorite ratio against fan latitude, latitude of input, latitude of source, and latitude of catchment. Not all the fans have known kaolinite and chlorite content, so the data are limited to ten fans. The kaolinite:chlorite ratio tends to decrease with increasing latitude of fan, but one abnormally low kaolinite:chlorite ratio at low latitude reduces the linear regression from $R^2 = 0.67$ ($p < 0.01$) to $R^2 = 0.24$ ($p > 0.05$), highlighting the limits of a small data set. A statistically significant linear correlation between decreasing kaolinite:chlorite ratio and increasing latitude of source ($R^2 = 0.51$, $p < 0.05$), input ($R^2 = 0.50$, $p < 0.05$), and catchment ($R^2 = 0.54$, $p < 0.05$) is shown in Figure 7.16B-D.

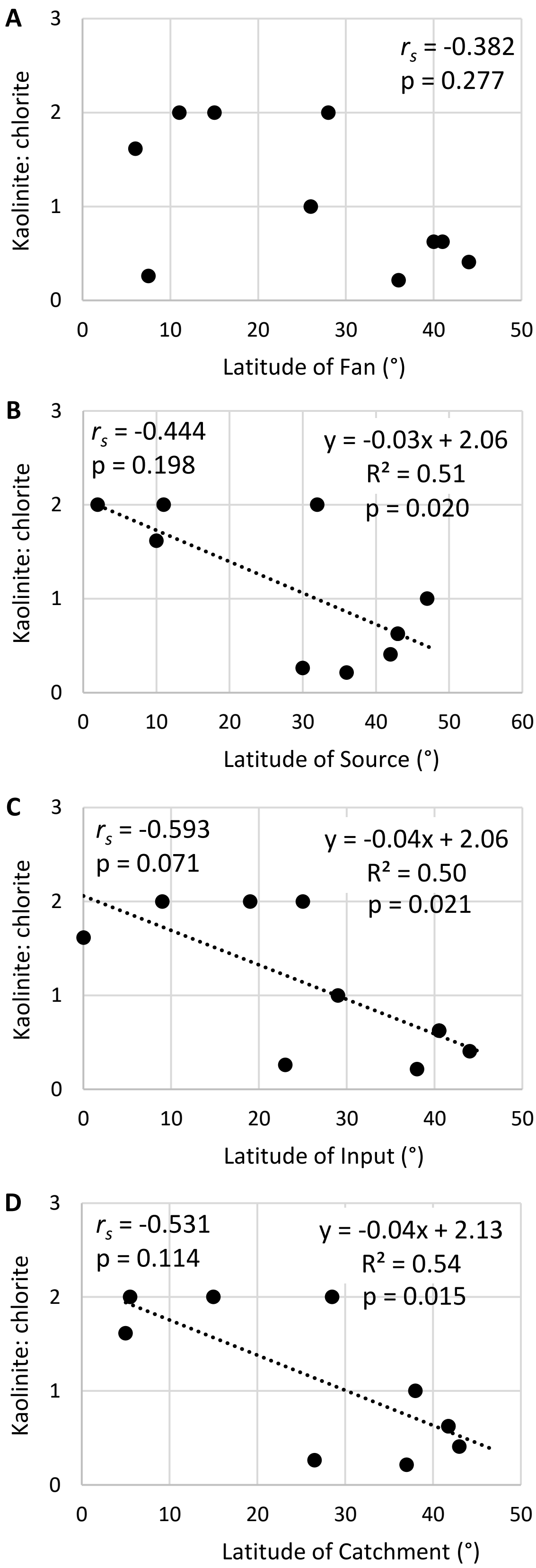

Figure 7.16: Kaolinite:chlorite ratio of the fans for the four latitudinal classes.

7.3.1.4 Multivariate analysis

The distance-based linear model results show that the latitude of fan input explains 20% of the variability in clay mineral assemblage between fans, whereas the latitude of catchment only explains 10% of the variability (Table 7.3). Using both predictors improves the model only slightly, with 22% of the variance explained. Since using two predictors doubles the complexity but produces a limited improvement on the variability captured, it is concluded that latitude of input is the best predictor for the clay mineral assemblages of the fans.

Table 7.3: Summary of the results from the permutational distance-based multivariate multiple regression for associations between the predictor variables and the clay mineral assemblages of the fans. The best model was selected based on Akaike's Information Criterion with a second-order bias correction applied (AICc), with the total variation explained (R^2) and the proportion of the variability in clay mineral assemblage that each predictor explains (% variability) rounded to nearest whole number.

Predictor	AICc	R^2	% variability
Latitude of input	94.501	0.19709	20
Latitude of catchment	95.995	0.099348	10
Latitude of input and catchment	97.616	0.21852	22

7.3.2 Clay mineral assemblage and fan properties

7.3.2.1 Dominant clay minerals

Figure 7.17 shows the average-vertical-fan-growth-rate, *H*, against dominant clay mineral type for fans with average volumetric fan growth rate, *V*, of < 100 km^3/ka. It should be noted the Danube fan (*H* = 2.1 m/ka) was considered an outlier and therefore not included in the illite box (Fig. 7.17). The median *H*-value of the fans increases from 0.02 m/ka for the kaolinite fans via 0.22 m/ka for the illite fans to 0.33 m/ka for the smectite fans. The interquartile range is small for the kaolinite fans and distinct from the illite and smectite fans. The interquartile ranges of the illite and smectite fans are larger compared to the kaolinite fans and overlap each other. Figure 7.18 presents the *H*-values for the three large fans with 100 < *V* < 350 km^3/ka. The two smectite fans have a large interquartile range and a median value of 0.23 m/ka. The only large illite fan has an average-vertical-fan-growth-rate of 0.07 m/ka, which is within the interquartile range of the smectite fans.

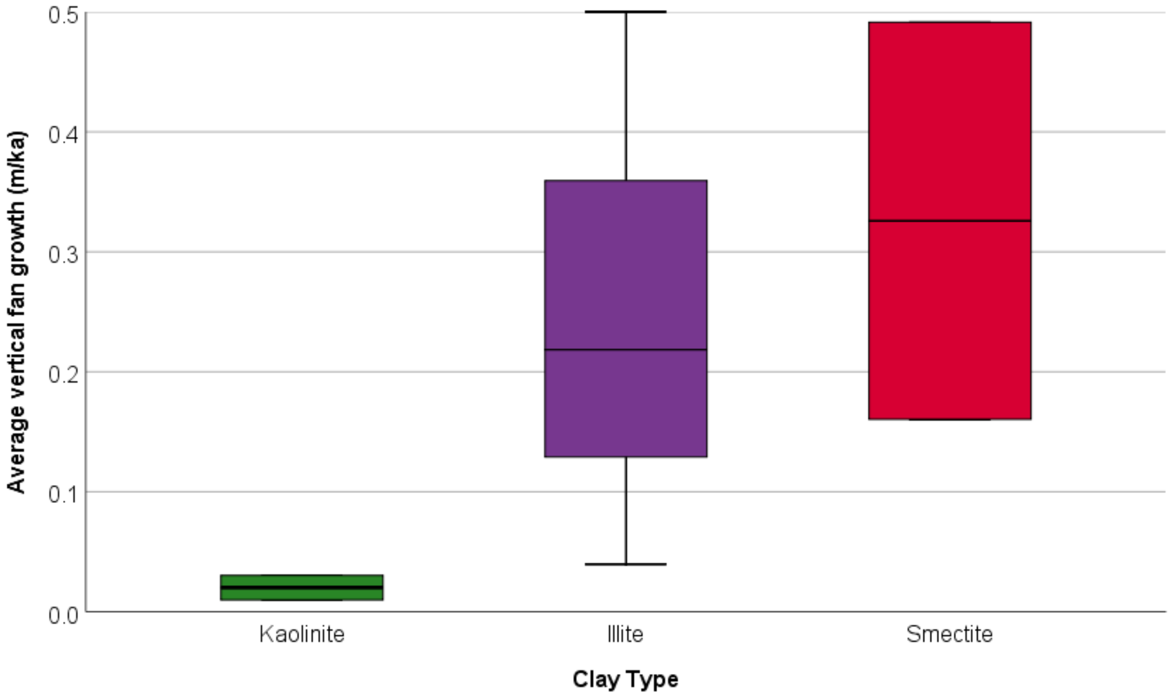

Figure 7.17: Box plot of average-vertical-fan-growth-rate for the small fans (V < 100 km^3/ka) for each dominant clay mineral. The illite-dominated Danube fan is considered an outlier and not shown. Kaolinite: N = 2; illite: N = 3; and smectite: N = 2, where N denotes the number of fans.

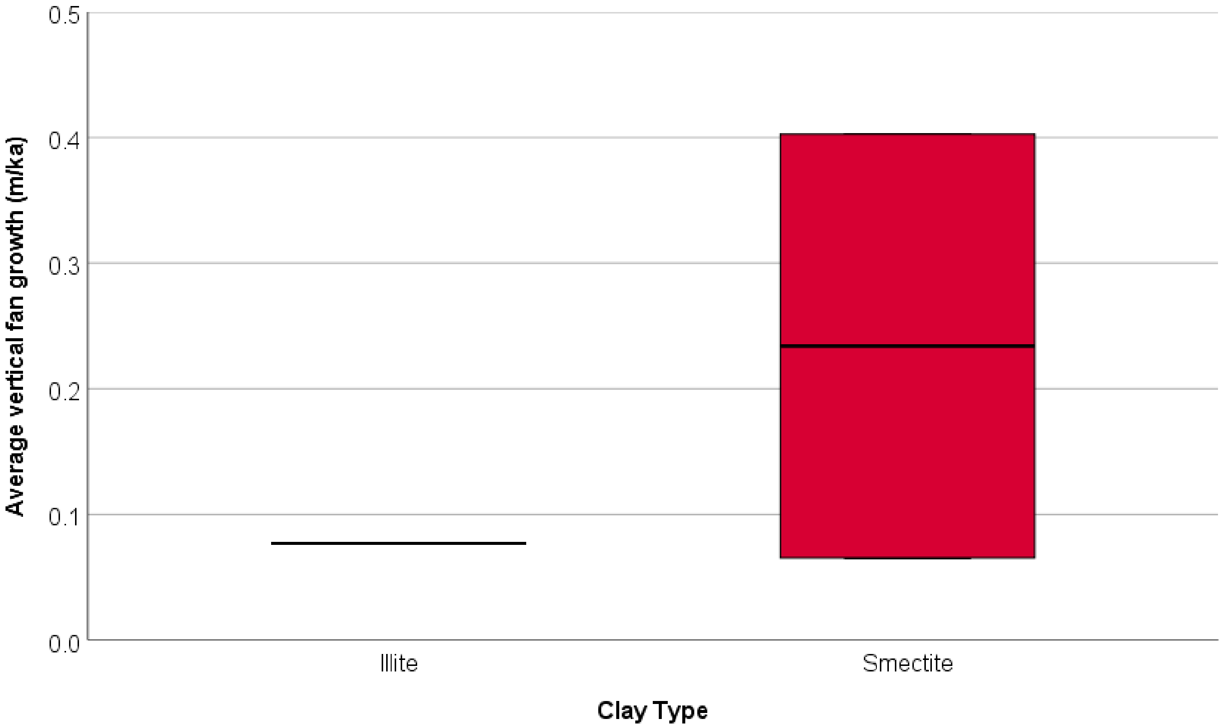

Figure 7.18: Average-vertical-fan-growth-rate of the large fans (100 < V < 350 km^3/ka) for illite- and smectite-dominated fans. Illite: N = 1; smectite: N = 2, where N denotes the number of fans.

7.3.2.2 Clay mineral assemblages

More detailed analysis was conducted by plotting the clay mineral assemblages against the average-vertical-fan-growth-rate (Fig. 7.19). The number of fans analysed was limited, as only eight fans had data on the percentages of all four clay mineral types. Therefore, the small and large fans were not analysed separately. No trend is observed between the average-vertical-fan-growth-rate and any of the clay mineral percentages and a large amount of scatter is observed (Fig. 7.19). It is useful to also consider the ratios of the rheologically distinct different clay minerals (Chapter 7.2.3.1). No trend is apparent for the kaolinite:smectite ratio and for the ratio of weakly to strongly cohesive clay minerals (Fig. 7.20). Yet, the two fans with the high kaolinite:smectite ratio have the lowest average-vertical-fan-growth-rate (Fig. 7.20A). Figure 7.20B demonstrates that the majority of the fans are dominated by cohesive clay minerals and only two fans predominantly contain weakly cohesive clay minerals.

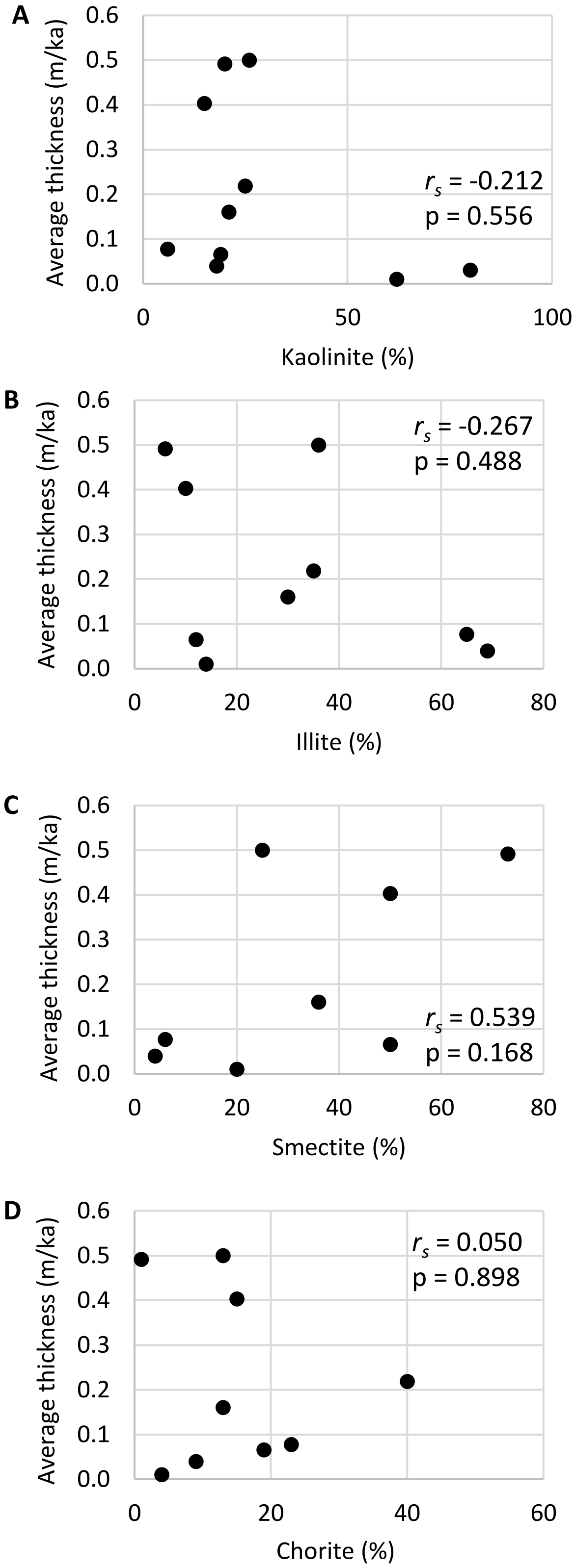

Figure 7.19: Average-vertical-fan-growth-rate (termed average thickness on y-axis) of fans against the percentages of (A) kaolinite, (B) illite, (C) smectite, and (D) chlorite.

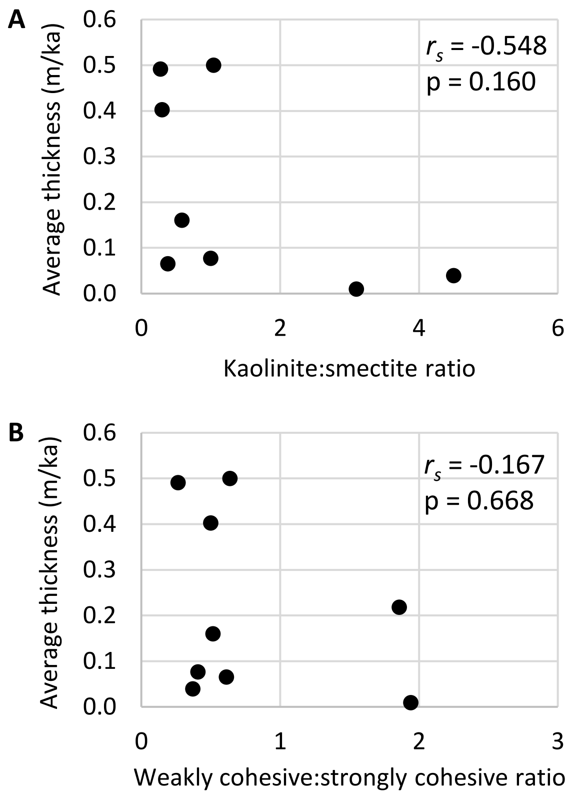

Figure 7.20: Average-vertical-fan-growth-rate (termed average thickness on y-axis) against (A) kaolinite:smectite ratio, and (B) ratio of weakly to strongly cohesive clay minerals.

7.3.3 Latitude and fan properties

The clay mineral data collected may not accurately represent the fans, since these data were collected from a limited number of cores that are often concentrated in a certain part of the fan, and only from the Pleistocene Epoch. It was therefore decided to circumvent clay mineral assemblage within the fans and investigate if there is a direct relationship between the latitude controls and average-vertical-fan-growth-rate. This analysis includes the Magdalena and the Rhône fans, which were not considered in Chapter 7.3.2, as these fans do not have published clay mineral data. As in Chapter 7.3.2, the Ebro, Wilmington, Danube and Cap Ferret fans were discounted because of their atypical deposit geometries. Twelve fans were considered in total and the small and large fans were not separated from each other. Figure 7.21 shows that the data are scattered for all four latitudinal classes, and none of the linear relationships between average-vertical-fan-growth-rate and latitude control type are statistically significant.

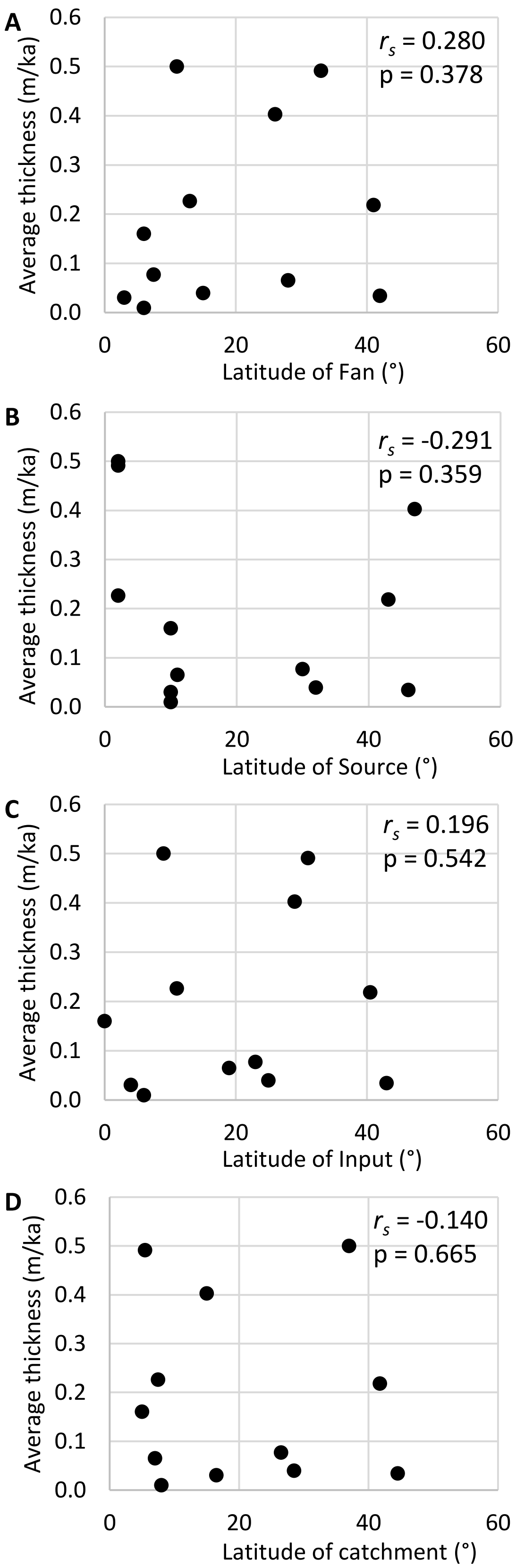

Figure 7.21: Average-vertical-fan-growth-rate (termed average thickness on y-axis) against (A) latitude of fan, (B) latitude of source, (C) latitude of input, and (D) latitude of catchment.

7.4 Discussion

7.4.1 Latitude of fans and clay mineral assemblage

7.4.1.1 Multidimensional scaling plot

The multidimensional scaling plot in Figure 7.9A and the grouping of the data in the dendrogram in Figure 7.9B allows easier exploration of the clay mineral assemblages in the fan sediment. Figure 7.9 shows four different groups of fans. This successful grouping of the data implies that there is multivariate structure and thus further exploration of the dataset is justified (Clarke *et al.*, 2008). The multidimensional scaling plot shows that there are very few fans dominated by either kaolinite or chlorite and most of the variation in the multidimensional scaling plot occurs along the smectite and illite axes (Fig. 7.9). This distribution matches the known trends in the clay mineral assemblage of recent deep-sea sediments in the World Ocean, where kaolinite and chlorite are the least abundant, accounting for approximately 15% of the clay size fraction each, and smectite and illite are most abundant, accounting for 35% of the clay size fraction each (Griffin *et al.*, 1968; Windom, 1976; Hillier, 1995). Two out of four clay mineral groups, Groups A and B, are characterised by a high illite content, again agreeing with the known prevalence of illite in the recent deep-sea sediments of the World Ocean. Group C includes many fans characterised by small amounts of chlorite and illite and by different combinations of smectite and kaolinite.

7.4.1.2 Dominant clay minerals

Figure 7.11 and Figure 7.12 suggest that the dominant clay mineral type within the fans is related to the latitude. For all the latitudinal classes, the median values show that illite-dominated fans are found at moderate to high latitudes, smectite-dominated fans prevail at moderate to low latitudes, and kaolinite-dominated fans are found at low, equatorial latitudes. For illite and kaolinite, this trend matches the climatic-driven force of clay mineral production. Illite clay is mainly produced at moderate to high latitudes from physical weathering, and kaolinite is predominantly generated at the equatorial latitudes under intense chemical weathering (Biscaye, 1965; Fagel, 2007). The specific latitudinal boundaries for the dominance of kaolinite clay generation are within the tropical-humid zone, 23.5° north and south of the equator (Rateev *et al.*, 1969). The two kaolinite fans included in this study fall within this range, with the average latitude of the fan, source, input and catchment of both fans located within 10° of the equator. The lack of high-latitude fans dominated by kaolinite is encouraging, but a larger dataset is needed to confirm the low-latitude preference of kaolinite-dominated fans.

Illite clay is produced predominantly between 30° and 90° latitude, increasing in abundance towards the higher latitudes in both hemispheres (Rateev *et al.*, 1969; Fagel, 2007). Of the eight illite-dominated fans included in this study, five are found above 30° latitude for all the latitudinal classes. However, the Bengal and Indus fans have a low latitude of fan, source, and catchment, and all the latitudinal controls are below 10° for the Orinoco fan (Figs 7.11 and 7.12). The Bengal and Indus fans have been shown to be illite-dominated because both have source areas in the Precambrian gneissic rocks of the Himalayas, which are subject to glacial weathering conditions (Fagel *et al.*, 1994; Kessarkar *et al.*, 2003). The Orinoco fan is fed by rivers that transport soils produced by physical weathering from the high parts of the South American continent and the Andean mountains (Chamley, 1989; Debrabant *et al.*, 1997; Gonthier *et al.*, 2002). Thus, for the Bengal, Indus, and Orinoco fans the effect of vertical climatic zonation on the production of clay particles appears to be greater than the latitudinal climatic influence. If the Bengal, Indus, and Orinoco fans are removed from the analysis of dominant clay mineral type within the fans and latitude, the illite-dominated fans never plot below 36° for any of the latitude classes (Figs 7.22 and 7.23). This strengthens the trend between the dominant clay mineral type within the fans and latitude, as the illite- and kaolinite-dominated fan box plots no longer overlap for any of the latitude classifications (Figs 7.22 and 7.23).

The smectite-dominated fans were found at a wide range of latitudes, with a median value of 24° for latitude of fan and latitude of input, and a median value of 10.5° and 15° for latitude of source and latitude of catchment. Detrital smectite forms in tropical, temperate, and semi-arid climates (Chamley, 1989; Thiry, 2000; Fagel, 2007), therefore smectite-dominated fans are expected to occur at a large latitudinal range of 0° to 60°. The fact that the smectite box plots overlap with the illite and kaolinite box plots in Figure 7.11 and Figure 7.12 support this wide latitudinal distribution. It is encouraging that the median latitude of the smectite fans fall in between the median latitudes of the high-latitude illite and the low-latitude kaolinite fans. However, the origin of smectite within deep-marine fans needs to be treated with caution as smectite can be authigenic in origin and form locally from volcanism and hydrothermal activity (Chamley, 1989).

It is worth noting that the dataset does not include mud-rich and mixed sand-mud fans with latitude of fan, source, input or catchment above 48°. This lack of high latitude fans is to be expected, since sediment at high latitudes has been heavily influenced by glaciation and submarine fans are therefore dominated by sand and gravel (Pickering & Hiscott, 2016). Chlorite clay produced by physical weathering is expected to be the dominant clay mineral forming within polar regions above 60° (Biscaye, 1965; Gradusov, 1974). Further work could focus on the chlorite content in high-latitude, sand-rich and gravel-rich fan sediment. However, this was not deemed to be useful for this study, because mud-rich and mixed sand-mud fan sedimentation follows physical rules that are different from sand-rich and gravel-rich fan sedimentation.

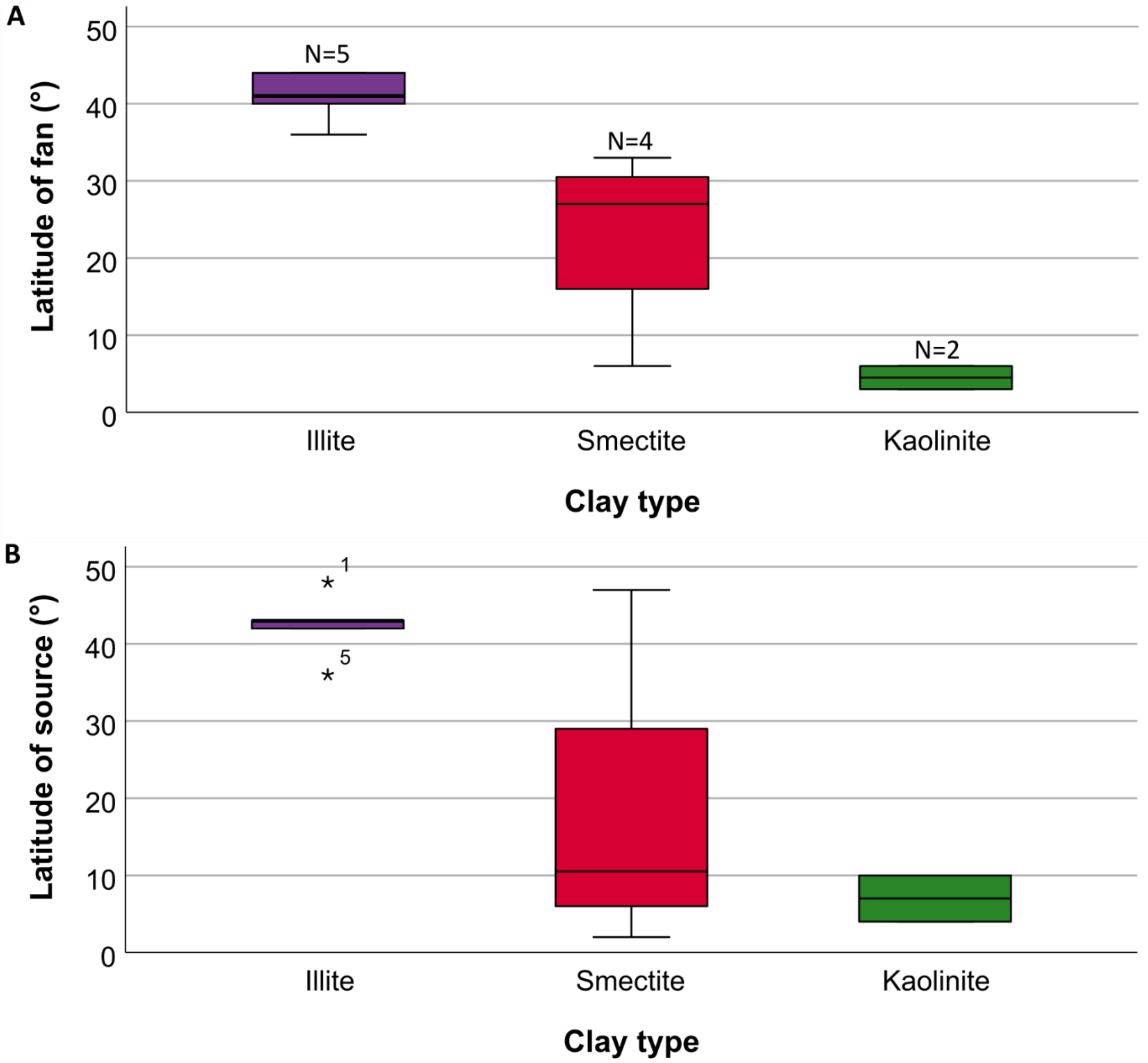

Figure 7.22: Box plots of dominant clay mineral against (A) latitude of fan and (B) latitude of source. The Bengal, Indus and Orinoco fans are not included in the analysis, as these fans are dominated by illite due to physical weathering at mountain ranges within their catchment. N denotes the number of fans for each box plot.

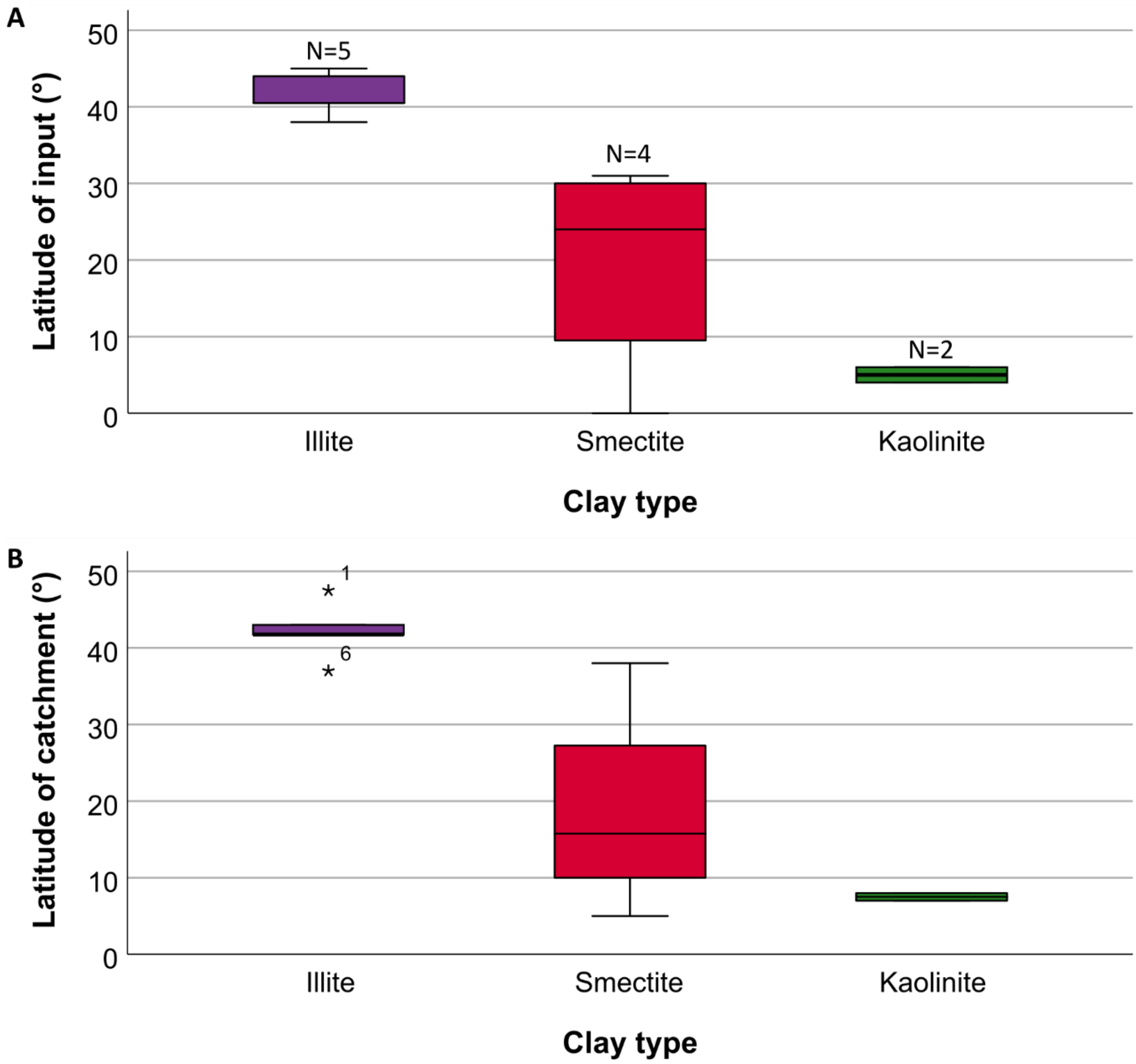

Figure 7.23: Box plot of dominant clay mineral type against (A) latitude of input and (B) latitude of catchment. The Bengal, Indus and Orinoco fans are not included as their clay mineral assemblage is interpreted to be driven by non-latitudinal controls. N denotes the number of fans for each box plot.

7.4.1.3 Clay mineral assemblage

Figures 7.13 to 7.15 show the relationships between the clay mineral assemblages and the latitudinal classes. In Figure 7.13 and Figure 7.14, only chlorite percentage produced a statistically significant relationship for all the latitudinal classes. The increase in chlorite with latitude matches its climate-driven origin, as it is expected to form by physical weathering at high latitudes (Biscaye, 1965; Gradusov, 1974). The other clay minerals show significant scatter with latitude for all the latitude classes. However, this is maybe to be expected considering that the clay mineral percentage data are closed sums, which can mask trends. No trend was expected for smectite percentage, as this clay mineral is predicted to occur between 0° and 60° (Fagel, 2007).

Latitudinal trends are easier to identify in Figure 7.15, in which the latitudinal data are plotted in 10° bins. This figure highlights that kaolinite and chlorite are the most latitudinally-driven clay minerals (Fagel, 2007), as their percentage clearly decreases and increases with latitude, respectively, for all latitudinal classes. Figure 7.15 also confirms that illite-dominated fans are present at high latitude (*cf.* Figs 7.11 and 7.12), as illite is the most dominant clay mineral at 40-50° latitude for all the latitudinal classes. Finally, Figure 7.15 demonstrates the anticipated high variability of smectite percentage within the fans.

Clay mineral ratios within the fans may be a better proxy for the climate on the continent than the dominant clay type or the clay mineral assemblage (Gingele *et al.*, 1998; Fagel, 2007). Indeed, the statistically significant linear relationship between reducing kaolinite:chlorite ratio and increasing latitude of the fan, source, input, and catchment, shown in Figure 7.16A-D, matches with the equatorial dominance of kaolinite and high-latitude prevalence of chlorite, shown in Figure 7.15. This decrease in kaolinite:chlorite ratio is driven primarily by an increase in chlorite at higher latitudes (Figs 7.13D,H and 7.14D,H), as there is no significant trend of reducing kaolinite percentage with increasing latitude (Figs 7.13A,E and 7.14A,E). Chlorite is expected to dominate at latitudes above 60°, but these data suggests that chlorite also increases in abundance with distance from 0° latitude.

It is difficult to select the latitude of fan, input, source, or catchment as the best latitudinal control for predicting the dominant clay mineral or clay mineral assemblage from the present dataset. Latitude of catchment could be considered as the best because the interquartile ranges of the box plots do not overlap (Fig. 7.12B). Furthermore, the latitude of catchment has the highest R^2-values for the chlorite percentage and the kaolinite:chlorite ratio, but latitude of source also has good R^2-values for these parameters. Using the latitude of catchment class would be a logical choice, as it is at this latitude that clay is produced in most systems. However, from a practical point of view, both latitude of catchment and latitude of source would be hard to obtain from fans in the geological record, as this would require paleogeographic knowledge of the source area of the fan. Latitude of the input is easiest to utilise for modern and ancient fans, as the latitude of the upper part of the fan should be close to the latitude of the input. Latitude of input is a better predictor than latitude of fan, based on this dataset.

7.4.1.4 Multivariate analysis

A distance-based multivariate multiple regression was conducted to test how much of the variance of the clay mineral assemblages in the fans can be explained by the latitudinal controls. The results showed that latitude of input performed better than latitude of catchment and could explain 20% of the variability in the clay mineral assemblages compared to 10%.

The result of latitude of input explaining 20% of the variance in the clay mineral assemblages can be considered a positive result, because of the many other controls on the clay mineral assemblages found within submarine fans. Additional controls on clay mineral production include: type of source rock; relief of the land; volcanic activity; size of sedimentary basins; sorting of clay during transport; stability of clay minerals; and clay mineral diagenesis (Chapter 1.6). These factors can disrupt the climatic signal of clay mineral assemblages as follows: 1) The type of source rock can determine the composition of the minerals formed by weathering; 2) The relief of the land can control the strength of the weathering, with greater physical weathering occurring in areas of high relief, potentially producing different clay minerals (Singer, 1984; Thiry, 2000); 3) Smectite can be produced as an alteration product of volcanic rock; 4) Large sedimentary basins may stretch across climate zones and muddle the climate signal within clay mineral assemblages; 5) The climatic signal may be distorted during transportation if the clay minerals of different size are sorted during transport; 6) Different clay minerals have different stabilities and some may transform into other clay minerals whilst in the sedimentary basin; 7) Diagenetic reactions alter detrital clay assemblages and have the potential to completely remove the climate signal of clay mineral assemblages (Curtis, 1990; Fagel, 2007).

Despite the many controls on clay mineral assemblage discussed above, the results from the distance-based multivariate multiple regression suggests that latitude is a non-trivial control on the clay mineral assemblages found in modern submarine fans. Future work should focus on quantifying the other controls on clay mineral assemblage, such as maximum relief within the catchment area to try to quantify the control of the relief of the land. This data could then be included within the distance-based multivariate multiple regression to test how much of the variance in the clay mineral assemblages within the fans can be explained by the other variables.

7.4.2 Clay mineral assemblage and fan properties

It is expected that high-density SGFs laden with weakly cohesive clay reach a greater distance from their origin than flows that carry strongly cohesive clay, at a similar suspended-sediment concentration. If the control of dominant clay mineral type on flow behaviour and deposit properties can be scaled up to the size of natural fans, fans dominated by weakly cohesive clay minerals should have thinner deposits per thousand years of fan growth. For the systems in this metadata study, the average-vertical-fan-growth-rate (H) should increase from kaolinite-dominated via illite-dominated to smectite-dominated fans, mirroring the increase in cohesive strength of the clay minerals.

The median H-values of the small fans (defined as fans with an average volumetric fan growth rate, V, of < 100 km^3/ka), increased from kaolinite-dominated via illite-dominated to smectite-dominated fans

(Fig. 7.17). For the large fans with $100 < V < 350$ km^3/ka, the illite-dominated fan had a lower median H-value than the smectite-dominated fans (Fig. 7.18). These results are encouraging because they match the expected relationship of H with the rheological properties of the dominant clay minerals. However, caution needs to be exerted, as these results are based on a limited number of fans with a large amount of scatter in the H-values. For example, one large illite-dominated fan is compared to two smectite-dominated fans, and the minimum H-value of the large smectite-dominated fans is 0.07 m/ka, which is less than the H-value of the illite-dominated Bengal fan (H = 0.08 m/ka). Moreover, the interquartile ranges of the small illite-dominated fans and smectite-dominated fans overlap and the H-values of the illite-dominated fans range by an order of magnitude ($0.04 < H < 0.50$ m/ka).

The illite-dominated Danube fan has an extremely high average-vertical-fan-growth-rate (H = 2.08 m/ka), which was considered an outlier and not included in the analysis. It is unclear why the sedimentation rate of the Danube fan is large compared to the other fans. The Danube fan is in the Black Sea, which has been shown to be isolated from the global oceans during sea-level lowstands; sea level was *c.* 30 m lower than the global sea level lowstand during the Last Glacial Maximum. This could have been a factor contributing to the high sedimentation rate (Winguth *et al.*, 2000). The Danube fan is also relatively young (900 ka) compared to the other fans used in this metadata study.

The relationship between average-vertical-fan-growth-rate and dominant clay type shown in Figure 7.17 and Figure 7.18 is not reflected in Figure 7.19 and Figure 7.20, in which H is plotted against the relative percentage of each clay mineral type. This suggests that the dominant clay type is a more useful measure than the clay mineral assemblage data. The kaolinite:smectite ratios and ratios of weakly to strongly cohesive clay minerals shown in Figure 7.20 demonstrate that the data are limited by the spread of the tested clay mineral assemblages. Only two fans are dominated by weakly cohesive clay minerals, containing ≥ 65% kaolinite and chlorite, whereas the rest of the fans are dominated by strongly cohesive clay minerals, comprising of ≥ 60% illite and smectite. The low number of fans dominated by weakly cohesive clay minerals renders it difficult to discern trends and it highlights that more fans need to be analysed. Of the clay mineral assemblage ratios tested, the ratio of weakly to strongly cohesive clay minerals might be the most suitable parameter, as it includes the total clay mineral assemblage. Although the kaolinite:smectite ratio is based on the most rheologically distinct clay minerals, it is limited in that fans dominated by illite or chlorite may have kaolinite:smectite ratios that do not represent the rheological properties of the flows that formed these fans.

The present study that does not take into account the large number of other variables, in addition to clay mineral type, that may control the large-scale geometry of submarine fans. This is a significant limitation, because it was shown in earlier chapters that, in particular, flow velocity and flow concentration are of vital importance for the balance between turbulent and cohesive forces in SGFs.

This balance helps determine whether the flows behave as LDTCs, HDTC, mud flows or slides. The effect of clay mineral type on the average-vertical-fan-growth-rate will be minimal if the majority of the flows constructing the submarine fan are low-concentration, relatively low-velocity LDTCs. If, however, the flows behave as high-concentration HDTCs, mud flows or slides, the effect of clay mineral type on the average-vertical-fan-growth-rate should be larger.

7.4.3 Latitude and fan properties

The different latitudinal controls of the fans were tested against the average-vertical-fan-growth-rate to test if there is a direct relationship between these variables. This was conducted as the clay mineral data may not accurately represent the fans, since the data were collected from only a few cores in specific parts of the fans, and only from the Pleistocene Epoch. It would also be very powerful if there is a direct relationship between the latitude controls and average-vertical-fan-growth-rate, as it would negate the need to know the clay mineral assemblage within the fans.

Figure 7.21 shows a large amount of scatter between the average-vertical-fan-growth-rate and the latitudinal controls. The scattered data and low correlation coefficients may be expected, as when the known latitudinal control on clay mineral production and the rheological properties of those different clay minerals are combined, a complex potential trend between average-vertical-fan-growth-rate with increasing latitude emerges. Firstly, the two most strongly latitudinally controlled clay minerals, low-latitude kaolinite and high-latitude chlorite, have similar rheological properties. Chlorite and kaolinite are both are weakly cohesive, so are expected to produce thin fans with long runout distances and low H-values when they dominate the clay mineral assemblages at high and low latitudes, respectively. The most cohesive clay mineral, smectite, has limited latitudinal control and is found from between 0° to 60°, although Chapter 7.3.1 suggests that smectite-dominated fans are primarily found between 10° and 30°. Illite, the second most cohesive clay mineral of the main four clay types, is expected to form at moderate to high latitudes, and increase towards high latitude. This is confirmed by the results in Chapter 7.3.1. Thus, if the trend of dominant clay minerals changes from kaolinite, to smectite, to illite, and finally to chlorite with increasing latitude, the smallest average-vertical-fan-growth-rate would be expected at low and high latitudes, with large average-vertical-fan-growth-rate anticipated at mid-latitudes. This idealised model is shown as a schematic plot in Figure 7.24. In Figure 7.21 the average-vertical-fan-growth-rate and latitudinal controls are tested for a linear relationship, but this is not correct considering the more complex expected trend suggested in Figure 7.24.

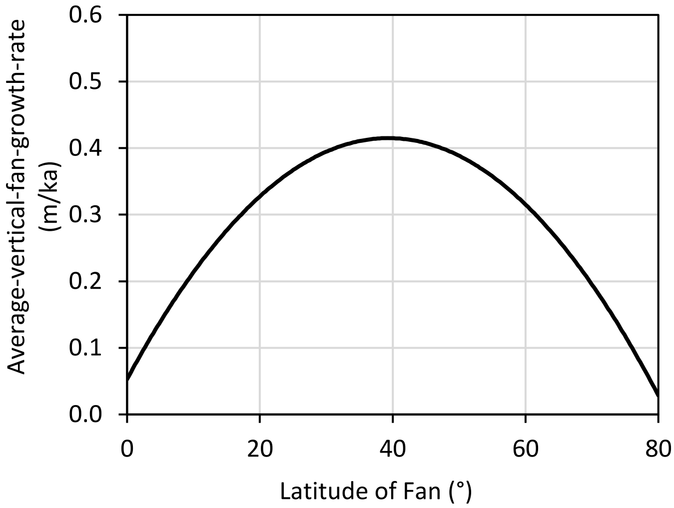

Figure 7.24: Idealised curve of average fan growth rate against the latitude of fan. At low and high latitudes, fans should be dominated by weakly cohesive kaolinite and chlorite, respectively, which should produce low average-vertical-fan-growth-rate values. At the mid-latitudes the fans should be dominated by smectite and illite, both of which are strongly cohesive and should produce fans with large average-vertical-fan-growth-rates.

The simplified predicted trend, of small average-vertical-fan-growth-rate at low and high latitudes and large average-vertical-fan-growth-rate at mid latitudes, is not observed in Figure 7.21. This suggests it is not possible to circumvent the clay mineral assemblage data and find a relationship directly between the latitude controls and average-vertical-fan-growth-rate. However, when the median latitudes of the fans dominated by different clay mineral types are plotted against the average-vertical-fan-growth-rate, the expected trend does emerge (Fig. 7.25). This plot uses the median latitude of fan input calculated for each group of fans classed by their dominant clay mineral for the *x*-axis (Fig. 7.12A). Care needs to be taken as the latitude of input in Figure 7.25 is an average value. However, Figure 7.25 does show that the kaolinite-dominated fans with low latitudes of fan input have the smallest median average-vertical-fan-growth-rate, the mid-latitude smectite-dominated fans have the largest median average-vertical-fan-growth-rate, and the high-latitude illite-dominated fans have the middle value of median average-vertical-fan-growth-rate, between the smectite- and kaolinite-dominated fans. The slightly lower median average-vertical-fan-growth-rate for illite fans compared to smectite fans is expected, as it matches their rheological properties.

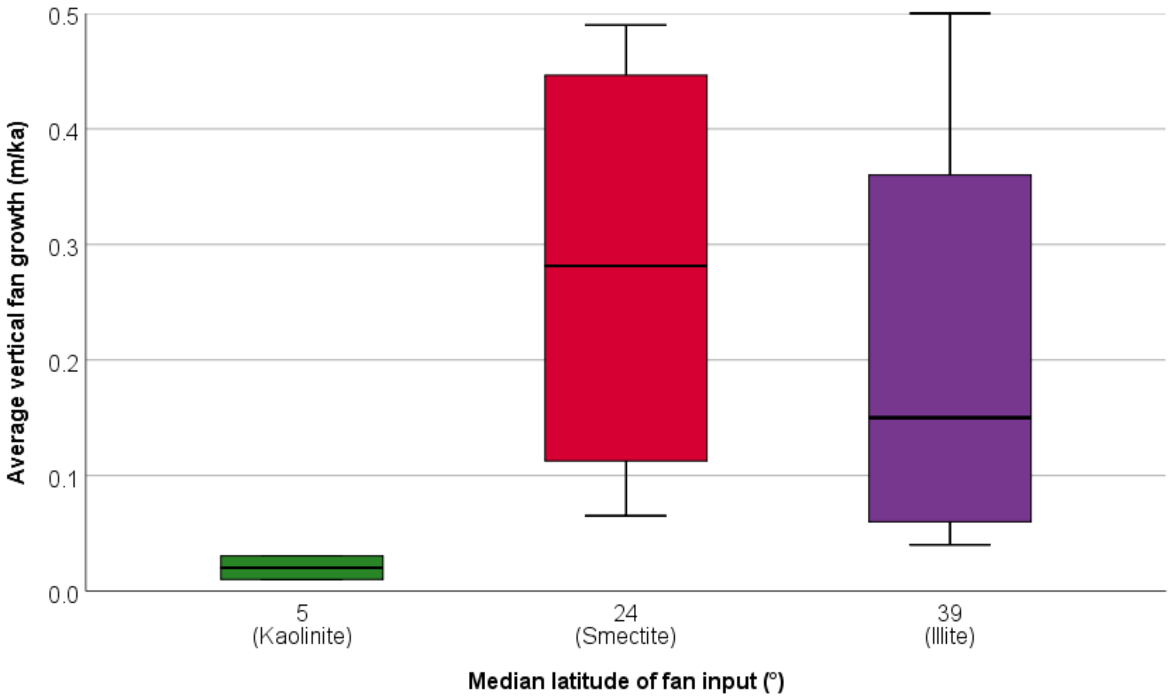

Figure 7.25: Box plot of average-vertical-fan-growth-rate against the median latitude of fan input of the fans sorted by their dominant clay mineral type.

7.4.4 Wider implications

Despite the other controls on the formation of clay minerals in submarine fans, the box plots of dominant clay mineral type against the latitudinal classes suggest that there is a relationship between the dominant clay mineral within submarine fans and their latitude (Figs 7.22 and 7.23). This is supported by the distance-based multivariate multiple regression which showed that latitude of input could explain 20% of the variability in the clay mineral assemblages within the fans. The results also suggest that clay mineral assemblage is a meaningful control on the geometry of modern submarine fans, as there is a relationship between average-vertical-fan-growth-rate and dominant clay mineral type within the fans that matches the rheological properties of the clay minerals. Further data analysis is needed to confirm that these relationships are robust, as they could have wide reaching implications.

If the relationship between the contemporary climate and the clay mineral assemblage in modern, mud-rich submarine fans is considered strong enough, marine clays in ancient submarine fan deposits could be used to reconstruct the palaeoclimates of their continental source areas. Provided that the original clay mineral assemblage can be reconstructed. Interpreting the palaeoclimate is important for geological reconstruction of past environments and clay mineral assemblage could be used as a valuable additional predictor. Alonso and Maldonado (1990) have already successfully demonstrated that this can be achieved. The authors used the kaolinite:chlorite ratio within the Ebro fan to recognise two climatic periods: an older cold period interpreted as the end of the Pleistocene (low kaolinite:chlorite ratios), and a younger warm period taken to represent the Holocene (high kaolinite:chlorite ratios). If the relationship between climate and clay mineral assemblage becomes better known, this could be an extremely useful tool to understand the history of formation of ancient submarine fans. The results from this metadata analysis suggest dominant clay mineral, chlorite percentage, and kaolinite:chlorite ratios may be the best palaeoclimate indicators.

The relationship between clay mineral assemblage and geometry of the modern, mud-rich submarine fans in this metadata analysis advocates that clay mineral type needs to be considered an important control when interpreting the depositional properties of fine-grained, mud-rich fans. This control may also extend to the fringe region of more sand-dominated systems, in which deposition has also been shown to be controlled by cohesive clay, *e.g.*, the sandy Late Jurassic deep-water fans in the North Sea (Haughton *et al.*, 2003). Clay mineral type may also control the smaller scale architecture within mud-rich submarine fans. This is particularly expected for architectural elements built by high-density SGFs, where clay mineral type is expected to control SGF behaviour, such as lobes.

A relationship was not found between the average-vertical-fan-growth-rate and the latitudinal classes of the fans. However, this may be because the expected relationship between fan latitude and fan geometry is expected to be complex and non-linear. A larger dataset is needed to test for these complicated expected trends. However, if a relationship between latitude and system architecture is found, the fan properties of ancient mud-rich submarine fans could be predicted based on their palaeolatitude. This would be particularly useful for large-scale fan properties which are rarely preserved in outcrop, such as fan area.

7.4.5 Future research

The growing discipline of seafloor geomorphology is providing increasing amounts of valuable data on the morphology of modern submarine fans. Improved technology now allows sampling of these deep-marine systems, *i.e.,* via cores, to be achieved at lower costs. This will help raise the potential of the present type and other types of metadata studies. Despite the valuable relationships between dominant clay type, fan shape and latitude found in this study, these results also highlight the need for more data. First and foremost, more data on clay mineral assemblages within a larger number of submarine fans and across a wider range of latitudes fans are needed. Moreover, a larger number of cores and surface samples are needed to characterise spatial changes in clay mineral assemblages across entire fans. The Magdalena and Mozambique fans are prime examples of fans that need to be understood better through more detailed surveying. Data is also lacking on the ability of cohesive SGFs to cause selective sorting of clay minerals during transport.

Higher-resolution data would allow smaller-scale architecture to be investigated for clay mineral type control. A powerful combination of high-resolution multi-beam, side-scan, seismic and core data would allow the comparison of the main mode of sediment transportation, *i.e.,* mass transport, debris flow deposits, and low- or high-density turbidity current deposits, between fans dominated by different clay mineral assemblages. In addition, general deposit shapes and thicknesses, facies stacking patterns, type and size of channel-levee systems, and lobe properties may all vary between fans dominated by clay mineral assemblages with different cohesive properties. More data would also allow additional controls on flow behaviour and deposit properties to be better constrained, such as mud-to-sand ratio. Constraining these controls is vital in distinguishing the influence of clay mineral type from other influences.

7.5 Conclusions

A metadata analysis was conducted to investigate if there are relationships between the clay mineral assemblage within modern, mud-rich submarine fans and their latitude, driven by the latitudinally regulated climatic control on the formation of clay minerals. The results show that fans dominated by illite, smectite, and kaolinite occur at progressively lower median latitudes for all the latitude classes considered. This matches the expected climate-driven trends in clay mineral production. When using relative percentages of kaolinite, smectite, illite and chlorite, only chlorite percentage exhibits a statistically significant increase with increasing latitude of fan, source, input and catchment. This suggests that dominant clay mineral type is a better parameter for characterising the relationship with latitude than full clay mineral assemblages and that the dominant clay mineral leads latitudinal control, regardless of the composition of the total clay mineral assemblage. The distance-based linear model shows that the latitude of input explains 20% of the variability in clay mineral assemblage between fans. This advocates that latitude is a first order control on the clay mineral assemblages found in modern submarine fans.

The metadata analysis also investigated if the geometry of modern submarine fans can be linked to the clay mineral assemblages within the fans, because of differences in rheological properties of the clay minerals. The median average-vertical-fan-growth-rate increased for fans dominated by kaolinite via illite to smectite, mirroring the increase in cohesive strength of the clay minerals. However, using relative percentages of the different clay minerals instead failed to obtain any relationships with average-vertical-fan-growth-rate. Again, this suggests that dominant clay mineral type is a better parameter for characterising the relationship with average-vertical-fan-growth-rate than full clay mineral assemblages.

The final part of the metadata analysis was aimed at finding relationships between average-vertical-fan-growth-rate and latitudinal control. This was to investigate if knowledge of the clay mineral assemblage within fans could be bypassed by using latitude as a proxy for dominant clay mineral type in the fans. The outcomes of this work showed that no statistically significant linear relationship was found for average-vertical-fan-growth-rate and latitudinal control. However, this is to be expected considering the complex relationships between the latitudinal control on clay mineral production and the rheological properties of the different clay minerals.

The results of this metadata analysis inspire confidence that there are relationships between latitude, clay mineral assemblage and the geometry of modern, mud-rich submarine fans, and these relationships should be further explored. There is ample scope for investigating these relationships in more detail, considering the rapid development of new technologies on affordable mapping of modern deep-marine systems, the collection of sediment samples from such systems, and the monitoring of modern SGFs.

8. Overall Summary and Synthesis

In this chapter, the main purpose of the thesis is reviewed briefly for context. The key findings, discussion points, and conclusions of each results chapter are then summarised under separate headings. For rigorous, specific discussions of results the reader is directed to the individual results chapters. The main themes of the chapters are then brought together, and the broad implications of the thesis are considered. Finally, specific applications of the results from this thesis for the hydrocarbon industry are presented.

8.1 Main purpose of the thesis

The purpose of this thesis, in general terms, was to investigate the transport and deposition of clay in deep-marine environments via cohesive sediment gravity flows (SGFs). Owing to the interplay between turbulent and cohesive forces**,** the flow dynamics of cohesive SGFs and their corresponding deposits are more complex than for non-cohesive SGFs. Literature on the effect of clay on the flow dynamics and deposit properties of cohesive SGF has grown in recent years (Marr *et al.*, 2001; Baas & Best, 2002; Amy *et al.*, 2006; Baas *et al.*, 2009; Sumner *et al.*, 2009; Kane & Pontén, 2012; Kane *et al.*, 2017; Hermidas *et al.*, 2018; Pierce *et al.*, 2019), partly encouraged by hydrocarbon exploration in mud-rich and mixed sand-mud deep-marine systems (*e.g.,* the Wilcox Formation; Kane & Pontén, 2012). These papers considered the clay mineral type as constant, although it is well known that different clay minerals have different chemical and physical properties, which control their cohesive strength (Lagaly, 1989). This thesis investigated the effect of clay mineral type and mixtures of clay minerals on the suspension rheology, flow behaviour, and deposit properties of cohesive SGFs in Chapters 3 and 4. In addition to their varying cohesive strength, clay minerals in the recent deep-sea sediments of the World Ocean have been observed to have a latitudinal distribution, driven by the climate on the adjacent continents (Biscaye, 1965; Griffin *et al.*, 1968; Rateev *et al.*, 1969; Chamley, 1989; Fagel, 2007). Climate controls the intensity of weathering, which in turn influences the clay minerals produced from the erosion of landmasses. Chapter 7 presents a metadata analysis to determine if there are relationships between the latitude, the clay mineral assemblages, and the geometry of modern submarine fans.

Adding clay to non-cohesive SGFs has been observed to produce complex transitional flow deposits and hybrid event beds (Haughton *et al.*, 2003, 2009; Talling *et al.*, 2004; Kane & Pontén, 2012; Kane *et al.*, 2017). However, little work has been done on how adding minor amounts of sand may influence the flow behaviour and deposit properties of cohesive SGFs. Chapter 5 considers how increasing the volume concentration of a pure-clay, high-density cohesive SGF by adding small amounts of fine sand changes the flow rheology, flow behaviour and deposits via laboratory experiments. The transient-turbulent behaviour of mixed sand-clay SGFs determines the interaction of the flow with the sediment bed and any sedimentary structures produced. Sedimentary structures are a vital tool for sedimentologists to reconstruct the depositional processes in ancient sedimentary environments. Chapter 6 presents the results of geological fieldwork conducted to investigate the impact of clay on the sedimentary structures formed by decelerating SGFs composed of sand, silt and clay in the fringe of the fan that makes up the Aberystwyth Grits Group and the Borth Mudstone Formation (Wales, U.K.).

8.2 The effect of clay mineral type on the properties of cohesive sediment gravity flows and their deposits

A series of lock-exchange experiments were conducted to contrast SGFs laden with non-cohesive silica flour, weakly cohesive kaolinite, and strongly cohesive bentonite in terms of flow behaviour, head velocity, runout distance, and deposit geometry across a wide range of suspended-sediment concentrations.

The three sediment types shared similar trends in the types of flows they developed, the maximum head velocity of these flows, and the deposit shape. As suspended-sediment concentration was increased, the flow type changed from low-density turbidity current via high-density turbidity current and mud flow to slide. As a function of increasing flow density, the maximum head velocity of low-density turbidity currents and relatively dilute high-density turbidity currents increased, whereas the maximum head velocity of the mud flows, slides, and relatively dense high-density turbidity currents decreased. The increase in maximum head velocity was driven by turbulent support of the suspended sediment and the density difference between the flow and the ambient fluid. The decrease in maximum head velocity comprised attenuation of turbulence by frictional interaction between grains in the silica-flour flows and by pervasive cohesive forces in the kaolinite and bentonite flows. The silica-flour flows changed from turbulence-driven to friction-driven at a volumetric concentration of 47% and a maximum head velocity of 0.75 m s^{-1}; the thresholds between turbulence-driven to cohesion-driven flow for kaolinite and bentonite were 22% and 0.50 m s^{-1}, and 16% and 0.37 m s^{-1}, respectively. The high-density turbidity currents produced deposits that were wedge-shaped with a block-shaped downflow extension, the mud flows produced wedge-shaped deposits with partly or fully detached outrunner blocks, and the slides produced wedge-shaped deposits without extension.

For the mud flows, slides, and most high-density turbidity currents, an increasingly higher concentration was needed to produce similar maximum head velocities and runout distances for flows carrying bentonite, kaolinite, and silica flour, respectively. The strongly cohesive bentonite flows were able to create a stronger network of particle bonds than the weakly cohesive kaolinite flows of similar concentration. The silica-flour flows remained mobile up to an extremely high concentration of 52%, and frictional forces were able to counteract the excess density of the flows and attenuate the turbulence in these flows only at concentrations above 47%.

Dimensional analysis of the experimental data shows that the yield stress of the pre-failure suspension can be used to predict the runout distance and the dimensionless head velocity of the SGFs, independent of clay type. Extrapolation to the natural environment suggests that high-density SGFs laden with weakly cohesive clay reach a greater distance from their origin than flows that carry strongly cohesive clay at a similar suspended-sediment concentration, whilst equivalent fine-grained, non-cohesive SGFs travel the farthest. The contrasting behaviour of fine-grained SGFs laden with different clay minerals may extend to differences in the architecture of large-scale sediment bodies in deep-marine systems.

8.3 Using rheological properties to understand mixed-clay sediment gravity flows and their deposits

The majority of experimental work on cohesive SGFs has focussed on flows carrying a single clay type. However, this is not realistic for natural SGFs, which typically contain a mixture of clay minerals. To improve our understanding of these natural flows, lock-exchange experiments were conducted, investigating the suspension rheology, flow behaviour, head velocity, runout distance and deposit geometry of SGFs carrying mixtures of strongly cohesive bentonite clay and weakly cohesive kaolinite clay at a fixed 20% volumetric concentration.

As the proportion of bentonite within the flow was increased to 20% of the total clay concentration, the maximum head velocity of the flows also increased. Thereafter, further increasing the amount of bentonite within the flow dramatically reduced the maximum head velocity. For the mixtures containing 0% to 20% bentonite, the flows reflected off the end of the 5-m long tank; from 35% bentonite the runout distance decreased as the proportion of bentonite increased. The flow behaviour also changed from weak high-density turbidity current, via strong high-density turbidity current and cohesive mud flow, to slide as the bentonite proportion was increased from 0% to 100%. The clay mixture rheology data show an increase in the yield stress, complex shear modulus, and apparent viscosity of the starting suspensions as the proportion of strongly cohesive bentonite increased above 20%. This is interpreted to result from bentonite increasing the number and the strength of inter-particle bonds within the clay gels, promoting the reduction in flow mobility for bentonite proportions above 20%. Unexpectedly, at the bentonite proportion of 10%, the yield stress, complex shear modulus, and apparent viscosity of the suspension reduced slightly, and the flow had a higher maximum head velocity, than the pure kaolinite flow. These results suggest that small amounts of bentonite clay reduce the strength or number of the inter-particle bonds, or otherwise changes the microstructure arrangement of the clay minerals so that the cohesive strength of the suspension is reduced.

The changes in the maximum head velocity and runout distance of the mixed-clay flows match the changes in the rheology of the mixed-clay suspensions, suggesting that rheological parameters can be utilised to predict the flow behaviour and deposit properties of natural cohesive SGFs. The equations presented in Chapter 3 were used to predict the yield stress of the mixed-clay flows by calculating the yield stress of an equivalent pure-clay suspension. This method produced good predictions of the yield stress, maximum head velocity and runout distance of the mixed-clay flows, suggesting that a model with non-linear interaction between clay minerals based on yield stress of the clay mineral components can be used to predict the behaviour of mixed-clay SGFs. A comprehensive understanding of how clay mineral assemblages can control the suspension rheology of cohesive SGFs is vital for the correct interpretation of the deposits of these flows in the modern environment and in the geological record.

8.4 Flow mobility of mixed sand-clay sediment gravity flows

SGFs in the natural environment commonly consist of a mixture of sand, silt and clay. It is challenging to predict how the dynamic balance between turbulent and cohesive forces changes when a small amount of sand is added to high-density SGFs controlled by cohesive forces. Chapter 5 presented laboratory experiments contrasting how increasing the volume concentration of a 14.4% and 16% bentonite-laden cohesive SGF by adding 25% of either fine sand or bentonite clay changed the flow behaviour and deposit geometry. Dam break experiments, following Balmforth *et al.* (2007) and Matson and Hogg (2007), were conducted to compare the yield stresses of the pure clay suspensions with the yield stresses of the sand-clay suspensions.

The dam break experiments found that increasing the volume concentration by adding 25% sand increased the yield stress of the 14.4% and 16% bentonite suspensions by a factor of 2.8 and 2.6, respectively. Of the theoretical mechanisms by which sand could increases the yield stress of the suspension, hydrodynamic interactions are hypothesised to be the most important mechanism. In particular, the excluded volume effect, which describes how adding sand reduces the volume of seawater and increases the effective clay concentration, is expected to be an important control.

The increase in the yield stress of the pure-clay suspensions from the addition of sand was matched by a reduction in the runout distance and head velocity profiles of the bentonite-sand flows compared to the original pure-bentonite flows. For the 16% bentonite flow, increasing the volume concentration by adding 25% sand changed the flow behaviour from a high-density turbidity current to a debris flow. These results highlight that the yield stress of natural cohesive SGFs containing sand and silt cannot be considered only in terms of the clay concentration and that the changes in the yield stress from the addition of sand can considerably alter the flow behaviour and deposit properties. It is hypothesised that sand can only increase the yield stress of the suspension and reduce the flow mobility if it can be held in the plug region of a flow by matrix strength. If the sand cannot be held in the cohesive plug it is likely to promote turbulence mixing within the flow and thus increase the flow mobility. The change in flow behaviour and rheology from the addition of sand has important implications for flow transformation, especially in the distal region of mud-rich submarine fans where the SGFs are decelerating and cohesive forces are likely to control the flow behaviour.

8.5 Formation of mixed sand-mud bedforms by transient turbulent flows in the fringe of submarine fans

The distal region and fringe of fine-grained deep marine systems often exhibit complex sedimentary facies and facies associations, as the presence of clay promotes the development of transient turbulent flows with complex depositional properties. Relatively little is known about the variation of current-induced sedimentary structures found within these facies. Chapter 6 provides the first comprehensive description and interpretation of mixed sandstone-mudstone bedforms observed in the distal region and fringe of the mud-rich submarine fan that makes up the Aberystwyth Grits Group and Borth Mudstone Formation (Wales, U.K.). Using detailed textural and structural descriptions, 158 bedforms in SGF deposits were characterised into three main types: “classic” sandy current ripples (59), large current ripples (41), and low-amplitude bed-waves (58). The sandy current ripples comprise clean sandstone, with average heights and lengths of 11 mm and 141 mm, respectively. The large current ripples are composed of mixed sandstone-mudstone and possess greater dimensions than the sandy current ripples, with an average height of 19 mm and an average length of 274 mm. The low-amplitude bed-waves have an average height and length of 10 mm and 354 mm, respectively, thus producing long thin bedforms composed commonly of mixed sandstone-mudstone and occasionally mud-poor sandstone.

Previous laboratory experiments on bedforms produced under rapidly decelerated, mixed sand-mud flows have shown a strong link between flow type and bedform type. In these experiments, sandy current ripples have been associated with turbulent flows, large current ripples with moderately cohesive, transient turbulent flows with enhanced near-bed turbulence, and low-amplitude bed-waves with strongly cohesive, transient turbulent flows with attenuated near-bed turbulence. The sandy current ripples, large current ripples, and low-amplitude bed-waves observed in the Aberystwyth Grits Group and Borth Mudstone Formation are interpreted to have formed under similar flow conditions as these laboratory counterparts, because of their strong similarity in shape, size, texture, and style of cross-lamination.

From the fan fringe to the distal fringe, the dominant bedform type changed from sandy current ripples, via large current ripples, to low-amplitude bed-waves, suggesting that the flows changed from turbulent to increasingly turbulence-modulated. It is proposed that the flow Reynolds number reduced, reflecting this flow transformation, from a combination of constant or decreasing flow height, flow deceleration from sediment deposition, and increasing flow viscosity following the shear-thinning nature of the clay-rich suspensions. Large current ripples and low-amplitude bed-waves were found in the H1 division of hybrid event beds, suggesting that the H1 division in mud-rich hybrid event beds can be produced by turbulence-modulated SGFs. Large current ripples and low-amplitude bed-waves are likely to be common in the fringe of other submarine fans. The presence and spatial trends in mixed sand-mud bedform types may be an important tool in interpreting fan fringe environments.

8.6 Metadata analysis of the relationships between latitude, clay mineral assemblage, and geometry of modern submarine fans

Clay minerals differ in both their rheological properties and in their latitudinal occurrence in the recent deep-sea sediments of the World Oceans. The latitudinal variation in clay mineral assemblage is driven by the intensity of weathering on adjacent continents which controls the clay mineral types produced. High-latitude chlorite and low-latitude kaolinite are the most latitudinally-driven clay minerals, produced under intense physical and chemical weathering, respectively. Illite, formed by physical weathering, is found at moderate to high latitudes, whereas smectite is expected to be produced in a broad latitudinal range in tropical, semi-arid, and temperate climates (Biscaye, 1965; Griffin *et al.*, 1968; Rateev *et al.*, 1969; Chamley, 1989; Fagel, 2007). A metadata analysis was conducted to determine if there are relationships between the latitude, the clay mineral assemblages, and the geometry of modern submarine fans. Four latitudinal controls were considered: latitude of source, latitude of catchment, latitude of input and latitude of fan.

The results demonstrate that the median fan latitude increased from kaolinite-dominated fans, via smectite-dominated fans, to illite-dominated fans. This matches the expected latitudinal trend of clay minerals described above. When the whole clay mineral assemblage of the fans is considered, the chlorite percentage and kaolinite:chlorite ratio within the fans show a statistically significant increase and decrease with increasing latitude, respectively. A distance-based linear model shows that the latitude of fan input explains 20% of the variability in clay mineral assemblage between the fans. However, non-latitudinal controls can disrupt the climatic signal of clay mineral assemblages. These controls need to be considered when assessing the relationship between clay mineral assemblage in a fan and its latitude. However, these initial results based on a limited number of fans suggest that latitude is a first order control on the dominant clay mineral in clay mineral assemblages found in modern submarine fans.

To test if the fan geometry of modern submarine fans can be linked to the clay mineral assemblages and clay-mineral rheology, the average-vertical-fan-growth-rate was tested against the dominant clay mineral in the fans. The median average-vertical-fan-growth-rate increased for fans dominated by kaolinite, via illite, to smectite, reflecting the cohesive strength of the clay minerals. However, no trend was observed for average-vertical-fan-growth-rate against the individual clay minerals in the assemblages. Finally, no statistically significant linear relationship was observed for the final test between the average-vertical-fan-growth-rate against the latitudinal controls. This was expected given the latitudinal control on clay mineral assemblages combined with their rheological properties. The results of this metadata analysis suggests that are relationships between latitude, clay mineral assemblage and the geometry of modern, mud-rich submarine fans, and these relationships should be further explored.

8.7 Broader implications

8.7.1 Implications for deep-marine systems

Clay mineral assemblages are expected to have an important influence on natural, cohesive SGFs that contain suspended clay at concentrations above the equivalent laboratory threshold of 10%. Below this threshold, the turbulent forces are predicted to dominate the flow behaviour. The cohesive properties of the clay mineral assemblages are expected to influence individual SGFs and their deposits, as well as the size and shape of architectural elements and the large-scale architecture of submarine fan systems. The results from Chapters 3 and 4 suggest that high-density SGFs containing a weakly cohesive clay mineral assemblage have a longer runout distance than flows that carry a strongly cohesive clay mineral assemblage, at a similar suspended-sediment concentration. Despite the limited number of fans available from literature, the results of the metadata analysis in Chapter 7 shows evidence that this relationship between runout distance and cohesive properties may extend to the overall architecture of deep-marine systems, as submarine fans dominated by weakly cohesive clay minerals have thinner deposits than submarine fans dominated by strongly cohesive clay minerals (Figs 7.17 and 7.18).

When studying modern submarine systems, the results presented in this thesis suggest that the effect of clay mineral assemblage should always be considered, *e.g.*, by means of X-ray powder diffraction (XRD) analysis, which is a relatively quick and inexpensive method for the identification of clay mineral assemblages. However, in the geological record, the original clay mineral assemblage of deep-marine systems is likely to have been overprinted by diagenetic reactions, which are generally considered to alter clay minerals at temperatures above 80°C (Chamley, 1989; Fagel, 2007). This renders the reconstruction of the original clay mineral assemblage, and hence the potential rheological properties of the flows, challenging. If the paleogeography of an ancient deep-marine system is well constrained and complicating additional controls on clay mineral assemblage can be accounted for or disregarded, inferences could be made of the dominant clay type from the latitude and the shape of the fan. The metadata analysis suggests that latitude of fan input may be the best latitudinal control to use for this purpose. In addition, as our understanding of clay mineral diagenetic reactions improves, the original clay mineral assemblage may be able to be determined from the diagenetically altered clay mineral assemblage. Currently, however, confidently reconstructing the original clay mineral assemblage from the deposits of ancient cohesive SGFs is unfeasible. This makes interpreting the rheological properties of clay mineral assemblage as a control on cohesive SGFs in the rock record a challenging exercise. This is further exacerbated by the fact that outcrops can only reveal parts of a deep-marine system, and core data provides an even smaller viewpoint of the system. However, to discount the effect of clay mineral assemblage may result in poor sedimentological process interpretation. Below, ideas on how the effect of clay mineral assemblage may be observed in ancient deep-marine systems are suggested.

The effect of clay mineral assemblage on ancient cohesive SGFs may be observed in the deposit shapes and the dominant deposit types. In deep-marine systems dominated by a weakly cohesive clay mineral assemblage, the mud-rich deposits may be relatively thin and spatially extensive, and low-density and high-density turbidity current deposits are more likely than mud flow and slide deposits. In contrast, the mud-rich beds may be thick and spatially confined in deep-marine systems in which SGFs carried a strongly cohesive clay mineral assemblage. Mud flow and slide deposits may be more common than low- and high-density turbidity current deposits in such systems. Mud flows and slides may have lower mud concentrations in systems dominated by strongly cohesive clay minerals than in systems dominated by weakly cohesive clay minerals.

The effect of clay mineral assemblage may also be observed in the rate of flow transformation of decelerating mud-rich SGFs in the distal part of deep marine systems. Flow transformation was observed from the fringe to distal fringe of the submarine fan that makes up the Aberystwyth Grits Group and Borth Mudstone Formation (Chapter 7). The deposits recorded the flow transformation via a thinning and reduction in the frequency of massive sandstone and structured sandstone facies, an increase in the number of muddy sandstone and heterolithic sandstone-mudstone facies, and a thickening of the mudstone facies. It is expected that systems with mud-rich SGFs containing strongly cohesive clay mineral assemblages will undergo flow transformation in their distal region more rapidly than systems with SGFs containing weakly cohesive clay mineral assemblages. This is supported by Chapter 3, in which it was demonstrated that the change in flow behaviour from turbulent to laminar occurs at a lower volume concentration and over a smaller concentration range for bentonite flows than for kaolinite flows. The field work in the Aberystwyth Grits Group and Borth Mudstone Formation also showed that the cohesive forces in mud-rich SGFs can be responsible for the generation of novel mixed sand-mud bedforms, *i.e.,* large current ripples and low-amplitude bed-waves. It is hypothesised that the formation of these mixed sand-mud bedforms is influenced by the clay mineral assemblage within the flow. In systems dominated by strongly cohesive clay minerals, the cohesive forces may be able to produce transitional flows more proximally in the system, and thus form deposits with large current ripples and low-amplitude bed-waves closer to the source compared to systems dominated by weakly cohesive clay minerals.

8.7.2 Implications for rheology to help understand sediment gravity flows

This thesis provides evidence that changes in the rheology of pure-clay suspensions, mixed-clay suspensions and clay-rich, clay-sand suspensions correlate with changes in the flow behaviour of these suspensions, including the maximum head velocity and runout distance of the flows. The predictive equations in Chapter 3 can calculate the runout distance and dimensionless head velocity of the laboratory SGFs based on the yield stress of the pre-failure suspension. This provides a proof of concept that the rheological properties of a suspension may be used to predict the flow behaviour of natural cohesive SGFs with the same composition as the suspension. Hermidas *et al.* (2018) has also suggested that a dimensionless yield stress parameter would be suitable to scale from laboratory flows to natural flows.

The successful use of rheological parameters to understand and interpret cohesive SGF behaviour in the laboratory advocates that future work on natural, modern cohesive SGFs should focus on the rheological characteristics of the flow, rather than or in addition to clay mineral assemblage and clay mineral concentration. The reasons for this are threefold: (1) clay minerals are natural products and variation may exist in the cohesive properties of individual clay mineral types; (2) mixtures of clay minerals may produce non-linear trends in the cohesive properties of the suspensions; and (3) rheological variables can also include the cohesive “effect” of non-cohesive material.

8.7.3 Implications for geohazard assessment

Seafloor networks of cables, pipelines and other seafloor infrastructure are vital for modern living, providing global communication links and energy supplies (Clare *et al.*, 2017). The growth of this infrastructure has resulted in seafloor cables crossing deep-water settings, making them vulnerable to hazards such as SGFs (Piper *et al.*, 1999; Anthony *et al.*, 2008; Hsu *et al.*, 2008; Zakeri, 2008). The laboratory results presented in this thesis may be useful in geohazard assessment of SGFs on deep-marine infrastructure. In an area prone to high-density, clay-rich SGFs, the clay mineral assemblage within the flows could have a direct effect on how hazardous a SGF may be to infrastructure. High-density cohesive SGFs composed of strongly cohesive clay minerals will travel a shorter distance and at a slower velocity than SGFs dominated by weakly cohesive clay minerals at a similar concentration. This suggests that high-density cohesive SGFs composed of strongly cohesive clay minerals may be less of a geohazard compared to flows containing weakly cohesive clay minerals. An area may also be less prone to triggering SGFs, if the substrate contains strongly cohesive clay minerals. Considering the latitudinal zonation of clay minerals in the recent deep-sea sediments of the World Oceans, this may mean there is a latitudinal trend in how hazardous SGFS may be to infrastructure. If the predictive equations in Chapter 3 can be scaled up, geohazard risk assessments will be able to calculate the “worst case scenario” SGF flow velocity and runout distance and plan cable placement and design accordingly.

8.8 Implications for the hydrocarbon industry

As hydrocarbon exploration looks to target deep-marine systems that are progressively finer-grained, cohesive SGF deposits are likely to form an increasing proportion of the reservoir volume in these future prospects. A good example is the successful Palaeogene Wilcox Formation in the Gulf of Mexico, which is characterised by stratigraphically and spatially isolated high-quality reservoir sandstones within mud-rich sandstones of marginal reservoir quality (Zarra, 2007; Kane *et al.*, 2017). Successful reservoir prediction of mixed sand-mud systems, such as the Wilcox Formation, at exploration and development scales is a challenge for the hydrocarbon industry because of their stratigraphic and spatial complexity (Porten *et al.*, 2016; Kane *et al.*, 2017). Insights on cohesive SGFs gained from this thesis have implications that apply to the hydrocarbon industry, as discussed below:

- **Clay mineral type does not affect the properties of fine-grained low-density turbidity current deposits.** The laboratory experiments in Chapter 3 showed that the electrostatic forces of attraction of clay minerals in fully turbulent, low-density turbidity currents are unable to hinder flow mobility. These deposits can thus be interpreted in terms of turbulence properties and density difference with the ambient water, and the clay mineral type can be ignored, even if these flows carried strongly cohesive clay minerals, such as bentonite (Fig. 8.1). In sandy turbidites, the clay mineral type is not expected to affect the fine-grained caps, *i.e.,* the $T_{d,e}$ facies, of the Bouma sequence (Bouma, 1962).

- **Clay mineral type does affect the deposits of fine-grained high-density SGFs.** Above suspended-sediment concentrations that are equivalent to the laboratory threshold of 10%, the clay concentration in SGFs is high enough for the clay minerals to collide, flocculate, gel, and enable the cohesive forces to outbalance the turbulent forces. This flow behaviour can be recognised within deep-marine successions as high-density turbidity current, mud flow and slide deposits, as well as in hybrid event beds. Based on differences in clay type, high-density turbidity current, mud flow and slide deposits dominated by weakly cohesive clay are expected to cover larger surface areas and have smaller bed thicknesses than similar deposits dominated by strongly cohesive clay (Fig. 8.1).

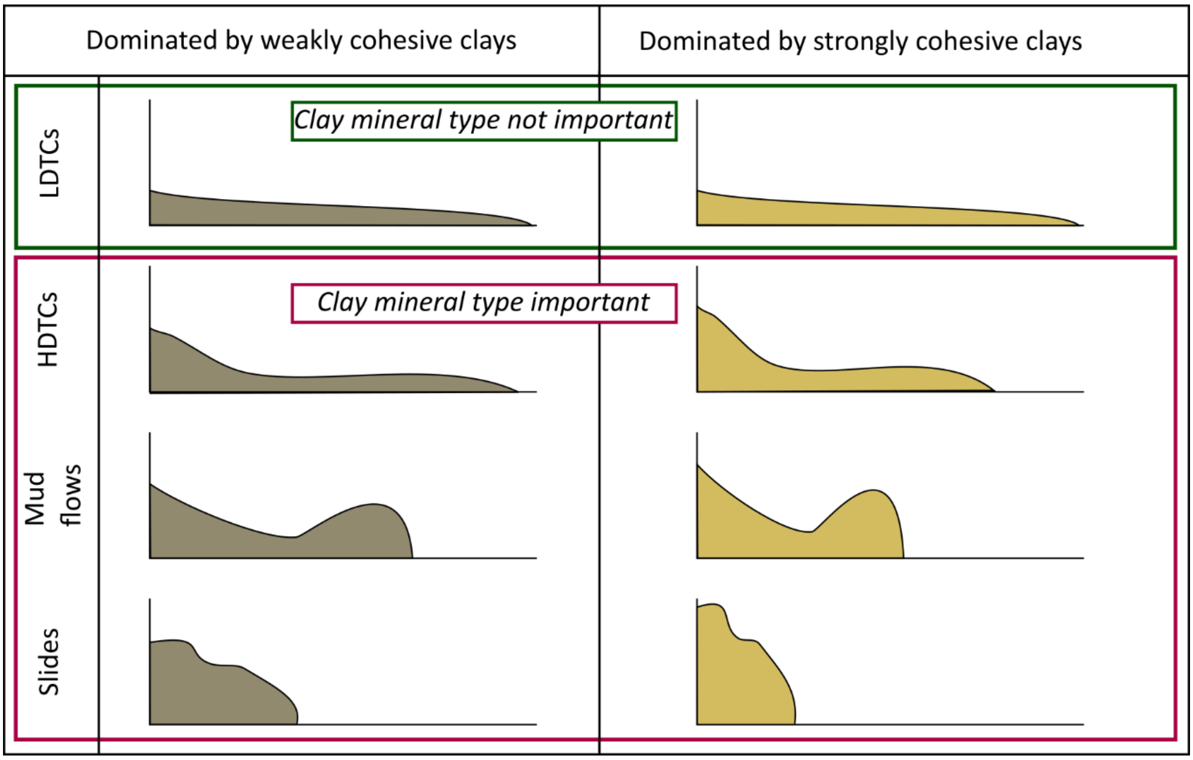

Figure 8.1: Schematic example of how clay mineral type may control the deposits of fine-grained sediment gravity flows.

- **Fine-grained architectural elements may be controlled by clay mineral type.** The effect of clay type is not expected to be important for fine-grained architectural elements dominated by low-density turbidity current deposits, such as levees. However, lobes, and in particular lobe fringes, have been found to contain complex deposits of turbulence-modulated cohesive flows, including hybrid event beds (Haughton *et al.*, 2009; Spychala *et al.*, 2017). These lobe fringe deposits may be effected by clay mineral type. Lobe fringes dominated by weakly cohesive clay minerals are expected to cover a larger areal extent and have thinner beds than lobe fringes dominated by strongly cohesive clay minerals. Spychala *et al.* (2017) demonstrated that lobe frontal fringes are dominated by hybrid events beds whereas lobe lateral fringes are dominated by thin beds, related to the downstream momentum of the high-density core of SGFs, in Fan 4 of the Skoorsteenberg Formation, Karoo Basin, South Africa. If this is valid for other systems, the effect of clay mineral type on the surface area of lobes may affect the length of the lobes more than their width. Hence, lobes dominated by weakly cohesive clay minerals may have higher length-to-width ratios than lobes dominated by strongly cohesive clay minerals.

- **Clay mineral type may affect flow-derived mud seals.** In mixed sand-mud deep-marine systems, the deposits of fine-grained high-density flows may act as baffles and barriers to oil and gas flow within a reservoir. The runout distance of these flows will govern the areal extent of the mud seals. Seals composed of the deposits of high-density SGFs dominated by strongly cohesive clay minerals are expected to have a smaller areal extent and greater bed thickness than seals produced by high-density flows dominated by weakly cohesive clay minerals. Thus, the thickness and surface area of flow-derived mud seals may be a function of clay mineral type, and govern the risk of oil and gas leakage and the compartmentalisation of the reservoir (Fig. 8.2).

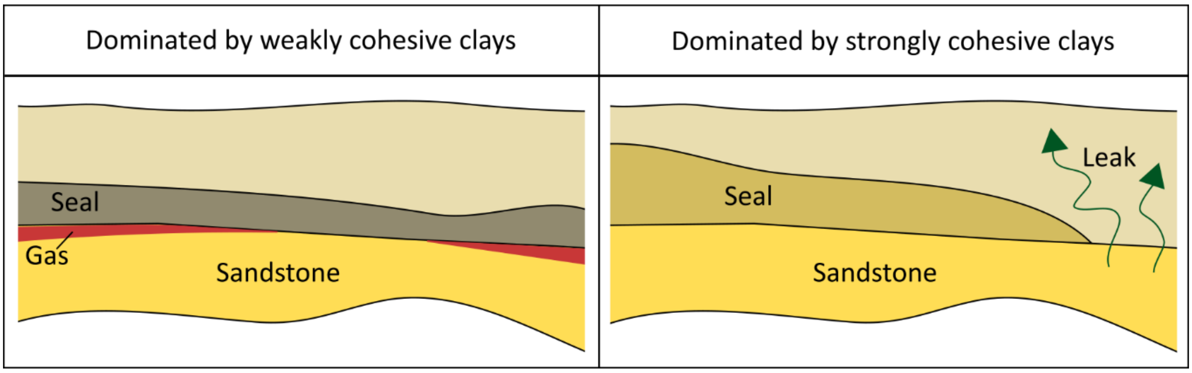

Figure 8.2: Schematic of how clay mineral type may affect flow-derived mud seals.

- **Sand can reduce the runout distance of high-density turbidity current, mud flow and slide deposits.** Adding small amounts of sand to natural cohesive SGFs with a cohesive plug can reduce the mobility of the flows, resulting in shorter runout distances and transformations to more cohesive flow behaviour (*e.g.,* high-density turbidity current to debris flow). Clay-dominated, mixed sand-mud deposits may therefore have smaller areal extents and be thicker than expected. Conversely, mixed sand-mud flows dominated by sand may have enhanced mobility, which promotes the formation of muddy sands in the form of turbidites that are relatively thin and spatially extensive.

- **Mixed sand-mud bedforms are an additional indicator of the fringe of deep-marine systems.** Low-amplitude bed-waves and large current ripples are likely to be common in the fringe of other submarine fans, where the flows are modulated by cohesive forces. They are therefore an additional tool to recognise the fringe of a lobe or a submarine fan. This is particularly useful for hydrocarbon exploration as these bedforms are small enough to be partly seen in core (Fig. 8.3).

- **Spatial trends in bedform type can disclose updip and downdip architectural changes of a deep-marine system.** For the case study presented in Chapter 6, the dominant bedform type changed from sandy current ripples, via large current ripples, to low-amplitude bed-waves from the fringe to the distal fringe of the fan, suggesting that the flows changed from turbulent to increasingly turbulence-modulated. If applicable to other systems, this trend can help geologists predict updip and downdip changes in sedimentary facies in the fringes of deep-marine fans.

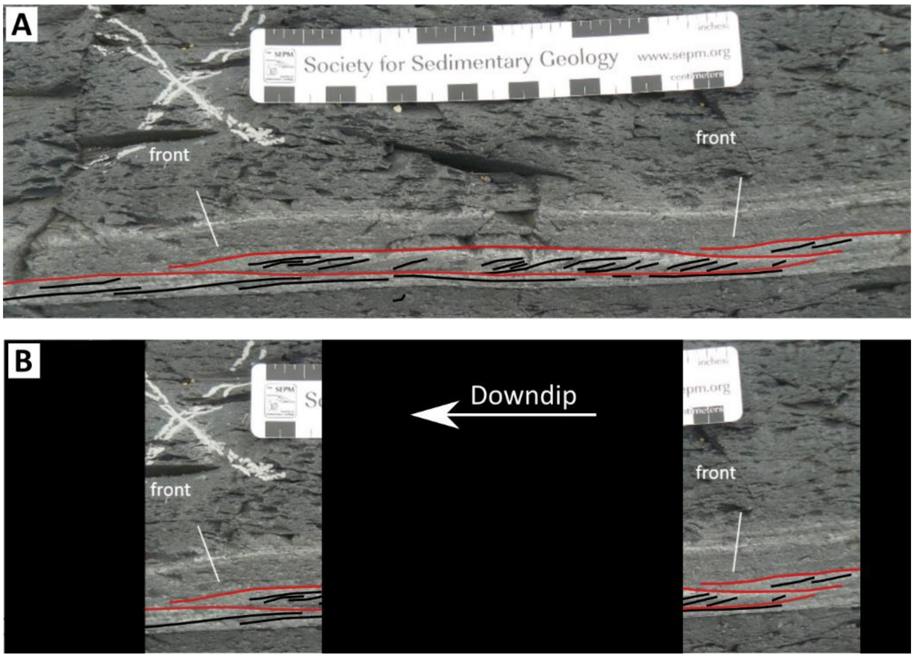

Figure 8.3: An example of how a low-amplitude bed-wave might look like in core and how it can help predict updip and downdip directions.

8.9 Future work

It is currently difficult to quantitatively compare the laboratory results in Chapters 3 to 5 with natural clay-rich SGFs and their deposits. For this, robust scaling relationships need to be developed and tested. Direct monitoring campaigns and accompanying technological advances offer an opportunity to do this. Future direct monitoring studies of mud-rich SGFs should aim to get concurrent measurements of flow velocity, concentration, and grain-size profiles, and collect suspended sediment samples, from which the yield stress and mineralogical composition of the sediment can be obtained. These data will allow valuable insights into how natural cohesive SGFs behave and enable relationships between laboratory and field flows to be developed.

As modern submarine fans continue to be explored by oceanographic campaigns, sediment samples from the fan should be analysed for clay mineral type as standard practice. Improved data sets of clay mineral type from submarine fans around the world would allow the relationships between clay mineral type and fan morphology in Chapter 7 to be further explored. It would also be fascinating to conduct a detailed study of clay mineralogy from the proximal to distal part of a mud-rich submarine fan to assess whether spatial changes in clay mineral assemblage occur due to selective sorting of clay minerals during SGF transport processes.

Rheological parameters are a quantitative way to understand the cohesive forces within cohesive SGFs, independently of clay mineral composition and clay concentration within the flow. Parameters that change with the flow velocity and shear rate, such as viscosity are the most useful. Suspended sediment samples combined with flow velocity measurements from direct monitoring campaigns could help guide a comprehensive set of rheological experiments to obtain the typical range of yield strength and viscosity values within natural SGFs. This dataset would have many applications to improve our understanding of mud-rich SGF behaviour, including allowing realistic flow Reynolds numbers to be determined to understand flow transformation in the distal part of mud-rich submarine fans. Accurate rheological values could also be used in computer models of cohesive SGFs and to inform future experiments on how to produce the most realistic flows possible by using appropriate clay concentrations and flow velocities.

References

Akaike, H. (1973) Information theory as an extension of the maximum likelihood principal. In: *Proceedings, Second International Symposium on Information Theory* (Eds B.N. Petrov and F. Caski), pp. 261–281, Akademiai Kiado, Budapest.

Ali, S. and **Bandyopadhyay, R.** (2016) Effect of electrolytes on the microstructure and yielding of aqueous dispersions of colloidal clay. *Soft Matter*, **12**, 414–421.

Allen, J.R.L. (1968) Current ripples: their relation to patterns of water and sediment motion. North-Holland Publishing Company, Amsterdam. 433 pp.

Allen, J.R.L. (1971) Instantaneous sediment deposition rates deduced from climbing-ripple cross-lamination. *J. Geol. Soc. London*, **127**, 553–561.

Allen, J.R.L. (1982) Sedimentary Structures, their Character and Physical Basis, Volumes 1, 2. Elsevier, Amsterdam, 593 pp., 663 pp.

Alonso, B. and **Maldonado, A.** (1990) Late Quaternary sedimentation patterns of the Ebro turbidite systems (northwestern Mediterranean): Two styles of deep-sea deposition. *Mar. Geol.*, **95**, 353–377.

Amy, L.A., **Talling, P.J.**, **Peakall, J.**, **Wynn, R.B.** and **Arzola Thynne, R.G.** (2005) Bed geometry used to test recognition criteria of turbidites and (sandy) debrites. *Sed. Geol.*, **179**, 163–174.

Amy, L.A., **Talling, P.J.**, **Edmonds, V.O.**, **Sumner, E.J.** and **Lesueur, A.** (2006) An experimental investigation of sand-mud suspension settling behaviour: Implications for bimodal mud contents of submarine flow deposits. *Sedimentology*, **53**, 1411–1434.

Ancey, C. and **Jorrot, H.** (2002) Yield stress for particle suspensions within a clay dispersion. *J. Rheol.*, **45**, 297–319.

Anderson, M., **Gorley, R.N.** and **Clarke, K.R.** (2008) PERMANOVA+ for PRIMER: Guide to Software and Statistical Methods. PRIMER-E, Plymouth, UK. 218 pp.

Anka, Z. and **Séranne, M.** (2004) Reconnaissance study of the ancient Zaire (Congo) deep-sea fan (ZaiAngo Project). *Mar. Geol.*, **209**, 223–244.

Antony, A., **Cittadini, L.**, **Karrenberg, R.**, **Kisteleki, R.**, **Refice, T.**, **Vest, T.**, and **Wilhelm R.** (2008) Mediterranean fiber cable cut (January-February 2008) analysis of network dynamics, Technical Report RT-DIA-124- 2008, University of Rome, Italy.

Arnott, R.W.C. and **Hand, B.M.** (1989) Bedforms, primary structures and grain fabric in the presence of suspended sediment rain. *J. Sed. Petrol.*, **59**, 1062–1069.

Ashley, G.M., **Southard, J.B.** and **Boothroyd, J.C.** (1982) Deposition of climbing-ripple beds: a flume simulation. *Sedimentology*, **29**, 67–79.

Atkinson, J. (2007) The Mechanics of Soils and Foundations. CRC Press, London. 442 pp.

Au, P.I. and **Leong, Y.K.** (2013) Rheological and zeta potential behaviour of kaolin and bentonite composite slurries. *Colloids and Surfaces A: Physicochemical and Engineering Aspects*, **436**, 530–541.

Baas, J.H. (1999) An empirical model for the development and equilibrium morphology of current ripples in fine sand. *Sedimentology*, **46**, 123–138.

Baas, J.H. (2003) Ripple, ripple mark, ripple structure. In: *Encyclopedia of Sediments and Sedimentary Rocks* (Ed. G. V. Middleton), pp. 565–568. Kluwer Academic Publishers, Dordrecht.

Baas, J.H. and **Best, J.** (2002) Turbulence modulation in clay-rich sediment-laden flows and some implications for sediment deposition. *J. Sed. Res.*, **72**, 336–340.

Baas, J.H., **van Kesteren, W.** and **Postma, G.** (2004) Deposits of depletive high-density turbidity currents: a flume analogue of bed geometry, structure and texture. *Sedimentology*, **51**, 1053–1088.

Baas, J.H., **McCaffrey, W.D.**, **Haughton, P.D.W.** and **Choux, C.** (2005) Coupling between suspended sediment distribution and turbulence structure in a laboratory turbidity current. *J. Geophys. Res. Oceans*, **110**, 1–20.

Baas, J.H., **Best, J.L.**, **Peakall, J.** and **Wang, M.** (2009) A phase diagram for turbulent, transitional, and laminar clay suspension flows. *J. Sed. Res.*, **79**, 162–183.

Baas, J.H., **Best, J.L.** and **Peakall, J.** (2011) Depositional processes, bedform development and hybrid bed formation in rapidly decelerated cohesive (mud-sand) sediment flows. *Sedimentology*, **58**, 1953–1987.

Baas, J.H., **Davies, A.G.** and **Malarkey, J.** (2013) Bedform development in mixed sand—mud: The contrasting role of cohesive forces in flow and bed. *Geomorphology*, **182**, 19–32.

Baas, J.H., **Best, J.L.** and **Peakall, J.** (2016) Predicting bedforms and primary current stratification in cohesive mixtures of mud and sand. *J. Geol. Soc.*, **173**, 12–45.

Baas, J.H., **Best, J.L.** and **Peakall, J.** (2016) Comparing the transitional behavior of kaolinite and bentonite suspension flows. *Earth Surf. Proc. Land.*, **41**, 1911–1921.

Baker, M.L., **Baas, J.H.**, **Malarkey, J.**, **Jacinto, R.S.**, **Craig, M.J.**, **Kane, I.A.** and **Barker, S.** (2017) The effect of clay type on the properties of cohesive sediment gravity flows and their deposits. *J. Sed. Res.*, **87(11)**, 1176–1195.

Balmforth, N.J., **Craster, R. V.**, **Perona, P.**, **Rust, A.C.** and **Sassi, R.** (2007) Viscoplastic dam breaks and the Bostwick consistometer. *J. Non-Newton fluid*, **142**, 63–78.

Barker, S.P., **Haughton, P.D.W.**, **McCaffrey, W.D.**, **Archer, S.G.** and **Hakes, B.** (2008) Development of rheological heterogeneity in clay-rich high-density turbidity currents: Aptian Britannia Sandstone Member, U.K. Continental Shelf. *J. Sed. Res.*, **78**, 45–68.

Barnes, N. and **Normark, W.R.** (1985) Diagnostic parameters for comparing modern submarine fans and ancient submarine systems. In: *Submarine Fans and Related Turbidite Systems* (Eds A. H. Bouma, W. R. Normark and P. M. Barnes), pp. 13–14. Springer-Verlag, New York.

Bayon, G., **Loncke, L.**, **Dupré, S.**, **Caprais, J.C.**, **Ducassou, E.**, **Duperron, S.**, **Etoubleau, J.**, **Foucher, J.P.**, **Fouquet, Y.**, **Gontharet, S.**, **Henderson, G.M.**, **Huguen, C.**, **Klaucke, I.**, **Mascle, J.**, **Migeon, S.**, **Olu-Le Roy, K.**, **Ondréas, H.**, **Pierre, C.**, **Sibuet, M.**, **Stadnitskaia, A.** and **Woodside, J.** (2009) Multi-disciplinary investigation of fluid seepage on an unstable margin: The case of the Central Nile deep sea fan. *Mar. Geol.*, **261**, 92–104.

Behl, R.J. (2011) Glacial demise and methane's rise. *PNAS*, **108**, 5925–5926.

Best, J.L. and **Bridge, J.S.** (1992) The morphology and dynamics of low amplitude bedwaves upon upper stage plane beds and the preservation of planar laminae. *Sedimentology*, **39**, 737–752.

Biscaye, P.E. (1965) Mineralogy and Sedimentation of Recent Deep-Sea Clay in the Atlantic Ocean and Adjacent Seas and Oceans. *Geol. Soc. Am. Bull.*, **76**, 803–832.

Blackbourn, G.A. and **Thomson, M.E**. (2000) Britannia Field, UK North Sea: Petrographic constraints on Lower Cretaceous provenance, facies, and the origin of slurry-flow deposits. *Petroleum Geoscience*, **6**, 329–343.

Bonnecaze, R.T., **Huppert, H.E.** and **Lister, J.R.** (1993) Particle-driven gravity currents. *J. Fluid Mech.*, **250**, 339–369.

Bonnel, C., **Dennielou, B.**, **Droz, L.**, **Mulder, T.** and **Berné, S.** (2005) Architecture and depositional pattern of the Rhône Neofan and recent gravity activity in the Gulf of Lions (western Mediterranean). *Mar. Petrol. Geol.*, **22**, 827–843.

Borg, I., **Groenen, P.J.** and **Mair, P.** (2012) Applied Multidimensional Scaling. Springer, New York. 112 pp.

Bouma, A.H. (1962) Sedimentology of some flysch deposits: a graphic approach to facies interpretation. Elsevier, Amsterdam. 168 pp.

Bouma, A.H., **Normark, W.R.** and **Barnes, N.E.** (1985) Submarine Fans and Related Turbidite Systems. Springer Verlag, New York, 351 pp.

Bridge, J.S. and **Best, J.L.** (1988) Flow, sediment transport and bedform dynamics over the transition from dunes to upper-stage plane beds: implications for the formation of planar laminae. *Sedimentology*, **35**, 753–763.

Brigatti, M., **Galan, E.** and **Theng, B.** (2006) Structures and mineralogy of clay minerals. In: *Handbook of Clay Science* (Eds Bergaya F., Theng B.K.G. and Lagaly G.), pp. 19–86. Elsevier, Amsterdam.

Britter, R.E. and **Simpson, J.E.** (1978) Experiments on the dynamics of a gravity current head. *J. Fluid Mech.*, **88**, 223–240.

Burnham, K.P. and **Anderson, D.R.** (2004) Multimodel inference – understanding AIC and BIC in model selection. *Sociological Methods and Research*, **33**, 261–304.

Cartigny, M.J.B., **Eggenhuisen, J.T.**, **Hansen, E.W.M**. and **Postma, G.** (2013) Concentration-dependent flow stratification in experimental high-density turbidity currents and their relevance to turbidite facies models. *J. Sed. Res.*, **83**, 1046–1064.

Chamley, H. (1989) Clay Sedimentology. Springer-Verlag, Berlin. 623 pp.

Cherns, L., Cocks, L.R.M., Davies, J.R., Hillier, R.D., Waters, R.A. and **Williams, M.** (2006) Silurian: the influence of extensional tectonics and sea-level changes on sedimentation in the Welsh Basin and on the Midland Platform. In: *The Geology of England and Wales* (Eds P.J. Brenchley and P.F. Rawson), pp. 75–102. The Geological Society, London.

Clare, M.A., **Vardy, M.E.**, **Cartigny, M.J.B.**, **Talling, P.J.**, **Himsworth, M.D.**, **Dix, J.K.**, **Harris, J.M.**, **Whitehouse, R.J.S.** and **Belal, M.** (2017) Direct monitoring of active geohazards: Emerging geophysical tools for deep-water assessments. *Near Surf. Geophys*, **15(4)**, 427–444.

Clarke, K.R., **Somerfield, P.J.** and **Gorley, R.N.** (2008) Testing of null hypotheses in exploratory community analyses: similarity profiles and biota-environment linkage. *J. Exp. Mar. Biol. Ecol.*, **366**, 56–69.

Cleary, W. J., **Pilkey, O. H.**, & **Nelson, J. C.** (1985) Wilmington Fan, Atlantic Ocean. In: *Submarine Fans and Related Turbidite Systems* (Eds A. H. Bouma, W. R. Normark and P. M. Barnes), pp. 157–164. Springer-Verlag, New York.

Clift, P.D., **Shimizu, N.**, **Layne, G.D.**, **Blusztajn, J.S.**, **Gaedicke, C.**, **Schlüter, H.U.**, **Clark, M.K.** and **Amjad, S.** (2001) Development of the Indus Fan and its significance for the erosional history of the Western Himalaya and Karakoram. *Geol. Soc. Am. Bull.*, **113**, 1039–1051.

Coussot, P. (1997) *Mudflow Rheology and Dynamics*. IAHR Monograph, Balkema, Rotterdam, 272 pp.

Coussot, P. and **Piau, J.M.** (1995) The effects of an addition of force-free particles on the rheological properties of fine suspensions. *Can. Geotech. J.*, **32**, 263–270.

Covault, J.A., **Shelef, E.**, **Traer, M.**, **Hubbard, S.M.**, **Romans, B.W.** and **Fildani, A.** (2012) Deep-water channel run-out length: insights from seafloor geomorphology. *J. Sed. Res.*, **82**, 21–36.

Cremer, M., **Orsolini, P.** and **Ravenne, C.** (1985) Cap-Ferret Fan, Atlantic Ocean. In: *Submarine Fans and Related Turbidite Systems* (Eds A. H. Bouma, W. R. Normark and P. M. Barnes), pp. 113–120. Springer-Verlag, New York.

Cremer, M., **Weber, O.** and **Jouanneau, J.M.** (1999) Sedimentology of box cores from the Cap-Ferret Canyon area (Bay of Biscay). *Deep-Sea Research Part II: Topical Studies in Oceanography*, **46**, 2221–2247.

Cruz, N., **Peng, Y.**, **Farrokhpay, S.** and **Bradshaw, D.** (2013) Interactions of clay minerals in copper-gold flotation: Part 1 - Rheological properties of clay mineral suspensions in the presence of flotation reagents. *Minerals Engineering*, **50–51**, 30–37.

Curray, J.R., **Emmel, F.J.** and **Moore, D.G.** (2002) The Bengal Fan: Morphology, geometry, stratigraphy, history and processes. *Mar. Petrol. Geol.*, **19**, 1191–1223.

Curtis, C.D. (1990) Aspects of climatic influence on the clay mineralogy and geochemistry of soils, palaeosols and clastic sedimentary rocks. *J. Geol. Soc.*, **147**, 351–357.

Davies, J.R., Fletcher, C.J.N., Waters, R.A., Woodhall, D.G. and **Zalasiewicz, J.A**. (1997) *Geology of the Country Around Llanilar and Rhayader.* Brit. Geol. Surv. Mem., Sheets 178 and 179 (England and Wales). Stationary Office, London.

Debrabant, P., **Lopez, M.** and **Chamley, H.** (1997) Clay mineral distribution and significance in Quaternary sediments of the Amazon Fan, *Proc. Ocean Drill. Program Sci. Results*, **155**, 177–192.

de Leeuw, J., **Eggenhuisen, J.T.** and **Cartigny, M.J.B.** (2016) Morphodynamics of submarine channel inception revealed by new experimental approach. *Nature Communications*, **7**, no. 10886.

Droz, L., **Marsset, T.**, **Ondre, H.**, **Lopez, M.** and **Savoye, B.** (2003) Architecture of an active mud-rich turbidite system: The Zaire Fan (Congo-Angola margin southeast Atlantic): Results from ZaiAngo 1 and 2 cruises. *AAPG Bull.*, **87**, 1145–1168.

Dyer, K.R. and **Manning, A.J.** (1999) Observation of the size, settling velocity and effective density of flocs, and their fractal dimensions. *J. Sea Res.*, **41**, 87–95.

Dytham, C. (2011) Choosing and using statistics: a biologist's guide. Wiley-Blackwell, Oxford. 298 pp.

Elverhøi, A., **Issler, D., De Blasio, F. V.**, **Ilstad, T.**, **Harbitz, C. B.** and **Gauer, P.** (2005) Emerging insights into the dynamics of submarine debris flows. *Natural Hazards and Earth System Science*, **5**, 633–648.

Fagel, N., **Debrabant, P.** and **André, L.** (1994) Clay supplies in the Central Indian Basin since the Late Miocene: climatic or tectonic control? *Mar. Geol.*, **122**, 151–172.

Fagel, N. (2007) Clay minerals, deep circulation and climate. *Develop. Mar. Geol.*, **1**, 139–184.

Figueiredo, J., **Hoorn, C.**, **van der Ven, P.** and **Soares, E.** (2009) Late Miocene onset of the Amazon River and the Amazon deep-sea fan: Evidence from the Foz do Amazonas Basin. *Geology*, **37**, 619–622.

Felix, M. and **Peakall, J.** (2006) Transformation of debris flows into turbidity currents: mechanisms inferred from laboratory experiments. *Sedimentology*, **53**, 107–123.

Flemming, B.W. (2002) Geographic distribution of muddy coasts. In: *Muddy Coasts of the World Processes, Deposits and Function* (Eds T. Healy, Y. Wang and Healy, J.A.), pp. 99–201. Elsevier, Amsterdam.

Fletcher, J.M., **Grove, M.**, **Kimbrough, D.**, **Lovera, O.** and **Gehrels, G.E.** (2007) Ridge-trench interactions and the Neogene tectonic evolution of the Magdalena shelf and southern Gulf of California: Insights from detrital zircon U-Pb ages from the Magdalena fan and adjacent areas. *Geol. Soc. Am. Bull.*, **119**, 1313–1336.

Fonnesu, M., **Haughton, P.**, **Felletti, F.** and **McCaffrey, W.** (2015) Short length-scale variability of hybrid event beds and its applied significance. *Mar. Petrol. Geol.*, **67**, 583–603.

Fonnesu, M., **Felletti, F.**, **Haughton, P.D.W.**, **Patacci, M.** and **Mccaffrey, W.D.** (2017) Hybrid event bed character and distribution linked to turbidite system sub-environments: The North Apennine Gottero Sandstone (north-west Italy). *Sedimentology*, **65(1)**, 151-190.

France-Lanord, C., **Spiess, V.**, **Klaus, A.**, **Schwenk, T.** and **the Expedition 354 Scientists** (2016) Bengal Fan. *Proceedings of the International Ocean Discovery Program, 354*.

Gingele, F.X., **Müller, P.M.** and **Schneider, R.R.** (1998) Orbital forcing of freshwater input in the Zaire Fan area - Clay mineral evidence from the last 200 kyr. *Palaeogeogr. Palaeoclimatol. Palaeoecol.*, **138**, 17–26.

Gingerich, P.D. (1969) Markov analysis of cyclic alluvial sediments. *J. Sed. Res.,* **39(1)**, 330–332.

Gladstone, C., **McClelland, H.L.O.**, **Woodcock, N.H.**, **Pritchard, D.** and **Hunt, J.E.** (2018) The formation of convolute lamination in mud-rich turbidites. *Sedimentology*, **65**, 1800–1825.

Gonthier, E., **Faugères, J.C.**, **Gervais, A.**, **Ercilla, G.**, **Alonso, B.** and **Baraza, J.** (2002) Quaternary sedimentation and origin of the Orinoco sediment-wave field on the Demerara continental rise (NE margin of South America). *Mar. Geol.*, **192**, 189–214.

Govil, P. and **Naidu, P.D.** (2008) Late Quaternary changes in depositional processes along the western margin of the Indus Fan. *Geo-Mar. Lett.*, 28, 1–6.

Grabowska-Olszewska, B. (2003) Modelling physical properties of mixtures of clays: Example of a two-component mixture of kaolinite and montmorillonite. *Appl. Clay Sci.*, **22**, 251–259.

Gradusov, B.P. (1974) A tentative study of clay mineral distribution in soils of the world. *Geoderma*, **12**, 49–55.

Griffin, J.J., **Windom, H.** and **Goldberg, E.D.**, (1968) The distribution of clay minerals in the world ocean. *Deep-Sea Res.*, **15**, 433–459.

Hallworth, M.A. and **Huppert, H.E.** (1998) Abrupt transitions in high-concentrations, particle-driven gravity currents. *Phys. Fluids*, **10**, 1083–1087.

Hallworth, M.A., **Hogg, A.J.** and **Huppert, H.E.** (1998) Effects of external flow on compositional and particle gravity currents. *J. Fluid Mech.*, 359, 109–142.

Hampton, M.A. (1972) The role of subaqueous debris flow in generating turbidity currents. *J. Sed. Petrol.*, **42**, 775–793.

Hampton, M.A., 1975, Competence of fine-grained debris flows: *J. Sed. Petrol.*, **45**, 833–844.

Haughton, P.D.W., **Barker, S.P.** and **McCaffrey, W.D.** (2003) 'Linked' debrites in sand-rich turbidite systems - origin and significance. *Sedimentology*, **50**, 459–482.

Haughton, P.D.W, **Davis, C.**, **McCaffrey, W.** and **Barker, S.P.** (2009) Hybrid sediment gravity flow deposits - Classification, origin and significance. *Mar. Petrol. Geol.*, **26**, 1900–1918.

Healy, T., **Wang, Y.** and **Healy, J.A.** (2002) Muddy Coasts of the World: Processes, Deposits and Function. Elsevier, Amsterdam. 556 pp.

Helm, C.E. (1962) Multidimensional Ratio Scaling Analysis of Perceived Color Relations. *J. Opt. Soc. Am.*, **54**, 256–262.

Heezen, B.C., **Menzies, R.J.**, **Schneider, E.D.**, **Ewing, W.M.** and **Granelli, N.C.L.**, (1964) Congo Submarine Canyon. *AAPG Bull.*, **48**, 1126–1149.

Hermidas, N., **Eggenhuisen, J.T.**, **Jacinto, R.S.**, **Luthi, S.M.**, **Toth, F.** and **Pohl, F.** (2018) A Classification of Clay-Rich Subaqueous Density Flow Structures. *J. Geophys. Res. Earth*, **123**, 945–966.

Hillel, D. (2004) Introduction to Environmental Soil Physics: Elsevier Academic Press, Amsterdam. 494 pp.

Hillier, S. (1995) Erosion, sedimentation and sedimentary origin of clays In: *Origin and Mineralogy of Clays* (Ed. B. Velde), pp. 162–219. Springer, Berlin.

Hodgson, D.M. (2009) Distribution and origin of hybrid beds in sand-rich submarine fans of the Tanqua depocentre, Karoo Basin, South Africa. *Mar. Petrol. Geol.*, **26**, 1940–1956.

Holtz, R.D. and **Kovacs, W.D.** (1981) An Introduction of Geotechnical Engineering. Prentice Hall, New York. 733 pp.

Hsu, S.K., **Kuo, J.**, **Lo, C.L.**, **Tsai, C.H.**, **Doo, W.B.**, **Ku, C.Y.** and **Sibuet, J.C.** (2008) Turbidity currents, submarine landslides and the 2006 Pingtung earthquake off SW Taiwan. *Terrestrial Atmos. Oceanic Sci.*, **19**, 767–772.

Huppert, H.E. and **Simpson, J.E.** (1980) The slumping of gravity currents: *J. Fluid Mech.*, **99**, 785–799.

Ilstad, T., **Elverhøi, A.**, **Issler, D.** and **Marr, J.G.** (2004) Subaqueous debris flow behaviour and its dependence on the sand/clay ratio: A laboratory study using particle tracking. *Mar. Geol.*, **213**, 415–438.

Iverson, R.M. (1997) Physics of Debris Flows. *Rev. Geo-phys.*, **35**, 245–296.

Jacobson, M.R. and **Testik, F.Y.** (2013) On the concentration structure of high-concentration constant-volume fluid mud gravity currents: *Phys. Fluids*, **25**, no. 016602.

Jobe, Z.R., **Lowe, D.R.** and **Morris, W.R.** (2012). Climbing-ripple successions in turbidite systems: Depositional environments, sedimentation rates and accumulation times. *Sedimentology*, **59**, 867–898.

Jopling, A. V and **Walker, R.G.** (1968) Morphology and origin of ripple-drift cross-lamination, with examples from the Pleistocene of Massachusetts. *J. Sed. Res.*, **38**, 971–984.

Kane, I. A. and **Pontén, A.S.M.** (2012) Submarine transitional flow deposits in the Paleogene Gulf of Mexico. *Geology*, **40**, 1119–1122.

Kane, I.A., **Pontén, A.S.M.**, **Vangdal, B.**, **Eggenhuisen, J.T.**, **Hodgson, D.M.** and **Spychala, Y.T.** (2017) The stratigraphic record and processes of turbidity current transformation across deep-marine lobes. *Sedimentology*, **64**, 1236–1273.

Kane, I.A., **McCaffrey, W.D.**, **Peakall, J.** and **Kneller, B.C.** (2010) Submarine channel levee shape and sediment waves from physical experiments. *Sed. Geol.*, **223**, 75–85.

Karunaratne, G.P., **Chew, S.H.**, **Lee, S.L.** and **Sinha, A.N.** (2014) Bentonite:Kaolinite Clay Liner. *Geosynth. Int.*, **8**, 113–133.

Kasperski, K.L., **Hepler, C.T.** and **Hepler, L.G.** (1986) Viscosities of dilute aqueous suspensions of montmorillonite and kaolinite clays. *Can. J. Chem.*, **64**, 1919–1924.

Kaufhold, S., **Dohrmann, R.**, **Koch, D.** and **Houben, G.** (2008) The pH of aqueous bentonite suspensions. *Clay Clay Mineral.*, **56**, 338–343.

Keevil, G.M., **Peakall, J.**, **Best, J.L.** and **Amos, K.J.** (2006) Flow structure in sinuous submarine channels: Velocity and turbulence structure of an experimental submarine channel. *Mar. Geol.*, **229**, 241–257.

Keller, W.D. and **Matlack, K.** (1990) The pH of clay suspensions in the field and laboratory, and methods of measurement of their pH, *Appl. Clay Sci.*, **5**, 123–133.

Kendall C. and **Haughton P.** (2006) Deepwater Source and Setting. *SEPM Sequence Stratigraphy Web*, http://www.sepmstrata.org/page.aspx?pageid=40, accessed 13 August 2019.

Keren, R. (1989) Rheology of mixed kaolinite montmorillonite suspensions. *J. Soil Sci. Soc. Am.*, **53**, 725–730.

Kessarkar, P.M., **Rao, V.P.**, **Ahmad, S.M.** and **Babu, G.A.** (2003) Clay minerals and Sr-Nd isotopes of the sediments along the western margin of India and their implication for sediment provenance. *Mar. Geol.*, **202**, 55–69.

Keulegan, G.H. (1957) Thirteenth progress report on model laws for density currents: An experimental study of the motion of saline water from locks into fresh water channels (vol. 5168). US Dept. of Commerce, National Bureau of Standards.

Keulegan, G.H. (1958) Twelfth progress report on model laws for density currents: The motion of saline fronts in still water (vol. 5831). US Dept. of Commerce, National Bureau of Standards.

Khabbazi Basmenj, A., **Mirjavan, A.**, **Ghafoori, M.** and **Cheshomi, A.** (2017) Assessment of the adhesion potential of kaolinite and montmorillonite using a pull-out test device. *Bulletin of Engineering Geology and the Environment*, 1–13.

Kneller, B. (1995) Beyond the turbidite paradigm: physical models for deposition of turbidites and their implications for reservoir prediction. In: *Characterisation of Deep Marine Clastic Systems* (Eds A.J. Hartley and D.J. Prosser), *Geol. Soc. London Spec. Publ.,* **94**, 29–46.

Kneller, B.C. and **Branney, M.J.** (1995) Sustained high-density turbidity currents and the deposition of thick massive sands. *Sedimentology*, **42**, 607–616.

Kneller, B. and **Buckee, C.** (2000) The structure and fluid mechanics of turbidity currents: a review of some recent studies and their geological implications. *Sedimentology*, **47**, 62–94.

Kneller, B., **Nasr-Azadani, M.M.**, **Radhakrishnan, S.** and **Meiburg, E.** (2016). Long-range sediment transport in the world's oceans by stably stratified turbidity currents. *J. Geophys. Res. Oceans*, **121**, 8608–8620.

Kolla, V., **Kostecki, J.A.**, **Henderson, L.** and **Hess, L.** (1980) Morphology and Quaternary sedimentation of the Mozambique Fan and environs, southwestern Indian Ocean. *Sedimentology*, **27**, 357–378.

Kooistra A., **Verhoef P.N.W.**, **Broere W.**, **Ngan-Tillard D.J.M.** and **Vantol A.F.** (1998) Appraisal of stickiness of natural clays from laboratory tests. In: *Proceedings of the 25th National Symposium of Engineering Geology.* pp. 101–113. Delft, Netherlands.

Kuenen, P.H. (1951) Properties of turbidity currents of high density. *SEPM Spec. Publ.*, **2**, 14–33.

Kuenen, P.H. and **Migliorini, C.I.** (1950) Turbidity Currents as a Cause of Graded Bedding. *J. Geol.*, **58**, 91–127.

Lagaly, G. (1989) Principles of flow of kaolin and bentonite dispersions. *Appl. Clay Sci.*, **4**, 105–123.

Lagaly, G. and **Ziesmer, S.** (2003) Colloid chemistry of clay minerals: The coagulation of montmorillonite dispersions. *Adv. Colloid Interf.*, **100–102**, 105–128.

Laxton, P.B. and **Berg, J.C.** (2006) Relating clay yield stress to colloidal parameters. *J. Colloid Interf. Sci.*, **296**, 749–755.

Lin, Y., **Cheah, L.K.J.**, **Phan-Thien, N.** and **Khoo, B.C.** (2016) Effect of temperature on rheological behavior of kaolinite and bentonite suspensions. *Colloids and Surfaces A: Physicochemical and Engineering Aspects*, **506**, 1–5.

Lovell, J.P.B. (1970) The palaeogeographical significance of lateral variations in the ratio of sandstone to shale and other features of the Aberystwyth Grits. *Geol. Mag.*, **107**, 147.

Lowe, D.R. (1979) Sediment gravity flows: their classification and some problems of application to natural flows and deposits. *SEPM Spec. Publ.*, **27**, 75–82

Lowe, D.R. (1982) Sediment gravity flows: II. Depositional models with special reference to high density turbidity currents. *J. Sed. Petrol.*, **52**, 279–297.

Lowe, D.R. (1988) Suspended-load fallout as an independent variable in the analysis of current structures. *Sedimentology*, **35**, 765–776.

Lowe, D.R. and **Guy, M.** (2000) Slurry-flow deposits in the Britannia Formation (Lower Cretaceous), North Sea: A new perspective on the turbidity current and debris flow problem. *Sedimentology*, **47**, 31–70.

Luckham, P. and **Rossi, S.** (1999) The colloidal and rheological properties of bentonite suspensions. *Advances in Colloid and Interface Science*, **82**, 43–92.

Luchi, R., **Balachandar, S.**, **Seminara, G.** and **Parker, G.** (2018). Turbidity Currents With Equilibrium Basal Driving Layers: A Mechanism for Long Runout. *Geophysical Research Letters*, **45**, 1518–1526.

Lüthi, S. (1981) Experiments on non-channelized turbidity currents and their deposits. *Mar. Geol.*, **40**, 59–68.

Maldonado, A., Got, H., **Monaco, A.**, **O'Connell, S.** and **Mirabile, L.** (1985) Valencia Fan (northwestern Mediterranean): Distal deposition fan variant. *Mar. Geol.*, **62**, 295–319.

Maldonado, A. and **Stanley, D.J.** (1981) Clay mineral distribution patterns as influenced by depositional processes in the Southeastern Levantine Sea. *Sedimentology*, **28**, 21–32.

Marr, J.G., **Harff, P.A.**, **Shanmugam, G.** and **Parker, G.** (2001) Experiments on subaqueous sandy gravity flows: The role of clay and water content in flow dynamics and depositional structures. *Geol. Soc. Am. Bull.*, **113**, 1377–1386.

Martinsen, O. (1994) Mass Movements. In: *The Geological Deformation of Sediments* (Ed. A. Maltman), pp. 127–165. Chapman and Hall, London.

Matson, G.P. and **Hogg, A.J.** (2007) Two-dimensional dam break flows of Herschel-Bulkley fluids: The approach to the arrested state. *J. Non-Newton fluid*, **142**, 79–94.

Mattern, F. (2005) Ancient sand-rich submarine fans: Depositional systems, models, identification, and analysis. *Earth-Sci. Rev.*, **70**, 167–202.

McArdle, B.H. and **Anderson, M.J.** (2001) Fitting multivariate models to community data: a comment on distance-based redundancy analysis. *Ecology,* **82**, 290–297.

McClelland, H.L.O., **Woodcock, N.H.** and **Gladstone, C.** (2011) Eye and sheath folds in turbidite convolute lamination: Aberystwyth Grits Group, Wales. *J. Struct. Geol.*, **33**, 1140–1147.

Mezger, T.G. (2006) The rheology handbook: for users of rotational and oscillatory. Vincentz Network, Hannover. 299 pp.

Middleton, G.V. (1966) Experiments on density and turbidity currents. I. Motion of the head. *Can. J. Earth Sci.*, **3**, 523–546.

Middleton, G.V. (1967) Experiments on density and turbidity currents. III. Deposition of sediment. *Can. J. Earth Sci.*, **4**, 475–505.

Middleton, G.V. (1993) Sediment deposition from turbidity currents. *Annu. Rev. Earth Planet. Sci.*, **21**, 89–114.

Middleton, G.V. and **Hampton, M.A.** (1973) Sediment gravity flows: mechanics of flow and deposition. In: *Turbidity and Deep Water Sedimentation* (Eds G.V. Middleton and A.H. Bouma), *SEPM, Pacific Section, Short Course Lecture Notes*, 1–38.

Middleton, G.V. and **Neal, W.J.** (1989) Experiments on the thickness of beds deposited by turbidity currents. *J. Sed. Petrol.*, **59**, 297–307.

Mohrig, D. and **Marr, J.G.** (2003) Constraining the efficiency of turbidity current generation from submarine debris flows and slides using laboratory experiments. *Mar. Petrol. Geol.*, **20**, 883–899.

Mohrig, D., **Whipple, K.X.**, **Hondzo, M.**, **Ellis, C.** and **Parker, G.** (1998) Hydroplaning of subaqueous debris flows. *Geol. Soc. Am. Bull.*, **110**, 387–394.

Mulder, T. and **Alexander, J.** (2001) The physical character of subaqueous sedimentary density flow and their deposits. *Sedimentology*, **48**, 269–299.

Murray, H.H. (1991) Overview - clay mineral applications. *Clay Clay Mineral.*, **5**, 379–395.

Mutti, E., **Tinterri, R.**, **Remacha, E.**, **Mavilla, N.**, **Angella, S.** and **Fava, L**. (1999) An introduction to the analysis of ancient turbidite basins from an outcrop perspective. *American Association of Petroleum Geologists Continuing Education Course Note Series*, **39**, American Association of Petroleum Geologists, Tulsa, UK. 61 pp.

Nasser, M.S. and **James, A.E.** (2009) The effect of electrolyte concentration and ph on the flocculation and rheological behaviour of kaolinite suspensions. *JESTEC*, **4**, 430–446.

Ndlovu, B., **Becker, M.**, **Forbes, E.**, **Deglon, D.** and **Franzidis, J.P.** (2011) The influence of phyllosilicate mineralogy on the rheology of mineral slurries. *Minerals Engineering*, **24**, 1314–1322.

Nelson, C.H. (1990) Estimated post-Messinian sediment supply and sedimentation rates on the Ebro continental margin, Spain. *Mar. Geol.*, **95**, 395–418.

Nelson, C. H., **Escutia, C.**, **Goldfinger, C.**, **Karabanov, E.**, **Gutierrez-Pastor, J.** and **De Batist, M.** (2009) External controls on modern clastic turbidite systems: three case studies. *SEPM Spec. Publ.*, **92**, 57–76.

Nyberg, B., **Helland-Hansen, W.**, **Gawthorpe, R.L.**, **Sandbakken, P.**, **Eide, C.H.**, **Sømme, T.** and **Hadler-Jacobsen, F.** (2018) Revisiting morphological relationships of modern source-to-sink segments as a first-order approach to scale ancient sedimentary systems. *Sed. Geol.*, **373**, 111–133.

Parker, G., **Garcia, M.**, **Fukushima, Y.** and **Yu, W.** (1987) Experiments on turbidity currents over an erodible bed. *J. Hydraul. Res.*, **25**, 123–147.

Pashley, R. and **Karaman, M.** (2004) Applied Colloid and Surface Chemistry. Wiley, London. 200 pp.

Paulsen, E. (2007) *Investigating the Effect of Coarse Particle Addition on the Measured Rheological Parameters of Fine Clay Slurries*. MSc thesis, University of Stellenbosch, Department of Process Engineering.

Pickering, K., **Stow, D.**, **Watson, M.** and **Hiscott, R.** (1986) Deep-water facies, processes and models: a review and classification scheme for modern and ancient sediments. *Earth-Sci Rev.*, **23**, 75–174.

Pickering, K.T. and **Hiscott, R.** (2016) Deep Marine Systems: Processes, Deposits, Environments, Tectonics and Sedimentation. Wiley, Chichester. 657 pp.

Pierce, C.S., **Haughton, P.D.W.**, **Shannon, P.M.**, **Pulham, A.J.**, **Barker, S.P.** and **Martinsen, O.J.** (2018). Variable character and diverse origin of hybrid event beds in a sandy submarine fan system, Pennsylvanian Ross Sandstone Formation, western Ireland. *Sedimentology*, **65**, 952–992.

Piper, D.J.W., **Stow, D.A. V** and **Normark, W.R.** (1984) The Laurentian Fan: Sohm Abyssal Plain. *Geo-Mar. Lett*, **3**, 141–146.

Piper, D.J.W., **Cochonat, P.** and **Morrison, M.L.** (1999) The sequence of events around the epicentre of the 1929 Grand Banks earthquake: initiation of debris flows and turbidity current inferred from sidescan sonar. *Sedimentology*, **46**, 79–97.

Porten, K.W., **Kane, I.A.**, **Warchoł, M.J.** and **Southern, S.J.** (2016) A sedimentological process-based approach to depositional reservoir quality of deep-marine sandstones: an example from the Springar Formation, north-western Vøring Basin, Norwegian Sea. *J. Sed. Res.*, **86**, 1269–1286.

Popescu, I., **Lericolais, G.**, **Panin, N.**, **Wong, H.K.** and **Droz, L.** (2001) Late Quaternary channel avulsions on the Danube deep-sea fan, Black Sea. *Mar. Geol.*, **179**, 25–37.

Pyles, D.R. and **Jennette, D.C.** (2009) Geometry and architectural associations of co-genetic debrite-turbidite beds in basin-margin strata, Carboniferous Ross Sandstone (Ireland): Applications to reservoirs located on the margins of structurally confined submarine fans. *Mar. Petrol. Geol.*, **26**, 1974–1996.

Rateev, M.A., **Lisitzyn, A.P.** and **Nosov, G.L.** (1969) The distribution of clay minerals in the oceans. *Sedimentology*, **13**, 21–43.

Reading, H.G. and **Richards, M.** (1994) Turbidite systems in deep-water basin margins classified by grain size and feeder system. *AAPG Bull.*, **78**, 792–822.

Schindler, R.J., **Parsons, D.R.**, **Ye, L.**, **Hope, J.A.**, **Baas, J.H.**, **Peakall, J.**, **Manning, A.J.**, **Aspden, R.J.**, **Malarkey, J.**, **Simmons, S.**, **Paterson, D.M.**, **Lichtman, I.D.**, **Davies, A.G.**, **Thorne, P.D.** and **Bass, S.J.** (2015) Sticky stuff: Redefining bedform prediction in modern and ancient environments. *Geology*, **43**, 399–402.

Segall, M.P., **Kuehl, S.A.** and **Gipson, M.** (1989) Clay-size minerals as indicators of modern sedimentary processes in submarine canyons: Application to the Wilmington Canyon System. *Mar. Geol.*, **90**, 175–192.

Sengun, M.Z. and **Probstein, R.F** (1989) Bimodal model of slurry viscosity with applications to coal slurries. Part 1. Theory and experiment. *Rheol. Acta.*, **28**, 382–393.

Shanmugam, G. and **Moiola, R.J.** (1995) Reinterpretation of depositional processes in a classic flysch sequence (Pennsylvanian Jackfork Group), Ouachita Mountains, Arkansas and Oklahoma. *AAPG Bull.*, **79**, 672–695.

Shanmugam, G. and **Moiola, R.J.** (1988) Submarine Fans: Characteristics, Models, Classification, and Reservoir Potential, *Earth-Sci. Rev.,* **24**, 383–428.

Singer, A. (1984) The paleoclimatic interpretation of clay minerals in sediments — a review. *Earth-Sci. Rev.*, **21**, 251–293.

Smith, R. (2004) Turbidite systems influenced by structurally induced topography in the multi-sourced Welsh Basin. *Confined Turbidite Systems*, **222**, 209–228.

Sømme, T.O., **Helland-hansen, W.**, **Martinsen, O.J.** and **Thurmond, J.B.** (2009). Relationships between morphological and sedimentological parameters in source-to-sink systems: A basis for predicting semi-quantitative characteristics in subsurface systems. *Basin Res.*, **21**, 361–387.

Southern, S. J., M. Patacci, F. Felletti. and **W. D. McCaffrey**. (2015) Influence of flow containment and substrate entrainment upon sandy hybrid event beds containing a co-genetic mud-clast-rich division. *Sedimentary Geology*, **321**, 105–122.

Spearman, J. and **Manning, A.J.** (2017) On the hindered settling of sand—mud suspensions. *Ocean Dynamics*, **67**, 465–483.

Sprague, A.R.G., **Garfield, T.R.**, **Goulding, F.J.**, **Beaubouef, R.T.**, **Sullivan, M.D.**, **Rossen, C.**, **Campion, K.M.**, **Sickafoose, D.K.**, **Abreu, V.**, **Schellpeper, M.E.**, **Jensen, G.N.**, **Jennette, D.C.**, **Pirmez, C.**, **Dixon, B.T.**, **Ying, D.**, **Ardill, J.**, **Mohrig, D.C.**, **Porter, M.L.**, **Farrell, M.E.** and **Mellere, D.** (2005) *Integrated slope channel depositional models: the key to successful prediction of reservoir presence and quality in offshore West Africa*. Colegio de Ingenieros Petroleros de Mexico, Veracruz, Mexico, pp. 1–13.

Spychala, Y.T., **Hodgson, D.M.**, **Prélat, A.**, **Kane, I.A.**, **Flint, S.S.** and **Mountney, N.P.** (2017) Frontal and lateral submarine lobe fringes: comparing sedimentary facies, architecture and flow processes. *J. Sed. Res.*, **87**, 75–96.

Stevenson, C.J., **Talling, P.J.**, **Masson, D.G.**, **Sumner, E.J.**, **Frenz, M.** and **Wynn, R.B.** (2014). The spatial and temporal distribution of grain-size breaks in turbidites. *Sedimentology*, **61**, 1120–1156.

Stow, D.A.V., **Reading, H.G.** and **Collinson, J.D.** (1996) Deep seas. In: *Sedimentary Environments: Processes, Facies and Stratigraphy* (Ed. H.G. Reading), pp. 395–453. Blackwell Science, Oxford, UK.

Stow, D.A.V., **Cremer, M.**, **Droz, L.**, **Meyer, A.W.**, **Normark, W.R.**, **Connell, S.O.**, **Pickering, K.T.**, **Stelting, C.E.**, **Angell, S.A.** and **Chaplin, C.** (1985) Mississippi Fan sedimatary facies, composition, and texture. In: *Submarine Fans and Related Turbidite Systems* (Eds A. H. Bouma, W. R. Normark and P. M. Barnes), pp. 259–266. Springer-Verlag, New York.

Sumner, E.J. and **Paull, C.K.** (2014) Swept away by a turbidity current in Mendocino submarine canyon, California. *Geophys. Res. Lett.*, **41**, 7611–7618.

Sumner, E.J., **Talling, P.J.** and **Amy, L. A.** (2009) Deposits of flows transitional between turbidity current and debris flow. *Geology*, **37**, 991–994.

Sumner, R.H. and **Westbrook, G.K.** (2001) Mud diapirism in front of the Bardos accretionary wedge: The influence of fracture zones and North America-South America plate motions. *Mar. Petrol. Geol.*, **18**, 591–613

Sumner, R.J., **Munkler, J.J.**, **Carriere, S.M.** and **Shook, C.A.** (2000) Rheology of Kaolin Slurries Containing Large Silica Particles. *J. Hydrol. Hydromech.,* **48**, 115–123.

Talling, P.J. (2001) On the frequency distribution of turbidite thickness. *Sedimentology*, **48**, 1297–1329.

Talling, P. J., (2013) Hybrid submarine flows comprising turbidity current and cohesive debris flow: Deposits, theoretical and experimental analyses, and generalized models. *Geosphere*, **9**, 460–488.

Talling, P.J., **Amy, L.A.**, **Wynn, R.B.**, **Peakall, J.** and **Robinson, M.** (2004) Beds comprising debrite sandwiched within co-genetic turbidite: origin and widespread occurrence in distal depositional environments. *Sedimentology*, **51**, 163–194.

Talling, P.J., **Wynn, R.B.**, **Masson, D.G.**, **Frenz, M.**, **Cronin, B.T.**, **Schiebel, R.**, **Akhmetzhanov, A.M.**, **Dallmeier-Tiessen, S.**, **Benetti, S.**, **Weaver, P.P.E.**, **Georgiopoulou, A.**, **Zühlsdorff, C.** and **Amy, L.A.** (2007) Onset of submarine debris flow deposition far from original giant landslide. *Nature*, **450**, 541–544.

Talling, P.J., **Masson, D.G.**, **Sumner, E.J.** and **Malgesini, G.** (2012) Subaqueous sediment density flows: Depositional processes and deposit types. *Sedimentology*, **59**, 1937–2003.

Talling, P.J., **Paull, C.K.** and **Piper, D.J.W.**, (2013) How are subaqueous sediment density flows triggered, what is their internal structure and how does it evolve? Direct observations from monitoring of active flows. *Earth-Sci. Rev.*, **125**, 244–287.

Talling, P.J., **Allin, J.**, **Armitage, D.A.**, **Arnott, R.W.C.**, **Cartigny, M.J.B.**, **Clare, M.A.**, **Felletti, F.**, **Covault, J. A.**, **Girardclos, S.**, **Hansen, E.**, **Hill, P.R.**, **Hiscott, R.N.**, **Hogg, A.J.**, **Clarke, J.H.**, **Jobe, Z.R.**, **Malgesini, G.**, **Mozzato, A.**, **Naruse, H.**, **Parkinson, S.**, **Peel, F.J.**, **Piper, D.J.W.**, **Pope, E.**, **Postma, G.**, **Rowley, P.**, **Sguazzini, A.**, **Stevenson, C.J.**, **Sumner, E.J.**, **Sylvester, Z.**, **Watts, C.** and **Xu, J.** (2015) Key future directions for research on turbidity currents and their deposits. *J. Sed. Res.*, **85**, 153–169.

Tan, X., **Hu, L.**, **Reed, A. H.**, **Furukawa, Y.** and **Zhang, G.** (2014) Flocculation and particle size analysis of expansive clay sediments affected by biological, chemical, and hydrodynamic factors. *Ocean Dynamics,* **64**, 143–157.

Tekiroglu, S.E., **Ediger, V.**, **Yemenicioglu, S.**, **Kapur, S.** and **AkÇA, E.** (2001). The experimental analysis on the Late Quaternary deposits of the Black Sea. *Oceanol. Acta*, **24**, 51–67.

Thiry, M. (2000) Palaeoclimatic interpretation of clay minerals in marine deposits: An outlook from the continental origin. *Earth-Sci. Rev.*, **49**, 201–221.

Tombácz, E. and **Szekeres, M.** (2006) Surface charge heterogeneity of kaolinite in aqueous suspension in comparison with montmorillonite. *Appl. Clay Sci.*, **34**, 105–124.

van den Berg, J.H. and **Van Gelder, A.** (1993) A new bedform stability diagram, with emphasis on the transition of ripples to plane bed in flows over fine sand and silt. In: Alluvial Sedimentation (Eds by M. Marzo and C. Puigdefabregas), *Int. Ass. Sed. Spec. Publ*., **17**, 11–21.

van Rijn, L.C. (1990) Principles of Fluid Flow and Surface Waves in Rivers, Estuaries, Seas and Oceans. AQUA Publications, Amsterdam**.** 335 pp.

van Rijn, L.C. (1993) Principles of Sediment Transport in Rivers, Estuaries and Coastal Seas. AQUA Publications, Amsterdam**.** 700 pp.

van Vliet, T. (2013) Rheology and Fracture Mechanics of Foods. CRC Press, London. 363 pp.

van Weering, T.C.E. and **van Iperen, J.** (1984) Fine-grained sediments of the Zaire deep-sea fan, southern Atlantic Ocean. In: *Fine-Grained Sediments: Deep-Water Processes and Facies* (Ed. by D.A.V. Stow and D.J.W. Piper), *Geol. Soc. London Spec .Publ.*, **15**, 95–113.

Vermeesch, P. and **Garzanti, E.** (2015) Making geological sense of 'Big Data' in sedimentary provenance analysis. *Chem. Geol.*, **409**, 20–27.

Wan, Z. (1982) *Bed Material Movement in Hyperconcentrated Flow*, Institute of Hydrodynamics and Hydraulic Engineering, Technical University of Denmark, Lyngby, Series Paper, pp. 16–24.

Wang, Z. and **Plate, E.C.H.J.** (1996) A preliminary study on the turbulence structure of flows of non-Newtonian fluid. *J. Hydraul. Res*, **34**, 345–361.

Wetzel, A. (1993) Transfer of river load to deep-sea. *AAPG Bull.*, **77**, 1679–1682.

Williams, G.J., **Knapp, I.S.**, **Maragos, J.E.** and **Davy, S.K.** (2011) Proximate environmental drivers of coral communities at Palmyra Atoll: Establishing baselines prior to removing a WWII military causeway. *Mar. Pollut. Bull.*, **62**, 1842–1851.

Wilson, D., **Davies, J.**, **Walters, R.** and **Zalasiewicz, J.** (1992) A fault-controlled depositional model for the Aberystwyth Grits turbidite system. *Geol. Mag.*, **129**, 595–607.

Windom, H.L. (1976) Lithogeneous material in marine sediments. In: *Chemical Oceanography* (Eds J.P Riley and R. Chester), pp. 103–135. Academic Press, New York.

Winguth, C., **Wong, H.K.**, **Panin, N.**, **Dinu, C.**, **Georgescu, P**., **Ungureanu, G.**, **Krugliakov, V. V.** and **Podshuveit, V.** (2000) Upper Quaternary water level history and sedimentation in the northwestern Black Sea. *Mar. Geol.*, **167**, 127–146.

Wintwerp, J.C. and **van Kesteren, W.G.M.** (2004). *Introduction to the Physics of Cohesive Sediment in the Marine Environment*. Elsevier, Developments in Sedimentology, Oxford, UK, 56. 559 pp.

Wood, A. and **Smith, A.J.** (1958) The sedimentation and sedimentary history of the Aberystwyth Grits (Upper Llandoverian). *Q. J. Geol. Soc.*, **114**, 163–195.

Xu, J. (2011) Measuring currents in submarine canyons: Technological and scientific progress in the past 30 years. *Geosphere*, **7**, 868–876.

Xu, J.P., **Sequeiros, O.E.** and **Noble, M.A.** (2014) Sediment concentrations, flow conditions, and downstream evolution of two turbidity currents, Monterey Canyon, USA. *Deep-Sea Res. Part I*, **89**, 11–34.

Yong, R.N., **Nakano, M.** and **Pusch, R.** (2012) Environmental Soil Properties and Behavior. CRC Press, London. 455 pp.

Yu, B., **Yu, M.** and **Qi, X.** (2014) Experimental Study on the Influence of Clay Minerals on the Yield Stress of Debris Flows. *J. Hydraul. Eng.*, **4**, 1–12.

Zakeri, A. (2008) A potentially devastating offshore geohazard – submarine debris flow impact on pipelines. *Explor. Prod. Oil Gas Rev.*, **6**, 118–121

Zarra, L. (2007) Chronostratigraphic framework for the Wilcox formation (Upper Paleocene-Lower Eocene) in the Deep-Water Gulf of Mexico: Biostratigraphy, Sequences, and Depositional Systems. In: The Paleogene of the Gulf of Mexico and Caribbean Basins: Processes, Events, and Petroleum Systems (Eds L. Kennan, J. Pindell and N.C. Rosen), GCSSEPM Foundation 27th Annual Bob F. Perkins Research Conference, 81–145.

Zhang, J., **Wu, S.**, **Wang, X.**, **Lin, Y.**, **Fan, H.**, **Jiang, L.**, **Wan, Q.**, **Yin, H.** and **Lu, Y.** (2015) Reservoir quality variations within a sinuous deep water channel system in the Niger Delta Basin, offshore West Africa. *Mar. Petrol. Geol.*, **63**, 166–188.

Zhang, Q., **Chen, M.**, **Liu, J.**, **Yu, Z.**, **Zhang, L.** and **Xiang, R.** (2015) Clay mineral assemblages at IODP Site U1340 in the Bering Sea and their paleoclimatic significance. *Sci. China Earth Sci.*, **58**, 707–717.